



Design and numerical modelling of integrated optical components

Wojciech Śmigaj

► To cite this version:

Wojciech Śmigaj. Design and numerical modelling of integrated optical components. Mathematical Physics. Université Paul Cézanne - Aix-Marseille III, 2010. English. <tel-00567213>

HAL Id: tel-00567213

<https://tel.archives-ouvertes.fr/tel-00567213>

Submitted on 18 Feb 2011

HAL is a multi-disciplinary open access archive for the deposit and dissemination of scientific research documents, whether they are published or not. The documents may come from teaching and research institutions in France or abroad, or from public or private research centers.

L'archive ouverte pluridisciplinaire **HAL**, est destinée au dépôt et à la diffusion de documents scientifiques de niveau recherche, publiés ou non, émanant des établissements d'enseignement et de recherche français ou étrangers, des laboratoires publics ou privés.

Thèse présentée à l'Université Paul Cézanne (Aix-Marseille III)
pour obtenir le grade de docteur en sciences

Conception et modélisation numérique de composants optiques en nanophotonique intégrée

Design and numerical modelling
of integrated optical components

Wojciech ŚMIGAJ

22 septembre 2010

Laboratoire d'accueil Institut Fresnel, équipe CLARTE
Formation doctorale physique théorique et mathématique

Membres du jury

Philippe LALANNE	rapporteur
Andrey A. FEDYANIN	rapporteur
Didier LIPPENS	examineur
Maciej KRAWCZYK	examineur
Mathias VANWOLLEGHEM	examineur
Stefan ENOCH	directeur de thèse
Boris GRALAK	tuteur de thèse

Contents

Acknowledgements	5
Résumé en français	7
I Preliminaries	15
1.1 Introduction	15
1.2 Outline of the thesis	16
1.3 Notational conventions	17
1.4 Maxwell's equations	18
2 Effective-medium model of photonic crystals	21
2.1 Introduction	21
2.2 Definition of the effective parameters of photonic crystals	22
2.2.1 Preliminaries: the homogeneous-medium case	22
2.2.2 Existing definitions	23
2.2.3 Proposed definition	24
2.3 Influence of symmetries on the effective parameters	27
2.3.1 Real-valuedness	28
2.3.2 Continuity and boundedness	28
2.4 Examples	31
2.4.1 Hexagonal lattice	31
2.4.2 Square lattice	35
2.4.3 Remarks	40
2.5 Validity of the single-mode approximation	40
2.6 Conclusions	44
3 Antireflection gratings for photonic crystals	45
3.1 Introduction	45
3.2 Types of antireflection structures	45
3.2.1 Antireflection structures for homogeneous media	45
3.2.2 Antireflection structures for photonic crystals	46
3.3 Design procedure	48
3.4 Examples	53
3.4.1 A photonic-crystal flat lens	53
3.4.2 A supercollimating photonic crystal	59
3.4.3 A photonic-crystal superprism	62
3.5 Conclusions	63

4	Magneto-optical circulators	65
4.1	Introduction	65
4.1.1	Basic characteristics of isolators and circulators	65
4.1.2	Routes to nonreciprocity	66
4.1.3	Experimental realisations of optical isolators and circulators	67
4.1.4	Outline of this chapter	72
4.2	Extension of the coupled-wave model	72
4.2.1	Inclusion of direct coupling between waveguides	72
4.2.2	Inclusion of radiation loss	77
4.3	Cavities with circular symmetry	79
4.4	Photonic-crystal-based circulators	82
4.5	Rib-waveguide-based circulators	90
4.5.1	Introduction	90
4.5.2	Numerical calculations	92
4.5.3	Geometry optimisation	97
4.5.4	Fabrication	101
4.6	Simulations of three-dimensional axisymmetric cavities	101
4.6.1	Evaluation of possible three-dimensional geometries	101
4.6.2	Towards cavities with higher quality factor	105
4.7	Conclusions and perspectives	111
5	Numerical methods	115
5.1	Multiple-scattering method for systems containing gyrotropic media	115
5.2	Calculation of photonic-crystal band structures with Fourier-Bessel expansions	118
5.2.1	Introduction	118
5.2.2	Formulation	119
5.2.3	Numerical examples	123
5.2.4	Conclusions	128
5.3	Finite-element simulations of three-dimensional axisymmetric cavities	128
5.3.1	Introduction	128
5.3.2	Formulation	129
5.3.3	Numerical implementation	137
5.3.4	Evaluation of accuracy	138
6	Conclusions and perspectives	143
	Bibliography	145

Acknowledgements

I have been very privileged to have undoubtedly the most supportive, reliable and friendly advisor anyone could ask for, namely Boris Gralak. While not hesitating to offer his advice and share his experience, he let me enjoy a complete liberty in the pursuit of my scientific interests. I really appreciated his eye for detail, his striving for clarity and precision (even as I am writing these words, Boris is still hunting for the remaining mistakes in the French summary of this thesis), as well as his inextinguishable optimism. In addition to being a mentor, he became a friend. I thank him and Mylène for all the evenings we spent together. I am also indebted to Stefan Enoch, who agreed to act as the director of this thesis, in spite of his numerous responsibilities as the associate director of Institut Fresnel.

My gratitude extends towards all the members of the CLARTE team in Institut Fresnel, who gave me a warm welcome upon my arrival to Marseille three years ago and have ensured an excellent working environment ever since. Four persons deserve a special mention. Gérard Tayeb was always willing to share his experience in the development of computational methods. On various occasions, he took time to participate in rehearsals of my oral presentations, and his help and advice was invariably much appreciated. I was also fortunate to be able to collaborate with Daniel Maystre, whose profound understanding of the mathematical foundations of numerical algorithms is unmatched by anyone I know. Sebastián Guenneau and Javier Romero-Vivas took active part in the development of magneto-optical circulators and performed numerous simulations that helped to optimise the devices. Besides, Javier and I shared the joys and sorrows of a foreigner in France (« C'est Marseille... »).

This thesis owes also a lot to collaborations with several research groups from outside Marseille.

The work on antireflection gratings for photonic crystals was done in collaboration with teams from Université de Lille I and Université de Bourgogne in Dijon. Maxence Hofman and Olivier Vanbésien from the DOME team in Université de Lille I manufactured samples of photonic-crystal flat lens covered with the antireflection gratings we had designed. Geoffroy Scherrer, Benoît Cluzel and Frédérique de Fornel from the OCP team in Université de Bourgogne performed the near-field characterisation of these samples. I would like to thank all of them for the interesting and fruitful meetings. Special thanks go to Olivier for giving us all a taste of the delicious Flemish cuisine. I am also indebted to Didier Lippens, director of the DOME team, for having accepted the invitation to act as a member of the examining board.

I greatly enjoyed the collaboration with the members of the MMS team in Institut d'Électronique Fondamentale (IEF) in Orsay on magneto-optical circulators. I am particularly grateful to Mathias Vanwolleghem, who introduced me to the fascinating topic of non-reciprocity in optics, infecting me with his enthusiasm. Luba Magdenko and Béatrice Dagens devoted a lot of effort to the fabrication of prototypes of the circulators, gradually taming the etch-resistant bismuth-iron-garnet substrates. Luba also took part in the numerical modelling of the circulators. Always ready to ask inconvenient questions and to point out the experimental constraints, she was fun to work with. Thanks are due to the whole team for the innumerable discussions and e-mail interchanges we have had, as well as for inviting Boris and me to spend a month at IEF.

I am no less indebted to Maciej Krawczyk from Adam Mickiewicz University in Poznań, the advisor for my Master's thesis, who has also accepted to be a member of the examination board. Thanks to

Maciej I have been able to keep in touch with my alma mater. I am grateful for his continuous support and for his genuine interest in the progress of my research. I am also indebted to Henryk Puzkarski, director of the Surface Physics Division in Poznań, for his willingness to share his experience and advice. I particularly want to thank all the members of Prof. Puzkarski's group for the warm welcome they gave me whenever I came back to Poznań.

I would like to extend my sincere gratitude to Philippe Lalanne from Institut d'Optique in Palaiseau and to Andrey A. Fedyanin from Lomonosov Moscow State University for accepting to write reviews of this thesis. I also acknowledge the French Ministry of Higher Education and Research for providing its funding.

Finally, I would like to thank all my friends and my family, whose presence has been absolutely invaluable during these three years. I am deeply grateful to my parents and sister for their continuing support, kindness and love. My fellow Ph.D. students from the CLARTE and HIPE teams in Institut Fresnel, Alexis, Fabien, Raphaël P., Raphaël L., Mohamed, Xiaoyun, Frédéric, Muamer and Guillaume contributed to making the lab the great place it was. My special thanks go to all the members of Aumônerie Jer'aum,* who made me feel at home in Marseille. I will miss you much when I leave! Lastly, I want to thank all of my Polish friends, especially Kasia, Małgosia, Milena, Alicja, Marcin, Jacek, Wawrzyniec and Karol.

Wojciech Śmigaj, Marseille, 1 September 2010

* Jean Pol and Jean, Louis and Paul, Jules Hervé and Estelle, Jeannette, Alexandra, Lucie, Marion, Alexis, Frédéric, Césaire, Romuald, Matthieu, Descartes, Jean-François and Yen, Rakia, Chinh, Olga, Damien, Jean-Marie, Charles and Yvri, Katell, Randy, Thibault, Priscilla, Melissa...

Résumé en français

Contexte historique

L'aube de la seconde moitié du XX^{ème} siècle a été marquée par l'invention des circuits électroniques intégrés fabriqués dans des couches minces semiconductrices. En raison de leur faible coût et de leur petite taille, les circuits intégrés ont rapidement presque supplanté les « gros » composants électroniques : les bobines, les tubes électroniques etc. Ils ont fourni les moyens de la révolution technologique qui a fait des appareils électroniques compacts une partie intégrante de la vie moderne.

Peu de temps après la première démonstration expérimentale du laser en 1960, le concept des circuits *optiques* intégrés est apparu. Par analogie avec leurs homologues électroniques, ils devaient ouvrir la voie à la miniaturisation des dispositifs optiques. Depuis la découverte du laser, des progrès significatifs ont été accomplis : de nombreux composants photoniques intégrés, tels que coupleurs, filtres ou multiplexeurs, sont couramment utilisés dans les dispositifs disponibles dans le commerce. Toutefois, il faut admettre que le développement de la technologie des circuits optiques intégrés a été beaucoup plus lent que celui des circuits électroniques. Pour preuve, si les processeurs modernes contiennent des millions de transistors sur une seule puce, les circuits intégrés optiques les plus complexes réalisés à ce jour se composent d'à peine quelques centaines de composants [1–4].

Il semble y avoir deux raisons principales à cette différence. Premièrement, la longueur d'onde de la lumière aux fréquences de télécommunications, qui est de l'ordre de 0.1–1 μm dans des matériaux diélectriques typiques, est beaucoup plus grande que la longueur de l'onde de Broglie d'un électron au niveau de Fermi d'un métal classique, 0.1–1 nm [5, p. 120]. Celle-ci est si petite que, jusqu'à récemment, les propriétés ondulatoires des électrons pourraient être quasiment ignorées dans la conception de composants électroniques, qui pourraient donc être miniaturisés sans encombre. Au contraire, la longueur d'onde de la lumière constitue une vraie limite de la taille des composants optiques.* Deuxièmement, pour des applications diverses, il est avantageux d'utiliser des substrats avec des propriétés physiques particulières, présentant par exemple d'importants effets électro-, magnéto- ou acousto-optiques. Étant donné que ces propriétés sont difficiles à obtenir simultanément dans un seul matériau, les premiers circuits optiques intégrés ont été construits de la façon dite hybride, où tous les composants sont fabriqués séparément en utilisant des matériaux et technologies différents avant d'être assemblés sur un seul substrat [7, p. 9]. Avec cette approche, chaque composant peut être optimisé séparément ; par contre, l'alignement et le couplage des différents éléments constituent une difficulté de taille. Ainsi, les circuits optiques intégrés hybrides ne comportent pas plus que quelques composants. Les circuits intégrés les plus complexes sont donc fabriqués de façon monolithique, où tout le système est gravé dans un seul substrat. Actuellement, la technologie de ce type la plus avancée est certainement celle qui est fondée sur le phosphore d'indium.

L'introduction de la notion de cristaux photoniques à la fin des années 1980 [8, 9] a profondément influencé la recherche sur les circuits optiques intégrés. Le cristal photonique est défini comme un sys-

* Les composants plasmoniques, qui constituent actuellement le sujet de recherches actives, pourraient néanmoins permettre d'aller plus loin dans la miniaturisation des dispositifs optiques [6].

tème dans lequel la permittivité et la perméabilité dépendent périodiquement de la variable d'espace : ainsi, il peut être considéré comme un analogue électromagnétique d'un solide cristallin. La périodicité de la permittivité et de la perméabilité peut donner lieu à des « gaps », c'est-à-dire, des bandes de fréquences où aucun état propagatif (transportant de l'énergie) n'existe à l'intérieur du cristal. Rapidement, pour des fréquences situées dans un gap, des défauts linéaires le long desquels des modes localisés peuvent se propager ont été imaginés dans des cristaux photoniques ; de tels défauts peuvent donc servir de guides d'onde [10]. En même temps, on a démontré que les défauts ponctuels dans les cristaux photoniques peuvent se comporter comme des résonateurs avec la valeur du ratio entre le facteur de qualité et le volume du mode potentiellement très importante [10]. Toutefois, c'est une autre découverte qui va révéler l'énorme intérêt envers les cristaux photoniques en tant que moyen de miniaturiser les circuits optiques intégrés : les modes de guides d'onde à cristaux photoniques peuvent se propager le long des coudes pratiquement sans pertes d'énergie [11]. En effet, les rayons de courbure des guides d'onde standards doivent être de l'ordre de quelques millimètres afin de maintenir les pertes à un niveau raisonnable [10]. En revanche, les guides à cristaux photoniques peuvent avoir des coudes avec un rayon de courbure d'environ un micromètre. Jusqu'ici, de nombreux dispositifs optiques basés sur les guides d'onde et résonateurs à cristaux photoniques ont été proposés, et plusieurs d'entre eux ont été réalisés expérimentalement. Pour une revue relativement récente de l'état actuel de la recherche sur les cristaux photoniques, le lecteur peut consulter la référence 12.

Alors que les premières études de cristaux photoniques ont porté principalement sur la recherche de structures fournissant le gap le plus large et sur la conception de composants fonctionnant dans le gap, la dernière décennie a vu la communauté porter une attention croissante aux propriétés inhabituelles des cristaux photoniques *en dehors* des gaps. Contrairement aux diélectriques homogènes, dont la surface d'isofréquence est une ellipsoïde, la forme de la surface d'isofréquence des cristaux photoniques peut être très compliquée.* En outre, la vitesse de groupe dans un cristal photonique peut être orientée dans n'importe quelle direction. Cette richesse de la relation de dispersion donne lieu à des phénomènes inhabituels [13], comme la réfraction négative de la lumière [14], l'apparition de faisceaux autocollimatés [15] ou l'effet « superprism » [16]. Ainsi, il a été reconnu que même les cristaux photoniques sans défauts (la présence de surfaces exceptée) peuvent constituer des dispositifs utiles, par exemple des lentilles planes [17, 18] ou des diviseurs de faisceau [19].

Structure de la thèse

Cette thèse est consacrée à la conception et l'analyse théorique et numérique de certains composants en cristaux photoniques. Dans le chapitre 1, nous donnons une brève introduction à la thématique de la thèse, nous définissons les notations utilisées dans la suite, et nous rappelons quelques faits de base sur les équations de Maxwell, fondement de tous les développements ultérieurs. L'essence de la thèse, les chapitres 2 à 5, se divise naturellement en trois parties distinctes. Dans les chapitres 2 et 3, nous étudions les cristaux photoniques bidimensionnels sans défauts, limités par une ou deux surfaces planes parallèles. En particulier, nous nous intéressons à la dépendance des propriétés de tels cristaux à l'égard de la structure des interfaces les séparant des milieux homogènes. Dans le chapitre 4, qui constitue la deuxième partie essentielle de cette thèse, nous tournons notre attention vers un type de composants optiques plus traditionnels, puisque basés sur les guides d'onde : les circulateurs magnéto-optiques. La troisième partie de la thèse, le chapitre 5, est consacrée à la présentation de quelques méthodes numériques développées pour les simulations des dispositifs analysés dans les chapitres précédents. La thèse se termine par le chapitre 6, dans lequel nous mettons en évidence les résultats qui nous semblent les plus importants

* On observe la même chose dans la théorie de l'état solide : la surface de Fermi dans un gaz d'électrons libres est sphérique, mais dans un solide réel, elle a souvent une forme très complexe, parfois appelée, judicieusement, un *monstre*.

et nous indiquons les perspectives des futurs travaux sur certains sujets. Ci-dessous nous résumons le contenu des chapitres qui constituent le corps de la thèse.

Chapitre 2 : Modèle du milieu effectif pour les cristaux photoniques

Comme mentionné ci-dessus, une caractéristique essentielle des cristaux photoniques réside dans la richesse de leur relation de dispersion. La forme des surfaces d'isofréquence des cristaux photoniques peut être très complexe : ils contiennent parfois des changements de direction brutaux séparant des régions planes ou même concaves. Toutefois, à certaines fréquences, ils peuvent également atteindre une forme ellipsoïdale, caractéristique pour des milieux homogènes. En conséquence, la question se pose si les cristaux peuvent alors être correctement décrits par le *modèle du milieu effectif*, dans lequel ils sont représentés par un matériau homogène avec une certaine permittivité ϵ et perméabilité μ . Comme les matériaux homogènes sont incomparablement plus faciles à analyser que les matériaux structurés, une réponse affirmative simplifierait le développement de dispositifs à cristaux photoniques, en particulier de ceux qui utilisent l'effet de la réfraction négative [14]. En effet, la plupart des composants basés sur ce phénomène, comme les célèbres *superlentilles* [17], ont été conçus pour des matériaux à indice négatif *homogènes* imaginés par Veselago [20].

De nombreux documents traitant de ce sujet ont déjà été publiés [21–32], donnant lieu à plusieurs définitions des paramètres effectifs des cristaux photoniques, reportées au paragraphe 2.2.2. Cependant, ces définitions sont généralement introduites de façon heuristique et manquent de justification formelle. En outre, pour toutes ces définitions, la confrontation du coefficient de réflexion du cristal calculé rigoureusement avec celui du milieu effectif correspondant n'a jusqu'alors été effectuée que pour l'incidence normale [24–26] ou quasi-normale [28]. Pourtant, de nombreuses applications, y compris celles utilisant la réfraction négative, s'appuient sur le comportement des ondes incidentes aux grands angles, voire des ondes évanescentes. Le domaine de validité de l'approximation du milieu effectif est, par conséquent, encore mal connu.

L'objectif du travail présenté dans le chapitre 2 est de remédier à ces lacunes. Dans la section 2.2, nous adoptons l'hypothèse de *l'approximation monomode* pour fournir une justification mathématique rigoureuse à une certaine définition des paramètres effectifs des cristaux photoniques bidimensionnels. Dans la section 2.3, nous étudions l'influence de la symétrie du plan de troncature du cristal et celle des modes propres du cristal sur le comportement de ses paramètres effectifs. En particulier, nous dérivons les conditions dans lesquelles les paramètres effectifs sont réels et bornés pour tous les angles d'incidence. Nous généralisons ainsi le résultat obtenu par Pierre and Gralak [27] dans le cas unidimensionnel. Pour évaluer la précision du modèle du milieu effectif, nous comparons dans la section 2.4 les valeurs du coefficient de la réflexion spéculaire prévu dans le cadre du modèle avec les résultats des calculs numériques rigoureux. Ces tests, effectués pour deux cristaux différents à un nombre de fréquences et dans tout le domaine d'angle d'incidence, indiquent que la précision du modèle est limitée par celle de l'hypothèse de départ, l'approximation monomode.

Ces résultats ont imposé d'analyser de façon précise le domaine de validité de l'approximation monomode. Dans la section 2.5, nous établissons un lien entre les amplitudes relatives d'excitation des modes propres d'un cristal et le spectre de Fourier des champs électrique et magnétique de ces modes sur le plan de troncature du cristal. Ce lien est utilisé pour formuler un critère d'estimation de la précision de l'approximation monomode : cette hypothèse est d'autant plus pertinente que la courbe d'isofréquence du cristal photonique se rapproche de celle du milieu homogène avec l'indice de réfraction égal à la moyenne de l'indice de réfraction du cristal. Enfin, nous considérons le cas particulier des modes engendrant la réfraction négative. Nous observons que leur excitation par une onde plane est accompagnée pour la plupart des angles d'incidence par une excitation simultanée d'autres modes (évanescents) avec

une amplitude importante. Dans ce cas, l'approximation monomode d'un cristal photonique présentant le phénomène de réfraction négative ne peut être considéré comme (relativement) précise que près de l'incidence normale. Notre analyse montre qu'il est hasardeux de traiter un tel cristal photonique comme un matériau homogène pour des angles d'incidence importants ou dans le régime d'ondes évanescentes. Finalement, le comportement de systèmes contenant des matériaux d'indice négatif homogènes peut s'avérer considérablement différent lorsque ces matériaux sont remplacés par des cristaux photoniques, même si les courbes d'isofréquence (et, par conséquent, les indices de réfraction définis par l'intermédiaire de la vitesse de phase) des deux milieux sont identiques.

Chapitre 3 : Réseaux antiréfléchissants pour des cristaux photoniques

Les courbes du coefficient de réflexion des cristaux photoniques étudiés dans le chapitre 2 (figures 2.5, 2.7, 2.10, 2.12 et 2.13) montrent que des ondes réfléchies d'amplitude importante sont souvent générées sur la surface des cristaux photoniques. Dans de nombreuses applications, il est au contraire souhaitable d'obtenir un transfert d'énergie parfait entre l'onde plane incidente et le mode propre propagatif du cristal photonique (ou, plus rarement, plusieurs modes propagatifs). Les ondes réfléchies de caractère propagatif doivent donc être éliminées. Le chapitre 3 concerne la conception de *structures antiréfléchissantes* qui, placées sur la surface d'un cristal photonique, diminuent significativement la fraction d'énergie perdue dans les ondes réfléchies. Après avoir examiné les classes de telles structures proposées à ce jour (section 3.2), dans la section 3.3, nous proposons une nouvelle méthode de conception de réseaux antiréfléchissants avec une tolérance angulaire importante.

L'algorithme de conception que nous proposons consiste en trois étapes. Premièrement, les paramètres d'une couche homogène antiréfléchissante sont calculés à partir d'un modèle du milieu effectif du cristal photonique en question. Deuxièmement, une théorie analytique du milieu effectif des réseaux lamellaires binaires est utilisée pour trouver les paramètres d'un réseau composé des seuls matériaux constitutifs du cristal, et dont les propriétés sont proches de celles de la couche obtenue à l'étape précédente. Troisièmement, la forme de la grille est raffinée à l'aide d'une routine numérique de recherche locale qui vise à minimiser la réflectance moyenne de la structure dans la gamme désirée d'angle ou de la fréquence. Cette dernière étape est nécessaire en raison des approximations faites dans les dérivations analytiques utilisées dans les deux premières étapes de la procédure.

Dans la section 3.4, nous appliquons la méthode proposée à trois cristaux dont les courbes d'isofréquence sont de courbure différente : un cristal présentant le phénomène d'autocollimation, avec une courbe isofréquence très plate ; un cristal présentant l'effet de réfraction négative, avec une courbe d'isofréquence presque circulaire ; et un cristal photonique du type « superprism », dont la courbe isofréquence a des cornes. Dans les deux premiers cas, nous réussissons à concevoir des réseaux antiréfléchissants garantissant une réflectance très faible dans une vaste gamme angulaire. Les structures obtenues sont très compactes et paraissent simple à fabriquer ; en fait, l'amélioration apportée par ces réseaux antiréfléchissants à la transmission à travers une lentille plate de cristal photonique (basée sur l'effet de réfraction négative) a déjà été confirmée expérimentalement [33]. Cependant, dans le cas du cristal du type « superprism », la procédure de conception échoue à cause de la violation de certaines contraintes sur l'impédance effective du cristal, qui doivent être remplies pour que la couche antiréfléchissante générée dans la première étape puisse être approchée par un réseau binaire constitué de matériaux réalistes. L'existence de ces contraintes est la limitation principale de la procédure présentée.

Chapitre 4 : Circulateurs magnéto-optiques

Dans le chapitre 4, nous étudions le problème de la miniaturisation des circulateurs optiques, qui appartiennent aux derniers composants optiques intégrés importants dont la version intégrée ne soit pas encore disponible dans le commerce. Le circulateur est un dispositif reliant $n \geq 3$ guides d'onde de telle sorte que l'énergie entrant par le guide W_i ($1 \leq i < n$) est entièrement transférée au guide W_{i+1} et l'énergie entrant par le guide W_n est transférée au guide W_1 . Un dispositif apparenté, l'isolateur, relie deux guides d'onde ainsi que le transfert d'énergie soit interdit dans un sens, mais autorisé dans l'autre. Manifestement, le circulateur peut également faire fonction d'isolateur.

Ces deux composants ont plusieurs applications importantes. Ils peuvent servir à éliminer les ondes réfléchies des composants d'impédance mal adaptée dans des circuits complexes ; la présence de telles ondes peut donner lieu à des interférences indésirables et couplages parasites [34]. Les composants en question sont également employés dans l'acheminement des signaux dans des dispositifs tels que les multiplexeurs [35]. Dans le domaine optique, l'application la plus importante des isolateurs est sans doute la protection des lasers de la lumière réfléchie, qui perturbe la configuration des ondes stationnaires dans une cavité laser et peut entraîner le laser à devenir instable [36].

Les circulateurs et les isolateurs sont dits des dispositifs *non-réciproques*. Cela signifie, en particulier, qu'ils ne peuvent pas être réalisés en utilisant uniquement des matériaux linéaires, invariants dans le temps et dont la permittivité et la perméabilité s'expriment par des tenseurs symétriques. La façon la plus commune d'obtenir un système non-réciproque est d'y inclure un matériau présentant l'*effet magnéto-optique* : par exemple, un grenat synthétique tel que le grenat de fer et bismuth. Traditionnellement, les isolateurs sont constitués d'une plaque d'un matériau magnéto-optique placée entre deux polariseurs, P_1 et P_2 , tournés de 45° l'un par rapport à l'autre. Le fonctionnement d'un tel isolateur s'appuie sur l'effet de Faraday, qui consiste en une rotation non-réciproque du plan de polarisation des ondes électromagnétiques traversant un matériau magnéto-optique dans la direction parallèle à celle d'un champ magnétique statique externe. Grâce à cet effet, le plan de polarisation des ondes qui entrent dans l'isolateur par le polariseur P_1 (par exemple) s'aligne progressivement avec l'axe du polariseur P_2 ; par conséquent, ces ondes sont transmises à travers le dispositif. En revanche, le plan de polarisation des ondes entrant par le polariseur P_2 devient perpendiculaire à l'axe du polariseur P_1 , par lequel ils sont donc absorbés.

Malheureusement, en raison de leur structure non plane, les isolateurs décrits ci-dessus ne peuvent être produits comme éléments d'un circuit optique intégré. En conséquence, dans les deux dernières décennies, beaucoup d'efforts ont été faits pour concevoir des isolateurs et des circulateurs adaptés à la fabrication sur puce (voir la référence 35 pour une revue de la littérature). Le fonctionnement de la plupart des dispositifs proposés jusqu'à présent est basé sur la conversion non-réciproque des modes propres d'un guide d'onde (un phénomène analogue à l'effet de Faraday) ou sur l'interférence des ondes se propageant dans deux ou plusieurs guides d'onde placés dans un champ magnétique statique externe. Cependant, l'effet magnéto-optique est généralement faible : il ne peut influencer sensiblement le comportement de la lumière que si celle-ci interagit avec un matériau magnéto-optique sur un chemin optique très long, typiquement $\sim 1000\lambda$, où λ est la longueur d'onde de la lumière. En conséquence, les isolateurs et circulateurs basés sur des guides d'onde sont très longs (~ 1 mm), ce qui rend difficile leur intégration avec d'autres composants optiques fondamentaux, beaucoup plus petits.

Une stratégie de miniaturisation potentielle consiste à employer des résonateurs optiques pour allonger le temps de l'interaction de la lumière avec le matériau magnéto-optique, au prix d'une réduction de la bande passante du composant. En 2005, Wang et Fan [34, 37] ont proposé un circulateur magnéto-optique inspiré d'une classe de dispositifs couramment utilisés dans le domaine micro-ondes, où, cependant, les effets induits par un champ magnétique statique externe sont beaucoup plus importants. Le circulateur de Wang et Fan se compose de trois guides d'onde à cristal photonique couplés à une cavité à cristal

photonique dans laquelle deux modes propres bien localisés peuvent être excités. Leurs fréquences sont décalées l'une par rapport à l'autre en présence d'un champ magnétique statique externe, la matrice du cristal photonique étant d'un matériau magnéto-optique. En utilisant le formalisme du couplage faible, on peut montrer qu'un tel système fonctionne comme un circulateur.

Il faut noter, cependant, que la séparation des fréquences des deux modes de la cavité originale présentée dans les références 34 et 37 est négligeable dans un champ magnétique statique externe *uniforme*. Elle ne devient acceptable que si le matériau magnéto-optique dans la cavité est divisé en de nombreux domaines magnétiques polarisés dans les sens contraires, chacun d'une superficie d'une fraction de μm^2 . La réalisation de tels domaines est, en pratique, très difficile technologiquement, car elle nécessite un contrôle précis – à l'échelle nanométrique – du champ magnétique statique externe appliqué. Pour cette raison, le dispositif conçu par Wang et Fan n'a jamais été fabriqué. L'objectif de la recherche présentée dans le chapitre 4 était d'élaborer la conception d'un circulateur s'appuyant sur un résonateur magnéto-optique et capable de fonctionner dans un champ magnétique statique externe *uniforme*, c'est-à-dire, avec tout le matériau magnéto-optique aimanté uniformément.

Nous commençons par étudier comment la géométrie d'une cavité magnéto-optique bidimensionnelle placée dans un champ magnétique statique externe influence le décalage des fréquences de ses deux modes propres (section 4.3). Afin de mieux comprendre le problème, nous nous concentrons sur le modèle simplifié d'une cavité axisymétrique, c'est à dire composée d'une série d'anneaux concentriques. De telles structures peuvent être traitées analytiquement ; en particulier, nous sommes en mesure de montrer que le décalage maximal des fréquences dans un champ magnétique statique externe uniforme est obtenu pour des cavités ayant la forme d'un miroir de Bragg annulaire. Nous obtenons ainsi une procédure explicite pour la conception de cavités axisymétriques optimisées pour le fonctionnement dans un champ magnétique statique externe uniforme, ce qui constitue le fondement de cette étude.

L'étape suivante de la conception du circulateur est de coupler efficacement la cavité avec les guides d'onde d'entrée et de sortie. Dans les sections 4.4 et 4.5, deux classes de structures sont examinées : les circulateurs à base de cristaux photoniques, semblables à ceux étudiés dans les références 34 et 37, et les circulateurs dans lesquels le revêtement à cristal photonique est supprimé et la cavité est couplée directement à des guides d'onde standards. Cette élimination du cristal photonique conduit à une simplification importante de la géométrie du dispositif. Néanmoins, l'analyse théorique de son fonctionnement devient un peu plus compliquée, car on doit tenir compte des effets du couplage direct entre les guides d'onde et des pertes d'énergie par le rayonnement dans le plan du dispositif, comme il est décrit dans la section 4.2. Les performances des deux catégories de circulateurs sont évaluées à l'aide de simulations numériques rigoureuses. Nous concluons que la simplification de géométrie résultant de l'élimination du cristal photonique ne doit pas être accompagnée d'une détérioration de la performance du composant. Par conséquent, dans la suite du chapitre 4 nous nous concentrons sur les circulateurs avec des guides standards, c'est-à-dire sans cristaux photoniques.

A ce stade, il convient de résumer les résultats des tests expérimentaux de nos circulateurs, fabriqués et caractérisés par L. Magdenko et B. Dagens (Institut d'Electronique Fondamentale, Orsay, France) dans des hétérostructures composées des grenats de bismuth et fer et de gadolinium et gallium. Ces résultats révèlent un problème significatif dans la conception originale des cavités : des pertes d'énergie importantes par rayonnement hors plan du dispositif. Elles sont une conséquence du fait que la conception n'était originellement basée que sur des simulations bidimensionnelles (l'approximation d'indice effectif utilisée dans certaines des simulations s'est avérée ne pas avoir été assez précise). C'est pourquoi, dans la dernière partie du chapitre 4, nous présentons les premiers résultats des simulations *tridimensionnelles* des cavités, obtenus avec la méthode des éléments finis décrite dans la section 5.3. Nous démontrons que le problème des pertes hors-plan peut être surmonté par un ajustement approprié de la géométrie de la cavité. Plus précisément, le facteur de qualité des modes propres peut être sensiblement amélioré en

recouvrant la cavité avec un matériau ayant un indice de réfraction proche de celui du substrat et par l'optimisation numérique des positions et des largeurs des anneaux constitutifs de la cavité. A ce jour, ce raffinement de la conception basé sur des simulations tridimensionnelles demande à être confirmé expérimentalement.

Chapitre 5 : Méthodes numériques

Dans le chapitre 5, nous présentons les méthodes de calcul développées au cours de cette thèse et utilisées pour obtenir une partie des résultats présentés dans l'ensemble des chapitres.

La section 5.1 est consacrée à la méthode de *diffusion multiple* [38–40] pour la solution du problème de la diffusion de lumière par des cristaux photoniques bidimensionnels composés de cylindres circulaires. Cette technique est reconnue depuis longtemps comme l'une des méthodes les plus efficaces pour traiter ce type de problèmes. La raison en est double. D'une part, les fonctions de base utilisées pour développer le champ électromagnétique (à savoir les séries de Fourier-Bessel) sont des solutions exactes des équations de Maxwell, et donc elles sont bien adaptées pour représenter le champ électromagnétique en présence de ces domaines. Deuxièmement, comme les fonctions de base sont séparables en coordonnées polaires, les conditions de continuité satisfaites par le champ électromagnétique sur les surfaces des cylindres sont simples à exprimer et imposer. Dans la section 5.1, nous montrons que la méthode en question peut être généralisée aisément au cas des cristaux photoniques contenant des milieux gyrotropiques qui respectent la même symétrie axiale que les tiges circulaires [les tenseurs de permittivité et perméabilité ont alors la forme donnée par l'équation (5.5)]. Nous notons, toutefois, qu'une extension similaire pour le cas des matériaux avec une anisotropie plus générale n'est pas possible, car la réduction des équations de Maxwell à l'équation de Helmholtz n'est alors possible qu'au prix d'un changement de coordonnées transformant des cercles en des ellipses, ce qui engendre des effets secondaires indésirables.

Compte tenu de l'efficacité et la simplicité de la méthode de diffusion multiple, cette méthode a été également appliquée au calcul de la relation de dispersion des cristaux photoniques *infinis* composés de cylindres ou de sphères [41–47]. Elle nécessite, pourtant, de calculer explicitement le champ produit par un nombre infini de diffuseurs disposés sur un réseau périodique. Ce champ peut être exprimé par une série dite « lattice sum ». Malheureusement, des telles séries sont lentement convergentes, et les techniques particulières nécessaires pour l'accélération de leur calcul compliquent considérablement la mise en œuvre de la méthode par rapport au cas d'un système fini.

Dans la section 5.2, nous proposons une technique élégante de calcul de la relation de dispersion des cristaux photoniques composés de cylindres circulaires. Comme la méthode de diffusion multiple, elle s'appuie sur le développement du champ électromagnétique sur des solutions exactes des équations de Maxwell (les séries de Fourier-Bessel), avec l'avantage d'éviter le calcul des « lattice sums ». L'idée de base est très simple : le champ dans une maille d'un cristal photonique est développé sur des solutions particulières de l'équation de Helmholtz, et les conditions de Bloch sur les limites de la maille sont imposées par collocation. Cette approche est en fait similaire à la technique utilisée dans les simulations de réseaux avec la méthode de sources fictives afin d'éviter le calcul des fonctions de Green périodiques [48]. La méthode proposée ici partage également de nombreuses caractéristiques avec la technique des opérateurs de Dirichlet-Neumann, mise au point dans le groupe de Lu [49, 50]. Par rapport à cette technique, la présente méthode est plus directe et plus efficace, mais aussi moins générale (spécialement adaptée aux calculs de la relation de dispersion).

La principale vertu de la méthode que nous proposons est sa grande efficacité : en raison de la convergence exponentielle des résultats, il est possible d'atteindre une précision relative meilleure que 10^{-10} avec un coût de calcul modeste, comme il est démontré dans plusieurs exemples étudiés dans le paragraphe 5.2.3. Par conséquent, la technique en question peut fournir des valeurs de référence extrê-

mement précises aux fins des tests d'autres méthodes numériques. La haute précision est aussi précieuse dans les études avec des effets faibles, tels que la non-réciprocité entraînée par l'influence d'un champ magnétique statique sur la propagation des ondes aux fréquences optiques.

Pour les cristaux photoniques dont la maille ne contient qu'une seule inclusion circulaire, la mise en œuvre de cette méthode est directe. Cependant, si plusieurs inclusions sont présentes, la maille doit être décomposée en sous-mailles englobant les inclusions individuelles, ce qui complique à un certain degré la mise en œuvre de la méthode. Les inconvénients principaux de la technique en question sont (1) sa restriction à des systèmes contenant des inclusions *circulaires* et (2) la dégradation visible de sa précision à la présence des sous-mailles dont la forme diffère nettement de celle d'un cercle centré sur l'inclusion.

Dans la section 5.3, nous décrivons une variante de la méthode des éléments finis utilisée pour calculer les modes propres de cavités axisymétriques tridimensionnelles ouvertes, contenant des matériaux gyrotropiques. Cette technique a été employée pour obtenir les résultats présentés dans la section 4.6. Elle combine des éléments de plusieurs approches décrites dans la littérature, en particulier celles présentées dans les références 51 et 52. L'apport original de ce travail consiste en l'extension de la méthode au cas des systèmes contenant des milieux gyrotropiques. Jusqu'à présent, elle n'avait été formulée que pour des matériaux avec des permittivité et perméabilité représentées par des tenseurs diagonaux, ce qui est le niveau de généralité nécessaire pour la modélisation des couches absorbantes parfaitement adaptées (PMLs) [51, 53, 54].

Nous donnons ici une caractérisation concise de la méthode décrite dans la section 5.3. Nous profitons d'abord de la symétrie axiale du domaine tridimensionnel en réduisant le problème original à un système dénombrable des problèmes propres découplés, posés sur un seul plan méridien (bidimensionnel). Nous utilisons des éléments finis nodaux scalaires pour développer la composante azimutale du champ électrique, et des éléments finis vectoriels pour développer une superposition particulière des composantes azimutale et méridienne de ce champ. Ce choix d'inconnues permet d'exprimer simplement les conditions de continuité sur l'axe de la cavité. Afin de supprimer les réflexions parasites sur les limites du domaine de calcul, nous les revêtons de PMLs. La mise en œuvre de la méthode est facilitée par la disponibilité de plusieurs outils d'open source, en particulier les bibliothèques Hermes (éléments finis) [55, 56] et SLEPc [57–59] (solution des problèmes aux valeurs propres avec des matrices creuses).

Les tests de convergence présentés dans le paragraphe 5.3.4 montrent que la fréquence propre des modes localisés d'une cavité magnéto-optique typique conçue de la manière décrite dans la section 4.6 peut être déterminée avec la précision relative de $\sim 10^{-5}$ dans un délai raisonnable sur un ordinateur de bureau. Nous montrons également que les résultats sont très peu sensibles aux changements des paramètres qui contrôlent la troncature du domaine.

Chapter I

Preliminaries

1.1 Introduction

The dawn of the second half of the 20. century was marked by the invention of electronic integrated circuits (ICs) fabricated in semiconductor thin films. Owing to their low cost and small size, ICs quickly all but displaced older “bulk” electronic components: coils, glass tubes and so on. They provided the means for the technological revolution that made compact electronic devices an integral part of modern life.

Shortly after the first experimental demonstration of the laser in 1960, the concept of *optical* ICs appeared. In analogy to their electronic counterparts, they were to pave the way to the miniaturisation of optical devices. Significant progress has been made from that time: numerous integrated photonic components, such as splitters, couplers or multiplexers, are routinely used in commercially available devices. However, it must be admitted that the development of the optical IC technology has been incomparably slower than that of electronic ICs. Suffice it to say that while state-of-the-art processors contain millions of transistors on a single chip, the most complex optical ICs realised to date consist of barely several hundred components [1–4].

There seem to be two principal reasons for this difference. First, the wavelength of light at telecommunication frequencies, which is on the order of 0.1–1 μm in typical dielectric materials, is much larger than the de Broglie wavelength of an electron at the Fermi level of a typical metal, 0.1–1 nm [5, p. 120]. The latter is so small that until recently the wave-like properties of electrons could be essentially ignored in the design of electronic components, which could therefore be rather straightforwardly miniaturised. In contrast, the wavelength of light is a real limit on the size of optical components.* Second, for specific applications it is advantageous to use substrates having particular physical properties, for example exhibiting strong electro-, magneto- or acousto-optical effects. Since these properties are difficult to obtain simultaneously in a single material, the first optical ICs were built with the so-called hybrid approach: their individual components were fabricated separately, possibly using different materials and technologies, and then bonded together to a single substrate [7, p. 9]. The advantage of this approach is that each component can be optimised separately; the disadvantage lies in the inherent difficulty of aligning and coupling the various elements. Thus, hybrid optical ICs hardly ever consist of more than a few components. ICs of larger complexity can only be fabricated using the monolithic approach, where the whole system is etched in a single substrate. Currently, the most advanced technology of this type seems to be that based on indium phosphide.

A boost to the research on optical ICs was given by the introduction of the concept of photonic crystals (PCs) in late 1980s [8, 9]. A PC is defined as a system in which the permittivity and permeability are periodically dependent on the position; thus, it can be viewed as an electromagnetic analogue of a

* Plasmonic components, which are currently an area of active research, might enable further miniaturisation of optical devices [6].

crystalline solid. The periodicity of the material properties can give rise to the appearance of *band gaps*, i.e., frequency ranges in which no propagative (energy-carrying) states can exist in the crystal. It was quickly recognised that linear defects in PCs can support localised eigenmodes with frequencies lying in the band gaps, and thus they can serve as waveguides [10]. Simultaneously, point defects in PCs were shown to act as resonant cavities with potentially very large quality factor–mode volume ratios [10]. However, it was the discovery that modes in PC waveguides can propagate around extremely sharp bends essentially without scattering losses [11] that led to an enormous increase of the interest in PCs as a possible means for further miniaturisation of optical ICs. Indeed, the bending radii of standard rib or ridge waveguides need be on the order of millimetres in order to keep the losses at a reasonable level [10]. Since then, an overwhelming number of optical components made of interconnected PC waveguides and cavities have been proposed, and several of them have seen experimental realisation. For a relatively recent review of the current state of research on PCs, see ref. 12.

While the early studies of PCs were focused primarily on the quest for structures providing the widest band gap and on the design of components operating within band gaps, in the last decade more and more attention has been devoted to the unusual properties of PCs *outside* band gaps. In contrast to homogeneous dielectrics, in which the equifrequency surfaces (EFSs) have the form of ellipsoids, the shape of the EFSs of PCs can be very complicated.* They can contain flat or even concave areas separated by sharp corners or edges. In addition, the group velocity need not point away from the origin of the reciprocal space. This richness of the dispersion relation gives rise to unusual phenomena [13], such as negative refraction of light [14], appearance of supercollimated beams [15] and the superprism effect [16]. Thus, it has been recognised that even defect-free (except for the presence of surfaces) PCs can constitute useful devices, for instance flat lenses [17, 18] or beam splitters [19].

1.2 Outline of the thesis

This thesis naturally splits into three parts. In chapters 2 and 3 we study defect-free two-dimensional (2D) PCs limited by one or two parallel surfaces. In particular, we are interested in the dependence of their properties on the structure of the interfaces separating them from the adjacent homogeneous media.

In chapter 2 we introduce the *single-mode approximation* and use it as a mathematical foundation for an effective-medium model of 2D PCs. In contrast to most previous work, we do not restrict our considerations to the case of waves impinging perpendicularly to the PC surface. We show that our model allows to reproduce the strong dependence of the effective material properties of a PC on the position of its truncation plane, observed by previous authors [21]. In particular, we demonstrate that the effective permittivity and permeability derived in the framework of the model are guaranteed to be real and continuous only if the truncation plane is chosen in certain particular ways. We test the validity of the model by comparing the values of the specular reflection coefficient it predicts for some specific PCs against results of rigorous numerical calculations. Since there has been a lot of interest in using PCs exhibiting the negative-refraction effect as lossless replacements of metamaterials, we pay particular attention to the accuracy of the effective-index description of bands with negative group velocity. We find, however, that it leaves much to be desired, especially for large incidence angles and in the evanescent-wave region. By means of a qualitative theoretical analysis, we argue that this behaviour is not restricted to the particular PC under study; instead, the low accuracy of the effective-index approximation is due to the inherent structure of the field of PC modes responsible for negative refraction.

In chapter 3 we consider the problem of reducing the reflection losses occurring at an interface between a semi-infinite PC and a homogeneous medium. This is an important issue, severely limiting

* This is analogous to what happens in solid-state theory: the Fermi's surface in a free electron gas is spherical, but in a real solid it can have a very complex form, sometimes called, fittingly, a *monster*.

the performance of practical PC devices, especially those using “bulk” PCs (as opposed to components based on PC waveguides). We propose to minimise these losses by superposing an additional structure—antireflection (AR) grating—on the PC surface, and present in detail an algorithm for the design of compact, wide-angle AR gratings for general 2D PCs. To assess its strengths and limitations, we apply it to three specific PCs, exhibiting the negative refraction, beam supercollimation, and superprism effect, respectively. In the first two cases, we obtain gratings ensuring a very significant decrease of the reflection loss; in the last case, however, the design procedure fails due to the violation of certain assumptions made in the derivation of our algorithm. The improvement brought by the proposed AR gratings to the transmission through a PC flat lens (based on the negative-refraction effect) has been confirmed experimentally [33].

In chapter 4, which constitutes the second major part of this thesis, we shift our attention to more traditional, waveguide-based optical devices. We study the problem of miniaturisation of optical circulators, one of the last important components whose integrated versions are not yet commercially available. We build on the design of a magneto-optical PC-based circulator proposed in 2005 by Wang and Fan [34, 37]. It consists of three PC waveguides coupled to a special PC cavity supporting a pair of modes whose frequencies are split in the presence of a static external magnetic field (SEMF). The mode frequency splitting of the original cavity from refs. 34 and 37 is negligible in a uniform SEMF; it can only be augmented if the magneto-optical material in the cavity is divided into many oppositely polarised magnetic domains, each having the area of a fraction of μm^2 . Fabrication of such domains presents serious experimental difficulties, as it requires a precise control of the applied SEMF on the nanometre scale. Here, using an analytical model of an axisymmetric resonant cavity, we show how to design cavities exhibiting maximum frequency splitting in a *uniform* SEMF. We present 2D numerical simulations of two classes of circulators containing the proposed cavities: PC-based circulators, similar to those studied in refs. 34 and 37, and circulators in which the PC coating is dispensed with and the cavity is coupled directly to rib waveguides. This elimination of the PC lattice leads to a significant simplification of the device geometry, without any deterioration of its performance. Subsequently, we comment briefly on the results of the experimental tests of the proposed devices that have been done in Institut d’Electronique Fondamentale (Orsay, France). They reveal a significant problem with the original design of the resonant cavities: large out-of-plane radiation losses. In the final part of chapter 4 we report on the initial results of full three-dimensional (3D) simulations of the cavities, which show that the above problem may be overcome by an appropriate adjustment of the geometry of the cavity.

In the last part of this thesis, chapter 5, we present several numerical methods developed for the sake of simulating some of the devices analysed in the earlier chapters. We start by discussing the extension of the multiple-scattering method, widely used to handle the problem of light scattering by finite PCs, to the case of 2D PCs containing gyrotropic materials. Next, we show how the band structures of 2D PCs composed of circular cylinders can be calculated to great accuracy using Fourier-Bessel expansions; remarkably, no lattice sum computations are necessary. Finally, we describe the implementation of the finite-element method for the calculation of eigenmodes of open, axisymmetric, 3D cavities containing gyrotropic materials.

1.3 Notational conventions

Throughout this thesis, symbols embellished with arrows (e.g., \vec{a}) will denote column vectors; with bars (\bar{a}), row vectors; and with hats (\hat{a}), matrices, tensors or operators. Complex conjugation will be indicated by an asterisk (*), transposition by the symbol T , and Hermitian conjugation by a dagger (\dagger). A unit vector in a given direction ξ will be written as \vec{e}_ξ . In particular, the unit vectors directed along the axes of a Cartesian coordinate system will be denoted by \vec{e}_x , \vec{e}_y and \vec{e}_z , and of a cylindrical coordinate

system, by \vec{e}_ρ , \vec{e}_ϕ and \vec{e}_z . Vector operators will be written using the nabla symbol; thus, $\vec{\nabla}a$, $\vec{\nabla} \cdot \vec{a}$ and $\vec{\nabla} \times \vec{a}$ will denote the gradient, divergence and curl of a or \vec{a} . Finally, unless otherwise noted, the terms *permittivity*, *permeability*, *impedance*, *admittance* and *immittance* will refer to *relative* permittivity, permeability etc.

I.4 Maxwell's equations

The electromagnetic fields in PCs and other optical systems are governed by Maxwell's equations [60, 61]. For convenience, we shall gather here the forms of these equations that will be most often referenced in later chapters of this manuscript. Since we shall only be concerned with the propagation of electromagnetic waves with wavelength λ much larger than the atomic dimensions (typically $\lambda > 1 \mu\text{m}$), we shall be using the *macroscopic* (phenomenological) Maxwell's equations, in which the effects of light-matter interaction are taken into account by help of so-called material parameters.

The most general differential form of macroscopic Maxwell's equations is [61, eq. (I.1a)]

$$\vec{\nabla} \times \vec{E} = -\frac{\partial \vec{B}}{\partial t}, \quad (1.1a)$$

$$\vec{\nabla} \times \vec{H} = \frac{\partial \vec{D}}{\partial t} + \vec{J}, \quad (1.1b)$$

$$\vec{\nabla} \cdot \vec{D} = \rho, \quad (1.1c)$$

$$\vec{\nabla} \cdot \vec{B} = 0, \quad (1.1d)$$

where \vec{E} denotes the electric field, \vec{H} the magnetic field, \vec{D} the electric displacement field, \vec{B} the magnetic induction, ρ the free charge density and \vec{J} the free current density. All quantities are, in general, functions of the position \vec{r} and time t ; for conciseness, this dependence has not been written explicitly. Throughout this thesis we shall assume all fields to be time-harmonic, i.e., to depend on time as $e^{-i\omega t}$, where i is the imaginary unit and ω the (angular) frequency. In this case, differentiation over t reduces to multiplication by $(-i\omega)$ and hence eqs. (1.1) become

$$\vec{\nabla} \times \vec{E} = i\omega \vec{B}, \quad (1.2a)$$

$$\vec{\nabla} \times \vec{H} = -i\omega \vec{D} + \vec{J}, \quad (1.2b)$$

$$\vec{\nabla} \cdot \vec{D} = \rho, \quad (1.2c)$$

$$\vec{\nabla} \cdot \vec{B} = 0. \quad (1.2d)$$

The fields \vec{D} and \vec{B} are related to \vec{E} and \vec{H} by so-called *constitutive relations*. We shall be dealing only with linear media, in which these relations take the form

$$\vec{D} = \epsilon_0 \hat{\epsilon} \cdot \vec{E} + \sqrt{\epsilon_0 \mu_0} \hat{\alpha} \cdot \vec{H} \quad \text{and} \quad \vec{B} = \sqrt{\epsilon_0 \mu_0} \hat{\beta} \cdot \vec{E} + \mu_0 \hat{\mu} \cdot \vec{H}, \quad (1.3)$$

where ϵ_0 and μ_0 denote the (absolute) permittivity and permeability of free space, $\hat{\epsilon}$ and $\hat{\mu}$ are the dimensionless (relative) position-dependent permittivity and permeability tensors of the system under study, and $\hat{\alpha}$ and $\hat{\beta}$ describe the strength of the magneto-electric coupling in this system. In the vast majority of materials used in practice, the elements of the two latter tensors are very small and can be neglected, as we shall do in the following. We shall also usually consider situations in which no free

charges or currents are present. Using all the above assumptions, eqs. (1.1) can be brought into the form

$$\vec{\nabla} \times \vec{E} = i\omega\mu_0\hat{\mu} \cdot \vec{H}, \quad (1.4a)$$

$$\vec{\nabla} \times \vec{H} = -i\omega\epsilon_0\hat{\epsilon} \cdot \vec{E}, \quad (1.4b)$$

$$\vec{\nabla} \cdot (\hat{\epsilon} \cdot \vec{E}) = 0, \quad (1.4c)$$

$$\vec{\nabla} \cdot (\hat{\mu} \cdot \vec{H}) = 0. \quad (1.4d)$$

It should be noted that owing to the identity $\vec{\nabla} \cdot (\vec{\nabla} \times \vec{F}) = 0$, valid for any vector field \vec{F} [60, eq. (A1.17)], eqs. (1.4c)–(1.4d) follow automatically from eqs. (1.4a)–(1.4b) as soon as the field is not static ($\omega \neq 0$), and therefore can be omitted.

In a large part of this manuscript we shall analyse 2D systems, in which the material properties $\hat{\epsilon}$ and $\hat{\mu}$ are invariant with respect to translations along a privileged axis, called ξ in the following. Under the additional conditions that (i) the fields \vec{E} and \vec{H} are also independent from ξ (the case of *in-plane propagation*) and (ii) the tensors $\hat{\epsilon}$ and $\hat{\mu}$ have the block form

$$\hat{\epsilon} = \begin{bmatrix} \hat{\epsilon}_t & \vec{0} \\ \vec{0} & \epsilon_\xi \end{bmatrix} \quad \text{and} \quad \hat{\mu} = \begin{bmatrix} \hat{\mu}_t & \vec{0} \\ \vec{0} & \mu_\xi \end{bmatrix} \quad (1.5)$$

eqs. (1.4a)–(1.4b) split into a pair of uncoupled systems of equations. Specifically, denoting by \vec{E}_t , \vec{H}_t and $\vec{\nabla}_t$ the components of the vectors \vec{E} , \vec{H} and $\vec{\nabla}$ perpendicular to ξ , we obtain

$$\vec{\nabla}_t \times \vec{H}_t = -i\omega\epsilon_0\epsilon_\xi E_\xi, \quad (1.6a)$$

$$\vec{\nabla}_t \times (E_\xi \vec{e}_\xi) = i\omega\mu_0\hat{\mu}_t \cdot \vec{H}_t \quad (1.6b)$$

and

$$\vec{\nabla}_t \times \vec{E}_t = i\omega\mu_0\mu_\xi H_\xi, \quad (1.7a)$$

$$\vec{\nabla}_t \times (H_\xi \vec{e}_\xi) = -i\omega\epsilon_0\hat{\epsilon}_t \cdot \vec{E}_t. \quad (1.7b)$$

It can be easily seen that eqs. (1.6) contain only the E_ξ and \vec{H}_t field components, whereas eqs. (1.7) contain solely \vec{E}_t and H_ξ . A field satisfying eqs. (1.6) and having $\vec{E}_t = 0$ and $H_\xi = 0$ will be called *s-polarised*. Conversely, a field satisfying eqs. (1.7) and having $E_\xi = 0$ and $\vec{H}_t = 0$ will be called *p-polarised*.

Chapter 2

Effective-medium model of photonic crystals

2.1 Introduction

As mentioned in section 1.1, a crucial feature of photonic crystals (PCs) is the richness of their dispersion relation. The shape of PC equifrequency surfaces can be very complex: they can contain sharp corners or edges separating flat or even concave areas. However, at specific frequencies, they can also attain ellipsoidal shape, characteristic for homogeneous media. In consequence, the question arises if the crystals can then be successfully described by the *effective-medium model*, in which they are approximated by a homogeneous material with specific values of permittivity ϵ and permeability μ —or, equivalently, refractive index $n = (\epsilon\mu)^{1/2}$ and impedance $\eta = (\mu/\epsilon)^{1/2}$. Since homogeneous materials are incomparably easier to analyse than structured ones, an answer in the affirmative would facilitate the development of PC devices, especially those using the negative-refraction effect [14]. Indeed, most components employing this phenomenon, like the famous *superlenses* [17], have been designed essentially with homogeneous negative-index materials, first analysed by Veselago [20], in mind.

Numerous papers dealing with this subject have already been published [21–32], giving rise to several competing definitions of the effective parameters of PCs, which will be reviewed in subsection 2.2.2. Unfortunately, as a rule, these definitions have been only heuristically motivated and lack a formal justification. Moreover, the ultimate verification of each such a definition, the comparison of the true reflection coefficient of the crystal with that of the corresponding effective medium, has so far been performed only for normal [24–26] or near-normal [28] incidence. Yet many applications, including those involving negative refraction, rely on waves incident at large angles, as well as evanescent ones. The range of validity of the effective-medium approximation is, therefore, still poorly known.

The aim of the work presented in this chapter is to address these shortcomings. In section 2.2 the concept of the *single-mode approximation* is used to provide a mathematical justification for a particular definition of the effective parameters of two-dimensional (2D) PCs. In section 2.3 we study the influence of the symmetry of the crystal's truncation plane and of the electromagnetic fields of its eigenmodes on the behaviour of its effective parameters, generalising the theorems obtained by Pierre and Gralak [27] in the one-dimensional (1D) case. To assess the accuracy of the effective-medium model, in section 2.4 we compare the values of the specular reflection coefficient predicted within the model's framework with the results of rigorous numerical calculations. These tests are done for two different crystals at a number of frequencies and in the full range of incidence angles. This leads to a detailed discussion of the applicability conditions of the single-mode approximation itself (section 2.5). We conclude that as far as the bands responsible for negative refraction are concerned, the single-mode approximation is (moderately) accurate only close to normal incidence. Thus, it does not make much sense to treat a PC exhibiting negative refraction as a homogeneous material for large incidence angles or in the evanescent-wave regime. In consequence, the behaviour of systems containing homogeneous negative-index materials can change

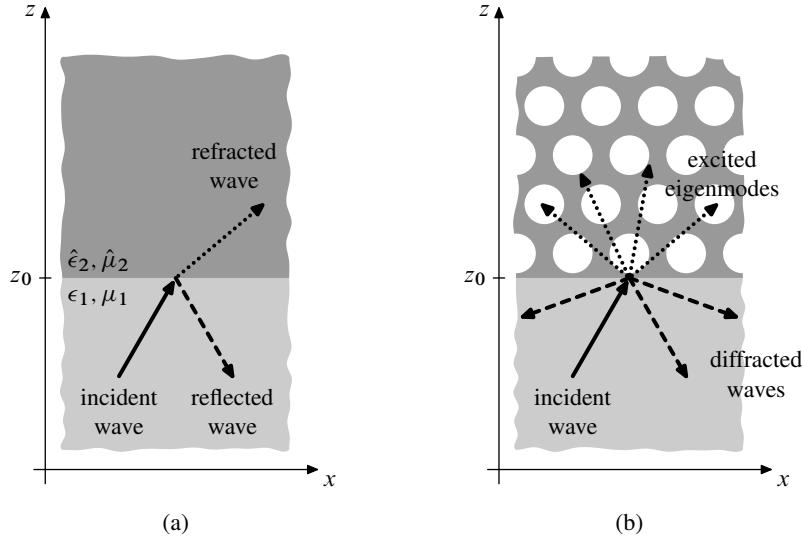


Figure 2.1 Schematic diagrams of the fields generated by an *s*- or *p*-polarised plane wave incident from an isotropic homogeneous medium on the surface of **(a)** another homogeneous medium and **(b)** a photonic crystal.

significantly if these materials are replaced with PCs, even if the equifrequency surfaces (and so the phase refractive indices) of both media are the same.

A substantial part of the results presented in this chapter has previously been published in refs. 62 and 63.

2.2 Definition of the effective parameters of photonic crystals

2.2.1 Preliminaries: the homogeneous-medium case

In the effective-medium approximation, a lossless 2D PC is modelled by a lossless, homogeneous, possibly anisotropic medium with one optical axis oriented along the invariant direction of the PC, hereafter taken to lie along the *y* axis. We shall begin with a brief analysis of the refraction of a plane wave incident on the interface between an isotropic medium, labelled 1, with permittivity ϵ_1 and permeability μ_1 , occupying the $z < z_0$ half-space, and this anisotropic material, labelled 2, characterised by tensorial $\hat{\epsilon}_2$ and $\hat{\mu}_2$, lying in the $z > z_0$ half-space [fig. 2.1(a)]. The wave is taken to propagate in the *xz* plane.

For the sake of simplicity, we shall restrict our attention to PCs whose point group includes a mirror plane perpendicular to the *x* or *z* axis or a three-fold rotation axis parallel to the *y* axis. In these cases, by Neumann's principle ("the symmetry elements of a physical property of a crystal must include the symmetry elements of the crystal point group" [64, p. 14]), the tensors $\hat{\epsilon}_2$ and $\hat{\mu}_2$ become diagonal in the chosen coordinate system,

$$\hat{\epsilon}_2 = \begin{bmatrix} \epsilon_{2x} & 0 & 0 \\ 0 & \epsilon_{2y} & 0 \\ 0 & 0 & \epsilon_{2z} \end{bmatrix}, \quad \hat{\mu}_2 = \begin{bmatrix} \mu_{2x} & 0 & 0 \\ 0 & \mu_{2y} & 0 \\ 0 & 0 & \mu_{2z} \end{bmatrix}. \quad (2.1)$$

Maxwell's equations (1.6) can then be used to derive the dispersion relation of, say, *s*-polarised plane waves (with electric field perpendicular to the propagation plane) with wave vector $\vec{k} = k_x \vec{e}_x + k_z \vec{e}_z$ propagating in medium 2,

$$\frac{k_x^2}{K_x^2} + \frac{k_z^2}{K_z^2} = 1 \quad \text{with} \quad K_x^2 \equiv \epsilon_{2y} \mu_{2z} \frac{\omega^2}{c^2} \quad \text{and} \quad K_z^2 \equiv \epsilon_{2y} \mu_{2x} \frac{\omega^2}{c^2}, \quad (2.2)$$

where ω denotes the frequency and $c \equiv 1/\sqrt{\epsilon_0\mu_0}$ the speed of light defined in terms of the (absolute) permittivity ϵ_0 and permeability μ_0 of free space. Thus, the equifrequency curve (EFC) of material 2 is an ellipse with principal axes of length $2K_x$ and $2K_z$.

When a plane wave with wave vector $\vec{k}_1 = k_x\vec{e}_x + k_{1z}\vec{e}_z$ falls on the interface separating media 1 and 2, reflected and refracted waves, with wave vectors $\vec{k}'_1 = k_x\vec{e}_x - k_{1z}\vec{e}_z$ and $\vec{k}_2 = k_x\vec{e}_x + k_{2z}\vec{e}_z$, respectively, are generated. By imposing the continuity conditions at $z = z_0$ on the field components parallel to the interface, the well-known Fresnel's formulas for the amplitude of the reflected and refracted waves can be derived:

$$r = \frac{\mu_{2x}/k_{2z} - \mu_1/k_{1z}}{\mu_{2x}/k_{2z} + \mu_1/k_{1z}}, \quad (2.3a)$$

$$t = \frac{2\mu_{2x}/k_{2z}}{\mu_{2x}/k_{2z} + \mu_1/k_{1z}}. \quad (2.3b)$$

These formulas can be written in a concise way by introducing the notion of *transverse impedance* of a material, defined as

$$Z_j = \frac{E_{jt}}{Z_0 H_{jt}} \quad (j = 1, 2), \quad (2.4)$$

where $Z_0 \equiv \sqrt{\mu_0/\epsilon_0}$ denotes the (absolute) impedance of free space, and E_{jt} (H_{jt}) is the amplitude of the transverse, i.e., parallel to the interface, component of the electric (magnetic) field of a plane wave propagating in the j th material in the given direction \vec{k}_j . Since in our case $E_{jt} = E_{jy} = E_{jy}^0 e^{i\vec{k}_j \cdot \vec{r}}$, $H_{1t} = -H_{1x} = (i\omega\mu_0\mu_1)^{-1} \partial E_{1y}/\partial z = (k_{1z}/\omega\mu_0\mu_1)E_{1y}$, and $H_{2t} = (k_{2z}/\omega\mu_0\mu_{2x})E_{2y}$, we obtain

$$Z_j = \frac{\omega \mu_{jx}}{c k_{jz}} \quad (2.5)$$

and

$$r = \frac{Z_2 - Z_1}{Z_2 + Z_1}, \quad t = \frac{2Z_2}{Z_2 + Z_1}. \quad (2.6)$$

By the duality theorem [65, p. 72–73], analogous results for p -polarised waves can be obtained by substituting $-\vec{H}$, \vec{E} , $\hat{\mu}$ and $\hat{\epsilon}$ for \vec{E} , \vec{H} , $\hat{\epsilon}$ and $\hat{\mu}$, respectively. Equations (2.6) must then be replaced by

$$r = \frac{Y_2 - Y_1}{Y_2 + Y_1}, \quad t = \frac{2Y_2}{Y_2 + Y_1}, \quad (2.7)$$

where

$$Y_j = \frac{\omega \epsilon_{jx}}{c k_{jz}} \quad (2.8)$$

is the *transverse admittance* of j th material. Introduction of the notion of transverse *immittance* \mathcal{E} of a medium, defined as its transverse impedance Z in the s -polarisation case and its transverse admittance Y in the p -polarisation case, lets us write the Fresnel's formulas (2.6) and (2.7) in a unified way:

$$r = \frac{\mathcal{E}_2 - \mathcal{E}_1}{\mathcal{E}_2 + \mathcal{E}_1}, \quad t = \frac{2\mathcal{E}_2}{\mathcal{E}_2 + \mathcal{E}_1}. \quad (2.9)$$

2.2.2 Existing definitions

Several authors [24–26, 28, 66] have attempted to generalise the concept of transverse immittance to non-homogeneous media, the main obstacle being, obviously, that in such media the ratio E_t/H_t is spatially dependent. The most straightforward is to define \mathcal{E} as the ratio of the spatial field *averages* over the

surface unit cell, as proposed by Lu and Prather [26]; while this might seem an oversimplification, in subsection 2.2.3 we shall show that this approach is in fact rigorous if the single-mode approximation, defined in the same subsection, is valid. In an attempt to preserve more information from the detailed field structure, other authors [24, 25, 28, 66] suggested empirical definitions of the transverse impedance, expressed in terms of the average electromagnetic energy and Poynting vector of the dominant crystal eigenmode. However, no mathematical justification of these definitions has been given.

Efros and Pokrovsky [23] and later Decoopman et al. [21] proposed an entirely different procedure. They considered the perturbation of the incident electromagnetic field caused by a PC slab embedded in a homogeneous medium whose permittivity ϵ and permeability μ were varied. The values of ϵ and μ corresponding to minimum perturbation were taken as the effective parameters of the crystal. Contrary to the approaches cited in the previous paragraph, this method is based on a full rigorous solution of Maxwell's equations. On the other hand, it requires a significant computational effort since, for each value of the frequency and angle of incidence, simulations need to be performed for multiple, possibly complex, values of ϵ and μ of the homogeneous medium. Therefore, it is not well-suited to the analysis of the general behaviour of the effective parameters, for which an—even approximate—semianalytical approach would be useful.

Finally, some authors [29–32] proposed definitions of effective parameters based on the extended Maxwell's-Garnett theory, where the crystal unit cell is replaced by a coated cylinder (or sphere) embedded in a homogeneous host medium whose parameters are determined from the condition of vanishing scattering, calculated by the Mie theory. This approach enabled them to reproduce the band structure of PCs, usually composed of dispersive (e.g., polaritonic) materials, with good accuracy. Nevertheless, the effective parameters they obtained are independent from the choice of the crystal truncation plane, whereas one of the key observations of Decoopman et al. [21] was the strong variability of effective ϵ and μ with the position of the crystal surface. Thus, the parameters introduced in refs. 29–32 could not be used to determine accurately the reflection coefficient of a truncated PC.

2.2.3 Proposed definition

To arrive at the proper definition of the effective parameters of PCs, let us consider a semi-infinite 2D PC invariant along the y axis, on whose surface, $z = z_0$, an s - or p -polarised plane wave with wave vector $\vec{k} = k_x \vec{e}_x + k_z \vec{e}_z$ is incident [fig. 2.1(b)]. Owing to the system's periodicity in the x direction, the reflected field will comprise infinitely many diffraction orders. Similarly, the transmitted field will be a superposition of infinitely many crystal eigenmodes (propagative and evanescent) characterised by different wave vectors. In contrast, as we have seen in subsection 2.2.1, if the crystal were replaced by a homogeneous material, only one transmitted plane wave would be excited. The effective-medium approximation can therefore be reasonably expected to give a good picture of reality only when some crystal eigenmode is excited with an amplitude significantly greater than the others. In other words, the validity of the effective-medium approximation is constrained by that of the *single-mode approximation*, which consists in neglecting all crystal eigenstates but the dominant one. We shall now show how this approximation leads to a natural definition of the crystal's effective parameters.

In the remaining part of this chapter we shall focus on s -polarised waves; formulas corresponding to p polarisation can be derived using the duality theorem and will be omitted for brevity. For the chosen polarisation, the electric field reduces to its component along the y axis, and Maxwell's equations (1.6) take the form

$$\frac{\partial E_y}{\partial x} = i\omega\mu_0\mu H_z, \quad (2.10a)$$

$$\frac{\partial E_y}{\partial z} = -i\omega\mu_0\mu H_x, \quad (2.10b)$$

$$\frac{\partial H_z}{\partial x} - \frac{\partial H_x}{\partial z} = i\omega\epsilon_0\epsilon E_y. \quad (2.10c)$$

We shall solve these equations separately in the homogeneous region and in the PC, and then match the solutions at the crystal surface by imposing the continuity of the E_y and H_x components, in accordance with Maxwell's boundary conditions.

We assume the PC to be oriented so that a (not necessarily primitive) rectangular unit cell (a_x, a_z) can be defined. The whole system is periodic with respect to the variable x , so it is possible to perform a Floquet-Bloch transform [13, 67] of the Maxwell's equations (2.10). After this transform, as is well known from grating theory, the solution of the Maxwell's equations in the homogeneous region is given by the Rayleigh's expansion [68, 69]

$$E_y^h(x, z) = e^{i[k_x x + \beta_0(z-z_0)]} + \sum_{n \in \mathbb{Z}} r_n e^{i[(k_x + G_{xn})x - \beta_n(z-z_0)]}, \quad (2.11)$$

where $G_{xn} \equiv 2\pi n/a_x$ and $\beta_n \equiv [\epsilon_1 \mu_1 (\omega/c)^2 - (k_x + G_{xn})^2]^{1/2}$ with the sign of the square root chosen so that $\text{Re } \beta_n + \text{Im } \beta_n \geq 0$. In the crystal, we can expand the field in terms of the PC eigenmodes with the x component of the Bloch vector equal to k_x , taking into account (i) propagative modes carrying energy in the $+z$ direction and (ii) evanescent modes decaying in the same direction [13, 41–43, 70–72]. These modes can be determined by several methods, most of which utilise some variant of the scattering-matrix algorithm [73]; in the numerical calculations presented later in this chapter we have used the differential method [69, 74–76]. The electric field of the m th eigenmode with Bloch vector $\vec{k}_m = k_x \vec{e}_x + \kappa_{mz} \vec{e}_z$ can be written as a 2D Fourier expansion with coefficients $(u_m^{np})_{n,p \in \mathbb{Z}}$:

$$E_{my}(x, z) = \sum_{n \in \mathbb{Z}} \sum_{p \in \mathbb{Z}} u_m^{np} e^{i[(k_x + G_{xn})x + (\kappa_{mz} + G_{zp})z]}, \quad (2.12)$$

where $G_{zp} \equiv 2\pi p/a_z$.^{*} Thus, the total electric field in the crystal will be

$$E_y^c(x, z) = \sum_{m \in \mathbb{N}} t_m E_{my}(x, z) \quad (2.13)$$

with “transmission coefficients” t_m denoting the amplitudes of individual modes.

The requirement of continuity of E_y and $H_x = -(i\omega\mu_0\mu)^{-1} \partial E_y / \partial z$ at $z = z_0$ leads to

$$\begin{aligned} & e^{ik_x x} + \sum_n r_n e^{i(k_x + G_{xn})x} \\ &= \sum_m t_m \sum_n \sum_p u_m^{np} e^{i[(k_x + G_{xn})x + (\kappa_{mz} + G_{zp})z_0]}, \end{aligned} \quad (2.14a)$$

$$\begin{aligned} & \frac{i\beta_0}{\mu_1} e^{ik_x x} - \sum_n \frac{i\beta_n}{\mu_1} r_n e^{i(k_x + G_{xn})x} \\ &= \sum_m t_m \sum_n \sum_p i(\kappa_{mz} + G_{zp}) u_m^{np} e^{i[(k_x + G_{xn})x + (\kappa_{mz} + G_{zp})z_0]}. \end{aligned} \quad (2.14b)$$

Using the identity $\int_0^1 e^{2\pi i n x} dx = \delta_{n0}$, where δ_{nm} equals 1 if $n = m$ and 0 otherwise, we arrive at the

^{*} Since we shall be studying the influence of shifting the surface of the crystal with respect to the origin of its unit cell, it is convenient to expand the field in the PC [eq. (2.12)] about the fixed point $(0, 0)$ rather than the point $(0, z_0)$ anchored on the surface.

following inhomogeneous system of linear equations with unknowns $(r_n)_{n \in \mathbb{Z}}$ and $(t_m)_{m \in \mathbb{N}}$:

$$\delta_{n0} + r_n = \sum_m u_m^n t_m, \quad (2.15a)$$

$$\frac{i\beta_n}{\mu_1}(\delta_{n0} - r_n) = \sum_m v_m^n t_m, \quad n \in \mathbb{Z}, \quad (2.15b)$$

with the coefficients u_m^n and v_m^n defined as

$$u_m^n \equiv \sum_p u_m^{np} e^{i(\kappa_{mz} + G_{zp})z_0}, \quad v_m^n \equiv \sum_p i(\kappa_{mz} + G_{zp}) u_m^{np} e^{i(\kappa_{mz} + G_{zp})z_0}. \quad (2.16)$$

This system can be written in the matrix form

$$\begin{bmatrix} -\hat{I} & \hat{u} \\ i\hat{\beta}/\mu_1 & \hat{v} \end{bmatrix} \begin{bmatrix} \vec{r} \\ \vec{t} \end{bmatrix} = \begin{bmatrix} \vec{a} \\ \vec{a}' \end{bmatrix}, \quad (2.17)$$

where \hat{I} denotes the identity matrix, \hat{u} and \hat{v} are matrices with elements u_m^n and v_m^n (the row and column indices being denoted by super- and subscripts, respectively), $\hat{\beta}$ is the diagonal matrix of the coefficients β_n , \vec{r} and \vec{t} are column vectors of the coefficients r_n and t_m , and the vectors \vec{a} and \vec{a}' , whose elements are given by

$$a_n \equiv \delta_{n0}, \quad a'_n \equiv i\beta_0 \delta_{n0} / \mu_1, \quad (2.18)$$

represent the incident field.

If the crystal were replaced by a homogeneous medium, the only nonzero reflection coefficient would be the specular one, r_0 . Using eqs. (2.15) corresponding to $n = 0$, the following relation between r_0 and the transmission coefficients of individual modes can be derived:

$$r_0 = \frac{\sum_m [u_m^0 - (\mu_1 / i\beta_0) v_m^0] t_m}{\sum_m [u_m^0 + (\mu_1 / i\beta_0) v_m^0] t_m}. \quad (2.19)$$

As we have already seen, the effective-medium approximation relies on the assumption that the transmission coefficient of a particular (*dominant*) mode is much larger than of all others; without loss of generality, we can denote this mode with the index 1, so that our assumption reads $|t_1| \gg |t_2|, |t_3|, \dots$. If it holds, expression (2.19) reduces to

$$r_0 \approx \frac{i u_1^0 / v_1^0 - \mu_1 / \beta_0}{i u_1^0 / v_1^0 + \mu_1 / \beta_0}. \quad (2.20)$$

Comparing eq. (2.20) to the Fresnel's formula (2.3a) and noting that β_0 and k_{1z} denote the same physical quantity—the z component of the wave vector of the incident plane wave—we conclude that $i u_1^0 / v_1^0$ in eq. (2.20) corresponds to μ_{2x} / k_{2z} in eq. (2.3a). In the homogeneous-medium case, k_{2z} is the z component of the wave vector of the refracted wave. Assuming that the EFC of the crystal at the considered frequency can be approximated by an ellipse with semiaxes K_x and K_z and centre $\vec{K}_0 \equiv (K_{0x}, K_{0z})$, as shown in fig. 2.2, it is natural to identify k_{2z} in the PC case with the z component of the Bloch vector of mode 1 *measured from the centre of this ellipse*, i.e., $\kappa'_{1z} \equiv \kappa_{1z} - K_{0z}$. In this way, we arrive at the following definition of the effective μ_x of the crystal:

$$\mu_x = i \kappa'_{1z} \frac{u_1^0}{v_1^0}. \quad (2.21)$$

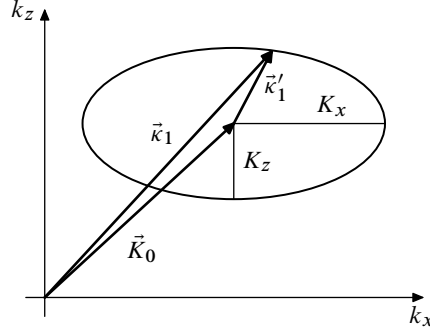


Figure 2.2 Relationship between the vectors \vec{K}_0 , \vec{k}_1 and \vec{k}'_1 .

The dispersion relation (2.2) provides then the formulas for the effective μ_z and ϵ_y ,

$$\mu_z = \frac{K_x^2}{K_z^2} \mu_x, \quad \epsilon_y = \frac{1}{\mu_x} \frac{K_z^2}{\omega^2/c^2}, \quad (2.22)$$

and eq. (2.5), for the effective transverse impedance,

$$Z = \frac{\omega}{c} \frac{i u_1^0}{v_1^0}. \quad (2.23)$$

Thus, within the framework of the single-mode approximation the PC produces the same reflected wave as the homogeneous medium with material parameters given by eqs. (2.21) and (2.22).

Finally, we note that the definition (2.23) of the effective transverse impedance agrees with that given by Lu and Prather [26, section 3], since from eqs. (2.10b), (2.12) and (2.16) it follows that u_1^0 and $-v_1^0/(i\omega\mu_0)$ are the average periodic parts of the E_y and H_x fields of mode 1 on the PC surface; substituting these values to eq. (2.4), we arrive at the expression (2.23).

2.3 Influence of symmetries on the effective parameters

“Standard” lossless homogeneous materials are characterised by purely real ϵ , μ and Z . From the Fresnel’s formula (2.3a) it follows that the reflection coefficient of a plane wave incident on the interface separating two such materials will also be purely real provided that both the incident and the transmitted wave are propagative, i.e., k_{1z} and k_{2z} are real. These properties do not always carry over to the PC case. Indeed, Pierre and Gralak [27] proved that for 1D PCs they are guaranteed to hold only if the crystal is truncated along one of its *mirror symmetry planes*; otherwise, the effective material properties and the reflection coefficient may take complex values.

Since the effective-medium description of PCs is an approximation, one might expect their effective material properties to have some k_x -dependence. This does no harm as long as the variation with k_x is fairly small. However, ref. 27 demonstrates that the effective parameters of a 1D PC cut elsewhere than along a mirror symmetry plane may diverge at the value of k_x where the crystal eigenmode turns from propagative to evanescent. In consequence, the usefulness of the effective-medium model in this case is rather limited.

In this section we shall extend the results from ref. 27 to the 2D case. It should be noted that in 1D systems mirror planes are in fact identical with inversion centres and two-fold rotation axes, so that *a priori* it is not obvious which of them turn out to be crucial in 2D.

2.3.1 Real-valuedness

We shall now prove the following sufficient condition for the real-valuedness of the effective parameters and the specular reflection coefficient of 2D PCs.

The reflection coefficient r_0 and the effective parameters μ_x , μ_z , ϵ_y , and Z of a 2D PC are real if:

- (i) *both the incident wave and the dominant eigenmode are propagative, i.e., β_0 and κ_{1z} are real,*
- (ii) *the truncation plane $z = z_0$ contains an inversion centre of the infinite crystal,*
- (iii) *the single-mode approximation is valid.*

Simple inspection of eqs. (2.20)–(2.23) shows that if the assumptions (i) and (iii) are fulfilled, the proposition is true provided the ratio iu_1^0/v_1^0 is real. This expression involves the Fourier coefficients u_1^{np} of the electric field of the dominant PC mode. By assumption (i), this mode is propagative, and therefore the coefficients in question can be obtained with the standard plane-wave method as described in ref. 77. Now, if the crystal is centrosymmetric with respect to a point (x_0, z_0) , the electric field of the mode can be written as

$$E_{1y}(x, z) = \sum_n \sum_p \tilde{u}_1^{np} e^{i[(k_x + G_{xn})(x - x_0) + (\kappa_{z1} + G_{zp})(z - z_0)]}, \quad (2.24)$$

where \tilde{u}_1^{np} are the elements of a vector equal to the product of a real diagonal matrix and an eigenvector of a real symmetric matrix [77]; hence, they can be taken to be real. Comparing eq. (2.24) with the general formula (2.13), we obtain

$$u_1^{np} = \tilde{u}_1^{np} e^{-i[(k_x + G_{xn})x_0 + (\kappa_{z1} + G_{zp})z_0]}, \quad (2.25)$$

and, using eqs. (2.16), we arrive at

$$\frac{iu_1^0}{v_1^0} = \frac{\sum_p \tilde{u}_1^{0p}}{\sum_p (\kappa_{1z} + G_{zp}) \tilde{u}_1^{0p}}. \quad (2.26)$$

Owing to the real-valuedness of \tilde{u}_1^{np} and κ_{1z} , the above expression is real, and the proposition follows.

On the contrary, if the interface contains no symmetry centres, a complex Hermitian eigenvalue problem is solved in the plane-wave method, so that the eigenvector elements \tilde{u}_1^{np} need not be real, and neither does iu_1^0/v_1^0 .

2.3.2 Continuity and boundedness

Preliminaries We proceed to the investigation of the behaviour of the effective permittivity and permeability of a 2D PC near a value of k_x at which its dominant eigenmode turns from propagative to evanescent, i.e., near a vertex $\vec{K}_v^\pm = (K_{0x} \pm K_x, K_{0z})$ of the elliptical EFC. At such a point, κ'_{1z} is zero; according to eqs. (2.21) and (2.22), this implies $\mu_x = \mu_z = 0$ and $|\epsilon_y| \rightarrow \infty$ unless v_1^0 is zero at the same time. In this subsection we shall study the circumstances in which this necessary condition for the continuity and boundedness of ϵ_y at the transition point is guaranteed to be met. The considerations are necessarily somewhat technical; the reader not interested in mathematical details can skip to the last paragraph of this subsection, where the obtained results are summarised.

We shall limit the discussion to PCs whose geometry is described by one of the *symmorphic* space groups.* Eigenmodes with a given Bloch vector \vec{k} can then be classified in terms of the irreducible

* A symmorphic space group is a space group that contains all elements of its point group [78, p. 18]. This means, in particular, that the set of its generators must consist solely of pure rotations and mirror reflections (no screw rotation axes and glide planes are allowed).

representations of the largest common subgroup of the PC's point group and the group of \vec{k} , i.e., the group of symmetry operations leaving \vec{k} invariant or transforming it to a Bloch vector \vec{k}' differing from \vec{k} by a reciprocal-lattice vector [79, chap. 3; 80, chap. 8].

If a vertex \vec{K}_V^\pm is located at a general reciprocal-space point, whose group consists solely of the identity operation I , no constraints on the symmetry of the corresponding eigenmode can be obtained. However, if $K_{0z} = 0$ or $K_{0z} = \pi/a_z$ —as, in practice, is very often the case—the group of \vec{K}_V^\pm contains additionally the operation of mirror reflection with respect to the x axis, σ_x .^{*} It follows that if the crystal itself has mirror planes parallel to x , the electric field of an eigenmode with Bloch vector \vec{K}_V^\pm is either symmetric or antisymmetric with respect to reflection about each of these planes. We shall assume the origin of the coordinate system to be chosen so that the mirror planes lie at $z = \frac{1}{2}qa_z$ for all $q \in \mathbb{Z}$ (it is easy to see that there are always two parallel planes per a rectangular unit cell). Let us now consider separately the cases of $K_{0z} = 0$ and $K_{0z} = \pi/a_z$.

The case of $K_{0z} = 0$ Setting κ'_{1z} to $K_{0z} = 0$ in the definition (2.16) of v_1^0 and using the definition of G_{zp} , we get

$$v_1^0 = \frac{2\pi i}{a_z} \sum_{p \in \mathbb{Z}} p u_1^{0p} e^{2\pi i p z_0 / a_z}. \quad (2.27)$$

Consider first the case of an eigenmode whose electric field $E_{1y}(x, z)$ is *symmetric* with respect to reflection about the plane $z = 0$, i.e., $E_{1y}(x, z) = E_{1y}(x, -z)$. Expression (2.13) for $E_{1y}(x, z)$ and the orthogonality of the Fourier basis yield

$$u_1^{n,-p} = u_1^{np} \quad \text{for all } n, p \in \mathbb{Z}. \quad (2.28)$$

It is easy to check that the above condition guarantees also the symmetry of $E_{1y}(x, z)$ with respect to all the other mirror planes $z = \frac{1}{2}qa_z$. Substituting eq. (2.28) into eq. (2.27), we obtain

$$v_1^0 = -\frac{4\pi}{a_z} \sum_{p>0} p u_1^{0p} \sin \frac{2\pi p z_0}{a_z}. \quad (2.29)$$

Without further constraints on u_1^{0p} , the coefficient v_1^0 is guaranteed to be null only if $2\pi z_0/a_z$ is an integral multiple of π , so that all the sine factors vanish. With z_0 restricted to the first unit cell ($0 \leq z_0 < a_z$), this is equivalent to $z_0 = 0$ or $z_0 = \frac{1}{2}a_z$. Thus, the crystal should be truncated along one of its mirror planes.

If the PC is based on a hexagonal or centred rectangular Bravais lattice, its primitive cell is two times smaller than the rectangular unit cell (a_x, a_z) we are using. It can then be shown that half of the Fourier coefficients u_1^{np} , namely those with $n + p$ odd, vanish. As a result, eq. (2.29) becomes

$$v_1^0 = -\frac{8\pi}{a_z} \sum_{p>0} p u_1^{0,2p} \sin \frac{4\pi p z_0}{a_z}. \quad (2.30)$$

It follows that all the sine factors, and hence the total sum too, will vanish on two more planes per unit cell: $z_0 = \frac{1}{4}a_z$ and $z_0 = \frac{3}{4}a_z$.

Let us now proceed to the case of electric field *antisymmetric* with respect to the plane $z = 0$. Instead of eq. (2.28) we have then

$$u_1^{n,-p} = -u_1^{np} \quad \text{for all } n, p \in \mathbb{Z}. \quad (2.31)$$

^{*} Note in particular that the vector $\sigma_x(K_{0x} \pm K_x, \pi/a_z) = (K_{0x} \pm K_x, -\pi/a_z)$ is equivalent to $(K_{0x} \pm K_x, \pi/a_z)$, since they differ by the reciprocal-lattice vector $(2\pi/a_z)\vec{e}_z$.

and the sines in eq. (2.29) are replaced by cosines. To ensure that v_1^0 vanishes for all sequences $(u_1^{0p})_{p \in \mathbb{N}}$, to each p must correspond a $q \in \mathbb{Z}$ such that $2\pi pz_0/a_z = (q + \frac{1}{2})\pi$. It is easy to see that this condition cannot be fulfilled for any value of z_0 . For a PC based on a hexagonal or centred rectangular Bravais lattice, the condition becomes $4\pi pz_0/a_z = (q + \frac{1}{2})\pi$, which has no solutions, either.

The case of $K_{0z} = \pi/a_z$ Instead of eq. (2.27), we have

$$v_1^0 = \frac{\pi i}{a_z} \sum_{p \in \mathbb{Z}} (2p+1) u_1^{0p} e^{\pi i (2p+1) z_0/a_z}. \quad (2.32)$$

Substitution of the expression (2.13) for $E_{1y}(x, z)$ to the condition of symmetry/antisymmetry with respect to plane $z = 0$, $E_{1y}(x, z) = \pm E_{1y}(x, -z)$, yields

$$\sum_n \sum_p u_m^{np} e^{i[(k_x + 2n\pi/a_x)x + (2p+1)\pi z/a_z]} = \pm \sum_n \sum_p u_m^{np} e^{i[(k_x + 2n\pi/a_x)x - (2p+1)\pi z/a_z]}, \quad (2.33)$$

so that from the orthogonality of the Fourier basis we obtain

$$u_m^{np} = \pm u_m^{n, -p-1} \quad \text{for all } n, p \in \mathbb{Z}. \quad (2.34)$$

It can also be shown that a mode with $k_z = \pi/a$ that is symmetric with respect to the plane $z = 0$ must be antisymmetric with respect to the plane $z = \frac{1}{2}a_z$ and vice versa; thus, without loss of generality, we can take the plus sign in the above equation. Substituting it into eq. (2.32), we get

$$\begin{aligned} v_1^0 &= \frac{\pi i}{a_z} \sum_{p \geq 0} (2p+1) u_1^{0p} [e^{i(2p+1)\pi z_0/a_z} - e^{-i(2p+1)\pi z_0/a_z}] \\ &= -\frac{2\pi i}{a_z} \sum_{p \geq 0} (2p+1) u_1^{0p} \sin \frac{(2p+1)\pi z_0}{a_z}. \end{aligned} \quad (2.35)$$

Vanishing of v_1^0 is thus ensured if $\sin[(2p+1)\pi z_0/a_z] = 0$ for all integer $p \geq 0$, which is equivalent to $z_0 = qa_z$ with $q \in \mathbb{Z}$. This corresponds to placing the truncation plane along a symmetry plane of the electric field of the crystal's dominant eigenmode. The situation is the same if the PC is based on a hexagonal or centred rectangular Bravais lattice: the condition for vanishing v_1^0 takes then the form $\sin[(4p+1)\pi z_0/a_z] = 0$ for all integer $p \geq 0$, which is again equivalent to $z_0 = qa_z$ with $q \in \mathbb{Z}$.

Conclusions From the above considerations we can establish the following rule:

The effective parameters μ_x , μ_z and ϵ_y are continuous and bounded at the point of the propagative-to-evanescent transition of the dominant PC eigenmode in the two following cases:

- (i)
 - the transition occurs at $\vec{k} = k_x \vec{e}_x$,
 - the crystal has mirror planes parallel to x ,
 - the electric field of the dominant mode is symmetric with respect to these planes, and
 - the crystal is truncated along one of these planes or, provided it is based on a hexagonal or centred rectangular Bravais lattice, midway between these planes;
- (ii)
 - the transition occurs at $\vec{k} = k_x \vec{e}_x + \pi/a_z \vec{e}_z$,
 - the crystal has mirror planes parallel to x , and
 - the crystal is truncated along a symmetry plane of the electric field of its dominant eigenmode.

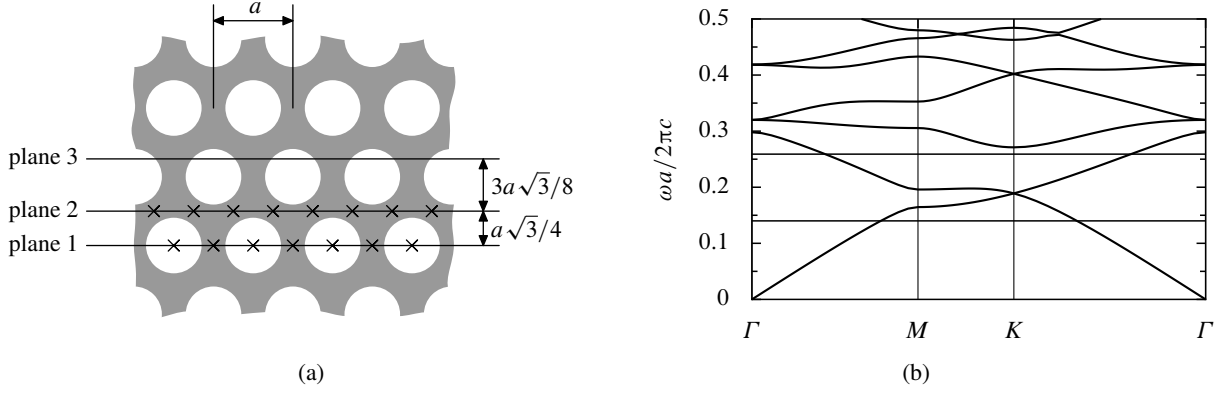


Figure 2.3 (a) Geometry of the hexagonal-lattice PC analysed in the text. Horizontal lines mark the position of truncation planes 1, 2, and 3; inversion centres of the PC located at these planes are marked with crosses. (b) Band structure of the crystal shown in part (a). Horizontal lines mark the frequency values $\omega = 0.14 \times 2\pi c/a$ and $0.259 \times 2\pi c/a$.

This rule is not a rigorous theorem. First, the sufficiency of the above conditions has not been proved. Assuming that the Taylor expansions of $u_1^0(\kappa'_{1z})$ and $v_1^0(\kappa'_{1z})$ about $\kappa'_{1z} = 0$ exist, the formula (2.21) for μ_x can be written as

$$\mu_x(\kappa'_{1z}) = i \frac{\kappa'_{1z} u_1^0(0) + (\kappa'_{1z})^2 (du_1^0/d\kappa'_{1z})_{\kappa'_{1z}=0} + \dots}{v_1^0(0) + \kappa'_{1z} (dv_1^0/d\kappa'_{1z})_{\kappa'_{1z}=0} + \dots}. \quad (2.36)$$

The effective permeability μ_x is then finite and different from zero if and only if exactly $q - 1$ lowest derivatives of u_1^0 and q lowest derivatives of v_1^0 , where $q \in \mathbb{N}$, vanish at $\kappa'_{1z} = 0$. We have proved that in the two cases listed above $v_1^0(0)$ vanishes; it can also be shown that in these cases $u_1^0(0)$ is in general non-zero. However, the proof that $(dv_1^0/d\kappa'_{1z})_{\kappa'_{1z}=0}$ does not vanish is missing.

Second, the above conditions have not been proved to be strictly necessary. Indeed, the coefficients u_1^{0p} can accidentally take such values that v_1^0 will vanish for some “random” truncation. This does not seem to be a major problem, though, and one should probably treat these situations like, for instance, accidental degeneracies in group theory.

These reservations notwithstanding, in the following section it will be shown that the effective parameters of two typical PCs at several distinct frequencies behave exactly as predicted by the above rule. So far, the author has not found any counterexample to it.

2.4 Examples

In this section we shall apply the theory presented above to the cases of two specific PCs, one with a hexagonal and one with a square lattice. In particular, the predictions of the effective-medium model will be compared with the results of numerical calculations made with the differential method [69, 74–76].

2.4.1 Hexagonal lattice

To begin with, we consider the crystal shown in fig. 2.3(a): the hexagonal lattice of air holes of radius $0.35a$, a being the lattice constant, embedded in a dielectric matrix with $\epsilon = 16$. Figure 2.3(b) presents its Brillouin diagram. At the frequency $\omega = 0.14 \times 2\pi c/a$, the EFC of the single s -polarised propagative crystal eigenmode has the shape of a circle centred at the $\Gamma = (0, 0)$ point [fig. 2.4(a), middle diagram, solid line]. In figs. 2.5(a), (d) and (g) the specular reflection coefficient of this crystal at the quoted

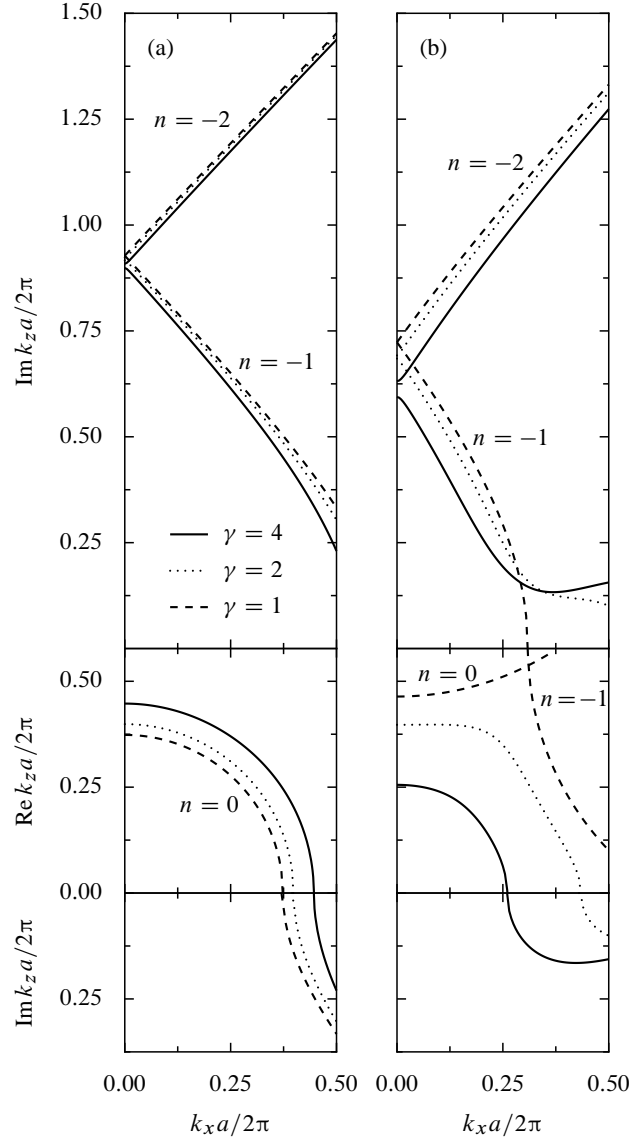


Figure 2.4 The EFCs at frequency **(a)** $\omega = 0.14 \times 2\pi c/a$ and **(b)** $\omega = 0.259 \times 2\pi c/a$ of three PCs of the type shown in fig. 2.3(a) with the same average refractive index $\langle \sqrt{\epsilon} \rangle = 2.67$, but different values of the index contrast $\gamma = \sqrt{\epsilon_b}/\sqrt{\epsilon_h}$ between the background and the holes: $\epsilon_b = 16$, $\epsilon_h = 1$, $\gamma = 4$ (solid lines), $\epsilon_b = 11.76$, $\epsilon_h = 2.94$, $\gamma = 2$ (dotted lines), and $\epsilon_b = \epsilon_h = 7.11$, $\gamma = 1$ (dashed lines). The middle part of the graphs shows the EFCs of the real bands ($\text{Re } k_z \neq 0$, $\text{Im } k_z = 0$), the bottom one, of the imaginary bands of the first kind [81] ($\text{Re } k_z = 0$, $\text{Im } k_z \neq 0$), and the top one, of the imaginary bands of the second kind ($\text{Re } k_z = 2\pi/a\sqrt{3}$, $\text{Im } k_z \neq 0$, i.e., lying on the edge of the first Brillouin zone). Only the three bands with lowest values of $\text{Im } k_z$ are shown in each case. The bands of the empty lattice ($\gamma = 1$) are labelled with the index n of the harmonic G_{xn} to which they correspond. For each mode with wave vector \vec{k} visible in the graph, the crystal supports three additional modes with wave vectors \vec{k}^* , $-\vec{k}$, and $-\vec{k}^*$ [81].

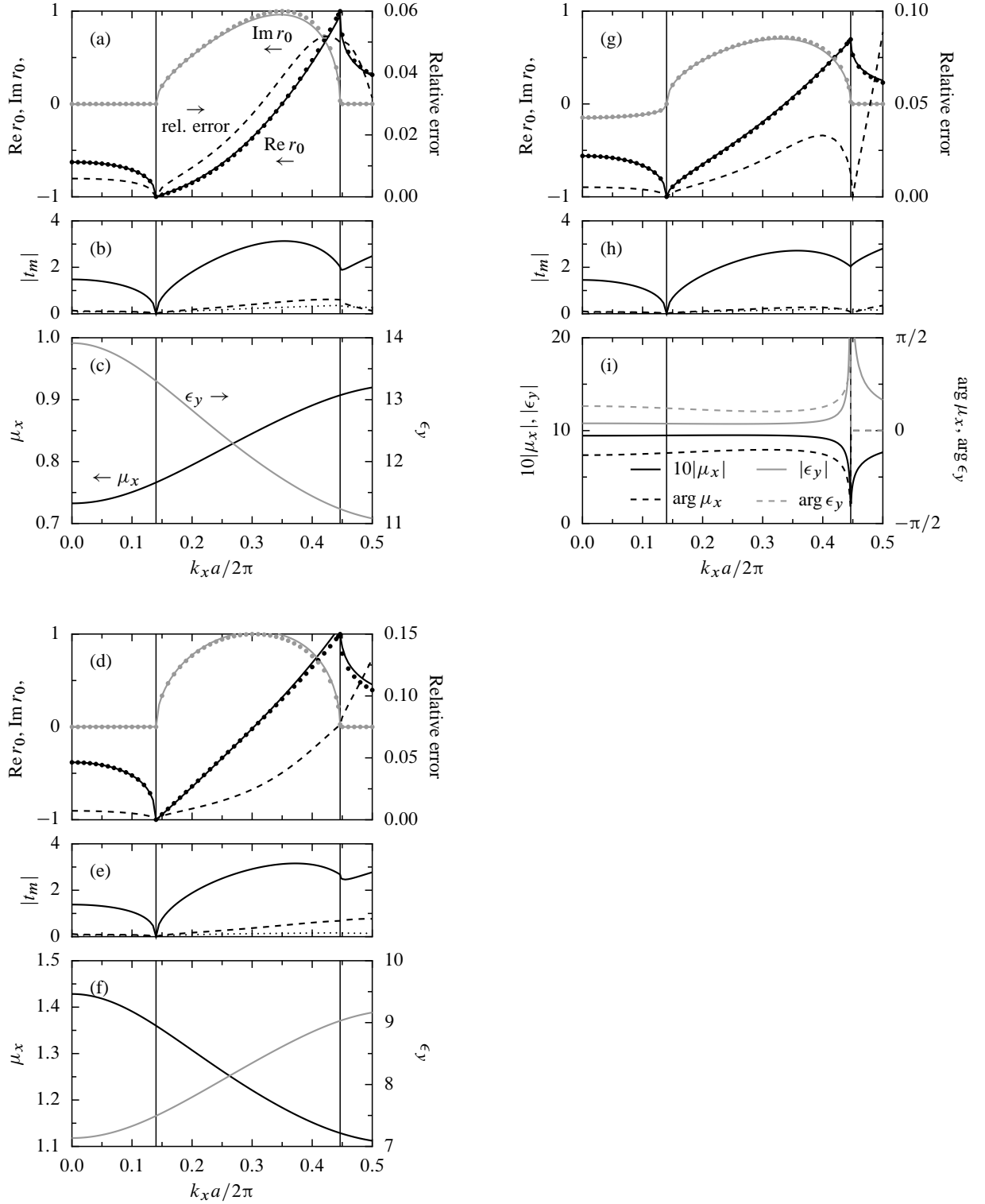


Figure 2.5 (a) The k_x -dependence of the specular reflection coefficient r_0 of the crystal from fig. 2.3(a) truncated along plane 1, at $\omega = 0.14 \times 2\pi c/a$. Solid lines: results of rigorous calculations, r_0^n ; circles: results of calculations made in the single-mode approximation, r_0^{sm} ; dashed line: relative error ρ of the single-mode approximation. The vertical lines at $k_x = 0.14 \times 2\pi/a$ and $0.447 \times 2\pi/a$ mark where the incident wave and the single propagating crystal eigenmode, respectively, turn from propagating to evanescent. (b) Amplitudes of the three most slowly decaying crystal eigenmodes excited in the above conditions (solid, dashed, and dotted line, in order of increasing $\text{Im } k_z$). (c) Effective μ_x (dark lines) and ϵ_y (light lines) of the crystal. (d)–(f) and (g)–(i) The same for planes 2 and 3.

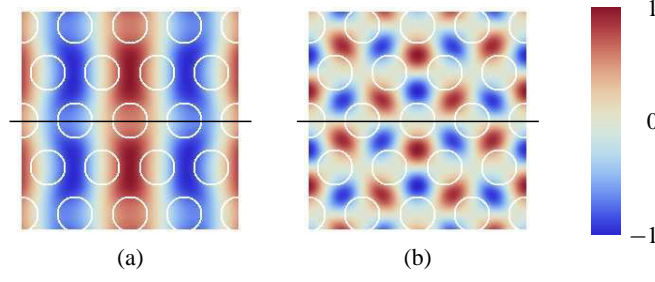


Figure 2.6 Real part of the electric field E_y of the modes of the crystal shown in fig. 2.3(a) with **(a)** $\omega = 0.14 \times 2\pi c/a$, $k_x = 0.447 \times 2\pi/a$, and $k_z = 0$, **(b)** $\omega = 0.259 \times 2\pi c/a$, $k_x = 0.259 \times 2\pi/a$, and $k_z = 0$. A mirror plane of the crystal parallel to its surface is marked with a horizontal line.

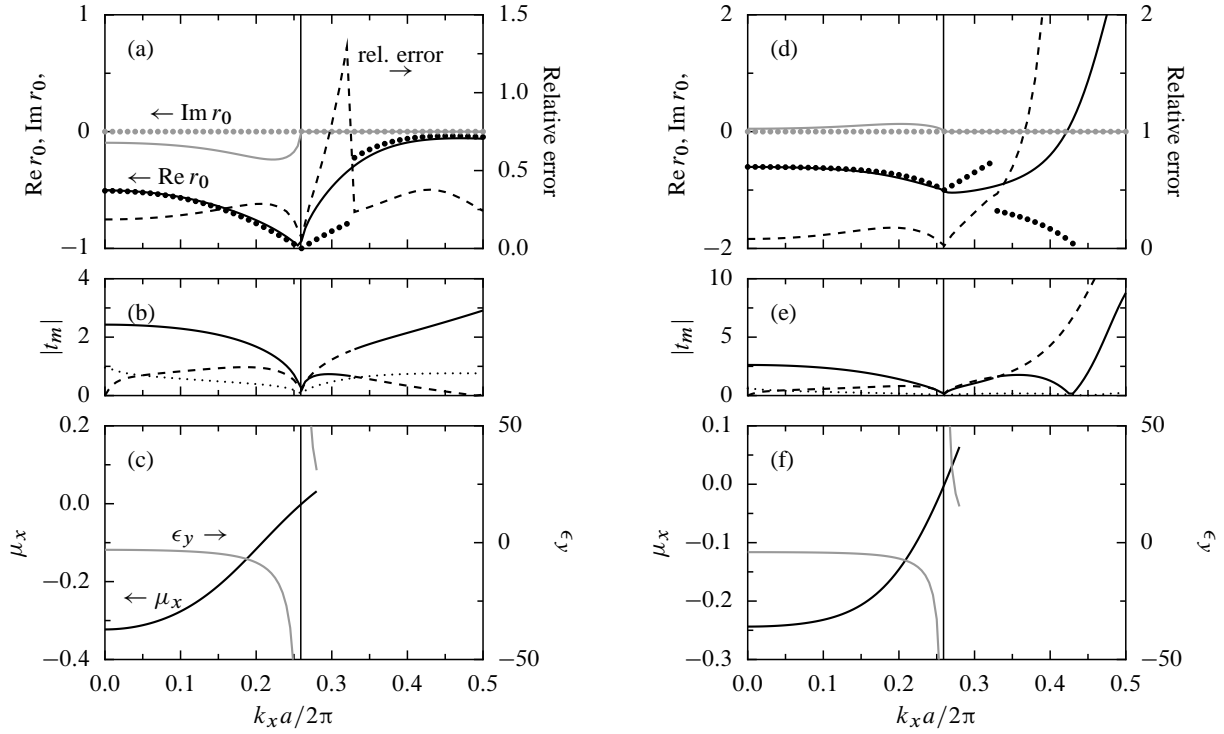


Figure 2.7 Same as fig. 2.5, at frequency $\omega = 0.259 \times 2\pi c/a$ and for truncation planes **(a)–(c)** 1 and **(d)–(f)** 2. Discontinuities in the plots of r_0^{sm} appear at $k_x = 0.33 \times 2\pi/a$, because at this value of k_x the two most slowly decaying crystal eigenstates “swap places”, and the calculations of r_0^{sm} are always done assuming the mode with the smallest $\text{Im } k_y$ to be dominant. The domain of the plots of effective parameters has been restricted to the range of k_x in which the relative error of the single-mode approximation is less than $\sim 25\%$.

frequency is plotted against the x component of the wave vector of the incident plane wave for three different positions, marked with horizontal lines in fig. 2.3(a), of the interface between the crystal and the homogeneous medium, taken to be vacuum ($\epsilon_1 = \mu_1 = 1$). In these graphs, the results of rigorous numerical calculations (r_0^{n} , solid lines) are juxtaposed with the values obtained from eq. (2.20) derived in the framework of the single-mode approximation (r_0^{sm} , circles). Evidently, for surfaces containing inversion centres $\text{Im } r_0^{\text{n}}$ is very small in the whole range $k_x < 0.14 \times 2\pi/a$, in which the incident wave is propagative [figs. 2.5(a) and (d)]. On the contrary, when the termination is chosen in an arbitrary way, r_0 acquires an appreciable imaginary part [fig. 2.5(g)]. This is in agreement with the rule formulated in subsection 2.3.1.

In all the three graphs, the relative error of the single-mode approximation, defined as $\rho \equiv |r_0^{\text{sm}} - r_0^{\text{n}}|/|r_0^{\text{n}}|$, is plotted with a dashed line. It is clear that at the chosen frequency (corresponding to the middle of the first band of the crystal) the single-mode approximation is very accurate for k_x corresponding to propagative incoming waves ($k_x < \omega/c$); for larger k_x , the accuracy degrades slightly, but the relative error seldom exceeds 10%.

Figures 2.5(c), (f) and (i) present the k_x -dependence of the effective μ_x and ϵ_y at $\omega = 0.14 \times 2\pi c/a$ for the three different termination planes of the crystal. As shown in fig. 2.6(a), at the chosen frequency (and in the whole first band) the electric field of the mode with $k_x = 0.447 \times 2\pi/a$ and $k_z = 0$ is symmetric with respect to the horizontal mirror planes of the crystal. Thus, the conditions enumerated in point (i) of the rule from subsection 2.3.2 are satisfied for truncation planes 1 and 2, and indeed, as shown in figs. 2.5(c) and (f), the effective permittivity ϵ_y is continuous and bounded for these truncation planes. In contrast, ϵ_y diverges at $k_x = 0.447 \times 2\pi/a$ when the crystal is truncated along the arbitrarily chosen plane 3 [fig. 2.5(i)].

It should be noted that shifting the truncation plane has a large influence on the numerical values of the effective parameters. For instance, at normal incidence, the crystal truncated along plane 1 has $\epsilon_y = 14.0$ and $\mu_x = 0.73$, whereas for the truncation plane 2 these values are $\epsilon_y = 7.1$ and $\mu_x = 1.43$ —a difference of a factor of two. This corroborates the earlier observations of Decoopman et al. [21].

As demonstrated above, at a frequency lying in the first band of the crystal under study the single-mode approximation works well, and so the effective-medium model is well-founded. In the second band, however, this approximation becomes much less accurate. We shall consider specifically the frequency $\omega = 0.259 \times 2\pi c/a$, at which the EFC of the crystal is, again, centred at Γ , approximately circular, and its radius corresponds to the effective index $n \approx -1$ [fig. 2.4(b), middle diagram, solid line]. In figs. 2.7(a) and (d) the rigorous value of the specular reflection coefficient of the crystal at this frequency is juxtaposed with that calculated from eq. (2.20). The relative error grows with k_x and is usually greater than 20% (plane 1) and 10% (plane 2). In the evanescent region, the single-mode approximation is clearly irrelevant. The graphs of the amplitudes of the three most slowly decaying crystal eigenmodes [figs. 2.7(b) and (e)] clearly show that the influence of the second mode is nonnegligible in the whole range of k_x , and for the first truncation plane even the third mode plays a significant part. Close inspection reveals that the ratios $|t_2/t_1|$ and $|t_3/t_1|$ tend to grow with the incidence angle; thus, the effective-medium model is a better approximation at near-normal than at grazing incidence (except for the immediate neighbourhood of $k_x = \omega/c$, where r_0 becomes exactly -1).

In addition, as shown in fig. 2.6(b), the electric field of the mode with $\omega = 0.259 \times 2\pi c/a$, $k_x = 0.259 \times 2\pi/a$ and $k_z = 0$ is antisymmetric with respect to the mirror planes of the crystal. Thus, ϵ_y is divergent at $k_x = 0.259 \times 2\pi/a$ regardless of the choice of the truncation plane [figs. 2.7(c) and (f)].

2.4.2 Square lattice

The second structure to be studied is the square lattice of air holes of radius $0.35a$, where a is the lattice constant, drilled in a dielectric matrix with $\epsilon = 11.56$ [fig. 2.8(a)]. Its Brillouin diagram is plotted in fig. 2.8(b). The analysis will be conducted at three discrete frequencies, $\omega = 0.13 \times 2\pi a/c$, $0.22 \times 2\pi a/c$ and $0.31 \times 2\pi a/c$, at which the EFCs of the crystal have an approximately circular or ellipsoidal shape, as demonstrated in fig. 2.9.

Figures 2.10(a), (d) and (g) show the k_x -dependence of the reflection coefficient r_0 at the frequency $\omega = 0.13 \times 2\pi a/c$ for the three positions of the truncation plane marked in fig. 2.8(a). Planes 1 and 2 contain inversion centres of the PC, while plane 3 does not. According to the theorem from subsection 2.3.1, for the former planes r_0 should be real as long as both the incident wave and the dominant crystal eigenstate are propagative, which is the case for $k_x < \omega/c = 0.13 \times 2\pi/a$. Figures

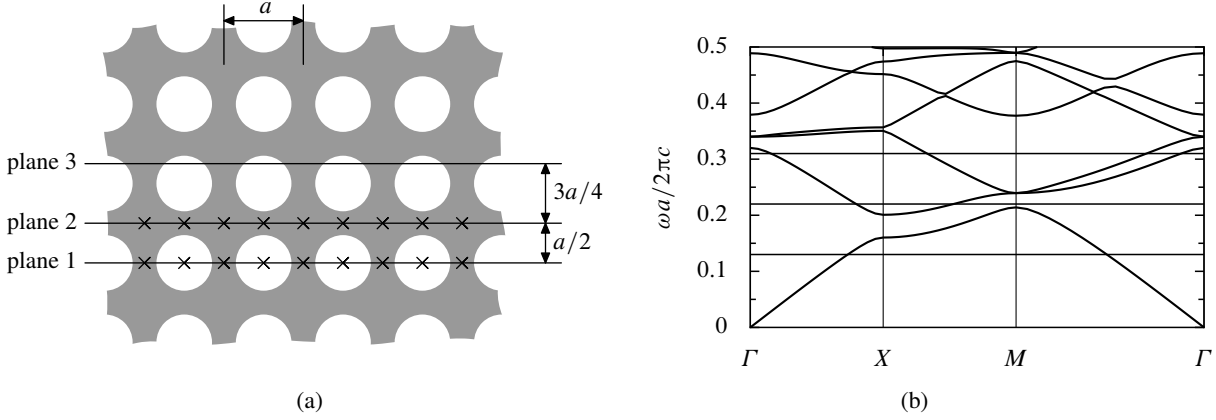


Figure 2.8 (a) Geometry of the square-lattice PC analysed in the text. Horizontal lines mark the position of truncation planes 1, 2 and 3; inversion centres of the infinite PC located at these planes are marked with crosses. (b) Band structure of the crystal shown in part (a). Horizontal lines mark the frequency values $\omega = 0.13 \times 2\pi c/a$, $0.22 \times 2\pi c/a$ and $0.31 \times 2\pi c/a$.

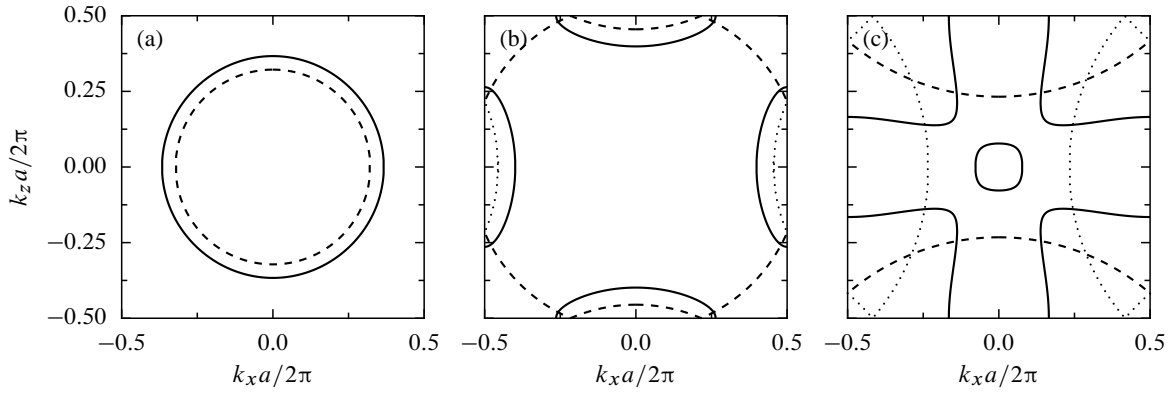


Figure 2.9 The EFCs at frequency (a) $\omega = 0.13 \times 2\pi c/a$, (b) $0.22 \times 2\pi c/a$, and (c) $0.31 \times 2\pi c/a$ of the PC shown in fig. 2.8(a) (solid lines) and the corresponding “empty lattice”, i.e., the homogeneous medium of refractive index 2.476 (dashed and dotted lines). The empty-lattice bands corresponding to the $n = 0$ harmonics are plotted with dashed lines, the rest with dotted lines.

2.10(a) and (d) confirm that this is fulfilled with a very good accuracy. In fact, $\text{Im } r_0^n$ does not exceed 0.002, that is, 0.3% of the magnitude of r_0^n ; this tiny imaginary part stems from the excitation of secondary crystal eigenmodes, which are neglected in the single-mode approximation. In turn, when the PC is truncated along plane 3, r_0 retains a large imaginary part also in the propagative-wave region [fig. 2.10(g)].

The plots of the relative error show that when the incident wave is propagative, the single-mode approximation is extremely accurate at the frequency in question (the relative error is less than 0.3%). For larger k_x , the error slowly grows, reaching $\rho \sim 0.6$ – 0.8 (planes 1 and 3) and $\rho \sim 0.2$ (plane 2) at the Brillouin zone edge. However, it does not exceed 10% until $k_x = 0.43 \times 2\pi/a$ for planes 1 and 3 and $k_x = 0.475 \times 2\pi/a$ for plane 2, so that the single-mode approximation is still relevant at $k_x = 0.39 \times 2\pi/a$, where κ_{1z} vanishes and the dominant eigenmode becomes evanescent. We may then proceed to the analysis of the behaviour of the effective parameters at this value of k_x . The EFC of the dominant eigenmode is centred at Γ , and its electric field at $k_x = 0.39 \times 2\pi/a$ and $k_z = 0$ is symmetric with respect to the horizontal mirror planes of the crystal, as evidenced by fig. 2.11(a). In consequence, the effective parameters $\mu_x = \mu_z$ and ϵ_y are continuous and bounded

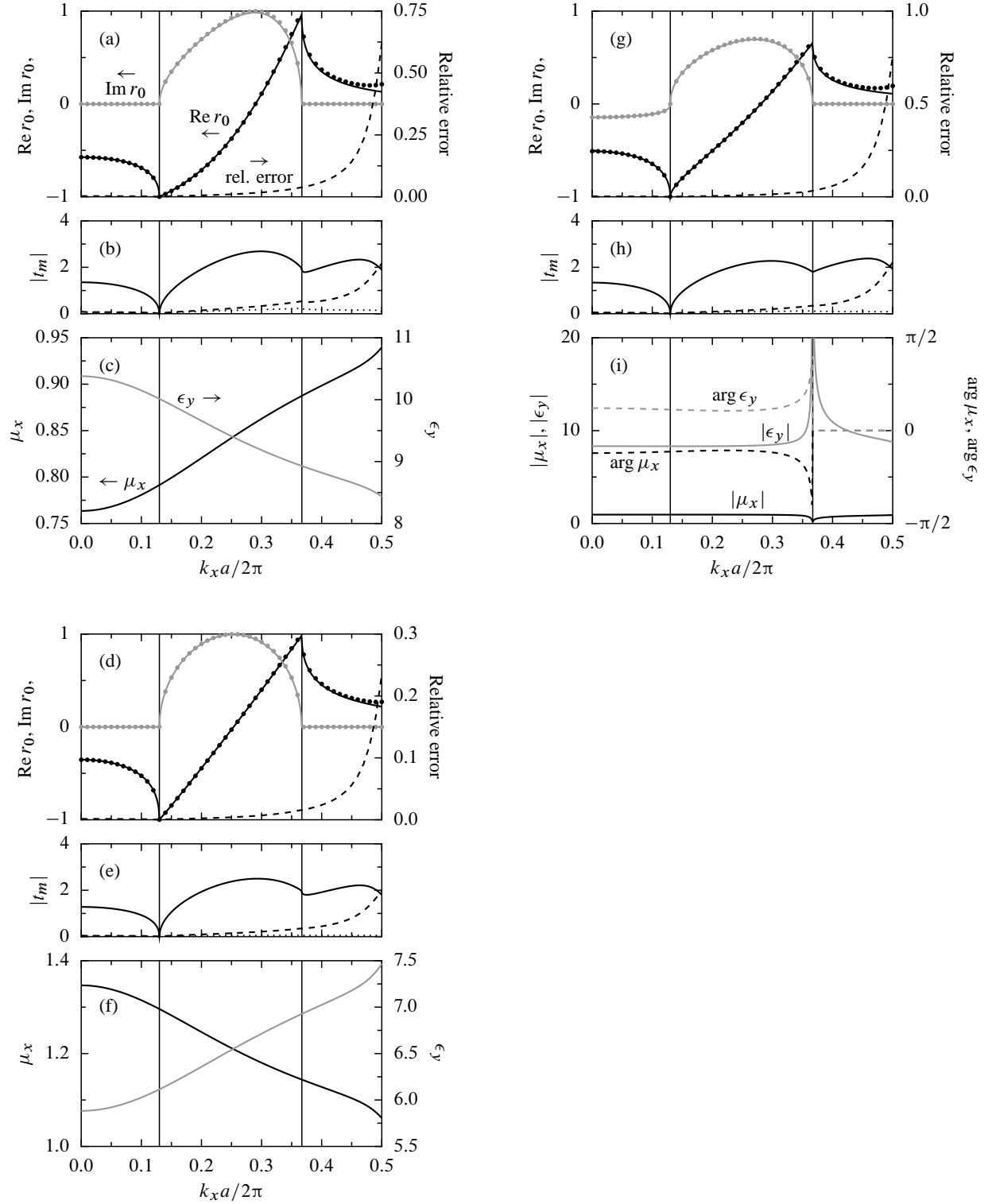


Figure 2.10 (a) The k_x -dependence of the specular reflection coefficient r_0 of the crystal from fig. 2.8(a) truncated along plane 1, at $\omega = 0.13 \times 2\pi c/a$. Solid lines: results of rigorous calculations, r_0^n ; circles: results of calculations made in the single-mode approximation, r_0^{sm} ; dashed line: relative error ρ of the single-mode approximation. The vertical lines at $k_x = 0.13 \times 2\pi/a$ and $0.367 \times 2\pi/a$ mark where the incident wave and the single propagating crystal eigenmode, respectively, turn from propagating to evanescent. (b) Amplitudes of the three most slowly decaying crystal eigenmodes excited in the above conditions (solid, dashed and dotted line, in order of increasing $\text{Im } k_z$). (c) Effective μ_x (dark lines) and ϵ_y (light lines) of the crystal. (d)–(f) and (g)–(i) The same for planes 2 and 3.

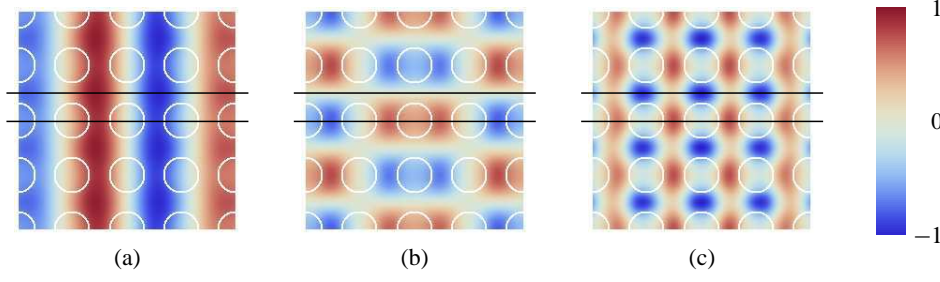


Figure 2.11 Real part of the electric field E_y of the modes of the crystal shown in fig. 2.8(a) with **(a)** $\omega = 0.13 \times 2\pi c/a$, $k_x = 0.367 \times 2\pi/a$ and $k_z = 0$, **(b)** $\omega = 0.22 \times 2\pi c/a$, $k_x = 0.264 \times 2\pi/a$ and $k_z = \pi/a$, **(c)** $\omega = 0.31 \times 2\pi c/a$, $k_x = 0.078 \times 2\pi/a$ and $k_z = 0$. Two nonequivalent mirror planes of the crystal parallel to its surface are marked with horizontal lines.

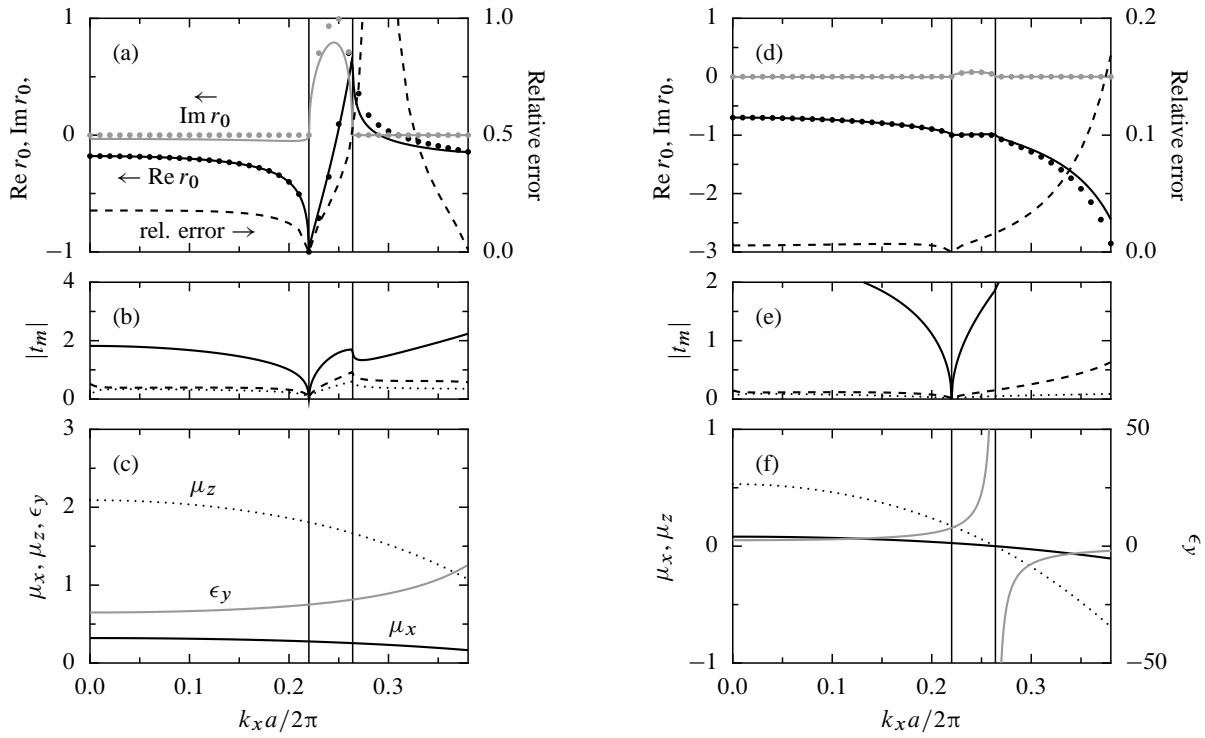


Figure 2.12 Same as fig. 2.10, at frequency $\omega = 0.22 \times 2\pi c/a$ and for truncation planes **(a)–(c)** 1 and **(d)–(f)** 2. The vertical lines at $k_x = 0.22 \times 2\pi/a$ and $0.264 \times 2\pi/a$ mark where the incident wave and the single propagating crystal eigenmode, respectively, turn from propagating to evanescent.

in the whole range of k_x for the cuts 1 and 2, which coincide with mirror planes of the PC [figs. 2.10(c) and (f)]. In contrast, truncating the crystal along plane 3 leads to divergence of ϵ_y at $k_x = 0.39 \times 2\pi a/c$.

We turn now to the study of the system at the frequency $\omega = 0.22 \times 2\pi a/c$. The EFC, shown in fig. 2.9(b), consists of two elliptical “branches” encircling the points $X = (0, \pi/a)$ and $X' = (\pi/a, 0)$. In the effective-medium model, we focus on the neighbourhood of the first EFC branch ($|k_x| < 0.39 \times 2\pi/a$) and use the dimensions of the ellipse encircling the X point to calculate the effective parameters. The electric field of the mode corresponding to the right vertex of this ellipse is plotted in fig. 2.11(b). It is symmetric with respect to plane 1, which passes through the cylinder centres, and antisymmetric with respect to plane 2, passing midway between the cylinders.

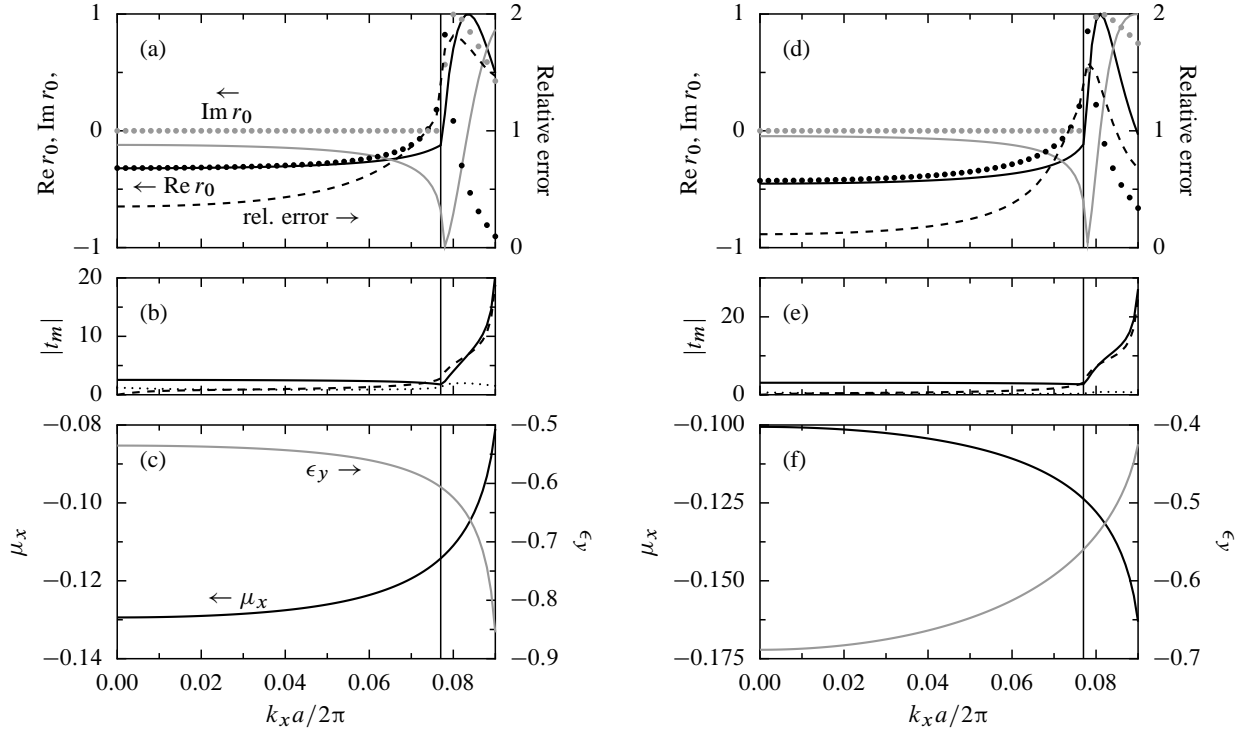


Figure 2.13 Same as fig. 2.10, at frequency $\omega = 0.31 \times 2\pi c/a$ and for truncation planes **(a)–(c)** 1 and **(d)–(f)** 2. The vertical line at $k_x = 0.078 \times 2\pi/a$ marks where the propagating crystal eigenmode turns evanescent (the incident wave is propagating throughout the k_x range presented on the plot).

Figures 2.12(a) and (d) show the k_x -dependence of the reflection coefficient r_0 for these two crystal terminations. As for $\omega = 0.13 \times 2\pi c/a$, the approximation accuracy is visibly better for plane 2 than 1: in the former case, r_0 is rendered faithfully well beyond the propagative-wave region. The superior performance achieved for plane 2 is probably due to the uniformity of the crystal permittivity on this plane, which leads to smaller spatial field variations, making fewer Fourier harmonics necessary to match the field in the crystal with that in free space. However, the antisymmetry of the eigenmode's electric field with respect to plane 2 implies that the effective permittivity ϵ_y diverges at $k_x = 0.26 \times 2\pi/a$ [fig. 2.12(f)]. In contrast, if the other truncation plane is chosen, all effective parameters are continuous and bounded [fig. 2.12(c)], but at the cost of a significant single-mode approximation error: $\rho \sim 17\%$ close to normal incidence. (This time, the relative error is not very meaningful in the evanescent-wave region, since the rigorous reflection coefficient passes through zero at $k_x = 0.29 \times 2\pi/a$, so that ρ blows up.)

Finally, we move on to the case of $\omega = 0.31 \times 2\pi c/a$. The EFC diagram shown in fig. 2.9(c) comprises an approximately circular part located at the centre of the Brillouin zone and four curves of irregular shape, together forming a closed path encircling the point $M = (\pi/a, \pi/a)$. The circular EFC represents a negative-refraction band. As seen from fig. 2.11(c), the electric field of the mode with $k_x = 0.078 \times 2\pi/a$ and $k_z = 0$ is symmetric with respect to planes 1 and 2, which assures the continuity of the effective parameters at $k_x = 0.078 \times 2\pi/a$, where the mode turns from propagating to evanescent. This is in contrast to the negative-refraction band of the hexagonal crystal analysed in the previous subsection, whose symmetry properties made ϵ_y diverge at the transition point. However, there is no improvement in the accuracy of the single-mode approximation: the comparison of the values of r_0 calculated rigorously and from eq. (2.20) [figs. 2.13(a) and (d)] reveals that the approximation introduces a significant error (above 33% for plane 1 and 11% for plane 2) due to the large excitation amplitude of secondary crystal eigenmodes [figs. 2.13(b) and (e)].

2.4.3 Remarks

In the context of metamaterials containing resonant components, such as metallic split rings, it has been observed that inside band gaps, the effective permittivity and permeability of these structures (defined at normal incidence) have large imaginary parts of opposite sign, regardless of the location of the truncation plane [82–85]. This is not in contradiction with our theory, since one of the assumptions of the condition for real-valuedness of ϵ and μ formulated in subsection 2.3.1 is the propagative nature of the fundamental crystal eigenstate (real κ_{1z}). Of course, inside band gaps all modes are evanescent, and so the condition in question is not applicable.

On the other hand, our results show that in general the effective parameters of a lossless PC can attain complex values even outside band gaps, if the truncation plane does not exhibit certain symmetries. In this case, the product $\epsilon\mu$ is real (due to the absence of losses), and either ϵ or μ has a negative imaginary part. This is visible, for example, in fig. 2.5(i) showing the k_x -dependence of the effective parameters for the low-symmetric truncation plane 3 of the PC from fig. 2.3(a): it is clear that $\arg \mu_x \in [-\frac{\pi}{2}, 0]$, so that $\text{Im } \mu_x < 0$. Only at specific truncation planes are effective ϵ and μ real. (It must be noted, though, that precisely these special truncation planes have usually been chosen in previous calculations of the effective parameters of PCs and metamaterials.)

2.5 Validity of the single-mode approximation

We have seen that the accuracy of the single-mode approximation for a given PC varies strongly with frequency and incidence angle. In some cases, one of the crystal modes is clearly dominant; in others, several eigenstates are excited with similar magnitude. In the following, we offer a qualitative argument relating the ratios $|t_m/t_1|$ of the excitation coefficients of the individual modes to the Fourier spectrum of their electromagnetic fields on the crystal surface. This leads us to conclusions regarding, in particular, the viability of the effective-medium description of negative-refraction bands.

Let us begin by writing the system (2.17) in a partitioned form, emphasising the rows corresponding to the nonzero elements of the vectors representing the incident field, a_0 and a'_0 , as well as the columns corresponding to the unknowns r_0 and t_k :

$$\begin{bmatrix} -\hat{I} & \vec{0} & \hat{0} & \hat{u}_{<k}^{<0} & \vec{u}_k^{<0} & \hat{u}_{>k}^{<0} \\ \vec{0} & -1 & \vec{0} & \vec{u}_{<k}^0 & u_k^0 & \vec{u}_{>k}^0 \\ \hat{0} & \vec{0} & -\hat{I} & \hat{u}_{<k}^{>0} & \vec{u}_k^{>0} & \hat{u}_{>k}^{>0} \\ i\hat{\beta}_{<0}/\mu_1 & \vec{0} & \hat{0} & \hat{v}_{<k}^{<0} & \vec{v}_k^{<0} & \hat{v}_{>k}^{<0} \\ \vec{0} & i\beta_0/\mu_1 & \vec{0} & \vec{v}_{<k}^0 & v_k^0 & \vec{v}_{>k}^0 \\ \hat{0} & \vec{0} & i\hat{\beta}_{>0}/\mu_1 & \hat{v}_{<k}^{>0} & \vec{v}_k^{>0} & \hat{v}_{>k}^{>0} \end{bmatrix} \begin{bmatrix} \vec{r}_{<0} \\ r_0 \\ \vec{r}_{>0} \\ \vec{t}_{<k} \\ t_k \\ \vec{t}_{>k} \end{bmatrix} = \begin{bmatrix} \vec{0} \\ 1 \\ \vec{0} \\ \vec{0} \\ i\beta_0/\mu_1 \\ \vec{0} \end{bmatrix}. \quad (2.37)$$

We remind the reader that the symbols embellished with arrows, bars and hats are column vectors, row vectors and matrices, respectively, while those without any embellishment are scalars (see section 1.3). The meaning of the indices should be clear; for example, $\hat{u}_{<k}^{<0}$ stands for the submatrix of the \hat{u} matrix corresponding to rows with negative indices and columns with indices less than k . From the Cramer's formula [86, p. 299], we have $t_l/t_k = D_l/D_k$, where D_j stands for the determinant of the matrix created by replacing the j th column in the right half of the matrix of the system from eq. (2.37) by the right-hand side of the system. After some algebra, where elementary properties of determinants are utilised,

we arrive at

$$\frac{t_l}{t_k} = (-1)^{l-k} \frac{\begin{vmatrix} -\hat{I} & \hat{0} & \hat{u}_{<l}^{<0} & \hat{u}_{>l}^{<0} \\ \hat{0} & -\hat{I} & \hat{u}_{<l}^{>0} & \hat{u}_{>l}^{>0} \\ i\hat{\beta}_{<0}/\mu_1 & \hat{0} & \hat{v}_{<l}^{<0} & \hat{v}_{>l}^{<0} \\ \hat{0} & i\hat{\beta}_{>0}/\mu_1 & \hat{v}_{<l}^{>0} & \hat{v}_{>l}^{>0} \end{vmatrix}}{\begin{vmatrix} -\hat{I} & \hat{0} & \hat{u}_{<k}^{<0} & \hat{u}_{>k}^{<0} \\ \hat{0} & -\hat{I} & \hat{u}_{<k}^{>0} & \hat{u}_{>k}^{>0} \\ i\hat{\beta}_{<0}/\mu_1 & \hat{0} & \hat{v}_{<k}^{<0} & \hat{v}_{>k}^{<0} \\ \hat{0} & i\hat{\beta}_{>0}/\mu_1 & \hat{v}_{<k}^{>0} & \hat{v}_{>k}^{>0} \end{vmatrix}}. \quad (2.38)$$

By means of the Laplace expansion [86, p. 259] of the determinants in the numerator and denominator along the columns containing \vec{u}_k and \vec{u}_l , respectively, the ratio t_l/t_k can be written as the ratio of two sums of terms proportional to the components of the Fourier expansion of the electric and magnetic fields at the crystal surface of, respectively, the k th and l th eigenmode:

$$\frac{t_l}{t_k} = \frac{\sum_{n \neq 0} (a_n u_k^n + b_n v_k^n)}{\sum_{n \neq 0} (a_n u_l^n + b_n v_l^n)}, \quad (2.39)$$

where a_n and b_n denote the appropriate coefficients resulting from the Laplace expansion. It is crucial to observe that these sums do not contain the *zeroth* Fourier component of either field.

The PC bands can be treated as mixtures of the eigenstates of the empty lattice with “average” ϵ and μ ; for a fixed k_x , these eigenstates are the plane waves $E_{yn}(x, z) = \exp[i(k_x + G_{xn})x + ik_{zn}z]$, where $k_{zn} = \sqrt{\epsilon\mu(\omega/c)^2 - (k_x + G_{xn})^2}$. When the index contrast of the PC is low enough, in some regions of the (ω, k_x) space each of the PC eigenstates comprises a single dominant plane wave, the perturbative components having low amplitude. This means that each of the sets of coefficients $(u_m^n)_{n \in \mathbb{Z}}$ corresponding to different modes m contains a single dominant component. From eq. (2.39) it follows that, in general, the mode whose dominant component is the zeroth one ($n = 0$) is then excited the most strongly. Indeed, labelling this mode with index $m = 1$, we see that in the expression (2.39) for the ratio t_l/t_1 ($l \neq 1$) the sum in the numerator does not contain terms proportional to u_1^0 and v_1^0 , which, by assumption, are the largest ones. On the contrary, the sum in the denominator contains two terms proportional to the dominant components of the l th mode, say, $u_l^{n_l}$ and $v_l^{n_l}$, since n_l is necessarily different from zero. Thus, we see that the fraction t_l/t_1 is a ratio of a “small” and a “large” quantity—and so $|t_l| \ll |t_1|$ for all $l \neq 1$, that is, the defining assumption of the single-mode approximation is fulfilled.

Conversely, if there is strong coupling between the zeroth harmonic and plane waves corresponding to different values of n , so that no mode with highly dominant zeroth component exists, the numerator in (2.39) for $k = 1$ is no longer a small quantity, and multiple eigenmodes can be excited with comparable amplitude.

We conclude that *the single-mode approximation should work best at those values of ω and k_x for which the mode originating from the $n = 0$ harmonic—the plane wave $\exp(ik_x x + ik_{z0} z)$ —does not contain significant contributions of other plane waves.* In practice, this usually means that when we consider the transition from the empty lattice to the final PC, the fragment of the EFC of the PC around a given value of k_x should form mainly from the circle corresponding to the $n = 0$ harmonic of the empty lattice. For example, as can be seen in fig. 2.4(a), the EFC of the single propagating mode of the hexagonal-lattice PC at frequency $\omega = 0.14 \times 2\pi c/a$ (solid line, middle diagram) is very similar to the original EFC of the $n = 0$ harmonic of the empty lattice (dashed line). In addition, the imaginary bands corresponding to $n = -1$ and $n = -2$ are very weakly perturbed (top diagram). We infer that the

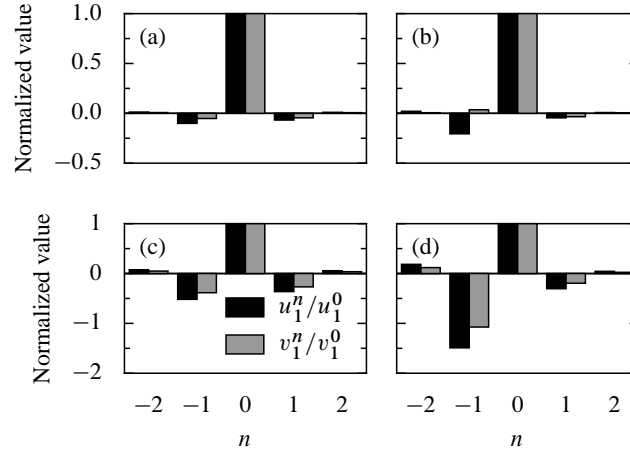


Figure 2.14 Values of the harmonics $(u_1^n)^2_{n=-2}$ and $(v_1^n)^2_{n=-2}$ of the propagative eigenmode of the crystal from fig. 2.3(a) on the truncation plane 1 and at **(a)** $\omega = 0.14 \times 2\pi c/a$, $k_x = 0.10 \times 2\pi/a$, **(b)** $\omega = 0.14 \times 2\pi c/a$, $k_x = 0.40 \times 2\pi/a$, **(c)** $\omega = 0.259 \times 2\pi c/a$, $k_x = 0.05 \times 2\pi/a$, **(d)** $\omega = 0.259 \times 2\pi c/a$, $k_x = 0.20 \times 2\pi/a$.

individual plane waves couple weakly, so that the zeroth harmonic of the field of the propagating crystal eigenmode should be dominant, and the eigenmode itself should be strongly excited. These claims are corroborated by figs. 2.14(a)–(b), where the amplitudes of several harmonics u_1^n and v_1^n of this mode at the truncation plane 1 are shown for two values of k_x , and fig. 2.5(b), where the amplitudes $|t_m|$ of individual eigenstates are juxtaposed.

Now let us turn our attention to fig. 2.4(b), where the evolution of the EFCs at the frequency $\omega = 0.259 \times 2\pi a/c$ is shown; this frequency lies in the second band, which exhibits negative group velocity. We can see that in this case the plotted quarter of the circular EFC of the single propagating crystal eigenstate is formed by merging of the $n = 0$ and $n = -1$ harmonics of the empty lattice. Their strong coupling is further indicated by the substantial alteration of the shape of the imaginary bands. We can expect the contribution of the zeroth harmonic to be strongest at small values of k_x , and so the accuracy of the single-mode approximation to be highest near normal incidence and deteriorate with increasing k_x . This is again confirmed by figs. 2.14(c)–(d) and 2.7(b).

To help establish a broader picture of the single-mode approximation's performance for the hexagonal-lattice PC, in fig. 2.15(b) the relative error of the reflection coefficient r_0 calculated in this approximation is plotted for a mesh of 101×100 points of the (k_x, ω) space. In turn, figs. 2.15(c) and (d) present the amplitude variations of the zeroth harmonic of the electric and magnetic field, respectively, of the most slowly decaying crystal mode (on the truncation plane 1). It can be seen that, although there is no one-to-one correspondence, the areas of significant error generally match those in which the $n = 0$ component of either the electric or magnetic field, or both, of the least-evanescent eigenmode has small amplitude. (In fact, the dependence of the approximation's accuracy on the Fourier spectrum of the magnetic field seems more pronounced than that on the electric field.)

Finally, it should be noted that the EFC from fig. 2.4(b) is in fact typical for negative-refraction bands. Indeed, the EFCs of the empty lattice are circular, with group velocity directed outwards, and the negative bands arise from convex figures formed by arcs of three, four or six such intersecting circles, necessarily including those corresponding to harmonics with nonzero G_{xn} (see fig. 2.16). Thus, the resulting bands do not fulfil the validity condition of the single-mode approximation, or do it only in the restricted range of k_x close to zero. Consequently, attribution of effective permittivity and permeability to negative-refraction bands makes sense at most for near-normal incidence, while in the evanescent regime the effective-medium description is definitely inappropriate.

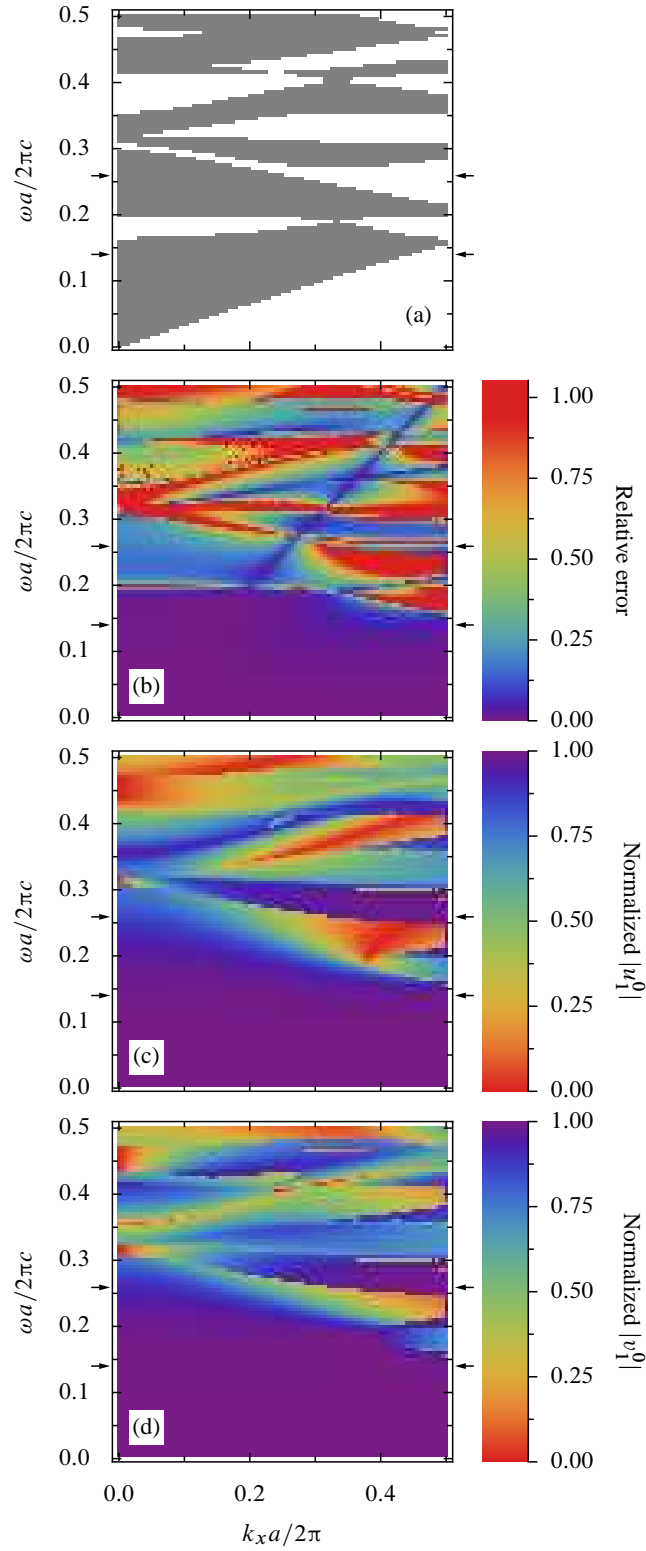


Figure 2.15 (a) Projection of the band structure of the PC shown in fig. 2.3(a) on the (k_x, ω) plane. Grey and white areas denote photonic bands and gaps, respectively. The arrows mark the frequency values $\omega = 0.14 \times 2\pi c/a$ and $0.259 \times 2\pi c/a$. (b) The dependence of the relative error of the single-mode approximation of this crystal's reflection coefficient on k_x and ω for the truncation plane 1. (c) The corresponding dependence of $|u_1^0|/[\sum_n |u_1^n|^2]^{1/2}$. (d) Same for $|v_1^0|/[\sum_n |v_1^n|^2]^{1/2}$.

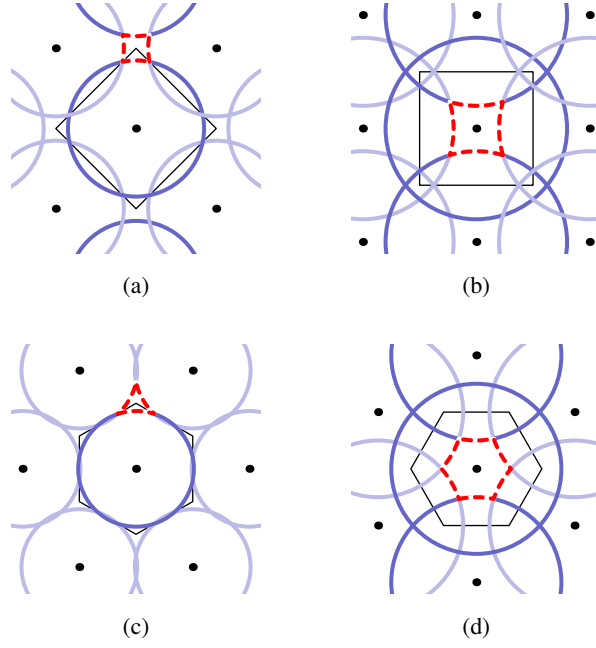


Figure 2.16 Typical configurations of empty-lattice EFCs leading to formation of negative-refraction bands after introducing sufficient lattice modulation. In each case, the direction of normal incidence is from the bottom; circles corresponding to harmonics with $G_{xn} = 0$ are drawn in darker blue. Thin lines mark the boundaries of the first Brillouin zone of each lattice, and black dots denote reciprocal lattice points. Top row: square lattice, bands encircling **(a)** the M point of the first Brillouin zone, **(b)** the Γ point; bottom row: hexagonal lattice, bands encircling **(c)** the K point, **(d)** the Γ point.

2.6 Conclusions

In this chapter, we have analysed in detail the effective-medium description of 2D PCs. Its validity has been shown to be restricted by the accuracy of the single-mode approximation, and a definition of the effective permittivity, permeability and transverse impedance, rigorous under this approximation, has been given. In the framework of the single-mode approximation, we have studied the dependence of the specular reflection coefficient r_0 of the crystal on the position of the truncation plane, deriving the conditions assuring r_0 , and consequently the effective parameters, to be real-valued. Continuity and boundedness of the latter have been shown to depend on the symmetry of the dominant eigenmode of the crystal.

Subsequently, the conditions of validity of the single-mode approximation have been studied. We have established a link between the relative excitation amplitudes of individual crystal eigenmodes and the Fourier spectrum of the electric and magnetic fields of these modes on the crystal truncation plane. This link has been employed to formulate a criterion for estimating the accuracy of the single-mode approximation by comparing the equifrequency diagrams of the PC and of the homogeneous medium with refractive index equal to the average refractive index of the PC. Finally, we discussed the special case of negative-refraction bands; we concluded that the effective-medium description of these bands is, quite generally, inaccurate, since their Fourier-space structure entails simultaneous excitation of other bands by plane waves incident at most angles, and so attributing a definite effective permittivity and permeability to these bands is not physically meaningful.

Chapter 3

Antireflection gratings for photonic crystals

3.1 Introduction

As can be seen from the plots of the reflection coefficient of PCs presented in chapter 2 (figs. 2.5, 2.7, 2.10, 2.12, and 2.13), reflected waves of significant amplitude are often generated at PC surfaces. In many applications, one strives after a perfect energy transfer between the incident plane wave and the propagative PC eigenmode (or, more rarely, several such modes). Propagative reflected waves should then be eliminated. This chapter concerns the design of *antireflection* (AR) *structures* that, placed on a PC surface, significantly diminish the fraction of energy lost to reflected waves. After reviewing the classes of these structures proposed to date (section 3.2), in section 3.3 we put forward a new method of designing AR gratings operating in a wide range of angles of incidence. This algorithm is illustrated in section 3.4 by means of several examples. We summarise the advantages and limitations of the proposed approach in section 3.5.

3.2 Types of antireflection structures

3.2.1 Antireflection structures for homogeneous media

Since the design of AR structures for PCs is often guided by the experience gained from the long-standing study of methods for eliminating reflections from interfaces separating homogeneous media, we shall begin with a brief review of the AR structures employed in this simpler case.

They can be divided into two broad classes. The refractive index n of *AR coatings* depends only on the coordinate z perpendicular to the interface; depending on whether $n(z)$ is piecewise-constant or not, we speak of *homogeneous-layer* or *inhomogeneous-layer* AR coatings [87]. In turn, the refractive index of *AR gratings* is also a function of the coordinates parallel to the interface. Figure 3.1 shows example AR structures belonging to these three classes.

The simplest homogeneous-layer AR coating consists of a single thin film with refractive index n and thickness d chosen so as to ensure destructive interference of waves reflected from its top and bottom surfaces, excited by a plane wave with a certain frequency ω and angle of incidence θ . The values of n and d can be obtained analytically. In order to improve the angular and frequency tolerance of the coating, one can increase the number of layers to make the transition between the refractive index of the super- and substrate more gradual [87], thus reducing the amplitude of waves reflected on the individual discontinuities of $n(z)$. In the limit of an infinite number of layers, one arrives at an inhomogeneous-layer coating with a continuous monotonic profile $n(z)$. Several specific profiles have been proposed in the literature (see ref. 88 for a review). Unfortunately, these “ideal” AR coatings, even the single-layer one, cannot usually be realised because of the lack of suitable materials with the required values of n . This is the case, in particular, for air-solid interfaces, where thin films with refractive index close to unity

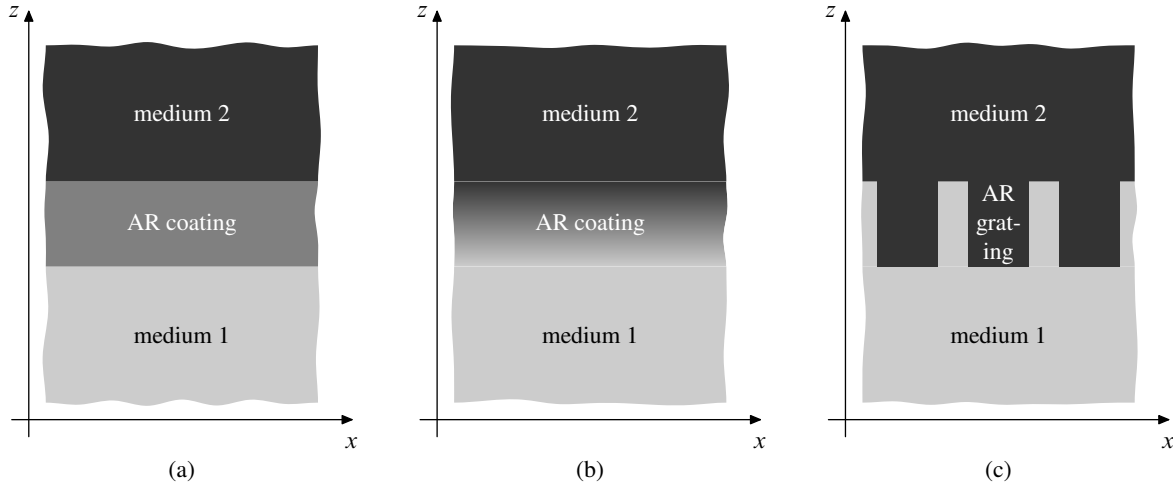


Figure 3.1 Example AR structures belonging to the three principal classes described in the text. Darker areas denote regions with higher refractive index. **(a)** A homogeneous-layer AR coating. **(b)** An inhomogeneous-layer AR coating. **(c)** A (binary lamellar) AR grating.

are needed. Short of using special ultra-low-index media, such as so-called Reststrahlen materials [87], there are two basic ways of circumventing this problem.

One of them consists in abandoning completely the structures based on a “continuous transition” between the super- and substrate refractive indices in favour of interference-based coatings [87]. In these systems, the total reflected wave vanishes thanks to the destructive interference of partial waves generated at interfaces between layers with *contrasting* values of n . For instance, so-called v -coatings consist of two layers with prescribed refractive indices n_1 and n_2 (corresponding to realistic materials) and thicknesses d_1 and d_2 adjusted so as to eliminate reflection at the desired values of ω and θ . Note that n_1 and n_2 must satisfy certain conditions in order that appropriate d_1 and d_2 can be found [89, p. 96]. A disadvantage of v -type AR coatings is that their angular and frequency tolerance are usually inferior even to those of the corresponding ideal single-layer coatings [89, p. 97; 90, p. 188].

The other solution consists in using subwavelength gratings to simulate AR coatings with arbitrary $n(z)$ profiles. In many cases, the effective-medium theory of gratings can be employed to calculate the grating profile mimicking the desired $n(z)$ dependence [88]. Several types of gratings, such as the lamellar, trapezoidal, sinusoidal, triangular and pyramidal ones, have been studied in the literature and shown to have good AR properties [88, 91–93]. A review of the experimental methods used to fabricate such AR structures can be found in ref. 94.

3.2.2 Antireflection structures for photonic crystals

As pointed out in chapter 2, a distinguishing feature of PCs is the dependence of their reflection coefficient on the position of their truncation plane. One could hope then that a significant reduction of a PC’s reflectance could be achieved without adding any AR structure, but simply by choosing an appropriate cut. For some crystals, this has indeed proved to be possible [95, 96]. In particular, Botten et al. [96] have shown that very low reflectance is a rather general feature of rod-type PCs truncated midway between successive layers of rods. For many crystals, however, no truncation plane provides a sufficiently small value of reflectance (see fig. 3.2). This method of reducing reflection is therefore not general enough, and one often has to resort to introducing some AR structure. Several types of them have been proposed in the literature. More often than not, they have much in common with one of the solutions developed with homogeneous materials in mind, reviewed in the previous subsection.

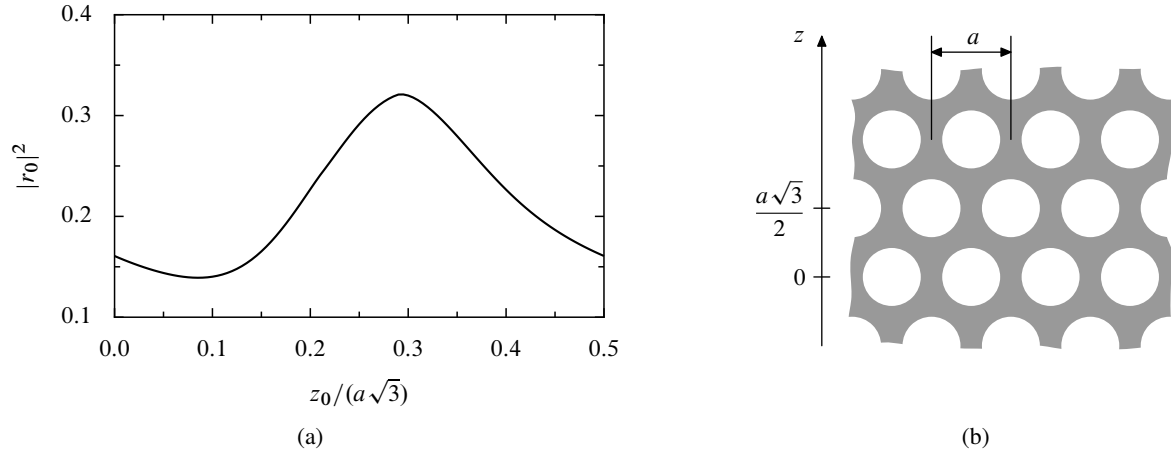


Figure 3.2 (a) The dependence of the reflectance $|r_0|^2$ of the PC shown in part (b), placed in air, on the location of the truncation plane $z = z_0$. The impinging wave is normally incident, s -polarised and has frequency $\omega = 0.311 \times 2\pi c/a$. It can be seen that $|r_0|^2$ does not fall under 0.13 for any truncation plane. (b) Geometry of the PC under study: a hexagonal lattice of air holes with radius $0.365a$, where a is the lattice constant, etched in a dielectric matrix with permittivity $\epsilon = 10.6$.

The simplest approach has been proposed by Li et al. [97]. It consists in placing in front of the crystal a v -type AR coating composed of two layers made of constituent materials of the crystal, usually air and a dielectric. Their thicknesses can be determined analytically or graphically as soon as the reflection coefficient of the semi-infinite uncoated PC at the selected operation frequency is known. This frequency is assumed to be low enough that only the zeroth diffraction order be propagative in the layer closest to the PC surface, so that all higher orders reflected by the crystal decay before reaching the boundary between the two layers. If it is not the case, the structure may still work, but the optimum layer thicknesses will not in general be given by the analytical formulas derived from the thin-film theory. The basic disadvantage of this otherwise very attractive approach is the relatively low angular and frequency tolerance of v -type AR coatings.

Another group has studied a similar approach, in which one of the homogeneous layers is replaced by a grating of rods or holes [98, 99]. The performance of the resulting AR gratings was shown to be similar to that of v -type coatings [99]. Related structures, albeit with only a single degree of freedom (the radius of the outermost rods of a rod-type PC), were also analysed by Jin and He [100]. In turn, Zhang and Li [101] proposed a more complex wide-angle AR grating for the interface between air and a PC flat lens, whose fabrication would be seriously hindered, though, by the presence of extremely thin air slits and dielectric veins.

In contrast to the above works, which concentrated on the low-frequency regime, the authors of refs. 102–104 endeavoured to eliminate the reflection from an interface between a PC and a semiconductor at a frequency where multiple propagative diffraction orders existed in the latter medium. They proposed an AR grating consisting of elongated drop-shaped air holes, this nonstandard form being motivated by the desire of ensuring a gradual transition between the two media. In fact, the shape of the resulting structure resembles closely the classical trapezoidal AR gratings studied, e.g., by Raguin and Morris [92]. The improvement brought about by these gratings has subsequently been demonstrated experimentally [105]. Unfortunately, Baba et al. did not provide any analytical guidelines regarding the choice of the geometrical parameters of the gratings, resorting instead to a time-consuming scan of the parameter space in order to find the optimum structure [102, 103].

A very important contribution was made by Lawrence et al. [106, 107], who introduced the concept of generalised *matrix-valued* effective immittance $\hat{\mathcal{E}}$ of gratings and showed that their effective-medium

description can be made arbitrarily accurate by allowing $\hat{\mathcal{E}}$ to have sufficiently large dimensions. Such matrix-valued immittance cannot serve as a drop-in replacement of the corresponding scalar quantity in standard formulas derived for homogeneous media [107]. Therefore, for instance, analytical determination of the optimum parameters of an AR structure for a given PC composed of layers described by a matrix $\hat{\mathcal{E}}$ is not possible. However, Lawrence et al. derived equations corresponding to the Fresnel formulas (2.9) involving the generalised immittances of two adjacent gratings, and showed that the immittance matrix of typical gratings can be truncated to 5×5 elements or less without a substantial loss in accuracy. Since numerical calculations involving such small matrices are very fast, it becomes feasible to design optimum AR gratings by performing a full scan of the available parameter space. Example AR structures presented in ref. 107 include, for instance, a relatively wide-band AR coating of a superprism-type PC at a frequency where multiple propagative diffraction orders exist in the adjacent dielectric. A slight limitation of the approach of Lawrence et al. is that the generalised immittance has only been defined for 2D gratings symmetrical with respect to a two-fold rotation axis parallel to the direction of invariance. Therefore, it does not cover, for instance, triangular or trapezoidal gratings.

All the AR structures discussed so far are relatively compact, with thickness rarely exceeding one or two lattice constants of the underlying PC. Some authors have advocated sacrificing compactness in favour of potentially larger frequency and angular tolerance offered by thick stacks of gratings, whose geometry changes gradually so as to ensure a smooth transition of the electromagnetic field of the incident plane wave towards the Bloch mode of the semi-infinite PC. Several design principles for such gratings have been proposed [108, 109]. In this work, we shall focus on compact AR structures, and therefore we do not consider adiabatic AR gratings in detail.

3.3 Design procedure

We shall now present an alternative method of designing AR gratings for PCs. Compared to the approaches reviewed in subsection 3.2.2, it has the following distinguishing features:

1. Instead of performing a potentially time-consuming global scan of possible geometries, we use an effective-medium model of PCs to calculate analytically the geometrical parameters of a “tentative” AR grating; then, if necessary, these parameters are refined with a numerical local-minimisation procedure. The end result of our procedure is a trapezoidal AR grating.
2. The resulting AR structures have good angular tolerance, which in some important applications of PCs is more significant than the frequency tolerance. For instance, the quality of the image produced by a PC flat lens with effective refractive index $n \approx -1$ depends in the first place on the angular range of incident propagative plane waves which are transmitted through the lens with little or no energy loss. On the other hand, frequency tolerance is not vital since n can be close to -1 only in a narrow frequency band.

We draw on the results of Raguin and Morris [92], who demonstrated that triangular and trapezoidal gratings allow a significant reduction of reflectance at interfaces between homogeneous media in a wide range of incidence angles. Let us now proceed to detailing the three constituent steps of the algorithm.

Step I We begin by using the classical theory of AR coatings to calculate the refractive index and thickness of a single-layer coating that should minimise the reflection from the PC surface at a fixed angle of incidence θ and frequency ω . The value of θ should lie approximately midway the desired angular operation range of the final AR structure.

Consider the system shown in fig. 3.3, in which a propagative plane wave with frequency $\omega = ck_0$ and wave vector $\vec{k}_1 = (k_x, k_{z1}) = (n_1 k_0 \sin \theta, n_1 k_0 \cos \theta)$ impinges from the dielectric 1 with refractive

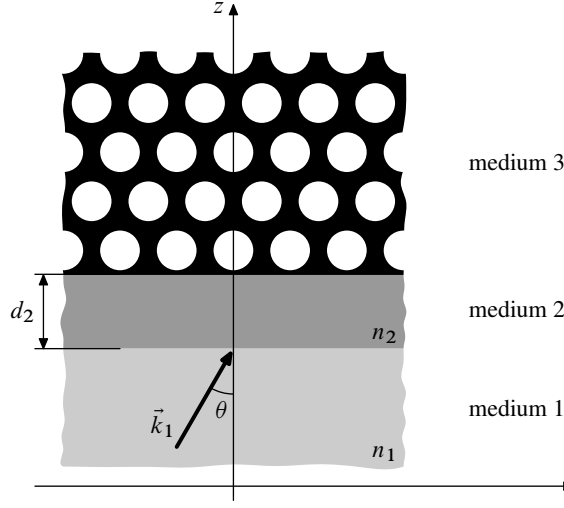


Figure 3.3 System considered in step 1 of the AR grating design procedure.

index n_1 on the surface of the homogeneous film 2 with thickness d_2 and refractive index n_2 coating the PC 3. Let us assume that medium 2 supports exactly one propagative diffraction order and is sufficiently thick for all the evanescent orders reflected from the PC surface to vanish at the interface between media 1 and 2. We can calculate the total amplitude of the reflected plane wave, r , by summing up all the multiple reflections occurring in the system:

$$r = r_{12} + t_{12}\Phi r_{23}\Phi \left[\sum_{n=0}^{\infty} (r_{21}\Phi r_{23}\Phi)^n \right] t_{21} = \frac{r_{12} + (t_{12}t_{21} - r_{12}r_{21})r_{23}\Phi^2}{1 - r_{21}r_{23}\Phi^2}, \quad (3.1)$$

where r_{ij} and t_{ij} denote the amplitudes of the waves reflected from the interface between media i and j and transmitted through it, respectively, and $\Phi \equiv e^{ik_{z2}d_2}$ with $k_{z2} \equiv (n_2^2 k_0^2 - k_x^2)^{1/2}$. From the Fresnel's formulas [cf. (2.9)]

$$r_{ij} = \frac{\mathcal{E}_j - \mathcal{E}_i}{\mathcal{E}_j + \mathcal{E}_i}, \quad t_{ij} = \frac{2\mathcal{E}_j}{\mathcal{E}_j + \mathcal{E}_i} \quad (3.2)$$

it immediately follows that $r_{21} = -r_{12}$ and $t_{12}t_{21} - r_{12}r_{21} = 1$, hence

$$r = \frac{r_{12} + r_{23}\Phi^2}{1 + r_{12}r_{23}\Phi^2}. \quad (3.3)$$

The parameters of the antireflection coating, n_2 and d_2 , can now be obtained by requiring the numerator of the fraction in the above equation to vanish. If the coating is lossless, so that $|\Phi| = 1$, the numerator vanishes if and only if (i) the moduli of r_{12} and r_{23} are equal and (ii) the thickness d_2 is such that

$$\arg r_{23} + 2k_{z2}d_2 = \arg r_{12} + (2m + 1)\pi, \quad (3.4)$$

where $m \in \mathbb{Z}$ and $\arg z$ stands for the argument of the complex number z . Solving for d_2 , we get

$$d_2 = \frac{\arg r_{12} - \arg r_{23} + (2m + 1)\pi}{2k_{z2}}. \quad (3.5)$$

It is usually best to choose the value of m corresponding to the smallest positive admissible value of d_2 ; otherwise, internal resonances in the coating layer can spoil its antireflective properties for some angles of incidence.

We shall now use condition (i) to determine the refractive index n_2 of the AR coating. Substituting the Fresnel's formulas (3.2) into the condition $|r_{12}|^2 = |r_{23}|^2$, we obtain

$$\frac{(\mathcal{E}_2 - \mathcal{E}_1)^2}{(\mathcal{E}_2 + \mathcal{E}_1)^2} = \frac{(\mathcal{E}_3 - \mathcal{E}_2)(\mathcal{E}_3^* - \mathcal{E}_2)}{(\mathcal{E}_3 + \mathcal{E}_2)(\mathcal{E}_3^* + \mathcal{E}_2)}. \quad (3.6)$$

Straightforward algebra leads to

$$\mathcal{E}_2^2 = \frac{-\operatorname{Re} \mathcal{E}_3 + |\mathcal{E}_3|^2 / \mathcal{E}_1}{\operatorname{Re} \mathcal{E}_3 - \mathcal{E}_1} \mathcal{E}_1^2. \quad (3.7)$$

The s - and p -polarisation cases need now to be considered separately. Assuming materials 1 and 2 to be nonmagnetic ($\mu_1 = \mu_2 = 1$), in the s -polarisation case we have $\mathcal{E}_2 = Z_2$ and eq. (2.5) gives

$$Z_2 = \frac{k_0}{k_{z2}} = \frac{k_0}{\sqrt{n_2^2 k_0^2 - n_1^2 k_0^2 \sin^2 \theta}}, \quad (3.8)$$

hence

$$n_2^2 = n_1^2 \sin^2 \theta + \frac{1}{Z_2^2}. \quad (3.9)$$

It can be seen that Z_2^2 must be non-negative in order that k_{z2} be real, as we have assumed.

For p polarisation, $\mathcal{E}_2 = Y_2$ and eq. (2.8) yields

$$Y_2 = \frac{n_2^2 k_0}{k_{z2}} = \frac{n_2^2 k_0}{\sqrt{n_2^2 k_0^2 - n_1^2 k_0^2 \sin^2 \theta}}. \quad (3.10)$$

This leads to the quadratic equation for n_2^2 ,

$$n_2^4 - Y_2^2 n_2^2 + Y_2^2 n_1^2 \sin^2 \theta = 0, \quad (3.11)$$

which has real solutions

$$n_2^2 = \frac{1}{2} \left(Y_2^2 \pm \sqrt{Y_2^4 - 4Y_2^2 n_1^2 \sin^2 \theta} \right) \quad (3.12)$$

provided that $Y_2^4 - 4Y_2^2 n_1^2 \sin^2 \theta \geq 0$. It can be shown that this condition, together with the condition of real-valuedness of k_{z2} [for *both* solutions of eq. (3.12)], is fulfilled if and only if

$$Y_2^2 \geq 4n_1^2 \sin^2 \theta. \quad (3.13)$$

In practice, there are further constraints on the choice of the constituent material of the coating. Other experimental issues aside, n_2 is bounded from below by the refractive index of air, and from above, by the index at which a second propagative diffraction order appears at the given value of k_x . We shall now show how such constraints of the general form

$$n_{\min}^2 \leq n_2^2 \leq n_{\max}^2 \quad (3.14)$$

can be transformed into equivalent constraints on the immittance of the PC, \mathcal{E}_3 .

We begin by noting that the conditions (3.14) can always be rewritten in the form

$$\mathcal{E}_{\min}^2 \leq \mathcal{E}_2^2 \leq \mathcal{E}_{\max}^2 \quad (3.15)$$

Range of n_{\min}^2, n_{\max}^2 and n_x^2	Y_{\min}^2	Y_{\max}^2
$0 < n_x^2 \leq \frac{n_{\min}^2}{2}, \quad n_{\min}^2 \leq n_{\max}^2$	$\frac{n_{\min}^4}{n_{\min}^2 - n_x^2}$	$\frac{n_{\max}^4}{n_{\max}^2 - n_x^2}$
$\frac{n_{\min}^2}{2} < n_x^2 < n_{\min}^2 \leq n_{\max}^2 \leq 2n_x^2$	$\frac{n_{\max}^4}{n_{\max}^2 - n_x^2}$	$\frac{n_{\min}^4}{n_{\min}^2 - n_x^2}$
$\frac{n_{\min}^2}{2} < n_x^2 < n_{\min}^2, \quad 2n_x^2 < n_{\max}^2 \leq \frac{n_{\min}^2 n_x^2}{n_{\min}^2 - n_x^2}$	$4n_x^2$	$\frac{n_{\min}^4}{n_{\min}^2 - n_x^2}$
$\frac{n_{\min}^2}{2} < n_x^2 < n_{\min}^2, \quad \frac{n_{\min}^2 n_x^2}{n_{\min}^2 - n_x^2} < n_{\max}^2$	$4n_x^2$	$\frac{n_{\max}^4}{n_{\max}^2 - n_x^2}$
$n_{\min}^2 \leq n_x^2 < n_{\max}^2 \leq 2n_x^2$	$\frac{n_{\max}^4}{n_{\max}^2 - n_x^2}$	∞
$n_{\min}^2 \leq n_x^2, \quad 2n_x^2 < n_{\max}^2$	$4n_x^2$	∞

Table 3.1 Minimum and maximum bounds on Y_2^2 sufficient and necessary for fulfilment of the condition (3.14) together with the constraint (3.13) for at least one of the solutions (3.12) of eq. (3.11). The symbol n_x^2 denotes $n_1^2 \sin^2 \theta$.

with appropriate \mathcal{E}_{\min} and \mathcal{E}_{\max} . Specifically, for s polarisation, the formulas for Z_{\min}^2 and Z_{\max}^2 follow readily from eq. (3.9):

$$Z_{\min}^2 = \frac{1}{n_{\max}^2 - n_1^2 \sin^2 \theta}, \quad Z_{\max}^2 = \frac{1}{n_{\min}^2 - n_1^2 \sin^2 \theta}. \quad (3.16)$$

For p polarisation, due to the more complex form of eq. (3.12) and the presence of the supplementary condition (3.13), several cases must be considered. The final formulas for Y_{\min}^2 and Y_{\max}^2 are given in table 3.1.

To arrive at the form of the constraints on \mathcal{E}_3 , we substitute eq. (3.7) into inequality (3.15) and introduce *reduced* immittances $\tilde{\mathcal{E}}_i \equiv \mathcal{E}_i / \mathcal{E}_1$ ($i = 3, \min, \max$), obtaining

$$\tilde{\mathcal{E}}_{\min}^2 \leq \frac{-\operatorname{Re} \tilde{\mathcal{E}}_3 + |\tilde{\mathcal{E}}_3|^2}{\operatorname{Re} \tilde{\mathcal{E}}_3 - 1} \leq \tilde{\mathcal{E}}_{\max}^2. \quad (3.17)$$

This expression can be rewritten as

$$\left[\left(\operatorname{Re} \tilde{\mathcal{E}}_3 - \frac{1 + \tilde{\mathcal{E}}_{\min}^2}{2} \right)^2 + (\operatorname{Im} \tilde{\mathcal{E}}_3)^2 - \left(\frac{1 - \tilde{\mathcal{E}}_{\min}^2}{2} \right)^2 \right] (\operatorname{Re} \tilde{\mathcal{E}}_3 - 1) \geq 0, \quad (3.18a)$$

$$\left[\left(\operatorname{Re} \tilde{\mathcal{E}}_3 - \frac{1 + \tilde{\mathcal{E}}_{\max}^2}{2} \right)^2 + (\operatorname{Im} \tilde{\mathcal{E}}_3)^2 - \left(\frac{1 - \tilde{\mathcal{E}}_{\max}^2}{2} \right)^2 \right] (\operatorname{Re} \tilde{\mathcal{E}}_3 - 1) \leq 0. \quad (3.18b)$$

It follows that the constraints (3.14) are equivalent to the following conditions on $\tilde{\mathcal{E}}_3$:

$$\begin{aligned} & (\tilde{\mathcal{E}}_3 \in \overline{\operatorname{ext} P_-} \quad \text{and} \quad \tilde{\mathcal{E}}_3 \in \overline{\operatorname{ext} C_{\min}} \quad \text{and} \quad \tilde{\mathcal{E}}_3 \in \overline{\operatorname{int} C_{\max}}) \\ \text{or} \quad & (\tilde{\mathcal{E}}_3 \in \overline{\operatorname{int} P_-} \quad \text{and} \quad \tilde{\mathcal{E}}_3 \in \overline{\operatorname{int} C_{\min}} \quad \text{and} \quad \tilde{\mathcal{E}}_3 \in \overline{\operatorname{ext} C_{\max}}), \end{aligned} \quad (3.19)$$

where P_- stands for the half-plane $\operatorname{Re} \tilde{\mathcal{E}}_3 < 1$, C_{\min} , the circle of radius $\frac{1}{2}|1 - \tilde{\mathcal{E}}_{\min}^2|$ centred at $(\frac{1}{2}(1 + \tilde{\mathcal{E}}_{\min}^2), 0)$, and C_{\max} , the circle of radius $\frac{1}{2}|1 - \tilde{\mathcal{E}}_{\max}^2|$ centred at $(\frac{1}{2}(1 + \tilde{\mathcal{E}}_{\max}^2), 0)$. The symbols $\operatorname{int} A$ and $\operatorname{ext} A$ denote the interior and exterior of a region A , and the overbar $\overline{}$ denotes set closure. Thus, for instance, $\overline{\operatorname{int} A}$ stands for the interior of the set A together with its boundary.

To illustrate various possible geometries of the region of the complex $\tilde{\mathcal{E}}_3$ plane determined by the constraints (3.14) transformed into the form (3.19), fig. 3.4 shows the shape of this region for s polarisation and three distinct choices of the parameters n_{\min} , n_{\max} , n_1 and θ .

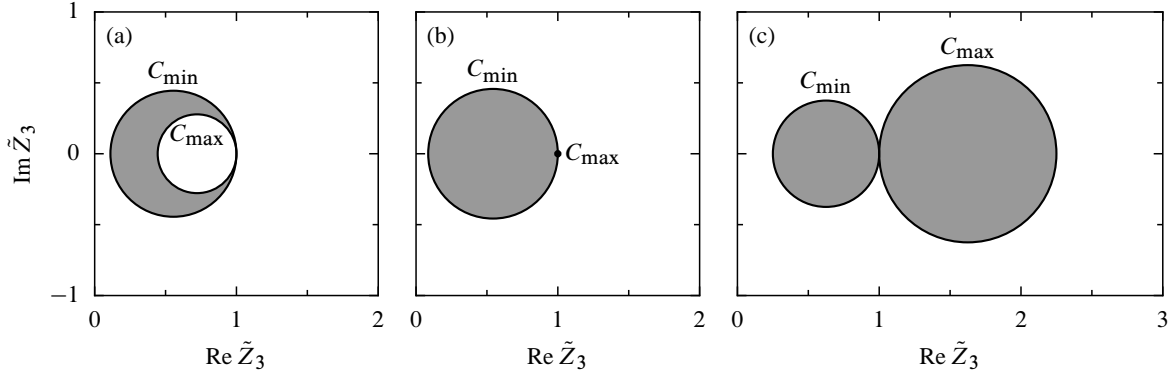


Figure 3.4 Regions of the complex \tilde{Z}_3 plane determined by the condition (3.19) equivalent to the constraint (3.14) for s polarisation and **(a)** $n_1 = 1, n_{\min} = 1.5, n_{\max} = 3, \theta = 0$, **(b)** $n_1 = 1, n_{\min} = 1, n_{\max} = 3, \theta = 30^\circ$, **(c)** $n_1 = 1.5, n_{\min} = 1, n_{\max} = 3, \theta = 0$. The circles C_{\min} and C_{\max} are defined in the text after eq. (3.19); note that in the case (b) C_{\max} degenerates into the point $(1, 0)$.

Step 2 The coating obtained in step 1 is not practical, since its fabrication would call for integration of the PC with a completely different solid; moreover, a suitable material with the required value of refractive index might not be easily available. However, as noted in subsection 3.2.1, a homogeneous thin film can often be replaced without adverse effects by a subwavelength grating. Such a grating could be easily etched in the same process as the underlying PC; it would then naturally be composed of the same materials as the PC, with permittivities, say, ϵ_1 and ϵ_h ($\epsilon_1 < \epsilon_h$).

In order to calculate the fill factor of a binary lamellar grating mimicking a layer with refractive index n_2 obtained in the previous step, one can resort to the classical second-order effective-medium theory of gratings due to Rytov, described in ref. 92. According to this theory, the effective permittivity $\tilde{\epsilon}_s$ of a binary grating with period a and fill factor f ($0 \leq f \leq 1$), composed of materials with permittivities ϵ_1 and ϵ_h , and operating in the s polarisation is

$$\tilde{\epsilon}_s = \bar{\epsilon}_s \left[1 + \frac{\pi^2}{3} \left(\frac{k_0 a}{2\pi} \right)^2 f^2 (1-f)^2 \frac{(\epsilon_h - \epsilon_1)^2}{\bar{\epsilon}_s} \right], \quad (3.20)$$

where

$$\bar{\epsilon}_s = f\epsilon_h + (1-f)\epsilon_1. \quad (3.21)$$

For p polarisation, the effective permittivity $\tilde{\epsilon}_p$ is

$$\tilde{\epsilon}_p = \bar{\epsilon}_p \left[1 + \frac{\pi^2}{3} \left(\frac{k_0 a}{2\pi} \right)^2 f^2 (1-f)^2 (\epsilon_h - \epsilon_1)^2 \bar{\epsilon}_s \left(\frac{\bar{\epsilon}_p}{\epsilon_h \epsilon_1} \right)^2 \right], \quad (3.22)$$

where

$$\bar{\epsilon}_p = \left[\frac{f}{\epsilon_h} + \frac{1-f}{\epsilon_1} \right]^{-1} \quad (3.23)$$

and $\bar{\epsilon}_s$ is given by eq. (3.21). Thus, the required fill factor can be obtained by setting $\tilde{\epsilon}_s$ or $\tilde{\epsilon}_p$ to n_2^2 in eq. (3.20) or (3.22) and solving it numerically for f .

It should be noted that in the domain of validity of Rytov's theory (small $k_0 a / 2\pi$) the functions $\tilde{\epsilon}_s(f)$ and $\tilde{\epsilon}_p(f)$ are monotonically increasing from ϵ_1 to ϵ_h . Thus, a binary grating cannot simulate a material with permittivity outside the range delimited by the permittivities of the grating's constituent materials. As a result, the bounds n_{\min}^2 and n_{\max}^2 mentioned in step 1 must fulfil $n_{\min}^2 \geq \epsilon_1$ and $n_{\max}^2 \leq \epsilon_h$, respectively.

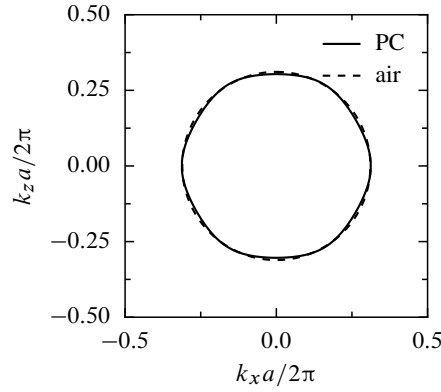


Figure 3.5 Solid line: EFC of the PC considered in subsection 3.4.1 at frequency $\omega = 0.311 \times 2\pi c/a$ and for s polarisation. Dashed line: EFC of air at the same frequency.

Step 3 The structure obtained at this stage should, in principle, ensure low reflectance for incidence angles close to θ . Nevertheless, owing to the applied approximations—neglect of higher diffraction orders excited by the PC and the AR grating—its geometrical parameters might not be precisely optimal. In addition, it is well known [91, 92] that trapezoidal and triangular AR gratings have larger angular and frequency tolerance than lamellar ones. Therefore, it is advisable to apply a numerical optimisation procedure to adjust the geometry of the grating, described by some small number of parameters, so as to minimise a given objective function ρ . The geometry obtained in step 2 can be expected to provide a good starting point for a local search algorithm, such as the Nelder-Mead simplex method [110, section 10.4].

3.4 Examples

3.4.1 A photonic-crystal flat lens

Preliminaries The first PC we shall consider is a hexagonal lattice of air holes of radius $r = 0.365a$, where a is the lattice constant, etched in a dielectric matrix of permittivity $\epsilon = 10.6$. These parameters correspond to the structure whose fabrication was reported in ref. 18. For s polarisation, at frequency $\omega = 0.311 \times 2\pi c/a$, the effective refractive index $n = -1$ can be attributed to the crystal, since its EFC takes an approximately circular shape (fig. 3.5) with radius $K \approx \omega/c$ and group velocity directed inwards. (Unless otherwise noted, all calculations whose results are presented in this subsection have been made with the differential method [69, 74–76].)

Veselago [20] predicted that a slab of material with $n = -1$ should act as a flat lens: an image of an object placed near one of the surfaces of the slab should be produced on the other side of the slab. Figure 3.6 shows the map of the modulus of the electric field generated by a wire source with current 1 A (ampere) located above a slab of the PC in question.* The parts (a) and (b) refer to slabs truncated in the ways shown in figs. 3.7(a) and (b), respectively; from now on, these two structures will be referred to as S1 and S2. In accordance with the theoretical predictions, images are formed below the slabs.

* The field maps shown in figs. 3.6 and 3.12 have been produced with the finite-element method using the RF module of the COMSOL program. The computational domains were rectangles of width $55a$ and height $30a$ surrounded by perfectly matched layers of thickness $3a$. The meshes consisted of about 225,000 second-order triangular Lagrangian elements of maximum size $0.2a$ (refined further in the neighbourhood of the point source). Numerical convergence was tested by comparing the results of a representative calculation against those obtained after refining the mesh by dividing each element into four. This produced no visible changes in the field map and the maximum amplitude of the image produced by the lens changed by less than 1%.

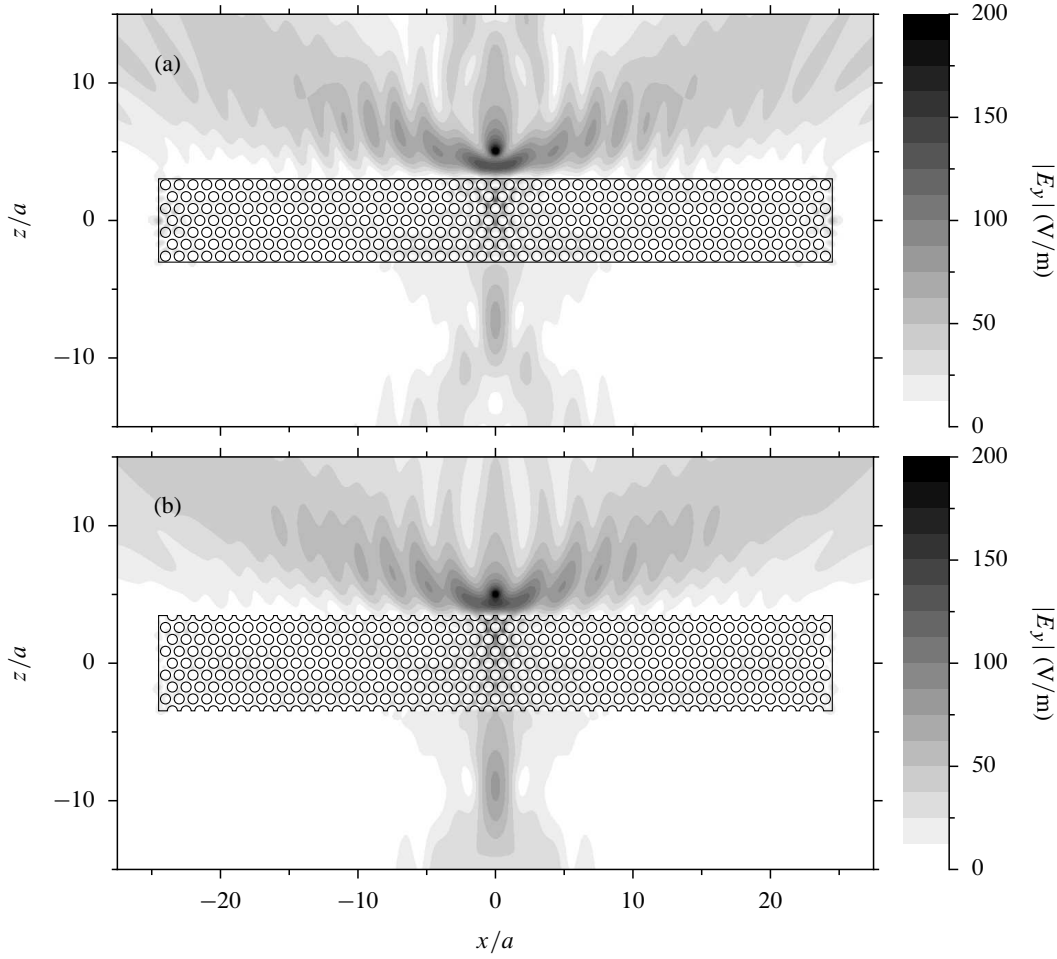


Figure 3.6 Modulus of the electric field generated by an *s*-polarised wire source with current 1 A located above a slab of the PC studied in subsection 3.4.1 truncated along a plane **(a)** lying midway between two neighbouring rows of holes, **(b)** crossing the centres of holes.

However, their amplitude is low (67 and 79 V/m for structures S1 and S2, respectively) and intense beams reflected from the top of the lenses are visible in the upper part of the plots. This suggests that only a small fraction of energy is transmitted through the lenses. Indeed, as shown in fig. 3.7(a), the reflectance of structure S1, $|r_0(\theta)|^2$, where r_0 is the specular reflection coefficient, exceeds 29% for all angles of incidence. Structure S2 performs better for low incidence angles, but degrades quickly with increasing θ . We shall now apply the algorithm presented in section 3.3 to design an AR grating for this PC.

Step I We have seen in section 2.4 that the effective-medium model of PCs tends to be more accurate for crystals truncated along a plane with constant permittivity profile, as is the case, for instance, for structure S1. Therefore in the first step of the design procedure we shall calculate the effective transverse impedance Z_3 of this structure. We consider two ways of obtaining this quantity. First, we calculate it from eq. (2.23), derived in the framework of the model presented in chapter 2. At frequency $\omega = 0.311 \times 2\pi c/a$ and angle of incidence $\theta = 45^\circ$ (corresponding to $k_x = 0.220 \times 2\pi/a$) we get $Z_1 = 1.414$ and $Z_3 = 0.319$. We should now check whether $\tilde{Z}_3 \equiv Z_3/Z_1 = 0.225$ lies within the region determined by the conditions (3.19) equivalent to the constraints (3.14) with $n_{\min} = 1$ and $n_{\max} = 2.51$ (the maximum index of a medium in which only a single propagative diffraction order exists). Figure 3.8, in which

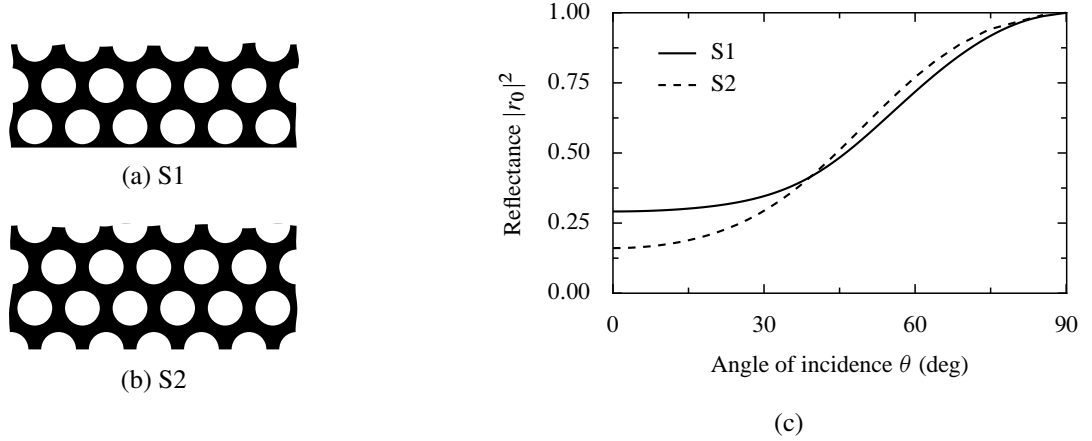


Figure 3.7 Geometry of the PC studied in subsection 3.4.1 truncated along a plane **(a)** lying midway between two neighbouring rows of holes, **(b)** crossing the centres of holes. **(c)** Angular dependence of the reflectance of the structures shown in parts (a) and (b).

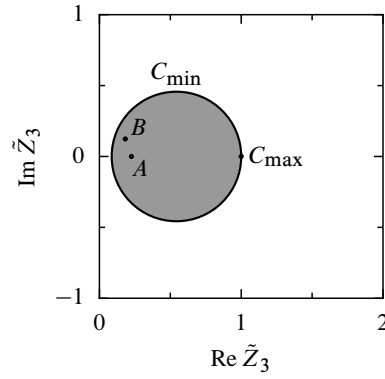


Figure 3.8 Shaded circle: region of the complex \tilde{Z}_3 plane determined by the condition (3.19) equivalent to the constraint (3.14) for s polarisation, $n_1 = n_{\min} = 1$ and $n_{\max} = 2.51$. Points A and B : reduced impedances \tilde{Z}_3 of structure S1 calculated in two different ways described in the text.

the value of \tilde{Z}_3 cited above is marked with point A , shows that this is indeed the case. Therefore eqs. (3.5) and (3.9) can be used to calculate the parameters of the AR coating of the crystal: refractive index $n_2 = 1.649$ and thickness $d_2 = 0.540a$. The geometry of this structure, called S3 from now on, is shown in fig. 3.9(a) and its reflectance is plotted in fig. 3.9(e) with a solid black line. It can be seen that the application of the coating reduces significantly the reflectance of the crystal, especially for small angles of incidence. However, the parameters of S3 are certainly not optimal, since its reflectance at the “design angle” $\theta = 45^\circ$ is as large as 9%. This is due to the relatively large error introduced by the single-mode approximation for negative-refraction PC bands, as pointed out in chapter 2.

We shall evaluate, therefore, an alternative method of obtaining Z_3 , which consists in calculating it directly from the rigorous specular reflection coefficient r_0 of the uncoated crystal at the chosen ω and k_x . In other words, we assume that r_0 can be expressed in the form $r_0 = (Z_3 - Z_1)/(Z_3 + Z_1)$ [cf. eq. (3.2)] and invert this formula to obtain $Z_3 = Z_1(1 + r_0)/(1 - r_0)$. Of course, the effective impedance defined in this way depends on the material properties of medium 1. Nevertheless, at least for the PC in question, this dependence is weak for sufficiently small n_1 : we obtain $Z_3 = 0.258 + 0.175i$ for $n_1 = 1$ and the effective impedance does not change by more than 10% up to $n_1 = 2.25$. As shown in fig. 3.8, the reduced impedance $\tilde{Z}_3 = 0.182 + 0.124i$ corresponding to the above value of Z_3 (marked with point B) also lies within the allowed region of the \tilde{Z}_3 plane. Taking this value of Z_3 , from eqs. (3.5) and (3.9)

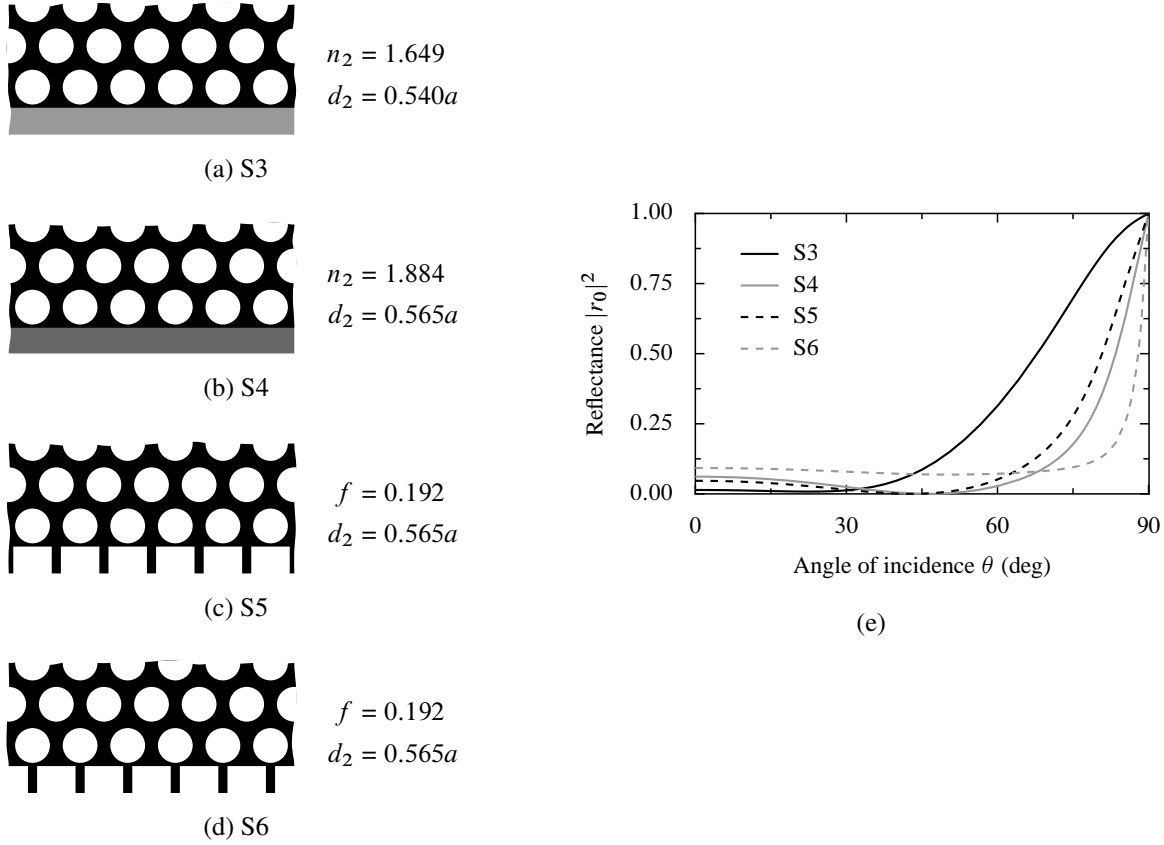


Figure 3.9 (a)–(b) Geometry of AR coatings S3 and S4, characterised by refractive index n_2 and thickness d_2 specified next to the drawings. (c)–(d) Geometry of binary lamellar AR gratings S5 and S6, characterised by fill factor f and thickness d_2 specified next to the drawings. (e) Angular dependence of the reflectance of the structures shown in parts (a)–(d).

we get $n_2 = 1.884$ and $d_2 = 0.565a$. The angular dependence of the reflectance of the PC covered with this coating, shown in fig. 3.9(b) and called S4 in the following, is plotted in fig. 3.9(e) with a solid grey line. It is evident that this structure has much better angular tolerance than S3; moreover, its reflectance at $\theta = 45^\circ$ is only 0.05%. Therefore we choose S4 as a basis for the further steps of the algorithm.

Step 2 Numerical inversion of eq. (3.20) gives the fill factor $f = 0.192$ of the binary grating mimicking a medium with $n = 1.884$. Since we would like the angular dependence of r_0 to be symmetric with respect to $\theta = 0$, the grating should be positioned so as to preserve the vertical mirror symmetry axes of the underlying PC. This can be done in two possible ways, shown in figs. 3.9(c) and (d). The reflectance of these two structures, called S5 and S6, is plotted in fig. 3.9(e). Clearly, grating S5 reproduces fairly faithfully the original reflectance curve of the AR coating S4. On the other hand, grating S6 behaves better in the high- θ region.

Step 3 The lamellar gratings obtained in step 2 provide already a remarkable improvement over the uncoated PC and, in contrast to the AR coatings from step 1, should be manufacturable. Nevertheless, their geometry can be further ameliorated. To this end, as mentioned in the last paragraph of section 3.3, we use the Nelder-Mead simplex algorithm to find the optimum values of the dimensions w_i , w_o , h_i , and h_o parametrising the trapezoidal grating shown in fig. 3.10. The objective function ρ is defined as the average of the numerically calculated reflectance of the given structure over the desired angular tolerance

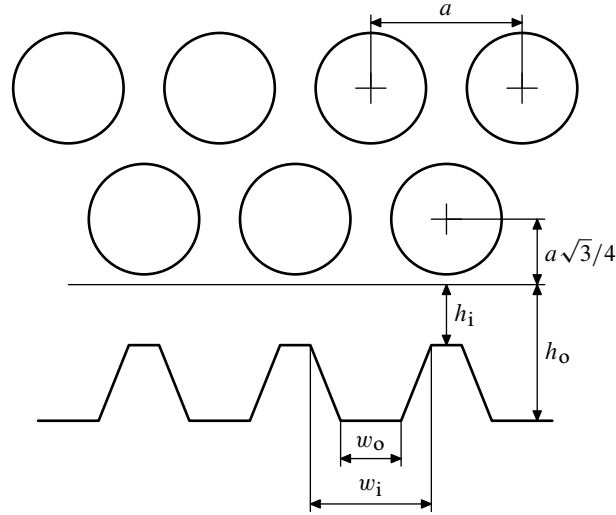


Figure 3.10 Definition of the geometrical parameters w_i , w_o , h_i , and h_o of a trapezoidal grating superposed on the surface of structure S1.

interval $[\theta_{\min}, \theta_{\max}]$,

$$\rho = \frac{1}{\theta_{\max} - \theta_{\min}} \int_{\theta_{\min}}^{\theta_{\max}} |r_0(\theta)|^2 d\theta. \quad (3.24)$$

The integral in eq. (3.24) is calculated with the 20-point Gauss-Legendre quadrature algorithm [110, section 4.5], whose typical relative accuracy, $\sim 10^{-5}$, is better than that of the reflectance calculations, $\sim 10^{-3}$. The initial shape of the grating is taken to correspond to one of the lamellar gratings obtained in step 2, i.e., $w_i = w_o = fa$, $h_i = 0$, and $h_o = d_2$. The search routine is terminated when the size of the simplex, defined as the average distance of its vertices from its geometric centre, falls below 10^{-5} . The final values of the geometrical parameters of the grating are determined by selecting the best among the 16 structures obtained by rounding each of the parameters delivered by the simplex algorithm upwards or downwards to a multiple of $0.01a$.

Application of this procedure with $\theta_{\min} = 0^\circ$, $\theta_{\max} = 90^\circ$ to grating S5 yields grating S7 shown in fig. 3.11(a). The plot in fig. 3.11(e) (solid black line) demonstrates the excellent antireflective properties of this structure (note the scale of the vertical axis). Its average reflectance is as low as 2.8%; in fact, $|r_0(\theta)|^2$ does not exceed 5.5% until $\theta = 87^\circ$. The structure does not seem to present special fabrication difficulties—e.g., acute angles—except possibly for the relatively thin dielectric veins separating the circular holes from the surface. Should this pose a real experimental difficulty, one can increase the value of h_i at the expense of a slight performance deterioration. For example, grating S8 with $h_i = 0.08a$ has average reflectance of 4.8%.

Figure 3.12 shows the map of the modulus of the electric field produced by a point source placed above a PC slab coated with AR gratings of type S7 from above and below. The comparison with fig. 3.6 reveals the significant improvement brought about by the AR grating: not only are the reflected beams prominent in the upper part of the latter figure suppressed, but the amplitude of the image formed by the lens grows to 159 V/m, which is two times better than in the situation from fig. 3.6(b).

Optimisation of structure S6 leads to gratings with average reflectance comparable to that of S7 and S8 but composed of “narrower” trapezoids ($w_i + w_o \approx 0.2a$), thus less suitable for fabrication. Therefore we omit the detailed discussion of these structures.

Other structures In refs. 111 and 112 two other trapezoidal AR gratings, here denoted S9 and S10, were presented. Their geometrical parameters, shown in figs. 3.11(c) and (d), were obtained by minimis-

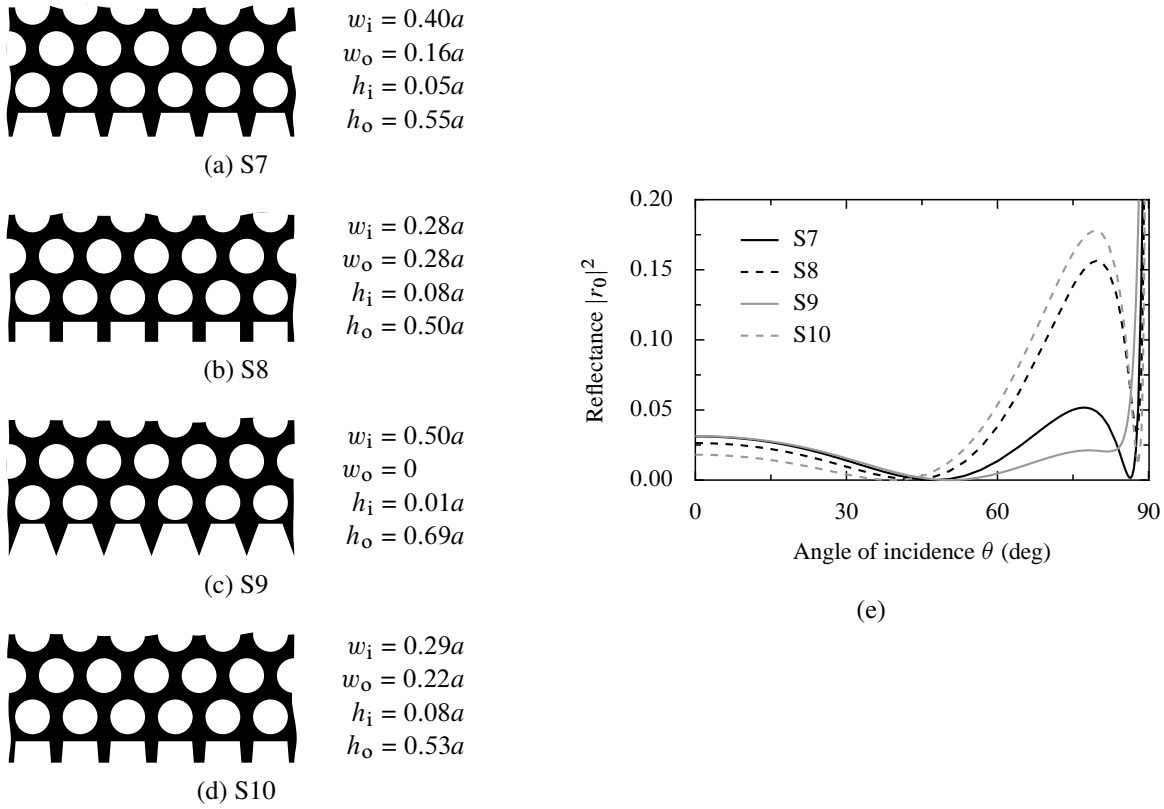


Figure 3.11 (a)–(d) Geometry of AR gratings S7–S10 characterised by parameters w_i , w_o , h_i , and h_o specified next to the drawings. (e) Angular dependence of the reflectance of the structures shown in parts (a)–(d). To help visualise the details of the $|r_0(\theta)|^2$ dependence, the y axis has been truncated at $|r_0|^2 = 0.2$.

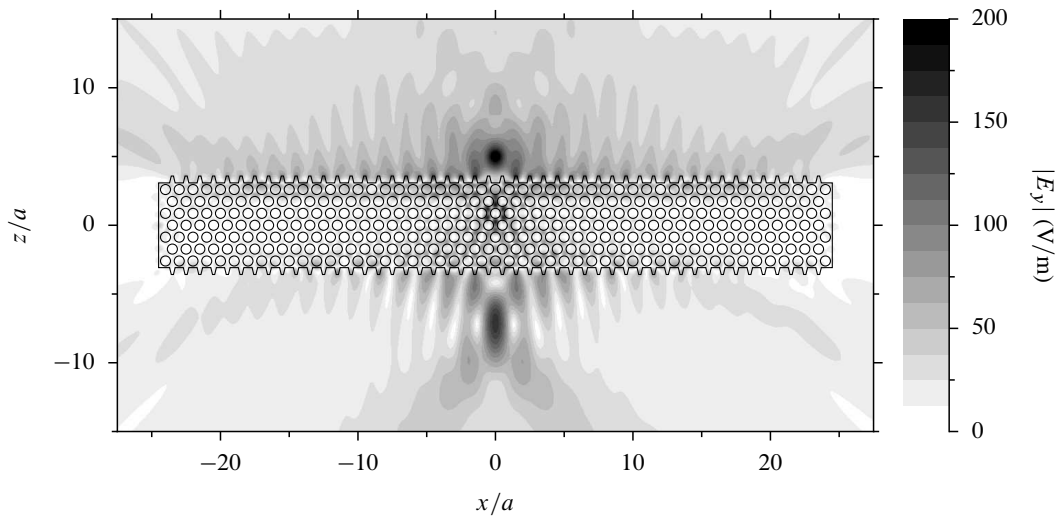


Figure 3.12 Modulus of the electric field generated by an s -polarised wire source with current 1 A located above a slab of the PC studied in subsection 3.4.1 with S7-type gratings placed on its horizontal surfaces.

θ_{\max}	w_i	w_o	h_i	h_o
90°	0.378–0.424 a (22 nm)	0.151–0.170 a (9 nm)	0.045–0.055 a (5 nm)	0.543–0.557 a (7 nm)
80°	0.330–0.463 a (63 nm)	0.132–0.186 a (26 nm)	0.033–0.062 a (14 nm)	0.530–0.569 a (19 nm)
60°	0.192–0.533 a (162 nm)	0.084–0.208 a (59 nm)	0 –0.082 a (39 nm)	0.497–0.586 a (42 nm)

Table 3.2 Ranges of geometrical parameters of grating S7 for which its average reflectance at frequency $0.311 \times 2\pi c/a$ in the angular range $0 \leq \theta \leq \theta_{\max}$ does not exceed 5%. The numbers in parentheses are the lengths of the tolerance intervals for $a = 476$ nm, which corresponds to operation wavelength $\lambda = a/0.311 = 1530$ nm. Note that the tolerance intervals correspond to perturbations of *one parameter at a time* (not all parameters simultaneously).

ing the objective function $\frac{2}{\pi} \int_0^{\pi/2} |r_0(\theta)| d\theta$ (average modulus of the specular reflection coefficient r_0) calculated with a less accurate quadrature algorithm. The average reflectance of structure S9 in the full 0° – 90° range, 2.8%, matches that of S7; in a more restricted range, say, 0° – 80° , the performance of grating S9 is even slightly better. Nonetheless, its disadvantage lies in the presence of very thin dielectric veins at the surface. Grating S10, with $h_i = 0.08a$, is devoid of this problem. However, it is superseded by structure S8 with identical h_i , which has somewhat lower average reflectance.

Tolerance to fabrication imperfections A fabrication process invariably perturbs the geometrical parameters of the manufactured structure. To assess the sensitivity of the proposed gratings to fabrication errors, we have determined the maximum perturbation of each of the four geometrical parameters of grating S7 for which the grating's average reflectance in the angular range $0 \leq \theta \leq \theta_{\max}$ did not exceed 5%. Three values of θ_{\max} were considered: 90° , 80° , and 60° . The results of this test are summarised in table 3.2. It can be seen that the grating is more sensitive to variations of the height of the trapezoids (via the h_o and h_i parameters) than of their width (w_o and w_i). The constraints for $\theta_{\max} = 90^\circ$ and $\theta_{\max} = 80^\circ$ are rather stringent and unlikely to be met in practice. In contrast, fabrication of a structure satisfying the constraints for $\theta_{\max} = 60^\circ$ seems well within reach of current technology.

We have also tested the frequency tolerance of grating S7, finding that its average reflectance stays below 5% for $0.3094 \leq \omega a/2\pi c \leq 0.3113$ ($\theta_{\max} = 90^\circ$), $0.3048 \leq \omega a/2\pi c \leq 0.3122$ ($\theta_{\max} = 80^\circ$), and $0.2511 \leq \omega a/2\pi c \leq 0.3173$ ($\theta_{\max} = 60^\circ$). This tolerance seems quite sufficient for applications related to lensing.

3.4.2 A supercollimating photonic crystal

Preliminaries The second example to be considered is a PC composed of a square lattice of air holes of radius $r = 0.3a$, where a is the lattice constant, etched in a dielectric matrix of permittivity $\epsilon = 12.25$. Near the frequency $\omega = 0.265 \times 2\pi c/a$ its EFCs for p polarisation take a square-like shape (cf. fig. 3.13). In consequence, supercollimated beams [16, 113] can propagate in the crystal. All calculations reported in this subsection have been made with a frequency-domain finite-difference method with subpixel smoothing implemented along the lines of ref. 114.

Figure 3.14(c) shows the angular dependence of the reflectance of this PC at $\omega = 0.265 \times 2\pi c/a$; two different truncation planes, shown in figs. 3.14(a)–(b) and called S11 and S12 in the following, are considered. It is seen that the crystal cut through hole centres has fairly low reflectance: about 10% at normal incidence and decreasing for larger angles up to $\theta \approx 65^\circ$. This level of power losses might in fact be already sufficient for practical applications. Nevertheless, for the sake of illustration, we shall present the design procedure of AR gratings that help to decrease even further the reflectance of the PC in question.

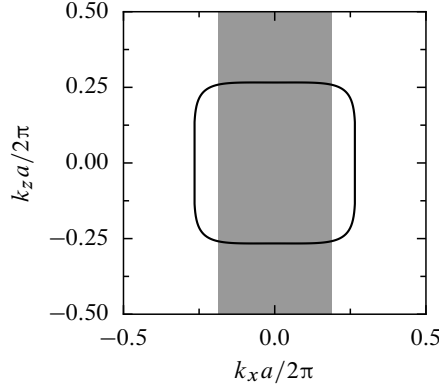


Figure 3.13 EFC of the PC studied in subsection 3.4.2 at frequency $\omega = 0.265 \times 2\pi c/a$. The shaded region corresponds to the range $\theta \leq 45^\circ$ ($|k_x| \leq 0.187 \times 2\pi/a$), where the EFC is approximately flat and for which the minimisation of the PC's reflectance is made.

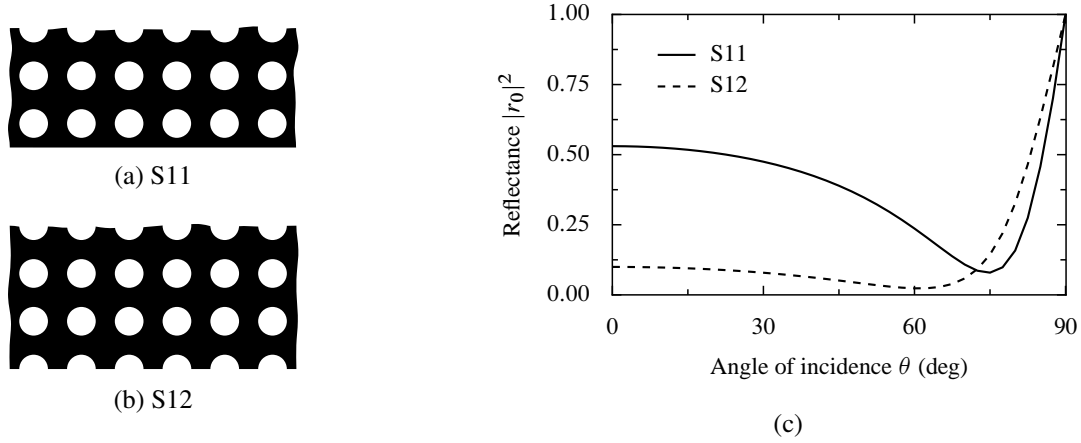


Figure 3.14 Geometry of the PC studied in subsection 3.4.2 truncated along a plane **(a)** lying midway between two neighbouring rows of holes, **(b)** crossing the centres of holes. **(c)** Angular dependence of the reflectance of the structures shown in parts (a) and (b).

Step I We are mostly interested in coupling the incoming light to modes lying on the flat horizontal part of the PC's EFC. As shown in fig. 3.13, at frequency $\omega = 0.265 \times 2\pi c/a$ this corresponds roughly to the range $|\theta| \leq 45^\circ$, i.e., $|k_x| \leq 0.187 \times 2\pi/a$. Therefore we choose $\theta = 22.5^\circ$ as the design angle of the AR coating. As in the previous subsection, we test two different ways of calculating the effective immittance (in this case, admittance) of the crystal cut along a constant-permittivity plane, i.e., structure S11. The effective-medium model presented in chapter 2 yields $Y_3 = 6.138$. In turn, the effective admittance calculated from the rigorous reflection coefficient of structure S11 embedded in air is $Y_3 = 6.075 - 1.191i$. Figure 3.15 shows that the reduced admittances corresponding to both these values lie within the region of the complex \tilde{Y}_3 plane determined by the conditions (3.19) equivalent to the constraints (3.14) with $n_1 = n_{\min} = 1$, $n_{\max} = 3.391$ (the refractive index for which the second propagative diffraction order appears) and $\theta = 22.5^\circ$. The parameters of the AR coatings determined from these two values of Y_3 are $(n_2 = 2.548, d_2 = 0.374)$ and $(n_2 = 2.595, d_2 = 0.391)$, respectively. Figure 3.16 shows the geometry of these coatings, henceforth referred to as S13 and S14, and the angular dependence of their reflectance. As in the PC lens case, the AR coating S14 designed using the value of Y_3 obtained from the rigorous reflection coefficient of the crystal performs slightly better than the other one. Therefore structure S14 shall be used in the subsequent design step.

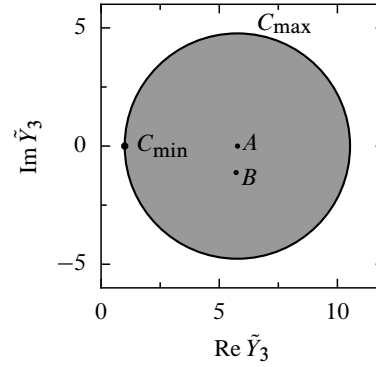


Figure 3.15 Shaded circle: region of the complex \tilde{Y}_3 plane determined by the condition (3.19) equivalent to the constraint (3.14) for p polarisation, $n_1 = n_{\min} = 1$ and $n_{\max} = 3.391$. Points A and B : reduced admittances \tilde{Y}_3 of structure S11 calculated in two different ways described in the text.

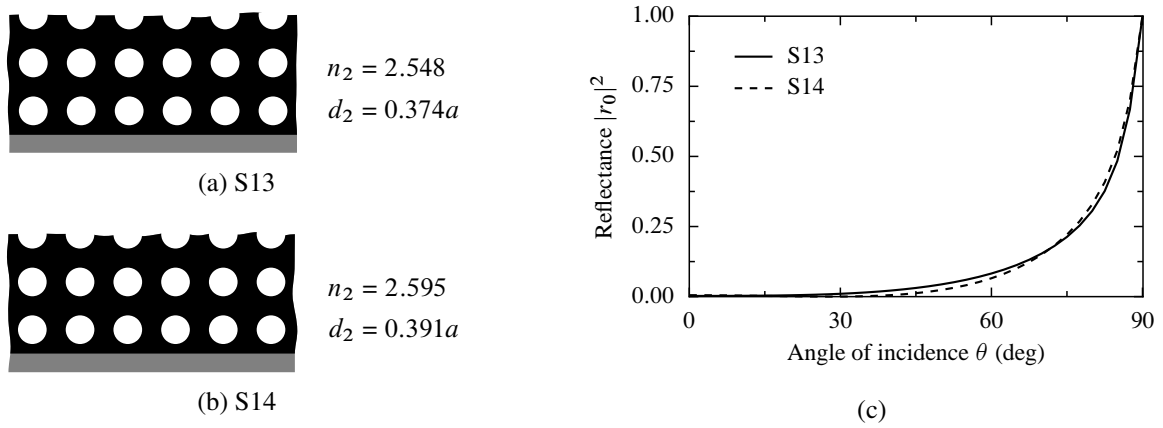


Figure 3.16 (a)–(b) Geometry of AR coatings S13 and S14, characterised by refractive index n_2 and thickness d_2 specified next to the drawings. (c) Angular dependence of the reflectance of the structures shown in parts (a) and (b).

Step 2 From numerical inversion of eq. (3.22) it follows that the fill factor of the binary grating mimicking a medium with $n = 2.595$ for p polarisation is $f = 0.812$. Figures 3.17(a)–(b) show the geometry of the two gratings, called S15 and S16, with this fill factor and a mirror symmetry plane perpendicular to the direction of periodicity. From the juxtaposition of their reflectance curves [fig. 3.17(c)] it follows that structure S15 has somewhat better performance than S16. Incidentally, there is some similarity between the geometry of grating S15 and the truncated crystal S12, which also exhibited fairly low reflectance: The surface of both these structures contains “teeth” shifted by $\frac{1}{2}a$ in the horizontal direction with respect to the positions of the circular holes. Therefore, one could view the crystal S12 as an imperfect realisation of the AR grating S15.

Step 3 The lamellar grating S15 can be further ameliorated by adjusting its thickness d_2 and fill factor f to minimise the objective function ρ defined in eq. (3.24). We take $\theta_{\min} = 0$, $\theta_{\max} = 45^\circ$ and, as before, perform the optimisation with the Nelder-Mead simplex algorithm. This leads to structure S17 with $d_2 = 0.37a$ and $f = 0.73$, shown in fig. 3.17(c). Its reflectance curve is plotted in fig. 3.17(d) (solid line). In the angular range $0 \leq \theta \leq 45^\circ$, the reflectance never exceeds 0.6%, on average amounting to only 0.12%. The structure does not seem to present any special fabrication problems. It is possible to continue the grating’s optimisation by allowing it to take a trapezoidal rather than a lamellar shape; however, in view of its already very good AR properties, this appears unnecessary.

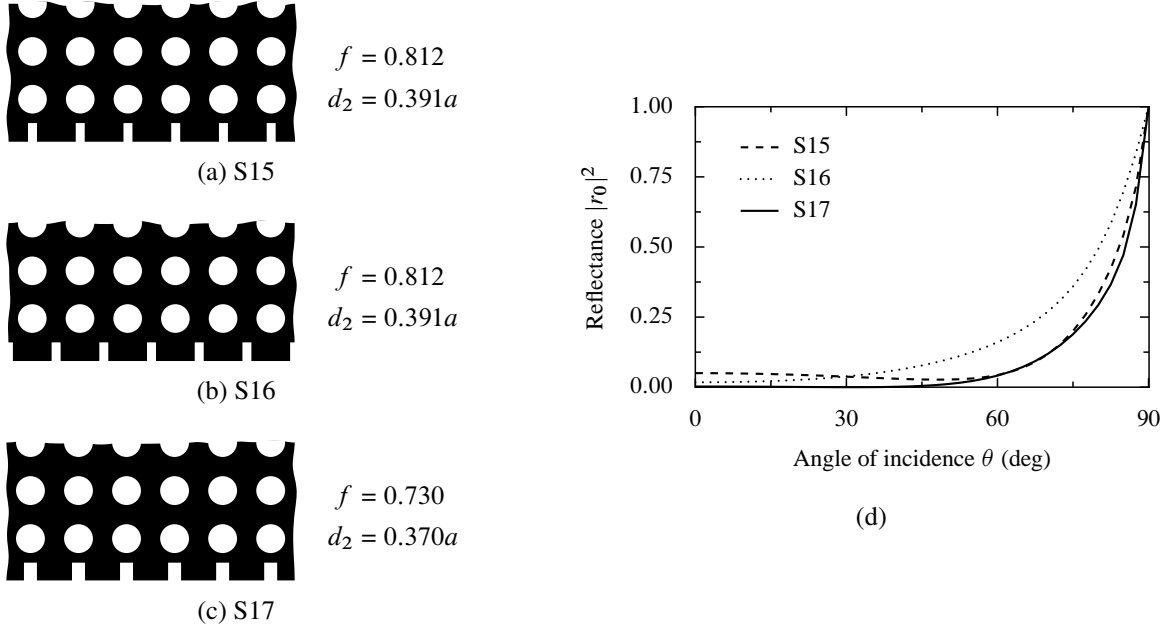


Figure 3.17 (a)–(c) Geometry of binary lamellar AR gratings S15, S16 and S17 characterised by fill factor f and thickness d_2 specified next to the drawings. (d) Angular dependence of the reflectance of the structures shown in parts (a)–(c).

3.4.3 A photonic-crystal superprism

We have also attempted to design an AR grating for the unidirectional mirror proposed by Vanwolleghem et al. [115]. This device, which will be analysed in some more detail in subsection 5.2.3, is a slab of the PC shown in fig. 3.18(a). The PC consists of a hexagonal lattice of triples of adjacent circular holes etched in a magneto-optical (MO) matrix characterised by a gyrotropic permittivity tensor

$$\hat{\epsilon} = \begin{bmatrix} (2.5)^2 & 0 & 0.1i \\ 0 & (2.5)^2 & 0 \\ -0.1i & 0 & (2.5)^2 \end{bmatrix}. \quad (3.25)$$

The presence of this MO material lifts the time-reversal symmetry of Maxwell's equations; the spatial inversion symmetry is also broken owing to the particular choice of the motif. As a result, the crystal becomes nonreciprocal, i.e., the usual property of the dispersion relation, $\omega(\vec{k}) = \omega(-\vec{k})$ [79, pp. 22–23], no longer holds. The p -polarisation EFC of this crystal at frequency $\omega = 0.3915 \times 2\pi c/a$, calculated with the method described in section 5.2, is shown in fig. 3.18(b). It can be seen that a plane wave impinging at the angle of about 58° (corresponding to $k_x \approx \pi/3a$) on the top surface of a slab made from this PC will be coupled to its propagative mode, and thus will be partially transmitted. However, a wave travelling in the opposite direction, incident from the bottom, will be totally reflected, since the crystal has no propagative modes with $k_x \approx -\pi/3a$. This behaviour justifies the name *unidirectional mirror*.

The problem with the presented device is its large forward loss: even waves propagating in the “allowed” direction undergo a significant reflection on the surfaces of the slab. Currently we do not have a reliable code allowing to calculate accurately the reflection coefficient of the MO PC from fig. 3.18(a) in p polarisation. Therefore we shall study instead the non-MO crystal in which the original motif composed of three circles is replaced by three overlapping squares, as shown in shown in fig. 3.19(a). The permittivity of the matrix is taken as $\epsilon = (2.5)^2$. [This modified geometry is due to K. Postava (Technical

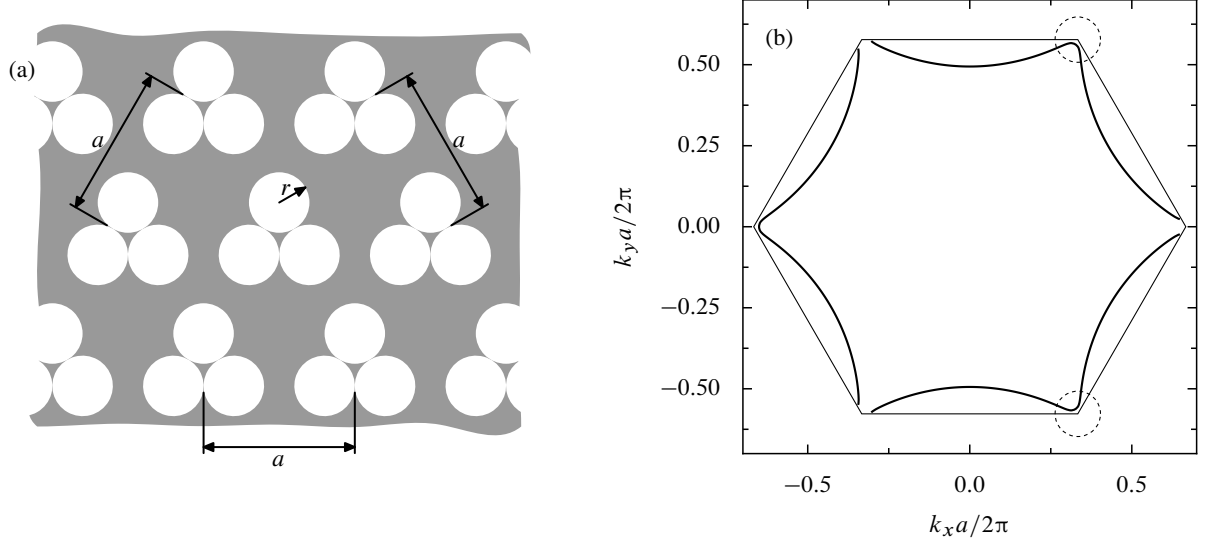


Figure 3.18 (a) Geometry of the PC composed of a hexagonal lattice of groups of three adjacent circular holes with radius $r = 0.20a$, where a is the lattice constant, etched in a magneto-optical matrix. (b) p -polarisation EFC of this crystal at frequency $\omega = 0.3915 \times 2\pi c/a$.

University of Ostrava, Czech Republic).] The EFC of this crystal at frequency $\omega = 0.4548 \times 2\pi c/a$, calculated with the differential method, is shown in fig. 3.19(b). Clearly, its shape in the regions marked by dashed circles is similar to that seen in fig. 3.18(b). Fig. 3.19(c) shows a magnification of this EFC near its inflection point $k_x = 0.309 \times 2\pi/a$, together with the k_x -dependence of the crystal's reflectance. It can be seen that the latter is very high. Therefore, to be useful in practice, the unidirectional mirror would need to be coated with some AR structure.

Unfortunately, the design of an appropriate AR grating using the procedure described in section 3.3 turns out to be impossible. For instance, at the inflection point of the EFC, the reflection coefficient of the uncoated PC is $r_0 = 0.969 - 0.086i$, which corresponds to $\tilde{Y}_3 = 6.50 - 20.5i$. As evidenced by fig. 3.19(d), this lies far outside the region of the complex \tilde{Y}_3 plane determined by the conditions (3.19) equivalent to the constraints (3.14) with $n_1 = n_{\min} = 1$ and $n_{\max} = 1.52$ (the refractive index of the least optically dense coating in which the second propagative diffraction order would appear). In fact, if we blindly apply eqs. (3.7) and (3.12) to calculate the refractive index of the optimum AR coating, we obtain $n_2 = 12.4$ or 0.68 . It is obvious that none of these indices can be simulated by any binary grating composed of the constituent materials of the PC. Therefore, an AR structure for the unidirectional mirror will probably need to be designed with some purely numerical method. In particular, Lawrence et al. [107] have shown their approach to give good results for a superprism that, uncoated, has an extremely high reflectance ($|r_0|^2 = 0.996$).

3.5 Conclusions

In this chapter we have presented a new method of designing gratings that, superimposed on surfaces of PCs crystals, will minimise their reflectance. The design algorithm consists of three steps. First, the parameters of a homogeneous-layer AR coating are calculated from an effective-medium approximation of the PC in question. Second, an analytical effective-medium theory of gratings is used to find the parameters of a binary lamellar grating composed solely of the constituent materials of the crystal and approximating the coating obtained in the previous step. Third, the shape of the grating is refined with a numerical local-search routine so as to minimise the reflectance of the structure in the desired angular

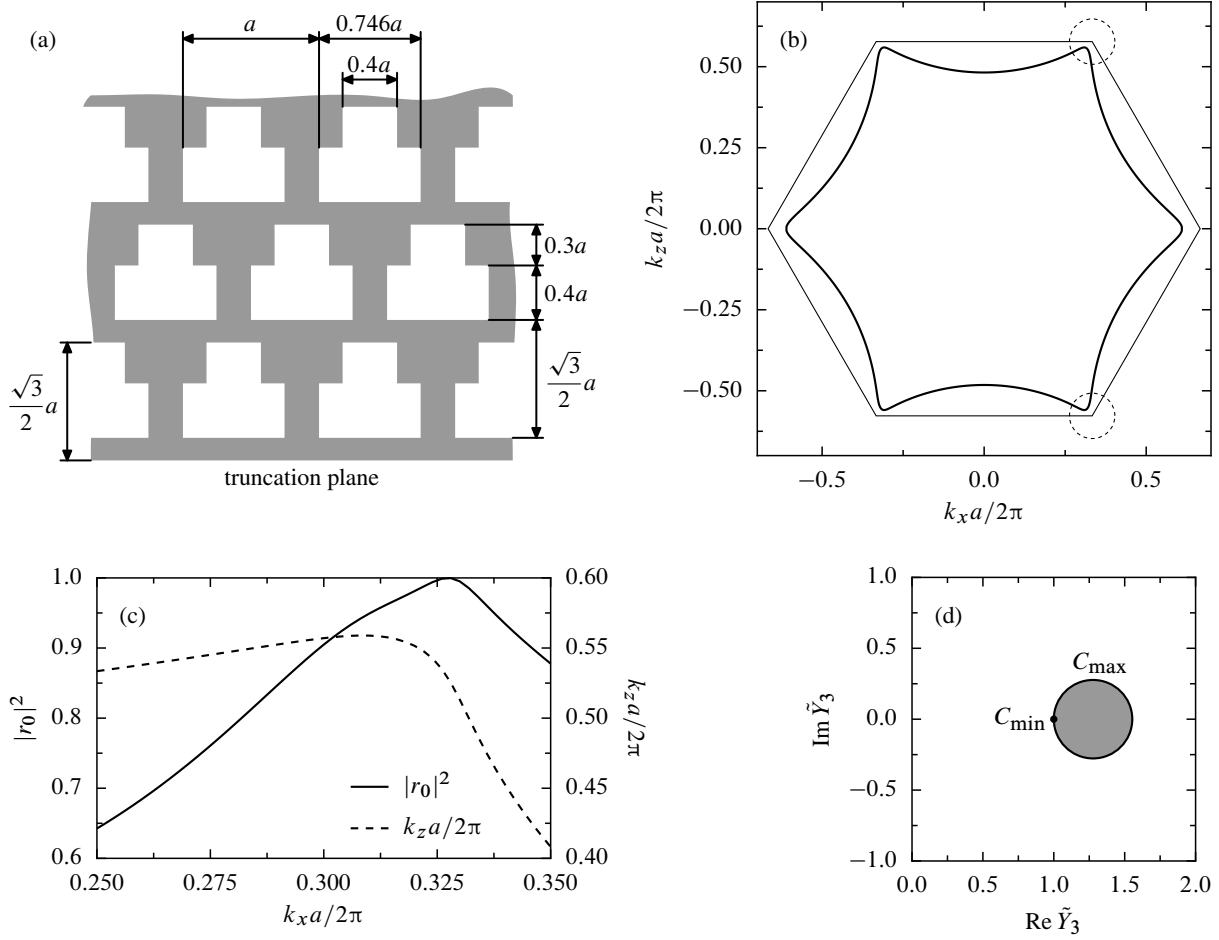


Figure 3.19 (a) Geometry of the PC composed of a hexagonal lattice of non-centrosymmetric motifs etched in a dielectric matrix. (b) p -polarisation EFC of this crystal at frequency $\omega = 0.4548 \times 2\pi c/a$. (c) Solid line: k_x -dependence of the reflectance $|r_0|^2$ of this crystal, placed in air and truncated in the way indicated in part (a). Dashed line: a fragment of the EFC from part (b). (d) Shaded circle: region of the complex \tilde{Y}_3 plane determined by the condition (3.19) equivalent to the constraint (3.14) for p polarisation, $n_1 = n_{\min} = 1$ and $n_{\max} = 1.52$. The reduced admittance of the crystal, $\tilde{Y}_3 = 6.50 - 20.5i$, lies far beyond the range of the graph.

or frequency range. This last step is necessary owing to the approximations made in the analytical derivations used in the first two steps of the procedure.

This algorithm of AR grating design can be viewed as complementary to the method proposed by Lawrence et al. [106, 107]. While their approach is based on an exhaustive scan of the whole parameter space (made very efficient by the application of the matrix-valued effective immittance of gratings), ours rests on approximate analytical considerations used to find a starting point for a *local* search procedure.

In section 3.4 the proposed method has been applied to three example crystals with EFCs of different curvature: a supercollimating crystal with a very flat EFC, a crystal exhibiting negative refraction, with almost circular EFC, and a PC superprism, whose EFC has a kink. In the two first cases, the design process succeeded in producing AR gratings ensuring very low reflectance in a wide angular range. The obtained structures are quite compact and apparently rather straightforward to fabricate. In the last case, the procedure broke down owing to the violation of the constraints (3.19) on the effective immittance of the crystal that must be satisfied in order that the AR coating produced in the first step can be approximated with a binary grating made of realistic materials. The existence of these constraints is the basic limitation of the presented procedure.

Chapter 4

Magneto-optical circulators

4.1 Introduction

4.1.1 Basic characteristics of isolators and circulators

This chapter will be devoted to the design of magneto-optical circulators optimised for operation at infrared frequencies in a uniform static external magnetic field (SEMF). Circulators and (closely related) isolators are devices widely used both in the optical and microwave domain. Their operation can be most easily explained with the formalism of scattering matrices. Consider the junction of waveguides W_1, W_2, \dots, W_n shown in fig. 4.1. On any cross-section P_j (called a *port*) of waveguide W_j located sufficiently far from the junction, the field can be represented solely in terms of the waveguide's propagative eigenmodes. Let us assume all the waveguides to be single-mode and denote the amplitudes of the incoming and outgoing mode of W_j on the port P_j by $s_{j,\text{in}}$ and $s_{j,\text{out}}$. If the system under study is linear, the amplitudes of the outgoing modes can be linked with those of the incoming ones by the *scattering matrix* \hat{S} of the junction [116, p. 249]:

$$\vec{s}_{\text{out}} = \hat{S} \vec{s}_{\text{in}}, \quad (4.1)$$

where $\vec{s}_{\text{in}} = [s_{1,\text{in}}, s_{2,\text{in}}, \dots, s_{n,\text{in}}]^T$ and $\vec{s}_{\text{out}} = [s_{1,\text{out}}, s_{2,\text{out}}, \dots, s_{n,\text{out}}]^T$. An ideal *isolator* is a two-port device that passes a wave coming from waveguide W_1 to waveguide W_2 , but blocks the transmission in the opposite direction. It is described by the scattering matrix [117, p. 523]

$$\hat{S} = \begin{bmatrix} 0 & 0 \\ 1 & 0 \end{bmatrix}. \quad (4.2)$$

In turn, a *circulator* is an n -port device that couples a wave coming from waveguide W_1 to waveguide W_2 only, a wave coming from W_2 to W_3 only, and so on [116, p. 468]. The simplest, 3-port circulator is described by the scattering matrix [117, p. 536]

$$\hat{S} = \begin{bmatrix} 0 & 0 & 1 \\ 1 & 0 & 0 \\ 0 & 1 & 0 \end{bmatrix}. \quad (4.3)$$

It is worth noting that a circulator can be used as a replacement of an isolator if we ensure that no incoming waves ever reach one of its ports. This can be easily achieved by connecting that port to a matched load, which does not generate reflected waves.

The above devices have several important applications. They can be used to eliminate waves reflected from imperfectly matched components of complex circuits; the presence of such waves can give rise to undesired interferences and parasitic couplings [34]. They are also employed in signal routing in devices

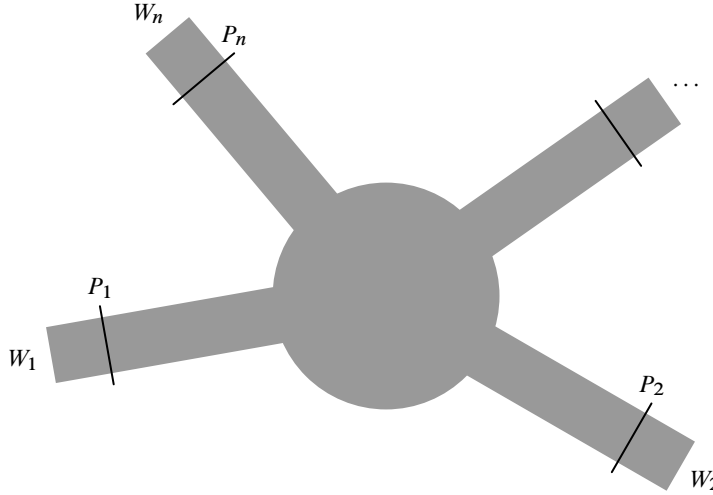


Figure 4.1 An n -port device.

such as multiplexers [35]. In the optical domain, possibly the most important application of isolators is the protection of lasers from back-reflected light, which disturbs the standing-wave pattern in a laser cavity and may cause the device to become unstable [36].

From the Lorentz reciprocity theorem it follows that the scattering matrix of a *reciprocal* system is *symmetric* provided that the amplitudes $s_{j,\text{in}}$ and $s_{j,\text{out}}$ are normalised so that any mode with unitary amplitude carries unitary power [116, pp. 235–236 and 249]. By a reciprocal system, we understand a system consisting of time-invariant, linear media whose material properties [cf. eq. (1.3)] satisfy the relations [118, p. 10]

$$\hat{\epsilon} = \hat{\epsilon}^T, \quad \hat{\mu} = \hat{\mu}^T \quad \text{and} \quad \hat{\alpha} = -\hat{\beta}^T. \quad (4.4)$$

Since the scattering matrices from eqs. (4.2) and (4.3) are not symmetric, isolators and circulators must by necessity contain nonreciprocal materials.

4.1.2 Routes to nonreciprocity

Among the possible ways of building nonreciprocal systems, by far the most common is the introduction of ferro- and ferrimagnetic materials. The propagation of low-amplitude microwaves in these media placed in a sufficiently strong SEMF is usually described by considering them to have a tensorial permeability of the form

$$\hat{\mu} = \begin{bmatrix} 1 + \chi_y + \chi_z & i\kappa_z & -i\kappa_y \\ -i\kappa_z & 1 + \chi_x + \chi_z & i\kappa_x \\ i\kappa_y & -i\kappa_x & 1 + \chi_x + \chi_y \end{bmatrix}, \quad (4.5)$$

where χ_i and κ_i ($i = x, y, z$) are proportional to the i th component of the magnetisation \vec{M} induced by the SEMF [119, p. 92; 117, p. 503]. For lossless media, $\hat{\mu}$ is Hermitian, so that all the parameters χ_i and κ_i are purely real. Therefore the diagonal part of the tensor defined in eq. (4.5) is real and (obviously) symmetric, while its off-diagonal part is imaginary and antisymmetric. Tensors with these properties are called *gyrotropic*.

Near the ferromagnetic resonance frequency, which for sub-tesla SEMFs falls in the microwave range, the magnitude of the off-diagonal components of $\hat{\mu}$ is comparable to that of the diagonal ones. This can lead to very strong nonreciprocal effects.

At optical frequencies, the propagation of electromagnetic waves in ferro- and ferrimagnetic media is more commonly handled by attributing them an anisotropic permittivity

$$\hat{\epsilon} = \begin{bmatrix} \epsilon & ig_z & -ig_y \\ -ig_z & \epsilon & ig_x \\ ig_y & -ig_x & \epsilon \end{bmatrix}, \quad (4.6)$$

where $g_i = KM_i$ and the parameter K describes the magneto-optical (MO) properties of the material [35; 119, p. 236]. MO effects are usually weak; therefore the SEMF-induced perturbation of the diagonal elements of $\hat{\epsilon}$ is commonly neglected. The real part of K is related to the specific Faraday rotation Θ_F by

$$\Theta_F = \frac{\pi}{\lambda \sqrt{\epsilon}} M_s \operatorname{Re} K, \quad (4.7)$$

where λ is the free-space wavelength and M_s denotes the characteristic saturation magnetisation of the medium. The imaginary part of K , in turn, is responsible for the effect of circular dichroism. In low-loss ferrimagnetic materials this imaginary part is often small and therefore in the rest of this chapter we shall assume K to be real. We shall also introduce the symbol $g \equiv M_s K$.

The most commonly used MO materials are (ferrimagnetic) synthetic garnets, of which the most well-known is yttrium iron garnet (YIG). It is usually grown on substrates made of gadolinium gallium garnet (GGG). The atoms of yttrium can be substituted by other elements, including bismuth and cerium. The specific Faraday rotation of partially cerium-substituted yttrium iron garnet (Ce:YIG) at $\lambda = 1550$ nm has been measured to be $-0.45^\circ/\mu\text{m}$, which corresponds to $g = -0.01$ [120]. Bismuth iron garnet (BIG), which is reputed to outperform Ce:YIG [121], has been found to have Θ_F as large as $-30^\circ/\mu\text{m}$ at $\lambda = 540$ nm, i.e., $g = -0.22$ [122]. Unfortunately Vertruyen et al. [122] do not report on measurements of the specific Faraday rotation of BIG in the infrared range. The available data indicate that Θ_F of this material diminishes with increasing wavelength, but the effect of this decrease on g is partially compensated by the growth of λ . It seems realistic to expect that $g \sim 0.05\text{--}0.1$ can be obtained at infrared frequencies. It is also worth noting that another (non-garnet) material, europium oxide, has been reported to have $g = 0.4$ in this frequency range [123]; however, its magneto-optical properties disappear above the Curie temperature of 69 K [124].

There are a few other methods of obtaining nonreciprocal behaviour. In the microwave domain it is possible to introduce off-diagonal imaginary components to the permittivity tensor of standard non-magnetic metals, such as gold, by placing them in a strong SEMF. Unfortunately, this method cannot be applied easily to optical systems because the strength of the necessary SEMF increases with frequency, reaching several teslas in the optical range; another obstacle consists in the relatively large losses exhibited by metals in this segment of the electromagnetic spectrum. Another possibility consists in using so-called Tellegen's media, in which the relation $\hat{\alpha} = -\hat{\beta}^T$ does not hold; however, in known materials of this type the magnitude of the real component of the tensors $\hat{\alpha}$ and $\hat{\beta}$ is very small, and therefore this method of inducing nonreciprocal behaviour remains so far largely unexplored. Finally, instead of using materials whose parameters do not meet conditions (4.4), one can violate the other conditions of validity of the standard Lorentz reciprocity theorem: introduce a time-dependent modulation of the material properties of the system or employ nonlinear effects.

4.1.3 Experimental realisations of optical isolators and circulators

Bulk magneto-optical isolators A basic feature of MO materials is the phase velocity difference between right- and left-circularly polarised plane waves propagating parallel to the magnetisation direction. As a result of this difference, the polarisation plane of a linearly polarised plane wave propagating

along the direction of \vec{M} gradually rotates; moreover, the direction of this rotation (clockwise or counter-clockwise), when viewed in the laboratory frame, does not depend on whether the wave propagates parallel or antiparallel to \vec{M} [116, p. 460–464]. This phenomenon, known as Faraday's effect, is the basis of the operation of the archetypical “bulk” optical isolator, shown schematically in fig. 4.2(a). It consists of a slab of a MO material sandwiched between two polarisers rotated by 45° with respect to each other [35]. The slab, magnetised perpendicularly to the planes of the polarisers, has thickness d such that the polarisation plane of waves traversing the medium rotates by 45° . Let us assume that this happens in the clockwise direction. Then a wave coming in through polariser 1 will eventually find its polarisation plane aligned with the axis of polariser 2. In contrast, the polarisation plane of a wave coming in through polariser 2 will become perpendicular to the axis of polariser 1. As a consequence, the former wave will be transmitted, whereas the latter will be absorbed.

As noted in subsection 4.1.2, the specific Faraday rotation (rotation angle per unit length) of commonly used MO materials is small. Therefore, optical isolators built in the way presented in the previous paragraph need to be rather thick ($d \sim 0.1\text{--}1\text{ mm}$). It is, however, possible to reduce d to tens of micrometres by replacing the single MO layer by a Fabry-Perot resonator composed of a stack of dielectric and MO thin films, at the cost of a reduced operation bandwidth [125].

Another way of reducing the thickness of a bulk isolator consists in the application of PCs. As noted first by Figotin and Vitebsky [126], a PC with both the spatial inversion symmetry and the time-reversal symmetry broken has a dispersion diagram that lacks inversion symmetry. From this it follows in particular that at a given frequency a band gap can exist for waves propagating in a direction \vec{k} , but not for those propagating in the direction $-\vec{k}$; thus, at such a frequency the PC behaves as an isolator. An example 1D PC of this type was presented in ref. 127. In this structure, the spatial inversion symmetry was lifted by the presence of MO layers polarised in opposite directions (but always parallel to the layers, unlike in Faraday rotators). Since fabrication of such layers might be difficult, Khanikaev and Steel [128] proposed to break the inversion symmetry by the introduction of a third material into the periodic lattice. They showed also an alternative resonator-type design, in which a single MO layer is sandwiched between two different dielectric Bragg mirrors. In turn, the isolator proposed by Vanwolleghem et al. [115] consists of a 2D PC composed of a lattice of holes drilled in a MO matrix magnetised in the out-of-plane direction. The shape of holes is chosen so that the system's spatial inversion symmetry is lifted.

Owing to their large lateral dimensions, bulk, non-planar structures are difficult to combine with integrated optical circuits. Therefore, in the last two decades there has been a lot of activity devoted to the design of isolators and circulators suitable for on-chip manufacturing. Most of these structures are intended for fabrication in MO garnet layers grown on GGG substrates, although methods of bonding garnet layers to semiconductor (e.g., silicon) substrates have also been developed. With respect to their geometry, the proposed devices can be divided into two broad classes: waveguide- and resonator-type components.

Waveguide-type devices The operation of the earliest waveguide-type isolators was based on the nonreciprocal conversion between quasi-TE and quasi-TM modes of rib waveguides, induced by a SEMF parallel to the waveguide axis. This phenomenon is analogous to Faraday's effect [35]. However, it must be noted that in this case the conversion occurs between states whose polarisation planes differ by 90° rather than 45° . Therefore, a 45° -long nonreciprocal Faraday rotator must be connected in series with a 45° -long *reciprocal* rotator. The presence of this additional element, together with the necessary polarisers at the input and output ports, complicates the fabrication procedure. The main deficiency of the design based on Faraday's effect, though, is that while in a bulk MO material the phase velocities of all plane waves polarised perpendicularly to \vec{M} are identical, the effective indices of quasi-TE and quasi-TM

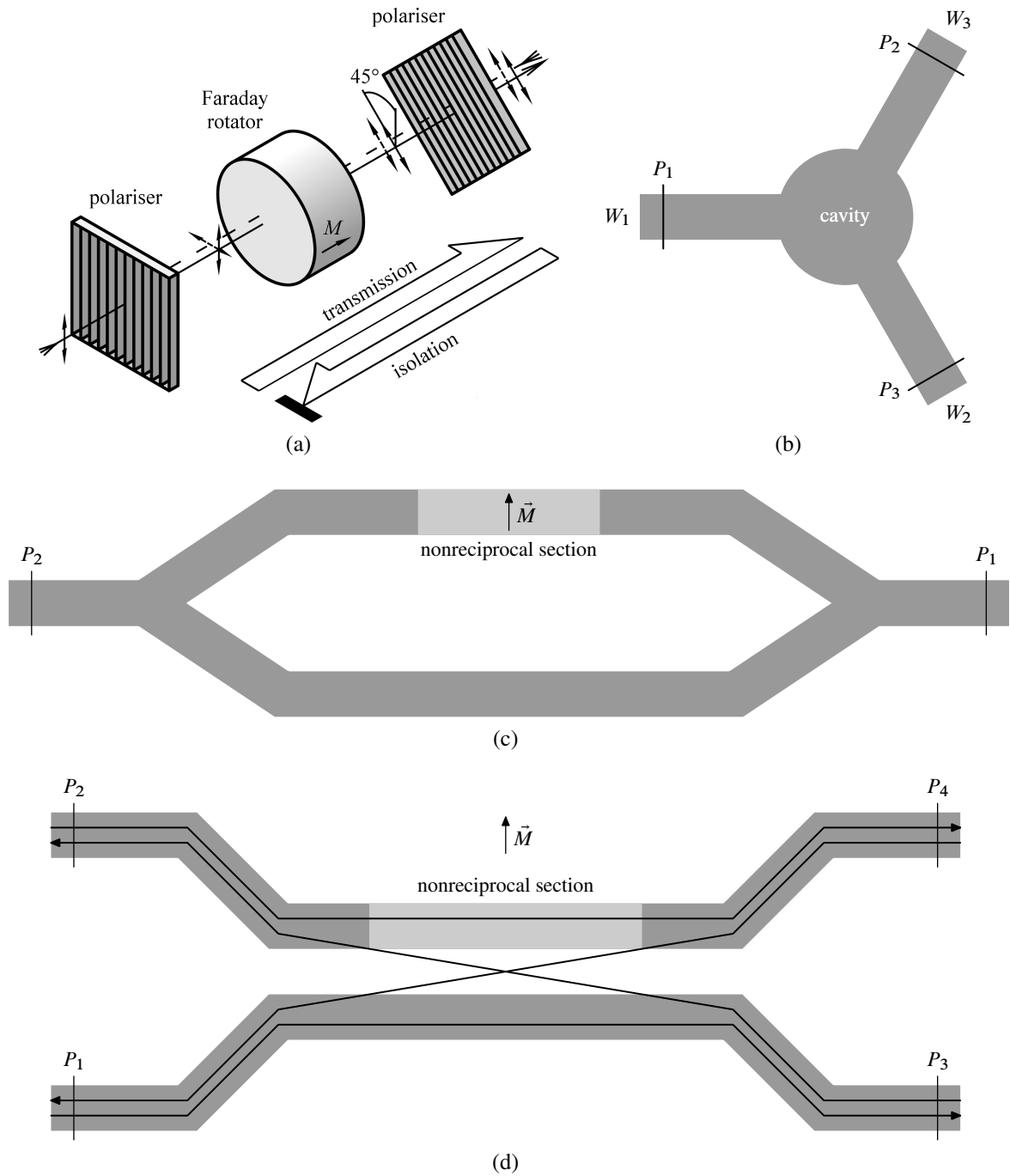


Figure 4.2 Selected types of optical isolators and circulators. **(a)** Bulk isolator based on Faraday rotation (after ref. 35). **(b)** Three-way resonator-type circulator. **(c)** Mach-Zehnder interferometer with one nonreciprocal arm. **(d)** Nonreciprocal coupler acting as a four-port circulator. The arrows indicate the directions of energy transfer.

waveguide modes are, in general, different. For high isolation, the waveguide geometry should therefore be adjusted to force a close match of these indices. In practice, this is not easy to obtain without post-fabrication etch-tuning or deposition of an additional dielectric layer [129, 130]. It is worth mentioning, however, that Dammann et al. [131] showed that the stringent requirements for index matching can be somewhat relaxed, at the cost of incurring a modest additional forward loss, if the polarisation plane of the input mode is rotated by 22.5° from the vertical direction.

The drawbacks listed in the previous paragraph are eliminated in devices exploiting the difference in the phase velocity of forward- and backward-propagating modes of MO waveguides lacking a mirror symmetry plane parallel to their axis and placed in a SEMF perpendicular to that axis. The simplest isolator based on this effect has the form of a Mach-Zehnder interferometer [fig. 4.2(c)] with its two arms designed so as to introduce a nonreciprocal phase shift of 90° and a reciprocal shift of the same value [120, 132, 133]. For a forward-propagating wave, these shifts cancel out, so that the waves coming from the two arms interfere constructively at the output; for a backward-propagating wave, the shifts add up, which leads to a destructive interference. Analogous structures based on PC waveguides have also been investigated [134]. In a different scheme, so-called *nonreciprocal multi-mode imaging*, a single multi-mode waveguide is used instead of two single-mode ones [135].

A related type of device is a four-port circulator composed of two coupled MO waveguides [fig. 4.2(d)], whose parameters are chosen so that the phase velocities of forward-propagating modes differ, while those of backward-propagating ones match. This leads to a difference in the coupling strength of the two pairs of modes. As a result, a forward-propagating mode stays in the original waveguide, while a backward-propagating one gradually leaks to the neighbouring waveguide. Both rib-waveguide-based [136] and PC-waveguide-based [137] designs have been proposed.

Another way of achieving isolation is to employ nonreciprocal absorption. This phenomenon occurs primarily in ferromagnetic metals, which are usually highly lossy at optical frequencies. The concept of an isolator based on the difference of the decay rates of forward- and backward-propagating waves was originally proposed by Zaets and Ando [138] and Takenaka and Nakano [139]. The first successful demonstration of such a device was made by Vanwolleghem et al. [140], who fabricated a system containing a layer of a cobalt-iron alloy embedded in indium phosphide. Improved version of this isolator were reported on in refs. 141 and 142 (the latter authors used manganese arsenide instead of the cobalt-iron alloy). In turn, Takeda and John [123] proposed the device consisting of a MO PC waveguide designed so that its forward- and backward-propagating eigenmodes have significantly different group velocities. Since the slower mode experiences a longer effective optical path, in the presence of absorption its decay rate exceeds that of the faster mode. In all these designs current injection is normally used to compensate for the undesired absorption of the forward-propagating mode.

Certain MO waveguides are characterised by a difference in the cut-off frequency of forward- and backward-propagating modes. Therefore, in the range between these two frequencies guided-wave propagation is possible in one direction only. As pointed out by the authors of refs. 143, 144 and 145, this effect can also be used for the construction of an isolator.

Wang et al. [146] have shown that a SEMF can lift degeneracies in the band structure of high-symmetry PCs containing materials with gyrotropic permittivity or permeability, thus leading to the creation of band gaps. They also predicted that unidirectional waveguide modes with frequencies lying within such band gaps can propagate along interfaces separating the just described PCs from dielectric PCs or metals. This has been subsequently confirmed experimentally [147]. However, these effects have so far been demonstrated only at microwave frequencies, where the permeability tensor can have off-diagonal components with magnitude comparable with that of the diagonal ones. The MO effects are much weaker, and it is not certain whether the band gaps generated in the optical regime will be robust against disorder [147].

Resonator-type devices More suitable for integration than their bulk counterparts, waveguide-type MO devices must still be rather long in order to provide a satisfactory isolation. For instance, arm lengths of ~ 1 mm are used in the state-of-the-art Mach-Zehnder interferometers whose fabrication was reported on in ref. 120. According to the review of Dötsch et al. [35], this value is typical. Isolators are thus much larger than other standard components used in integrated circuits. A possible way of miniaturising them consists in employing resonant cavities to lengthen the time during which light interacts with the MO material. Of course, a drawback of this approach is the reduction of the operation bandwidth of the devices.

Circulators based on resonant cavities are commonly used in the microwave domain [117]. A typical device of this type is composed of three identical reciprocal waveguides W_i ($i = 1, 2, 3$) coupled to a single resonant cavity containing a ferrimagnetic material and, in the absence of SEMF, supporting two degenerate localised modes of frequency ω_0 [fig. 4.2(b)]. In a SEMF perpendicular to the plane of the system, this degeneracy is lifted: the modes couple and form two linear combinations corresponding to left- and right-rotating modes with frequencies ω_- and ω_+ [34, 148]. At the frequency $\frac{1}{2}(\omega_- + \omega_+)$, a wave incoming from, say, waveguide W_1 excites such a superposition of these two eigenmodes that they interfere constructively in front of one output waveguide (say, W_2), and destructively in front of the other (W_3). As a result, an outgoing mode with a significant amplitude appears only in waveguide W_2 , while W_3 is isolated from the incoming power. Analogously, owing to the three-fold rotational symmetry of the device, energy transfer occurs in the directions $W_2 \rightarrow W_3$ and $W_3 \rightarrow W_1$. The scattering matrix of the system is then given by eq. (4.3). If the SEMF polarisation is flipped, the direction of the energy transfer reverses, too.

In 2005 Wang and Fan [34, 37] proposed an analogous device intended for operation at optical frequencies, composed of a 2D PC cavity coupled to three PC waveguides. Using a model based on the coupled-wave theory [149], they showed the bandwidth of the circulator to grow with the frequency splitting $\Delta\omega \equiv |\omega_+ - \omega_-|$. This frequency splitting, in turn, was demonstrated to be proportional to the integral of the out-of-plane component of the cross product of the electric fields of the cavity modes, weighted with g , over the area of the cavity.

The authors of ref. 34 observed that in a typical PC cavity the sign of the cross product mentioned above oscillates rapidly, leading, as a result, to a severe diminution of $\Delta\omega$. To remedy this, they proposed to divide the MO material in the cavity into several domains polarised in opposite directions, thus flipping locally the sign of g and forcing the overall sign of the integrand to be constant everywhere. Unfortunately, the resulting structure is almost impossible to manufacture with the current technology, since the creation of the necessary magnetic subdomains would require the application of a SEMF inhomogeneous on the scale of hundreds of nanometres, with the inhomogeneities precisely aligned with the geometric structure of the cavity.

In a follow-up paper [150] the same authors presented a design of a four-port circulator composed of two straight PC waveguides coupled to a single MO cavity with a subdomain structure determined along analogous principles. In turn, Kono and Koshiba proposed a rib-waveguide-based circulator consisting of a Mach-Zehnder interferometer coupled to an exterior ring [151], and, subsequently, a device similar to that from ref. 150, but built from rib waveguides coupled to a MO microdisk [152]. Another contribution of the latter paper was the introduction of a method of increasing the circulator's bandwidth by including several coupled resonators instead of just one. In all these designs, however, division of the MO material into oppositely-polarised domains is still required.

It is worth noting that in ref. 34 a solution alternative to the introduction of magnetic domains was also considered, namely the inclusion of a single MO rod in an standard dielectric PC. In principle, it is possible, but it would also pose serious technological problems related to the growth of two different materials on a single substrate and the necessity of aligning precisely the structures obtained in two

etching processes. In any case, to the best of our knowledge, none of the devices proposed in refs. 34, 37, 150, 151 and 152 has ever been fabricated.

Non-magneto-optical devices As has been noted before, introduction of ferro- and ferrimagnetic materials is not the only method of making a system nonreciprocal. Therefore a number of isolator and circulator designs based on the alternative approaches have also appeared in the literature. For instance, Gallo et al. [153] described optical analogues of diodes employing nonlinear optical processes. Yu and Fan [154] proposed an isolator based on a time-dependent modulation of the refractive index of parts of a dielectric waveguide. In turn, Yu et al. [155] showed that the SEMF-induced gyrotropy of metals in the microwave domain can lead to the creation of unidirectional waveguide modes at the interfaces of these metals and dielectric PCs.

4.1.4 Outline of this chapter

The aim of the research reported on in this chapter was to design a three-port MO circulator of the type shown schematically in fig. 4.2(b), suitable for operation in a uniform SEMF, i.e., with all the MO material magnetised in the same direction. The plan of the text is as follows. In section 4.2 we set the stage by extending the coupling-wave model of the device in question, introduced by Wang and Fan [34], to include the influence of direct coupling between the three waveguides and the effect of radiation loss. These results are used later. In section 4.3 we derive an analytical axisymmetric model of a 2D MO PC cavity and use it to formulate a design principle of cavities exhibiting maximum frequency splitting in the presence of a uniform SEMF. This is the key result of this chapter.

Section 4.4 is devoted to PC-based circulators. Having shown how to convert an axisymmetric cavity designed along the rules established in section 4.3 to a component liable for integration with a periodic lattice, we demonstrate numerical simulations of a complete circulator embedded in a 2D PC. In section 4.5 we investigate rib-waveguide-based devices, which should be simpler to fabricate than PC-based ones, but present design problems of their own due to imperfect in-plane light confinement. We begin by detailing the design process of a rib-waveguide-based circulator intended for fabrication in a GGG-BIG heterostructure. This design is based on 2D finite-element simulations with the influence of the third dimension taken into account by help of the effective-index approximation. In subsection 4.5.4 we report briefly on the outcome of the first attempts to manufacture and characterise this device, made at Institut d'Electronique Fondamentale (Orsay, France). The measurements indicate that the vertical confinement provided by the cavity is insufficient. Therefore, in section 4.6 we describe the results of rigorous three-dimensional (3D) simulations of axisymmetric cavities designed by the method presented in section 4.3 and discuss various methods of improving the vertical confinement. Finally, in section 4.7 we summarise the results of our work on MO devices.

Some of the results presented in sections 4.3 and 4.4 have appeared previously in ref. 148.

4.2 Extension of the coupled-wave model

4.2.1 Inclusion of direct coupling between waveguides

Let us consider a circulator composed of three identical single-mode waveguides, W_1 , W_2 , and W_3 , weakly coupled with a resonant cavity and arranged so that the whole system has C_{3v} symmetry,* as shown schematically in fig. 4.2(b). We assume that in the absence of SEMF the cavity supports a pair of degenerate orthonormal eigenmodes belonging to the unique two-dimensional irreducible representation

* The symmetry elements of the group C_{3v} are a three-fold rotation axis and three mirror planes intersecting each other at the angle of 120° along this axis [80, p. 325].

of the C_{3v} point group and having frequency ω_0 . They can be classified as even or odd, according to their symmetry with respect to reflection about the axis of waveguide W_1 , which is assumed to lie along the $-x$ axis. The circulator's operation at frequency ω is described by the coupled-mode equations [149]

$$-i\omega\vec{a} = -(i\hat{\Omega} + \hat{F})\vec{a} + \hat{D}^T\vec{s}_{\text{in}}, \quad (4.8a)$$

$$\vec{s}_{\text{out}} = \hat{C}\vec{s}_{\text{in}} + \hat{D}\vec{a}, \quad (4.8b)$$

where the vector $\vec{a} = (a_e, a_o)^T$ contains the cavity mode amplitudes, $\vec{s}_{\text{in}} = (s_{1,\text{in}}, s_{2,\text{in}}, s_{3,\text{in}})^T$ and $\vec{s}_{\text{out}} = (s_{1,\text{out}}, s_{2,\text{out}}, s_{3,\text{out}})^T$, the amplitudes of the in- and outgoing waveguide modes, the matrix \hat{C} describes the direct coupling between waveguides, \hat{D} the cavity-waveguide coupling, $\hat{\Omega}$ the mode eigenfrequencies and their coupling, and \hat{F} their decay. These matrices are subject to the fundamental constraints [149]

$$\hat{D}^\dagger \hat{D} = 2\hat{F}, \quad (4.9a)$$

$$\hat{C} \hat{D}^* = -\hat{D}. \quad (4.9b)$$

Together with those following from the system's symmetry, these constraints can be used to reduce the number of independent parameters necessary for the characterisation of the device. We shall now consider each of the matrices occurring in eqs. (4.8) in turn.

Owing to the three-fold symmetry of the circulator, the \hat{C} matrix must have the form

$$\hat{C} = \begin{bmatrix} r & t & t \\ t & r & t \\ t & t & r \end{bmatrix}, \quad (4.10)$$

where $t \equiv |t| e^{i\tau}$ and $r \equiv |r| e^{i(\tau+\Delta)}$ are the transmission and reflection coefficients of waveguide modes in the absence of the cavity. If the system is lossless, as we shall assume in this subsection, we can use the condition of unitarity of \hat{C} to express t and r as

$$t = -\frac{2 \cos \Delta e^{i\tau}}{\sqrt{1 + 8 \cos^2 \Delta}}, \quad r = \frac{e^{i(\tau+\Delta)}}{\sqrt{1 + 8 \cos^2 \Delta}}. \quad (4.11)$$

Note that the case of no direct coupling, considered in ref. 34, corresponds to $\Delta = \frac{\pi}{2}$ and $\tau = \frac{\pi}{2}$.

The \hat{D} matrix has the general form

$$\hat{D} = \begin{bmatrix} d_{1e} & d_{1o} \\ d_{2e} & d_{2o} \\ d_{3e} & d_{3o} \end{bmatrix}, \quad (4.12)$$

where d_{im} ($i = 1, 2, 3$; $m = e, o$) describes the coupling of m th cavity mode with i th waveguide. These coupling parameters are proportional to the values of the electromagnetic field of the modes along the waveguide axes. Making use of the assumed symmetry of the mode fields, it can be shown that these six parameters can be expressed in terms of a single complex coupling constant $d \equiv |d| e^{i\delta}$:

$$\hat{D} = d \begin{bmatrix} 1 & 0 \\ -\frac{1}{2} & \frac{\sqrt{3}}{2} \\ -\frac{1}{2} & -\frac{\sqrt{3}}{2} \end{bmatrix}. \quad (4.13)$$

Substituting this formula into eq. (4.9a), we obtain

$$\hat{F} = \gamma \begin{bmatrix} 1 & 0 \\ 0 & 1 \end{bmatrix}, \quad \text{where} \quad \gamma \equiv \frac{3}{4}|d|^2. \quad (4.14)$$

The second constraint, eq. (4.9b), yields

$$(t - r)d^* = d. \quad (4.15)$$

Noting that from eq. (4.11) we have

$$t - r = \frac{-2 \cos \Delta - e^{i\Delta}}{\sqrt{1 + 8 \cos^2 \Delta}} e^{i\tau} = \frac{3 \cos \Delta + i \sin \Delta}{|3 \cos \Delta + i \sin \Delta|} e^{i(\pi + \tau)} = e^{i[\pi + \tau + \arg(3 \cos \Delta + i \sin \Delta)]} \quad (4.16)$$

and writing d in its polar form, we obtain the expression for δ :

$$\delta = \frac{1}{2}[(2n + 1)\pi + \tau + \arg(3 \cos \Delta + i \sin \Delta)], \quad (4.17)$$

where n is an integer. Lastly, since the coupling between the cavity modes is assumed to result solely from their interaction with the SEMF, the $\hat{\Omega}$ matrix takes the form [34]

$$\hat{\Omega} = \begin{bmatrix} \omega_0 & i|V| \\ -i|V| & \omega_0 \end{bmatrix}, \quad (4.18)$$

where V is the mode coupling strength. The eigenvalues of this matrix, $\omega_{\pm} \equiv \omega_0 \pm |V|$, are the frequencies of the eigenmodes of the cavity in isolation (uncoupled to waveguides). The frequency splitting $\Delta\omega \equiv \omega_+ - \omega_- = 2|V|$ is proportional to the mode coupling strength. As noted in ref. 148, it is often convenient to write $|V|$ as $|V| = g\omega_0 v$, where g is the magnitude of the off-diagonal component of the permittivity tensor of the MO constitutive material of the cavity, and v , called *reduced mode coupling strength*, depends solely on the geometry of the cavity.

Substituting eqs. (4.10), (4.11), (4.13), (4.14), (4.17), and (4.18) to the coupled-mode equations (4.8), taking W_1 to be the input waveguide by setting $\vec{s}_{\text{in}} = (1, 0, 0)^T$, and solving for \vec{s}_{out} , we obtain

$$s_{1,\text{out}} = \frac{e^{i\tau}}{\sqrt{1 + 8 \cos^2 \Delta}} \left\{ e^{i\Delta} - \frac{4(3 \cos \Delta + i \sin \Delta)}{3} \frac{\gamma[\gamma - i(\omega - \omega_0)]}{[\gamma - i(\omega - \omega_0)]^2 + |V|^2} \right\}, \quad (4.19a)$$

$$s_{2,\text{out}} = \frac{2e^{i\tau}}{\sqrt{1 + 8 \cos^2 \Delta}} \left\{ -\cos \Delta + \frac{3 \cos \Delta + i \sin \Delta}{3} \frac{\gamma[\gamma - |V|\sqrt{3} - i(\omega - \omega_0)]}{[\gamma - i(\omega - \omega_0)]^2 + |V|^2} \right\}, \quad (4.19b)$$

$$s_{3,\text{out}} = \frac{2e^{i\tau}}{\sqrt{1 + 8 \cos^2 \Delta}} \left\{ -\cos \Delta + \frac{3 \cos \Delta + i \sin \Delta}{3} \frac{\gamma[\gamma + |V|\sqrt{3} - i(\omega - \omega_0)]}{[\gamma - i(\omega - \omega_0)]^2 + |V|^2} \right\}. \quad (4.19c)$$

This solution is valid provided that the matrix $i(\hat{\Omega} - \omega\hat{I}) + \hat{\Gamma}$, where \hat{I} denotes the 2×2 identity matrix, is invertible. This is the case if

$$\omega \neq \omega_0 \pm |V| \quad \text{and} \quad \gamma \neq 0. \quad (4.20)$$

It is easily seen that the reflectance $R \equiv |s_{1,\text{out}}|^2$ and transmittances $T_i \equiv |s_{i,\text{out}}|^2$ ($i = 2, 3$) are independent of τ and π -periodic in Δ . Moreover,

$$|\vec{s}_{i,\text{out}}(\Delta, \omega)|^2 = |\vec{s}_{i,\text{out}}(\pi - \Delta, 2\omega_0 - \omega)|^2 \quad \text{for } i = 1, 2, 3. \quad (4.21)$$

Therefore it is sufficient to study the properties of R and T_i in the interval $\Delta \in [0, \frac{\pi}{2}]$.

We are primarily interested in the behaviour of the isolation factor of the circulator, defined as $I \equiv T_3/T_2$. Figure 4.3 shows the dependence of I on the frequency shift $(\omega - \omega_0)$ and the waveguide-cavity coupling parameter γ for a few representative values of Δ and a fixed mode coupling strength

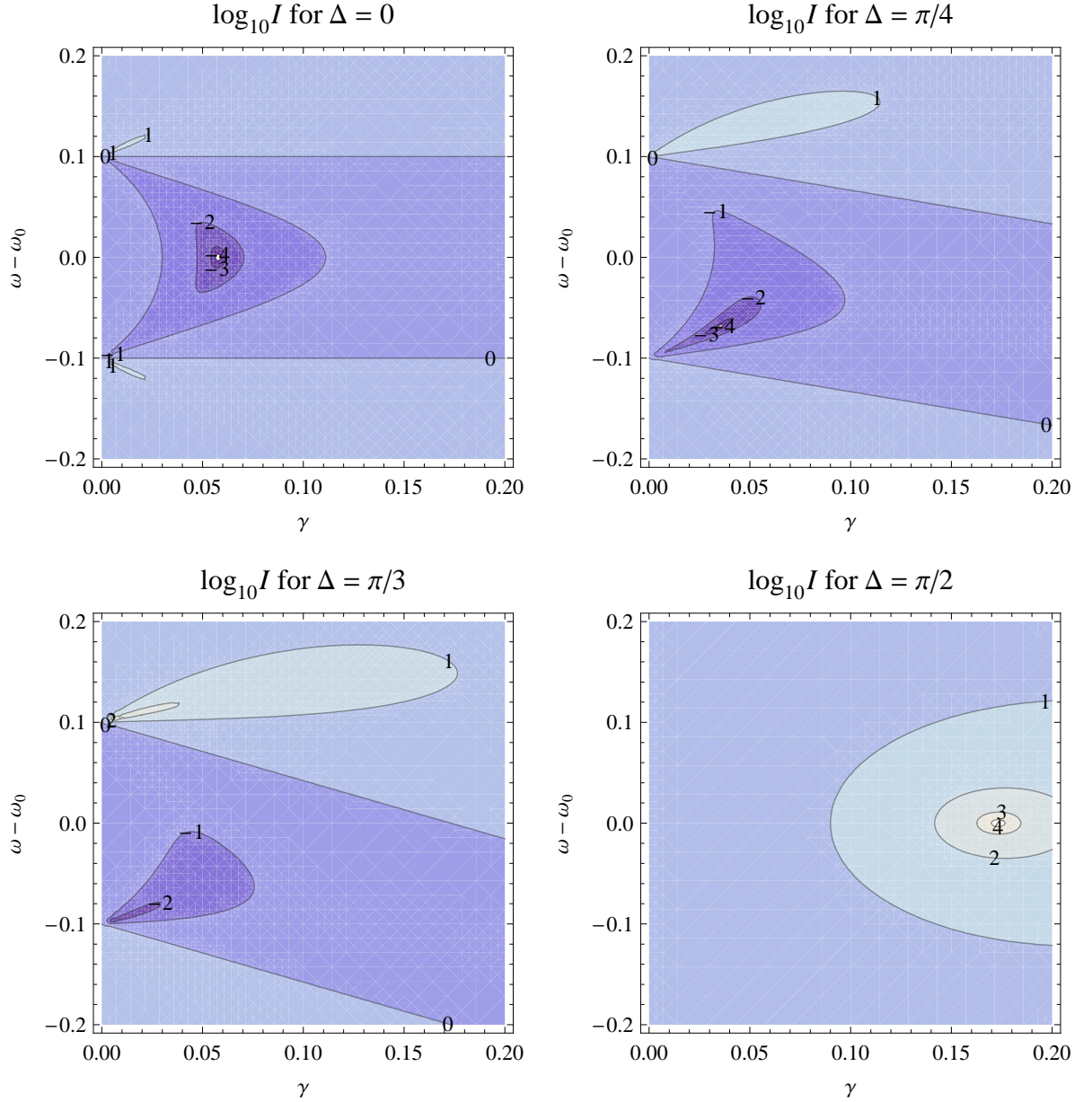


Figure 4.3 Isolation I as a function of γ and $\omega - \omega_0$ for $\Delta = 0, \frac{\pi}{4}, \frac{\pi}{3}$ and $\frac{\pi}{2}$ (logarithmic scale).

$|V| = 0.1$. It can be conjectured that for any $\Delta \neq \frac{\pi}{3}$ infinite isolation factor can be obtained for a specific value of ω and γ . However, in practice one is more concerned with the maximum bandwidth $B(I_{\min})$, defined as the maximum range of frequencies for which the isolation factor or its inverse exceeds a predetermined threshold I_{\min} . Figure 4.3 shows that this bandwidth is particularly large for vanishing ($\Delta = \frac{\pi}{2}$) and maximum ($\Delta = 0$) direct waveguide-to-waveguide coupling. In these cases, the isolation factor is an even function of $(\omega - \omega_0)$, and infinite isolation occurs at $\omega = \omega_0$ and $\gamma = |V|\sqrt{3}$ ($\Delta = \frac{\pi}{2}$) or $\gamma = |V|/\sqrt{3}$ ($\Delta = 0$). It is also at these “optimum” values of γ that maximum bandwidth is obtained.

Figure 4.4 illustrates the frequency dependence of the transmittances and the isolation factor for $\Delta = \frac{\pi}{2}$ and 0, with γ set to the respective “optimum” values cited above. In the first case, $I > 1$ everywhere: for the chosen SEMF polarisation, waveguide W_3 receives more power than W_2 at all operation frequencies. In contrast, the device with $\Delta = 0$ acts as a switch: transmission occurs preferentially to

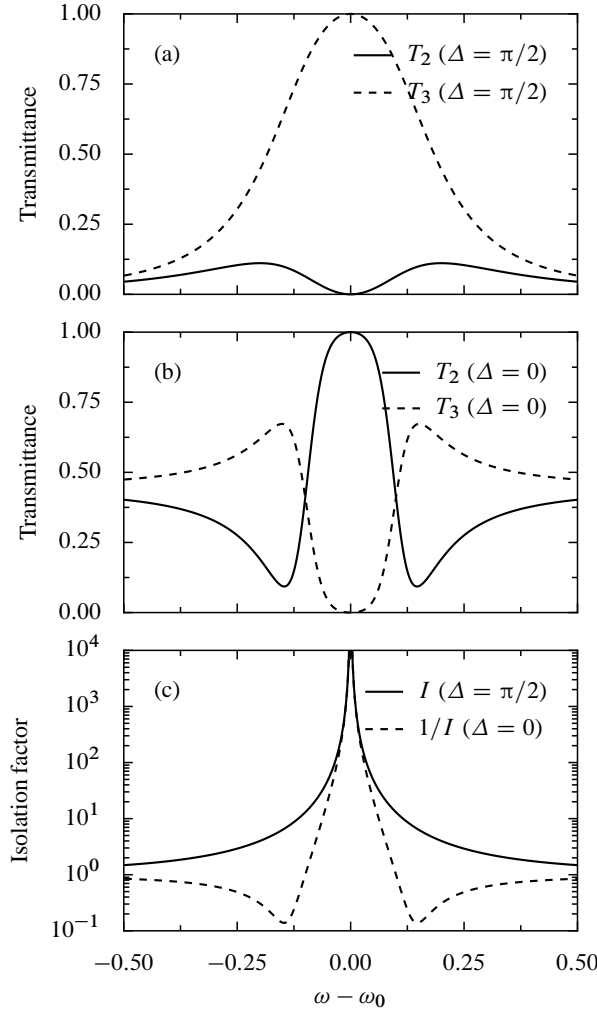


Figure 4.4 (a) Frequency dependence of the transmittances T_2 and T_3 for a circulator with $\Delta = \frac{\pi}{2}$ and $\gamma = |V|\sqrt{3}$. (b) Same for a circulator with $\Delta = 0$ and $\gamma = |V|/\sqrt{3}$. (c) Frequency dependence of the isolation factor I of the two circulators. In both cases $|V| = 0.1$.

waveguide W_2 for $|\omega - \omega_0| < |V|$ and to W_3 outside this frequency range. In consequence, the bandwidth of the system with maximum coupling ($\Delta = 0$) is inferior to that of the one with no direct coupling ($\Delta = \frac{\pi}{2}$) regardless of the chosen threshold I_{\min} . However, fig. 4.4(c) shows that the difference in bandwidth becomes less and less pronounced as I_{\min} grows: for very high isolation factors, the bandwidths of both structures are virtually indistinguishable.

The conclusions from the previous two paragraphs, based in part on an analysis of plots made for several specific cases, can also be reached in a rigorous manner. We shall first derive the values of ω and γ at which the isolation factor or its inverse becomes infinite. By definition of I , this will be the case provided that exactly one of $s_{2,\text{out}}$ and $s_{3,\text{out}}$ vanishes. Rewriting the condition $s_{2,\text{out}} = 0$ as ($\text{Re } s_{2,\text{out}} = 0$ and $\text{Im } s_{2,\text{out}} = 0$) and using assumption (4.20), we obtain

$$3[|V|^2 + \gamma|V|\sqrt{3} - (\omega - \omega_0)^2] \cos \Delta - \gamma(\omega - \omega_0) \sin \Delta = 0, \quad (4.22a)$$

$$\gamma[3(\omega - \omega_0) \cos \Delta + (\gamma - |V|\sqrt{3}) \sin \Delta] = 0. \quad (4.22b)$$

One solution of these equations, $\omega = \omega_0 \pm |V|$ and $\gamma = 0$, is obviously incompatible with assumption (4.20). The other can be obtained by solving eq. (4.22b) for ω and substituting the result into eq. (4.22a).

This yields

$$\omega = \omega_0 + \frac{2 \sin(2\Delta)}{1 + 8 \cos^2 \Delta} |V| \sqrt{3} \quad \text{and} \quad \gamma = \frac{1 - 4 \cos^2 \Delta}{1 + 8 \cos^2 \Delta} |V| \sqrt{3}. \quad (4.23)$$

Comparing the expressions (4.19b) and (4.19c) for $s_{2,\text{out}}$ and $s_{3,\text{out}}$, one immediately sees that the condition for $s_{3,\text{out}} = 0$ is given by formula (4.23) with $|V|$ replaced by $-|V|$. Noting further that, by definition (4.14), γ cannot be negative, we arrive at the following conclusion.

The isolation factor I of a lossless circulator is infinite if and only if

$$|\cos \Delta| < \frac{1}{2}, \quad \omega = \omega_0 + \frac{2 \sin(2\Delta)}{1 + 8 \cos^2 \Delta} |V| \sqrt{3} \quad \text{and} \quad \gamma = \frac{1 - 4 \cos^2 \Delta}{1 + 8 \cos^2 \Delta} |V| \sqrt{3}. \quad (4.24a)$$

The factor I is zero if and only if

$$|\cos \Delta| > \frac{1}{2}, \quad \omega = \omega_0 - \frac{2 \sin(2\Delta)}{1 + 8 \cos^2 \Delta} |V| \sqrt{3} \quad \text{and} \quad \gamma = \frac{4 \cos^2 \Delta - 1}{1 + 8 \cos^2 \Delta} |V| \sqrt{3}. \quad (4.24b)$$

Restricting Δ to the interval $[0, \frac{\pi}{2}]$, we see that $|\cos \Delta| \leq \frac{1}{2}$ if and only if $\Delta \geq \frac{\pi}{3}$. It should be noted that for $\Delta = \frac{\pi}{3}$ there exist no solutions of eq. (4.22) compatible with assumption (4.20).

It is convenient to introduce the *reduced frequency*

$$\tilde{\omega} \equiv \frac{\omega - \omega_0}{|V|} \pm \frac{2 \sin(2\Delta)}{1 + 8 \cos^2 \Delta} \sqrt{3} \quad \text{for} \quad |\cos \Delta| \leq \frac{1}{2}. \quad (4.25)$$

It can be shown that the isolation I at the optimum level of coupling γ quoted in conditions (4.24) can be written solely as a function of Δ and $\tilde{\omega}$. The plot of this function is shown in fig. 4.5(a). It can be seen that for any I_{\min} the bandwidth $B(I_{\min})$ depends strongly on the value of Δ , and it is always the largest for $\Delta = \frac{\pi}{2}$. The behaviour of $B(I_{\min})$ in the interval $\Delta \in [0, \frac{\pi}{3}]$ is quite interesting. For sufficiently low values of I_{\min} , maximum bandwidth is obtained for some value of Δ lying in the interior of this interval. However, as soon as I_{\min} exceeds ~ 55 , the optimum value of Δ in the interval in question becomes equal to 0. As noted earlier, the difference in bandwidth at $\Delta = 0$ and $\Delta = \frac{\pi}{2}$ diminishes as I_{\min} grows. This effect is demonstrated in fig. 4.5(b), in which the ratio of $B(I_{\min}, \Delta = \frac{\pi}{2})$ and $B(I_{\min}, \Delta = 0)$ is plotted as a function of I_{\min} .

In summary, direct waveguide-to-waveguide coupling has a detrimental effect on a circulator's operation bandwidth, and therefore should be minimised in a properly designed device. Nevertheless, a little paradoxically, devices with maximum direct coupling also provide a comparatively large bandwidth, exhibiting, in addition, an interesting switching effect.

4.2.2 Inclusion of radiation loss

Another effect that can play an important part in the operation of rib-waveguide-based circulators and three-dimensional (3D) PC circulators alike is the loss of energy to the free space surrounding the device. This loss can be fairly easily handled by the coupled-wave theory. We shall limit our discussion to the case without direct coupling ($\Delta = \frac{\pi}{2}$), which in the previous subsection was found to yield maximum bandwidth. We shall also assume the energy to be lost solely owing to radiation of the cavity mode into free space, neglecting the energy radiated when the incident waveguide mode is reflected from the end of the input waveguide.

Following ref. 156, pp. 208–212, we incorporate the cavity radiation loss in the coupled-wave equations (4.8) by replacing \hat{F} by $\hat{F} + \hat{F}_1$, where $\hat{F}_1 \equiv \gamma_1 \begin{bmatrix} 1 & 0 \\ 0 & 1 \end{bmatrix}$ and γ_1 is the decay constant related to radiation

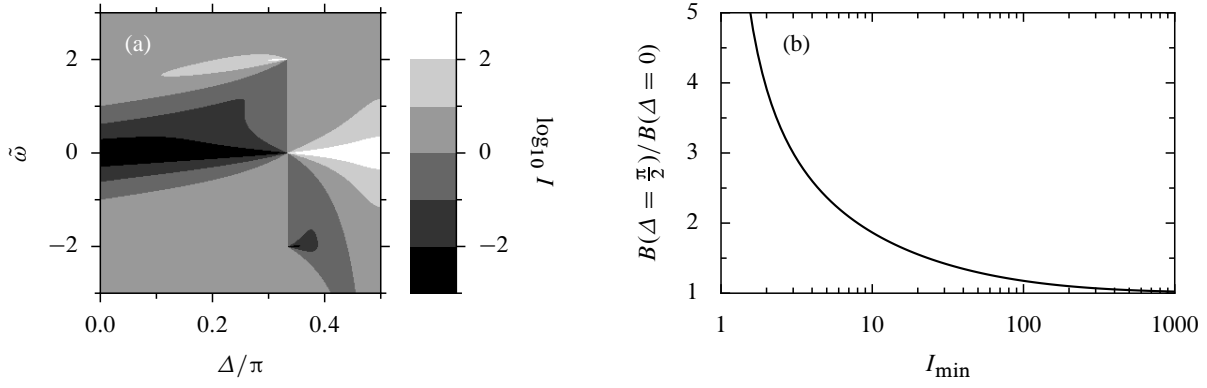


Figure 4.5 (a) Dependence of the isolation I on Δ and $\tilde{\omega}$ when the coupling level γ is maintained at its optimum value given by eqs. (4.24). The visible discontinuity of I at $\Delta = \frac{\pi}{3}$ is due to the fact that at this value of Δ we switch from the conditions for zero isolation [eq. (4.24b)] to those for infinite isolation [eq. (4.24a)]. (b) Ratio of the maximum bandwidths $B(I_{\min})$ of the two circulators with $\Delta = \frac{\pi}{2}$ and $\Delta = 0$ as a function of I_{\min} . The coupling level γ is still maintained at its optimum value.

loss. Proceeding analogously as before, we solve the coupled-wave equations for the amplitudes of the outgoing modes in the three waveguides:

$$s_{1,\text{out}} = -1 + \frac{4}{3} \frac{\gamma[\gamma + \gamma_1 - i(\omega - \omega_0)]}{[\gamma + \gamma_1 - i(\omega - \omega_0)]^2 + |V|^2}, \quad (4.26a)$$

$$s_{2,\text{out}} = -\frac{2}{3} \frac{\gamma[\gamma + \gamma_1 - |V|\sqrt{3} - i(\omega - \omega_0)]}{[\gamma - i(\omega - \omega_0)]^2 + |V|^2}, \quad (4.26b)$$

$$s_{3,\text{out}} = -\frac{2}{3} \frac{\gamma[\gamma + \gamma_1 + |V|\sqrt{3} - i(\omega - \omega_0)]}{[\gamma - i(\omega - \omega_0)]^2 + |V|^2}. \quad (4.26c)$$

From eqs. (4.26b) and (4.26c) it can be immediately seen that despite the presence of loss, infinite isolation I can still be obtained at frequency $\omega = \omega_0$ provided that the coupling coefficient γ is taken as

$$\gamma = |V|\sqrt{3} - \gamma_1. \quad (4.27)$$

Interestingly, when γ is chosen in this way, the isolation $I(\omega)$ becomes independent from γ_1 :

$$I(\omega) = 1 + \frac{12|V|^2}{(\omega - \omega_0)^2}. \quad (4.28)$$

However, the power transmitted to the ‘hot’ waveguide, T_3 , obviously decreased when the loss coefficient γ_1 increases. With γ given by eq. (4.27), the expression for the maximum value of T_3 takes the form

$$T_3(\omega = \omega_0) = \frac{(\sqrt{3} - \gamma_1/|V|)^2}{3}. \quad (4.29)$$

This formula is important because it allows to determine the minimum quality factor $Q_1 \equiv \omega_0/(2\gamma_1)$ of a cavity with a given SEMF-induced relative frequency splitting $\Delta\omega/\omega_0$ that can be used to build a circulator with a prescribed minimum level of transmitted power, $T_{3,\min}$. (Note that Q_1 describes solely the decay caused by radiation to free space, rather than that due to interaction with waveguide modes.) Indeed, expressing γ_1 in eq. (4.29) in terms of Q_1 and using the relation $\Delta\omega = 2|V|$, we obtain that

$$T_3(\omega = \omega_0) \geq T_{\min} \quad \text{if and only if} \quad Q_1 \geq \left[\frac{\Delta\omega}{\omega_0} (1 - \sqrt{T_{\min}}) \sqrt{3} \right]^{-1}. \quad (4.30)$$

Thus, a circulator built with a cavity having $\Delta\omega/\omega_0 = 0.001$ (a typical value) can provide 50-percent peak transmission if $Q_1 \geq 1970$. A quality factor $Q_1 \geq 11,250$ is needed for 90-percent efficiency, and $Q_1 \geq 115,000$ for 99-percent.

4.3 Cavities with circular symmetry

Wang and Fan [34] used the perturbation theory to derive a formula for the mode coupling strength V , introduced in the previous subsection, of a cavity containing a MO material polarised in the z direction. From eq. (4.6) it follows that such a material is characterised by the permittivity tensor

$$\hat{\epsilon} = \begin{bmatrix} \epsilon & ig & 0 \\ -ig & \epsilon & 0 \\ 0 & 0 & \epsilon \end{bmatrix}, \quad (4.31)$$

where $g \equiv KM_z$. From now on we shall assume g to be real. The authors of ref. 34 obtained*

$$V = -\frac{i}{2} \frac{\omega \int g(\vec{r}) \vec{e}_z \cdot [\vec{E}_e^*(\vec{r}) \times \vec{E}_o(\vec{r})] d\vec{r}}{\sqrt{\int \epsilon(\vec{r}) |\vec{E}_o(\vec{r})|^2 d\vec{r} \int \epsilon(\vec{r}) |\vec{E}_e(\vec{r})|^2 d\vec{r}}}, \quad (4.32)$$

where the integrals run over the whole cavity volume, \vec{E}_e and \vec{E}_o are the electric fields of the even and odd modes of the cavity unperturbed by the SEMF, and ω is their frequency (denoted ω_0 in the previous section). Thus, the magnitude of V is proportional to the cross product of the electric fields \vec{E}_e and \vec{E}_o weighted by the off-diagonal component of the permittivity tensor, ig . To understand better the behaviour of this cross product and to formulate a design principle for resonant cavities with large frequency splitting in a uniform SEMF, we shall now study the restricted class of 2D cavities having perfect rotational symmetry. In contrast to general PC cavities, circularly symmetric cavities can be handled analytically, which makes it possible to get a better insight into their properties.

We consider, then, a system of concentric rings [see fig. 4.6(a)], described by a piecewise-constant relative permittivity $\epsilon(\rho)$ independent from the azimuthal coordinate ϕ and the vertical coordinate z . The relative permeability μ is taken to be 1 everywhere. In the p -polarisation case [waves propagating in the (ρ, ϕ) plane with the magnetic field parallel to the z axis] the Maxwell's equations

$$\frac{1}{\rho} \frac{\partial H_z}{\partial \phi} = -i\omega\epsilon\epsilon_0 E_\rho, \quad (4.33a)$$

$$\frac{\partial H_z}{\partial \rho} = i\omega\epsilon\epsilon_0 E_\phi, \quad (4.33b)$$

$$\frac{\partial E_\phi}{\partial \rho} + \frac{1}{\rho} E_\phi - \frac{1}{\rho} \frac{\partial E_\rho}{\partial \phi} = i\omega\mu_0 H_z, \quad (4.33c)$$

reduce to the Helmholtz equation for the z component of the magnetic field, H_z :

$$\epsilon \frac{\partial}{\partial \rho} \left(\frac{1}{\epsilon} \frac{\partial H_z}{\partial \rho} \right) + \frac{1}{\rho} \frac{\partial H_z}{\partial \rho} + \frac{1}{\rho^2} \frac{\partial^2 H_z}{\partial \phi^2} + \epsilon \frac{\omega^2}{c^2} H_z = 0. \quad (4.34)$$

Here ω denotes the frequency, ϵ_0 and μ_0 the permittivity and permeability of free space, and $c = 1/\sqrt{\epsilon_0\mu_0}$ the speed of light in vacuum. By the usual method of separation of variables one can show

* The difference in sign between eq. (6) from ref. 34 and eq. (4.32) is caused by the difference in the convention chosen for harmonic time-dependence ($e^{-i\omega t}$ here vs. $e^{i\omega t}$ in ref. 34).

that the eigenmodes of the system occur in degenerate pairs of “even” and “odd” modes with magnetic field of the general form

$$H_{ze}(\rho, \phi) = R(\rho) \cos(l\phi) \quad \text{and} \quad H_{zo}(\rho, \phi) = R(\rho) \sin(l\phi), \quad (4.35)$$

respectively, where the azimuthal order l is an integer. (Of course, the exception is the modes with $l = 0$, which are not degenerate.) Within an arbitrary ring, the radial dependence $R(\rho)$ of the magnetic field of a mode with azimuthal order l can be expressed as a superposition of the Bessel functions of the first and second kind:

$$R(\rho) = a_m J_l(n_m k_0 \rho) + b_m Y_l(n_m k_0 \rho), \quad (4.36)$$

where m is the ring's number, n_m its refractive index, a_m and b_m constant coefficients, and $k_0 \equiv \omega/c$ the free-space wave number.

From eq. (4.35) and the Maxwell's equations (4.33) we can derive the general expressions for the cross product of the electric fields corresponding to a pair of degenerate modes with azimuthal order l ,

$$\vec{e}_z \cdot (\vec{E}_e^* \times \vec{E}_o) = \frac{l R(\rho) R'(\rho)}{\omega^2 \rho \epsilon(\rho)^2}, \quad (4.37)$$

and their norm,

$$\int \epsilon(\vec{r}) |\vec{E}_e(\vec{r})|^2 d\vec{r} = \int \epsilon(\vec{r}) |\vec{E}_o(\vec{r})|^2 d\vec{r} = \int_0^\infty \frac{l^2 [R(\rho)]^2 + \rho^2 [R'(\rho)]^2}{\rho \epsilon(\rho)} d\rho, \quad (4.38)$$

with $R'(\rho)$ denoting the derivative of $R(\rho)$. Substituting eqs. (4.37) and (4.38) to the general formula for the coupling strength (4.39), we obtain

$$V = - \frac{i\omega l \int_0^\infty \frac{g(\rho) R(\rho) R'(\rho)}{\epsilon(\rho)^2} d\rho}{\int_0^\infty \frac{l^2 [R(\rho)]^2 + \rho^2 [R'(\rho)]^2}{\rho \epsilon(\rho)} d\rho}. \quad (4.39)$$

Clearly, the sign of the integrand in the numerator of the above expression depends on the sign of the product $g(\rho) R(\rho) R'(\rho)$. In general, this sign will oscillate due to the oscillatory behaviour of the function $R(\rho)$ itself. Therefore, to avoid unnecessary cancellations in the integral in question, the ring boundaries need to be placed so that the product $g(\rho) R(\rho) R'(\rho)$ be always nonnegative (or nonpositive). *Excluding the possibility of introducing inversely-magnetised domains, this can only be achieved by ensuring that the boundaries between the MO and non-MO material coincide with the zeros of the product $R(\rho) R'(\rho)$, i.e., the zeros and extrema of $R(\rho)$.* With this design principle in mind, we offer the following method for the determination of the radii of the alternating MO and non-MO rings making up a cavity supporting a pair of degenerate modes with azimuthal order $l \geq 1$ at a particular frequency $\omega = k_0 c$.

As a first step, we determine the radius ρ_0 of the central rod (“zeroth ring”), assumed to have refractive index n_0 . In this rod, the radial field dependence is expressed solely by means of the Bessel function of the first kind $J_l(n_0 k_0 \rho)$, since the $Y_l(n_0 k_0 \rho)$ function has a singularity at the origin. Hence, $b_0 = 0$ and, since the global mode amplitude is arbitrary, a_0 can be set to 1. It is then evident that the product $R(\rho) R'(\rho)$ in the central rod will not change sign until the first extremum of the $J_l(n_0 k_0 \rho)$ function. Therefore, we set the rod's radius, ρ_0 , to the value of ρ corresponding to the location of this extremum.

The amplitudes a_1 and b_1 of the Bessel functions in the first ring, having refractive index n_1 , can now be determined from the condition of continuity of H_z and E_ϕ . The outer radius of the first ring, ρ_1 ,

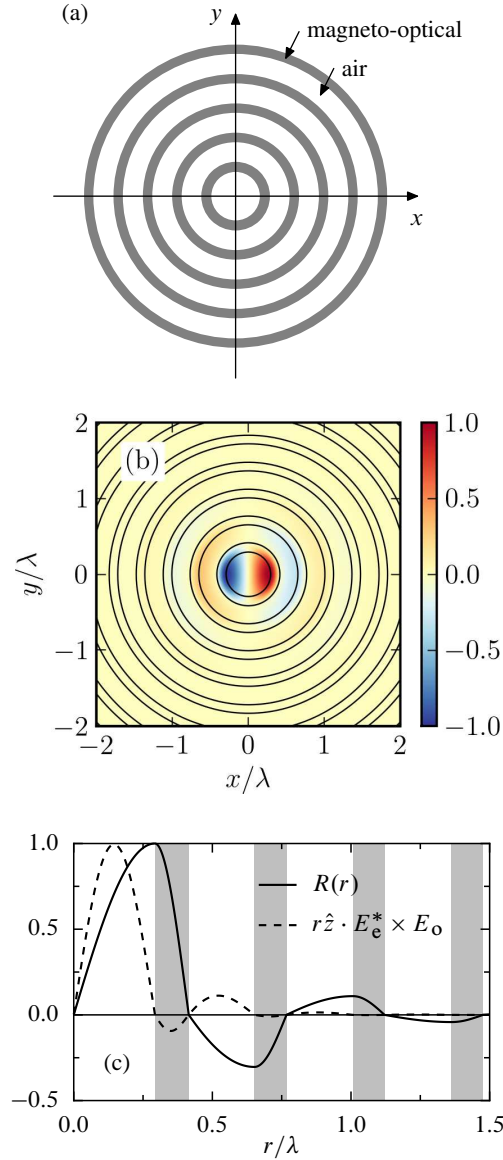


Figure 4.6 (a) The geometry of a cavity composed of a sequence of rings made of air and a MO material with refractive index 2.25. (b) The magnetic field H_z of the even eigenmode of azimuthal order $l = 1$ supported by the cavity at frequency $\omega = 2\pi c/\lambda$. (c) Radial dependence of the magnetic field H_z of the cavity eigenmodes and of the cross product of their electric fields. Both functions are normalised to their maximum values. The areas filled with the MO material are shaded.

should then be chosen so as to coincide with the first zero of the function $a_1 J_l(n_1 k_0 \rho) + b_1 Y_l(n_1 k_0 \rho)$ located in that ring, as which point the product $R(\rho)R'(\rho)$ will again change sign. By repeating this process, we obtain the radii of the subsequent rings. The outer radii of the even rings (with refractive index n_0) coincide with the extrema of the function $R(\rho)$, and those of the odd rings (with refractive index n_1), with its zeros. Thus, the cavity designed in this way resembles an annular Bragg grating [157], with each layer a quarter-wavelength thick (in the sense of the Bessel-function quasi-periodicity).

We need now to make sure that the field of the mode constructed in this way is localised, i.e., that $R(\rho)$ decays as ρ tends to infinity. Let us estimate the ratio of $R(\rho)$ at its two successive extrema, located at ρ_{2n} and ρ_{2n+2} , where $n \gg 1$. The Bessel functions of large arguments can be approximated by [158,

eqs. (9.2.1) and (9.2.2)]

$$J_l(x) \approx \sqrt{\frac{2}{\pi x}} \cos\left(x - \frac{\pi}{2}l - \frac{\pi}{4}\right), \quad (4.40a)$$

$$Y_l(x) \approx \sqrt{\frac{2}{\pi x}} \sin\left(x - \frac{\pi}{2}l - \frac{\pi}{4}\right). \quad (4.40b)$$

By construction, the field in the $(2n + 1)$ th ring, located between ρ_{2n} and ρ_{2n+1} , behaves approximately as

$$R(\rho) \approx c_{2n+1} \rho^{-1/2} \cos[n_1 k_0 (\rho - \rho_{2n})], \quad (4.41)$$

and in the $(2n + 2)$ th ring as

$$R(\rho) \approx c_{2n+2} \rho^{-1/2} \sin[n_0 k_0 (\rho - \rho_{2n+1})], \quad (4.42)$$

where c_{2n+1} and c_{2n+2} are constant coefficients. Since the rings are supposed to be a quarter-wavelength thick, the expressions $n_1 k_0 (\rho_{2n+1} - \rho_{2n})$ and $n_0 k_0 (\rho_{2n+2} - \rho_{2n+1})$ are approximately equal to $\frac{\pi}{2}$ and the successive extremal values of $R(\rho)$ are

$$R(\rho_{2n}) \approx c_{2n+1} \rho_{2n}^{-1/2} \quad (4.43a)$$

and

$$R(\rho_{2n+2}) \approx c_{2n+2} \rho_{2n+2}^{-1/2} \approx c_{2n+2} \left[\rho_{2n} + \frac{\pi}{2k_0} \left(\frac{1}{n_0} + \frac{1}{n_1} \right) \right]^{-1/2}. \quad (4.43b)$$

From the requirement of continuity of $E_\phi \propto R'(\rho)/\epsilon(\rho)$ at $\rho = \rho_{2n+1}$ it follows that $c_{2n+2}/c_{2n+1} = -n_0/n_1$. Hence,

$$\left| \frac{R(\rho_{2n+2})}{R(\rho_{2n})} \right| \approx \frac{n_0}{n_1} \left[1 + \frac{\pi}{2k_0 \rho_{2n}} \left(\frac{1}{n_0} + \frac{1}{n_1} \right) \right]^{-1/2} \xrightarrow{n \rightarrow \infty} \frac{n_0}{n_1}. \quad (4.44)$$

Thus, a localised mode is obtained only if the refractive index of the central rod, n_0 , is chosen smaller than that of the first ring, n_1 .

Figure 4.6(a) shows the geometry of an example cavity constructed with the above algorithm. The system consists of an alternating sequence of rings made of air (refractive index $n_0 = 1$) and a MO material with refractive index $n_1 = 2.25$. It supports a pair of degenerate localised eigenmodes of azimuthal order $l = 1$. The magnetic field of the even mode is plotted in fig. 4.6(b); the field of the odd mode can be obtained by rotating the map from fig. 4.6(b) by 90° in the counter-clockwise direction. In fig. 4.6(c), the radial dependence of these magnetic fields, $R(\rho)$, is juxtaposed with the radial dependence of $\vec{e}_z \cdot \vec{E}_e^* \times \vec{E}_o$ calculated from eq. (4.37). Clearly, $R(\rho)R'(\rho)$ is negative throughout the MO rings and positive elsewhere; as a result, no cancellations in the upper integral in eq. (4.39) occur. The reduced coupling strength of this pair of modes is $v = 0.00874$.

4.4 Photonic-crystal-based circulators

The insight gained in the previous section is valuable not only in the design of axisymmetric cavities with maximum frequency splitting induced by a uniform SEMF, but also of PC-based ones. Figure 4.6(c) shows that the cross product $\vec{E}_e^* \times \vec{E}_o$ in a well-designed axisymmetric cavity has a significant amplitude only within the rings closest to the cavity centre. Thus, one can conclude that the frequency

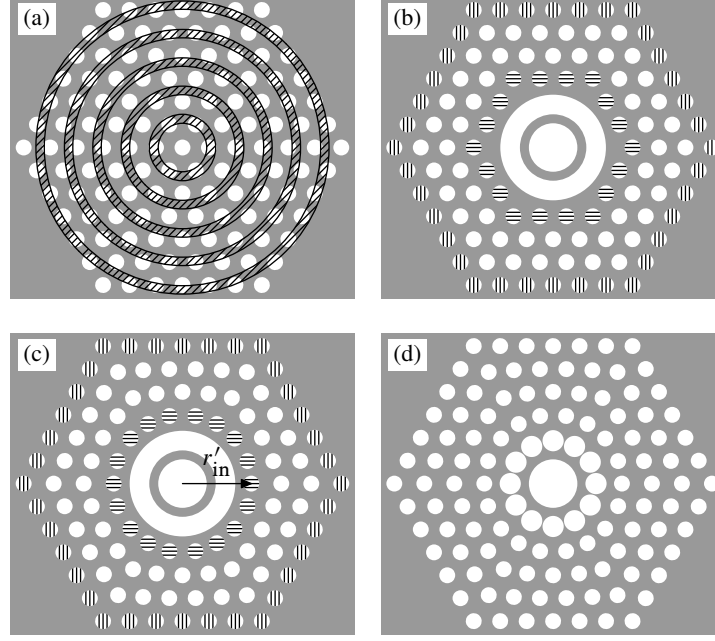


Figure 4.7 Adjustment of an axisymmetric cavity for integration into a PC lattice. **(a)** Superposition of the cavity and a hexagonal block of the PC. **(b)** Structure obtained by combining the central air hole and the innermost air ring of the cavity with the external region of the PC block. **(c)** The result of shifting the circular air holes of the cavity from part (b) in the radial direction, according to the mapping described in the text. **(d)** The cavity from part (c) with its air ring approximated by a string of circular air holes.

splitting of the cavity modes depends mostly on the geometry of the innermost region, whereas the primary function of the external rings is to provide a sufficient isolation from the surrounding free space. The MO properties of the cavity should not suffer, therefore, if the inner air rings were preserved, whereas the outer ones were replaced by a regular photonic lattice.

In practice, some difficulties related to geometric constraints can arise. Consider, for instance, a 2D PC made up of a hexagonal lattice of circular air holes with radius $0.30a$, where a is the lattice constant, etched in a matrix of a MO material with refractive index $n = 2.5$ (close to that of BIG at infrared frequencies). This crystal has a band gap for p -polarised waves with frequencies between $\omega = 0.285$ and $0.350 \times 2\pi c/a$. In fig. 4.7(a) its geometry is juxtaposed with the contours of the BIG rings of the axisymmetric cavity composed of BIG and air and supporting a pair of eigenmodes with azimuthal order $l = 1$, frequency $\omega = 0.320 \times 2\pi c/a$ and reduced coupling strength $v = 0.0062$. The dimensions of the rings are listed in table 4.1. It can be seen that no matter how many inner rings are preserved, a wide gap will appear between them and the surrounding PC. Its presence will certainly shift the eigenfrequencies of the cavity modes and diminish the frequency splitting between them: the modes will be more weakly localised, and hence the denominator of expression (4.32) for V will increase, while the numerator will stay roughly the same. In order to overcome this difficulty, we propose to adjust the positions of the PC holes using an appropriate coordinate transform. While its optimum form remains an open problem, we obtained satisfactory results with a simple mapping whose principle is illustrated in figs. 4.7(b) and (c). The mapping has the form $(\rho, \phi) \mapsto (a(\phi)\rho + b(\phi), \phi)$, where the coefficients $a(\phi)$ and $b(\phi)$ are chosen so that the centres of the holes hatched horizontally in fig. 4.7(b) move onto a circle of radius ρ'_{in} , as shown in fig. 4.7(c), while the position of the ones hatched vertically does not change. We have found the value of $\rho'_{in} = 2.60a$ to be approximately optimal for the considered system.

Ring number	Inner radius	Outer radius
1	$0.916a$	$1.255a$
2	$1.995a$	$2.319a$
3	$3.068a$	$3.387a$
4	$4.143a$	$4.461a$
5	$5.221a$	$5.538a$

Table 4.1 Radii of the high-index rings of the cavity with $\epsilon_h = (2.5)^2 = 6.25$ and $\epsilon_l = 1$ supporting a resonant mode with azimuthal order $l = 1$ at frequency $\omega = 0.32 \times 2\pi c/a$.

#	x/a	y/a	r/a	#	x/a	y/a	r/a	#	x/a	y/a	r/a
1	0.000	0.000	0.92	8	2.967	3.426	0.30	15	4.000	3.464	0.30
2	1.403	0.810	0.40	9	3.001	1.733	0.30	16	4.451	0.857	0.30
3	1.620	0.000	0.40	10	3.433	0.849	0.30	17	4.500	2.598	0.30
4	1.965	1.702	0.30	11	3.496	2.595	0.30	18	4.867	0.000	0.30
5	2.452	2.548	0.30	12	3.500	4.330	0.30	19	5.000	1.732	0.30
6	2.457	0.851	0.30	13	3.733	0.000	0.30	20	5.500	0.866	0.30
7	2.600	0.000	0.30	14	3.995	1.730	0.30	21	6.000	0.000	0.30

Table 4.2 Cartesian coordinates (x, y) and radii r of the circular air holes making up the cavity shown in fig. 4.7(d). For brevity, only the holes lying in the sector $0 \leq \phi < 60^\circ$ are included.

To simulate PC-based cavities and circulators, we have been using the multiple-scattering method extended to systems containing MO materials (see section 5.1). At present, our code cannot handle scatterers composed of several concentric layers. Therefore we have approximated the preserved air ring with a string of air holes with radius $0.4a$ arranged on a circle of radius $1.62a$, in the hope that this will not seriously deteriorate the MO properties of the cavity. In this way we arrived at the final geometry of the proposed PC-based cavity, shown in fig. 4.7(d). For completeness, the positions and radii of its constituent air holes are listed in table 4.2.

By means of the multiple-scattering method we have found that in the absence of SEMF the cavity in question supports a pair of degenerate dipolar modes at the complex frequency $\omega = (0.31241 - 0.00037i) \times 2\pi c/a$ [148]. Figures 4.8(a) and (b) show the magnetic field H_z corresponding to these modes, and fig. 4.8(c), the cross product of their electric fields weighted with $g(\vec{r})$ taken to be 1 in the MO material and 0 in air. It can be seen that the cross product remains positive practically everywhere in the MO material. The reduced mode coupling strength is $v = 0.0048$, which is slightly less than the value obtained for the initial axisymmetric cavity. This deterioration could probably be reduced by a more careful optimisation of the transition between the inner region, approximately axisymmetric, and the surrounding PC lattice. However, the obtained value of v is still eight times larger than that of the cavity from ref. 34, figs. 2 and 3(a)–(b), *placed in a uniform SEMF, i.e., without introduction of oppositely-magnetised domains*. For the sake of comparison, the map of $g\vec{e}_z \cdot (\vec{E}_e^* \times \vec{E}_o)$ of that cavity is shown in fig. 4.8(d). It can be seen that the cross product changes sign inside the defect, so that the contributions of the areas with positive and negative $\vec{e}_z \cdot (\vec{E}_e^* \times \vec{E}_o)$ almost cancel out.

The next step in the design of a PC circulator is the determination of the geometry of waveguides. The simplest would be to make them by removing a single row of holes from the chosen hexagonal-lattice PC. Yet, as can be seen on the dispersion diagram in fig. 4.9(a), such waveguides, while being technically single-mode at the resonant frequency of the cavity, $\omega_0 = 0.31241 \times 2\pi c/a$, support another mode, whose cut-off frequency, $0.314 \times 2\pi c/a$, is barely higher than ω_0 . Its decay constant can therefore be expected to be small. As a result, even relatively long waveguides of this type might still exhibit multi-mode be-

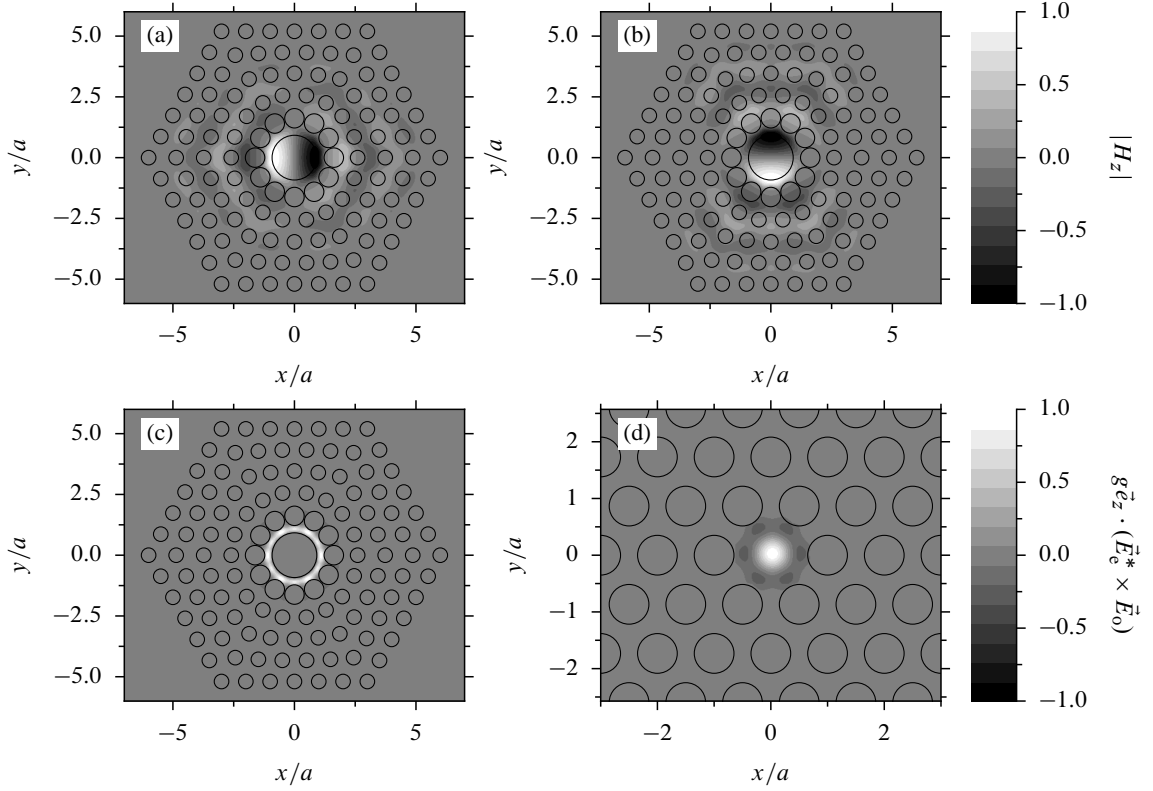


Figure 4.8 (a)–(b) Magnetic field H_z of the degenerate eigenmodes of the cavity from fig. 4.7(d). (c) Distribution of $g\vec{e}_z \cdot (\vec{E}_e^* \times \vec{E}_o)$ of the same cavity. (d) Distribution of $g\vec{e}_z \cdot (\vec{E}_e^* \times \vec{E}_o)$ of the cavity from ref. 34, figs. 2 and 3(a)–(b). All plots show the real parts of the respective quantities normalised to the interval $[-1, 1]$; with the chosen global phase of eigenmode fields, the imaginary parts are negligible.

haviour. This problem can be eliminated by bringing the holes nearest to the waveguide axis even closer to it, which causes a blueshift of the dispersion curves of both the modes. The dispersion curve of the lower-frequency mode must not be allowed to move up too much, though, since this would lead to a substantial decrease of its group velocity at frequency ω_0 . Such a decrease would be accompanied by an increase of absorption [123] and scattering losses [159] in the presence of structural defects, unavoidable in an experimentally manufactured device. The waveguide obtained by shifting its innermost holes by $d_w = 0.09a$ towards its axis seems a reasonable compromise; its dispersion diagram is shown in fig. 4.9(b).

We can now proceed to simulations of a complete circulator. The device to be considered, shown schematically in fig. 4.10, is composed of the cavity from fig. 4.7(d) and three waveguides designed as described in the previous paragraph. The holes marked by hatching, located near the ends of the waveguides, will be modified for reasons explained in what follows. The waveguides comprise $N = 12$ unmodified unit cells and the total thickness of their cladding is $d_{\text{clad}} = 5\sqrt{3}a$. The whole system is embedded in the MO material, assumed to have $g = 0.1$. The system is excited by a point source placed close to the inlet of waveguide W_1 . As in the case of the isolated cavity, the simulations are done with the multiple-scattering method.

We have tested two ways of measuring the power transmitted through the circulator. The first consists in integrating the Poynting flux over the “ports” P_j ($j = 2, 3$) of length $4\sqrt{3}a$, shown in fig. 4.10. The results obtained in this way would be severely perturbed by reflections occurring at the outlets of the waveguides W_2 and W_3 . To eliminate them, we have modified the radius r_h of the holes lying closest to waveguide ends, hatched horizontally in fig. 4.10. Using the method described in ref. 160, we have

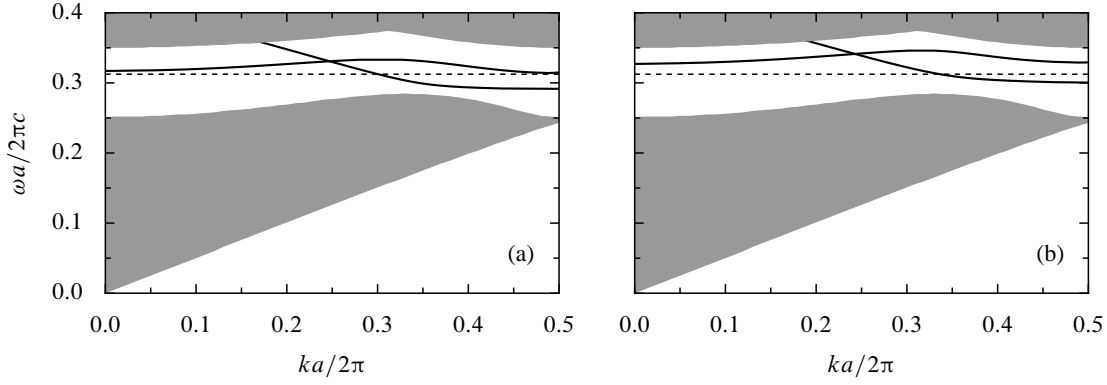


Figure 4.9 Dispersion relation of p -polarised modes of **(a)** a waveguide created by removing a row of air holes from the PC studied in section 4.4, **(b)** the waveguide from part (a) after shifting the holes nearest to the waveguide axis by $0.09a$ towards it. The regions of the (k, ω) -space in which bulk PC modes exist have been shaded. Dashed horizontal lines mark the resonant frequency of the cavity from fig. 4.7(d), $\omega = 0.31241 \times 2\pi c/a$. All calculations have been done with the method described in section 5.2.

verified that if r_h is reduced from $0.17a$, the modal reflectance of the waveguide outlet at frequency ω_0 decreases to barely 0.04%.

The second technique for obtaining the scattering matrix of the system consists in fitting the field in the waveguides with a linear combination of their forward- and backward-propagating guided modes. Since there are practically no reflections at the waveguide outlets, we can approximate the magnetic field at points $Q_{j,n}$ marked in fig. 4.10 by

$$H_z(Q_{1,n}) = H_{\text{inc}}\Phi^n + rH_{\text{inc}}\Phi^{2N-n}, \quad (4.45a)$$

$$H_z(Q_{2,n}) = t_2H_{\text{inc}}\Phi^{N+n}, \quad (4.45b)$$

$$H_z(Q_{3,n}) = t_3H_{\text{inc}}\Phi^{N+n}, \quad (4.45c)$$

where $\Phi \equiv e^{ika}$, k denotes the wave number of the waveguide eigenmode, H_{inc} stands for the excitation amplitude, r is the reflection coefficient of the circulator, and t_2 and t_3 , the transmission coefficients into waveguides W_2 and W_3 . Since the wave number k is known from the dispersion diagram shown in fig. 4.9(b), we can find the coefficients r , t_2 and t_3 simply from a linear least-squares fit of formulas (4.45) to the data obtained in simulations. To avoid perturbations induced by the presence of evanescent modes near the waveguide ends, in the fitting procedure we have disregarded the points $Q_{j,n}$ with indices $n < 3$ and $n > N - 3$. The spirit of this approach is similar to that advocated in ref. 160. In contrast to the method based on Poynting flux integration, it allows to calculate not only the transmittances $T_j \equiv |t_j|^2$ ($j = 2, 3$), but also the reflectance $R \equiv |r|^2$ and the amount of power lost to non-guided modes, $1 - (R + T_2 + T_3)$.

Figure 4.11 shows a juxtaposition of the values of the isolation coefficient $I \equiv T_2/T_3$ obtained with the two above methods for the circulator from fig. 4.10. Clearly, there is an excellent match between the two sets of data. Therefore in the following we shall limit our discussion to the results obtained with the second, more powerful approach.

Figure 4.12(a) presents the frequency dependence of the transmittances T_2 and T_3 of the same circulator, along with the total power passed to guided modes, $P \equiv R + T_2 + T_3$. It can be seen that in the neighbourhood of ω_0 the amount of power not accounted for by the guided modes increases to about 10%. We believe this power deficit to be primarily a consequence of radiation occurring from the cavity, and possibly also from the waveguides, into free space. These losses might conceivably be reduced if the thickness of the cladding were increased.

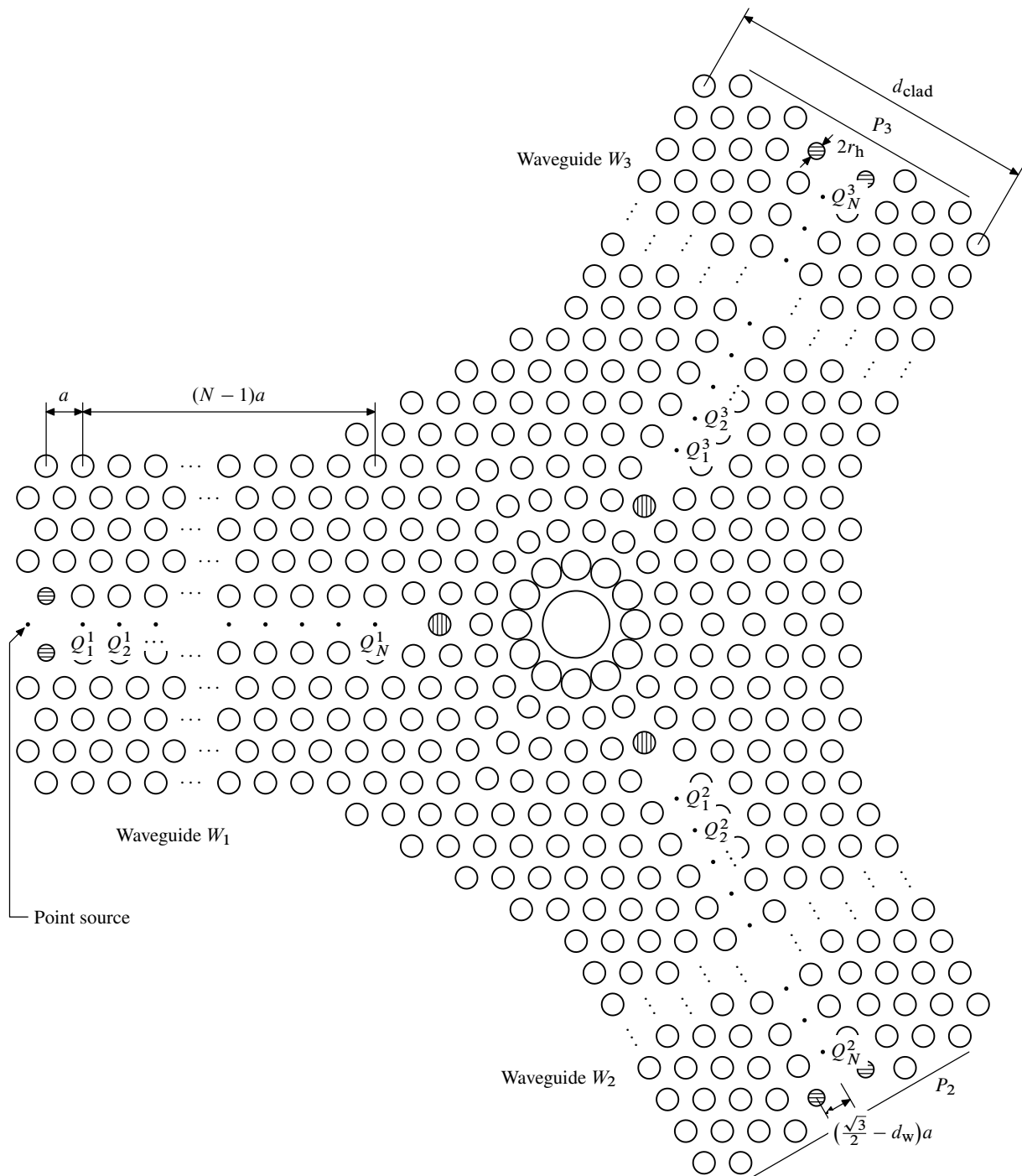


Figure 4.10 Schematic of the PC circulator described in the text.

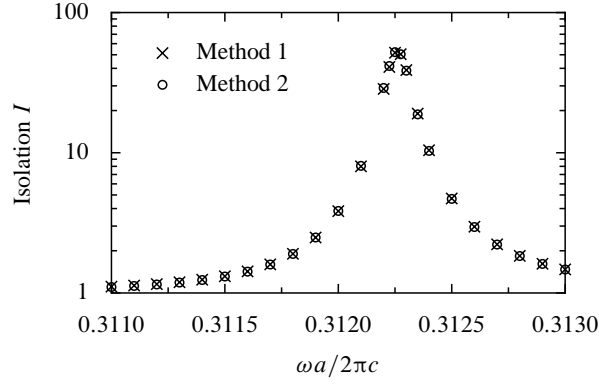


Figure 4.11 Comparison of the isolation I of the circulator from fig. 4.10 calculated by integrating the Poynting fluxes through ports P_2 and P_3 (“method 1”, crosses) and by fitting the data obtained in multiple-scattering simulations with formulas (4.45) (“method 2”, circles).

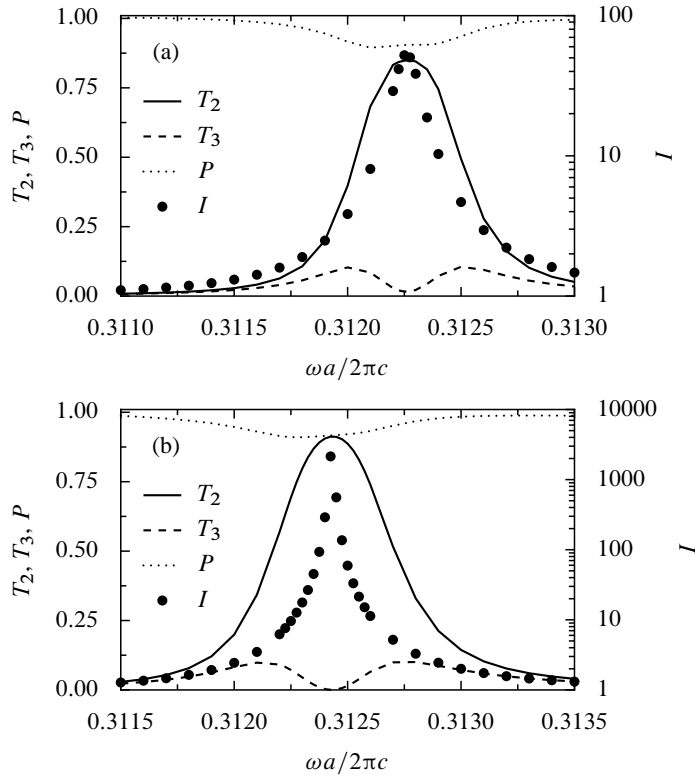


Figure 4.12 Frequency dependence of the transmittances T_2 and T_3 , isolation I , and the sum $P \equiv R + T_2 + T_3$ of the circulator shown in fig. 4.10 with the vertically hatched holes shifted by **(a)** $d_h = 0$ and **(b)** $d_h = -0.038a$ in the radial direction with respect to their original position. All the quantities were calculated by fitting the data obtained in multiple-scattering simulations with formulas (4.45).

#	x/a	y/a	r/a	#	x/a	y/a	r/a	#	x/a	y/a	r/a
1	0.000	0.000	0.92	32	5.922	8.705	0.30	63	8.422	13.035	0.30
2	0.810	1.403	0.40	33	6.000	0.000	0.30	64	8.500	6.062	0.30
3	1.403	0.810	0.40	34	6.000	1.732	0.30	65	8.500	7.794	0.30
4	1.620	0.000	0.40	35	6.000	3.464	0.30	66	8.500	9.526	0.30
5	1.965	1.702	0.30	36	6.000	5.196	0.30	67	8.500	11.258	0.30
6	2.452	2.548	0.30	37	6.000	6.928	0.30	68	8.922	13.901	0.30
7	2.457	0.851	0.30	38	6.422	9.571	0.30	69	9.000	6.928	0.30
8	2.600	0.000	0.30	39	6.500	0.866	0.30	70	9.000	8.660	0.30
9	2.967	3.426	0.30	40	6.500	2.598	0.30	71	9.000	10.392	0.30
10	3.001	1.733	0.30	41	6.500	4.330	0.30	72	9.000	12.124	0.30
11	3.422	4.375	0.30	42	6.500	6.062	0.30	73	9.500	7.794	0.30
12	3.433	0.849	0.30	43	6.500	7.794	0.30	74	9.500	9.526	0.30
13	3.496	2.595	0.30	44	6.922	10.437	0.30	75	9.500	11.258	0.30
14	3.733	0.000	0.30	45	7.000	0.000	0.30	76	9.500	12.990	0.30
15	3.922	5.241	0.30	46	7.000	1.732	0.30	77	10.000	8.660	0.30
16	3.995	1.730	0.30	47	7.000	3.464	0.30	78	10.000	10.392	0.30
17	4.000	3.464	0.30	48	7.000	5.196	0.30	79	10.000	12.124	0.30
18	4.422	6.107	0.30	49	7.000	6.928	0.30	80	10.000	13.856	0.30
19	4.451	0.857	0.30	50	7.000	8.660	0.30	81	10.500	9.526	0.30
20	4.500	2.598	0.30	51	7.422	11.303	0.30	82	10.500	11.258	0.30
21	4.500	4.330	0.30	52	7.500	0.866	0.30	83	10.500	12.990	0.30
22	4.867	0.000	0.30	53	7.500	2.598	0.30	84	10.500	14.722	0.30
23	4.922	6.973	0.30	54	7.500	4.330	0.30	85	11.000	10.392	0.30
24	5.000	1.732	0.30	55	7.500	6.062	0.30	86	11.000	12.124	0.30
25	5.000	3.464	0.30	56	7.500	7.794	0.30	87	11.000	13.856	0.30
26	5.000	5.196	0.30	57	7.500	9.526	0.30	88	11.500	11.258	0.30
27	5.422	7.839	0.30	58	7.922	12.169	0.30	89	11.500	12.990	0.30
28	5.500	0.866	0.30	59	8.000	5.196	0.30	90	12.000	12.124	0.30
29	5.500	2.598	0.30	60	8.000	6.928	0.30	91	12.000	13.856	0.30
30	5.500	4.330	0.30	61	8.000	8.660	0.30	92	12.500	12.990	0.30
31	5.500	6.062	0.30	62	8.000	10.392	0.30	93	9.422	14.767	0.17

Table 4.3 Cartesian coordinates (x, y) and radii r of the circular air holes making up the optimised circulator shown in fig. 4.13. For brevity, only the holes lying in the sector $0 \leq \phi \leq 60^\circ$ are included.

The maximum isolation obtained with the circulator from fig. 4.10, $I \sim 50$, is somewhat unsatisfactory. According to the coupled-wave model from section 4.2, low maximum I may be caused by a suboptimal coupling level between the cavity and the waveguides. This level can be controlled by fine-tuning the positions of the holes in the neighbourhood of the cavity. We have found that by shifting the holes hatched vertically in fig. 4.10 by $d_h = -0.038a$ in the radial direction, the maximum isolation can be boosted to about 2600, as shown in fig. 4.12(b). The isolation I stays above 100 in a frequency band of width $B(100) = 0.00011 \times 2\pi c/a$, which corresponds to 81 GHz for the operation wavelength $\lambda = 1300$ nm. The level of power losses to radiative modes, $1 - P$, does not change appreciably with respect to the case from fig. 4.12(a). Figure 4.13 shows the map of the magnetic field excited by a point source placed close to the entrance of waveguide W_1 of the “optimised” circulator with $d_h = -0.038a$ at frequency $\omega = 0.3124 \times 2\pi c/a$, where maximum isolation is obtained. The standing-wave ratio in the input waveguide is very small, which reflects the good quality of the match between the waveguides and the cavity. Table 4.3 lists the positions and radii of the air holes making up the optimised circulator.

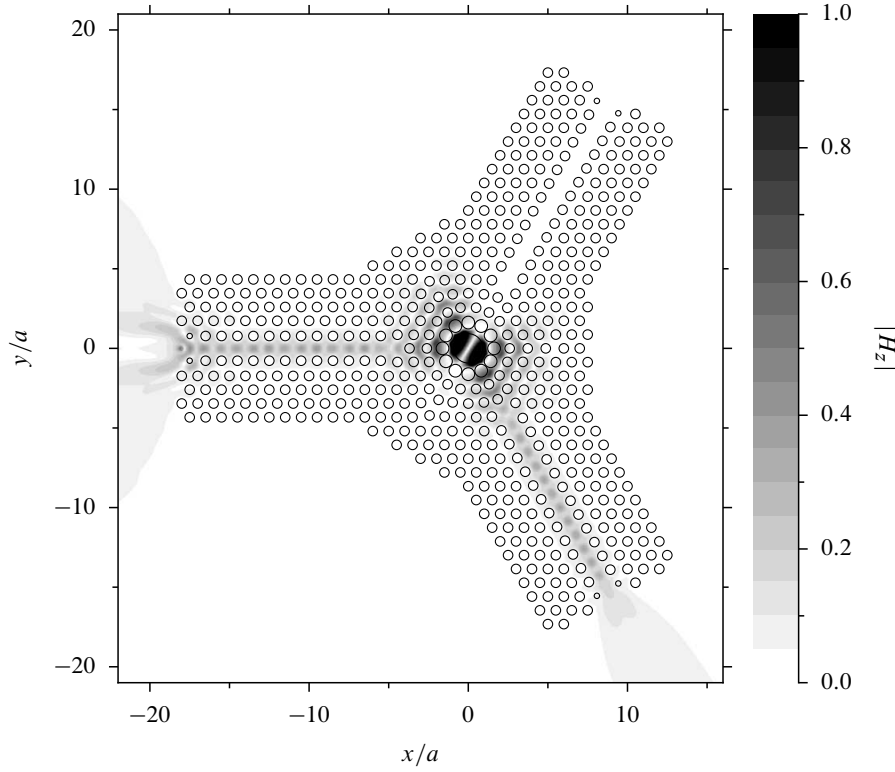


Figure 4.13 Magnitude of the magnetic field H_z in the circulator with $d_h = -0.038a$, excited by a point source of frequency $\omega = 0.3124 \times 2\pi c/a$.

4.5 Rib-waveguide-based circulators

4.5.1 Introduction

In section 4.4 we have shown how an axisymmetric cavity designed along the rules derived in section 4.3 can be adapted for embedding in a PC lattice and coupling with PC waveguides. One could well ask, however, whether the introduction of a periodic lattice is strictly necessary. At first sight, the answer is no. Having the form of a circular Bragg grating, the cavity is by itself well isolated from the surrounding medium (at least in-plane), so there is little to be gained by embedding it additionally in a PC exhibiting a band gap. The PC waveguides can also be straightforwardly replaced by rib waveguides with constant cross-section, whose operation is based on the index-guiding mechanism. To obtain a working circulator, however, one needs also to ensure the appropriate level of coupling between the localised cavity and waveguide modes and to minimise the power lost to free space during the energy transfer between these two families of modes. The latter objective is much easier to fulfil in a PC-based circulator, which operates in the band gap of the periodic lattice surrounding all the functional elements. Nevertheless, in this section we shall study a class of non-PC-based systems that allow to achieve the two goals mentioned above, at least to a certain degree.

The general geometry of the structured to be considered is shown in fig. 4.14. The depicted circulator consists of a resonant cavity, composed of n_f full and n_s split rings with inner and outer radii determined by the procedure described in section 4.3, and three identical waveguides of width d_{wg} . The distance from the centre of the cavity to the ends of the waveguides is ρ_{wg} , while the widths of the slits in the split rings are denoted by $d_{\phi n}$ with $n = n_f + 1, n_f + 2, \dots, n_f + n_s$. The rings and waveguides are made of a

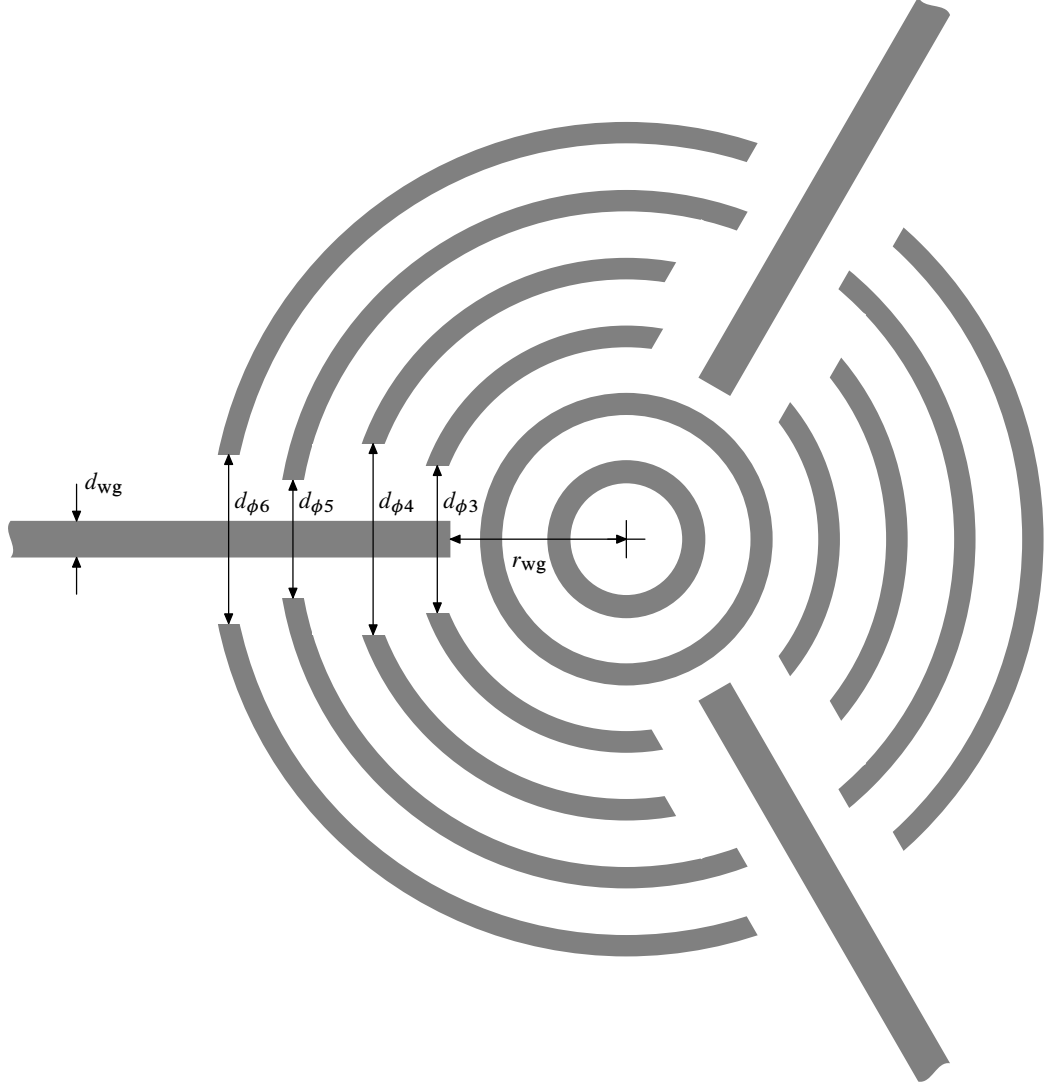


Figure 4.14 Geometry of an example rib-waveguide-based circulator with $n_f = 2$ full and $n_s = 4$ split rings.

MO material with permittivity

$$\hat{\epsilon}_h = \begin{bmatrix} \epsilon_h & ig & 0 \\ -ig & \epsilon_h & 0 \\ 0 & 0 & \epsilon_h \end{bmatrix} \quad (4.46)$$

and are embedded in an isotropic medium with permittivity ϵ_1 .

The level of coupling between the cavity and waveguide modes, and hence the circulator's performance, will of course depend on the values of all the geometrical parameters, which should therefore be optimised. The space spanned by them is rather large, and it is not possible to scan it exhaustively. Therefore our optimisation of the presented structure has been somewhat heuristic. We have chosen the material parameters as $\epsilon_h = (2.25)^2 = 5.0625$, $\epsilon_1 = 1$ and $g = 0.1$; the quoted value of ϵ_h corresponds approximately to the effective index of the fundamental s -polarised guided mode of a planar waveguide composed of a BIG layer of thickness 340 nm sandwiched between GGG and air. The waveguide width d_{wg} was fixed to 250 nm. The radii of the rings, listed in table 4.4, were determined with the procedure described in section 4.3 to ensure the existence of a pair of cavity modes with the azimuthal order $l = 1$ at the wavelength $\lambda = 1300$ nm.

Ring number	Inner radius (nm)	Outer radius (nm)
1	381	539
2	847	998
3	1309	1457
4	1772	1919
5	2236	2382
6	2700	2846
7	3165	3310

Table 4.4 Radii of the high-index rings of the cavity with $\epsilon_h = (2.25)^2 = 5.0625$ and $\epsilon_l = 1$ supporting a resonant mode with azimuthal order $l = 1$ at wavelength $\lambda = 1300$ nm.

With the chosen value of g , the relative frequency splitting of the cavity is $\Delta\omega/\omega_0 = 2gv = 0.00175$. From eq. (4.27), in the absence of losses the optimum value of γ/ω_0 is 0.00151, i.e., the quality factor $Q \equiv \omega_0/(2\gamma)$ describing the cavity-waveguide coupling should be $Q = 330$. The quality factors of the chosen cavity with 3 and 4 rings are 163 and 829, respectively. Therefore one can expect that the waveguides of an optimally designed circulator should end somewhere close to the third innermost ring—or possibly even inside it, since the coupling to waveguides is doubtlessly less efficient than to the whole surrounding free space.

The total number of rings necessary for ensuring a prescribed level of peak transmission T_{\min} could in principle be estimated from eq. (4.30): for instance, for $T_{\min} = 0.9$ the quality factor Q_1 describing radiation loss should be greater than 6430. This is already ensured by a cavity composed of 6 rings, whose quality factor reaches 21,140. However, the quality factors of cavities with split outer rings will necessarily be smaller than of those with full rings; therefore, a larger number of rings might be necessary to ensure a 90-percent efficiency. In our calculations, we restricted our attention to systems with at most 7 rings.

The results of the optimisation process will be reported on in subsection 4.5.3. In the meantime, we shall describe the numerical method used to analyse these systems and evaluate the accuracy of calculations.

4.5.2 Numerical calculations

The calculations of the transmission through the circulators studied in this section, and shown schematically in fig. 4.14, have been performed with the finite-element method (FEM) using the RF module of the COMSOL program. In contrast to the multiple-scattering method used to analyse PC-based circulators in ref. 148, FEM can easily handle structures composed of scatterers with complex (especially elongated) shapes. On the other hand, unlike that method, it requires a finite computational domain. Since the system shown in fig. 4.14 is, in principle, infinite, it must be truncated for the sake of FEM calculations.

Problems involving light scattering by finite objects are routinely handled with FEM by letting the computational domain consist of a finite region enclosing the objects in question and surrounded by a *perfectly matched layer* (PML) of finite thickness, which ideally behaves as a perfect non-reflecting absorber [53]. In our case, the situation is complicated by the presence of infinite waveguides; the scatterer to be modelled obviously cannot fit within any finite contour. To circumvent this problem, we construct the computational domain in the way shown in fig. 4.15. The region surrounded by the dashed line is a fragment of the physical system shown in fig. 4.14. The parts of its boundary lying “far” from the waveguide ends are covered with PMLs of thickness d_{PML} . We have used standard PMLs adapted

Circulator	n_f	n_s	ρ_{wg} (nm)	d_ϕ (nm)	ϕ_{cone} (°)
C1	3	3	1250	1570	—
C2	3	4	1240	1770	—
C3	3	4	1210	—	35.1

Table 4.5 Geometrical parameters of the circulators analysed in the text. The ring radii are listed in the first ($n_f + n_s$) rows of table 4.4.

for cylindrical coordinates, implemented in COMSOL by means of the coordinate transform*

$$\rho \mapsto \frac{\rho - \rho_{in}}{d_{PML}} s_{PML} (1 - i), \quad (4.47)$$

where ρ is the radial coordinate measured from the centre of the cavity, ρ_{in} denotes the radius of the inner PML boundary, and s_{PML} , called the *PML strength*, influences the field decay rate inside the PML [161, p. 44]. On the other hand, the electromagnetic fields on the segments P_n ($n = 1, 2, 3$) perpendicular to the waveguides are constrained to be a superposition of the incoming and outgoing guided modes of the corresponding waveguides, which are assumed to be single-mode. The profile of these modes is calculated analytically and normalised to unitary power, and the amplitude of the incoming mode is set to unity on P_1 and to zero on P_2 and P_3 . Physically, these constraints correspond to the assumption that all the radiative waveguide modes excited by the cavity decay before reaching the ports P_n . Mathematically, they reduce to Robin's boundary conditions and are implemented as COMSOL's *matched boundary conditions*. On the remaining part of the computational domain's boundary (solid line in fig. 4.15) perfect-electric-conductor boundary conditions are imposed. The domain is divided into triangular Lagrangian elements of order p . The mesh density is controlled by fixing the maximum allowed size of individual elements in each subdomain with constant permittivity ϵ to $h_{max}/\sqrt{\epsilon}$, where h_{max} is a constant. The mesh in areas with higher permittivity is made finer, since the fields in these regions are expected to vary faster.

In our calculations we are primarily interested in the isolation factor $I = T_2/T_3$, where T_2 and T_3 are the powers transmitted through ports P_2 and P_3 . We can see that the numerically calculated value of I of a given circulator at a fixed free-space wavelength λ depends on the following six parameters:

- maximum element size in air, h_{max} ,
- element order, p ,
- PML thickness, d_{PML} ,
- PML strength, s_{PML} ,
- length of the part of the waveguides extending past the outermost ring, d_{sep} ,
- port height, d_{port} .

To determine the values of these parameters sufficient for obtaining satisfactory accuracy, we have studied the influence of their variation on the isolation I of a particular circulator, denoted henceforth as C1, whose parameters are listed in the first row of table 4.5.

We tested first the dependence of I on h_{max} and p for fixed values of the remaining parameters. Figure 4.16(a) shows the values of I obtained for $p = 2$ and five different values of h_{max} , whereas fig. 4.16(b) presents the dependence of I on the element order p with h_{max} fixed to 500 nm. We see that the convergence with increasing p is much faster than with decreasing h_{max} . Therefore in future calculations we have taken $h_{max} = 500$ nm and $p = 5$.

* In COMSOL simulations the $e^{i\omega t}$ convention for time-harmonic dependence is used, opposite to that employed here.

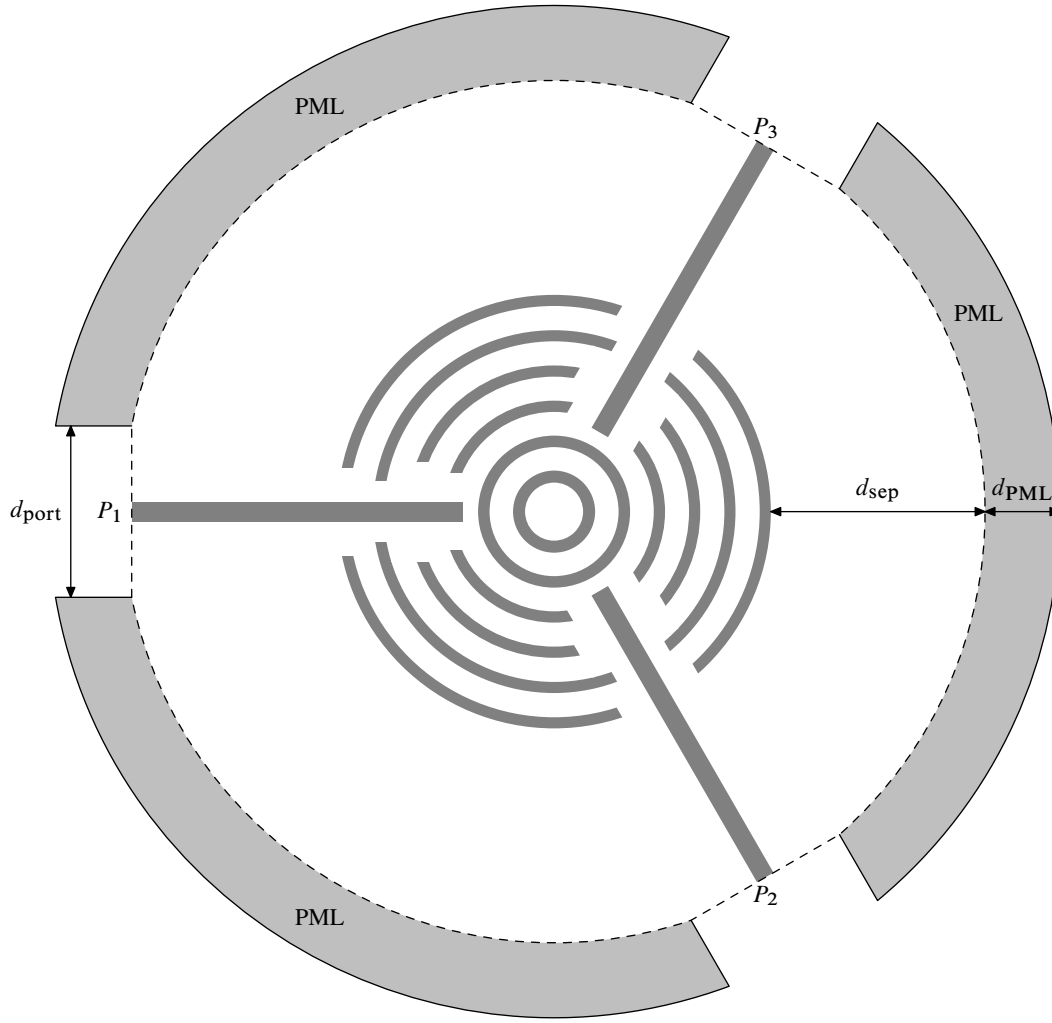


Figure 4.15 Geometry of the domain used in FEM calculations.

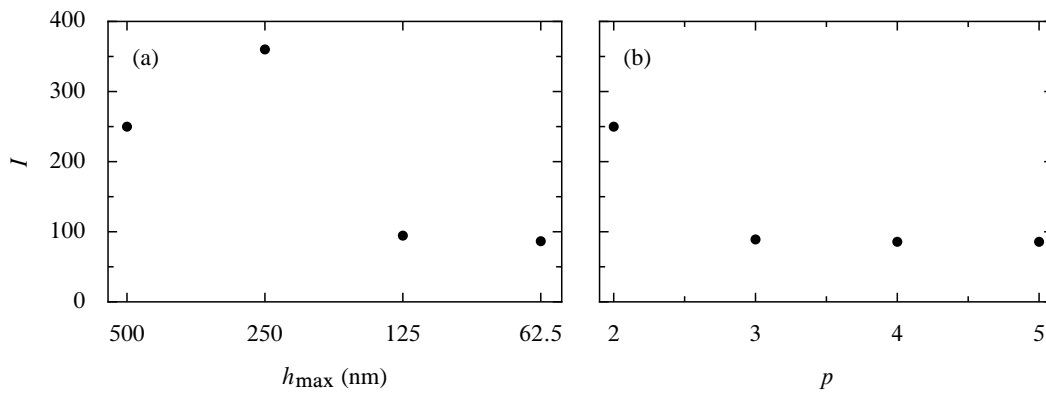


Figure 4.16 Influence of the finite-element expansion parameters, h_{\max} and p , on the calculated value of the isolation I of circulator C1. The parameters related to the truncation of the computational domain are fixed to $d_{\text{sep}} = 5000$ nm, $d_{\text{PML}} = 600$ nm, $s_{\text{PML}} = \lambda$ and $d_{\text{port}} = 2250$ nm. The wavelength $\lambda = 1299.5$ nm was chosen to lie in the proximity of the maximum of $I(\lambda)$, but not exactly at it. **(a)** Convergence of I with decreasing maximum element size in air, h_{\max} , at fixed element order $p = 2$. **(b)** Convergence of I with increasing element order p at fixed $h_{\max} = 500$ nm.

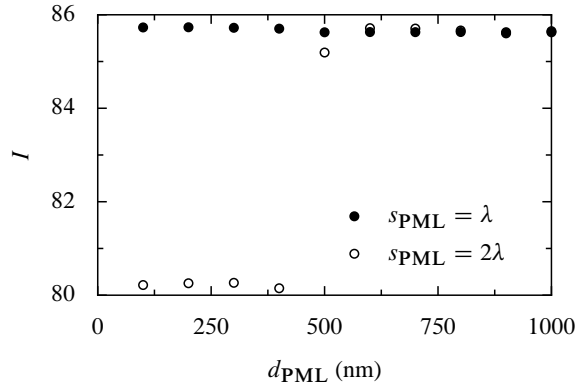


Figure 4.17 Convergence of the isolation I of circulator C1 with increasing PML thickness d_{PML} . Two PML strengths, $s_{\text{PML}} = \lambda$ and 2λ , are considered; the wavelength $\lambda = 1299.5$ nm. The other parameters are fixed as $h_{\text{max}} = 500$ nm, $p = 5$, $d_{\text{sep}} = 5000$ nm and $d_{\text{port}} = 2250$ nm.

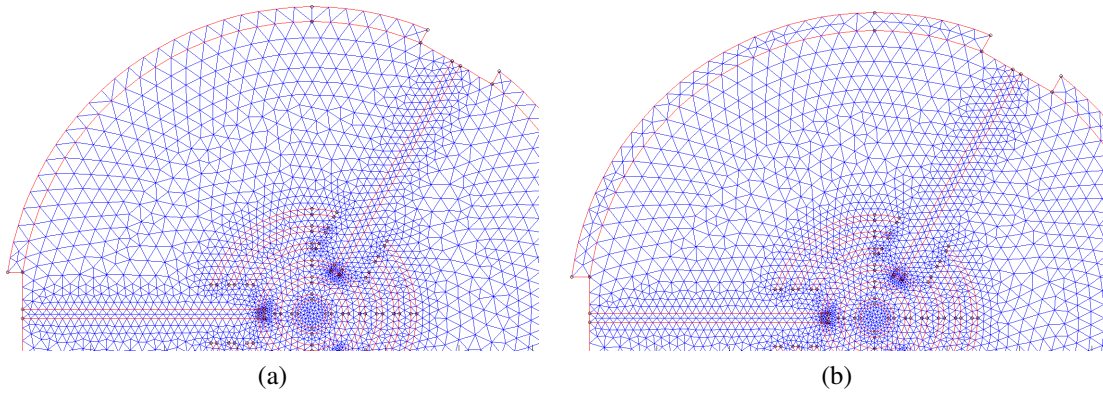


Figure 4.18 Change of the mesh structure in the PML with d_{PML} increasing from **(a)** 400 nm to **(b)** 500 nm. Note that in the former case the mesh of the PML consists of two interleaving rows of triangles, whereas in the latter case the number of rows increases to four.

We proceeded to the study of the influence of the PML parameters, d_{PML} and s_{PML} . Figure 4.17 shows the dependence of I on the PML thickness for two different PML strengths, $s_{\text{PML}} = \lambda$ and 2λ . It can be seen that the values obtained with $s_{\text{PML}} = \lambda$ (which is COMSOL's default) are very stable with respect to d_{PML} : the difference between the maximum and minimum value of I does not exceed 0.15%. On the other hand, the $I(d_{\text{PML}})$ curve corresponding to $s_{\text{PML}} = 2\lambda$ has a noticeable jump between $d_{\text{PML}} = 400$ and 500 nm. This jump is due to a change in the mesh structure: as illustrated in fig. 4.18, for $d_{\text{PML}} = 400$ nm the mesh in the PML region consists of two rows of triangles, while for $d_{\text{PML}} = 500$ nm two more rows appear. For $d_{\text{PML}} \geq 600$ nm the isolation factor obtained with both PML strengths are very similar; moreover, the subsequent appearance of another pair of rows, occurring between $d_{\text{PML}} = 800$ and 900 nm, does not have any discernible effect on the $I(d_{\text{PML}})$ curves. All in all, the detailed choice of the PML parameters does not seem very important for the accuracy of the calculations. Therefore, we continue to take $d_{\text{PML}} = 600$ nm and $s_{\text{PML}} = \lambda$.

We studied next the sensitivity of I to d_{sep} . The $I(d_{\text{sep}})$ curves shown in fig. 4.19, corresponding to two different wavelengths, exhibit irregular oscillations of amplitude roughly equal to 3% of the mean value. We interpret them as stemming mainly from the interference of the fundamental waveguide mode with slowly decaying radiative modes excited by the cavity. Another culprit might be the mesh modifications induced by changes of the location of the domain's boundary. Elimination of these oscillations would be difficult without considerable enlargement of the computational domain, which would neces-

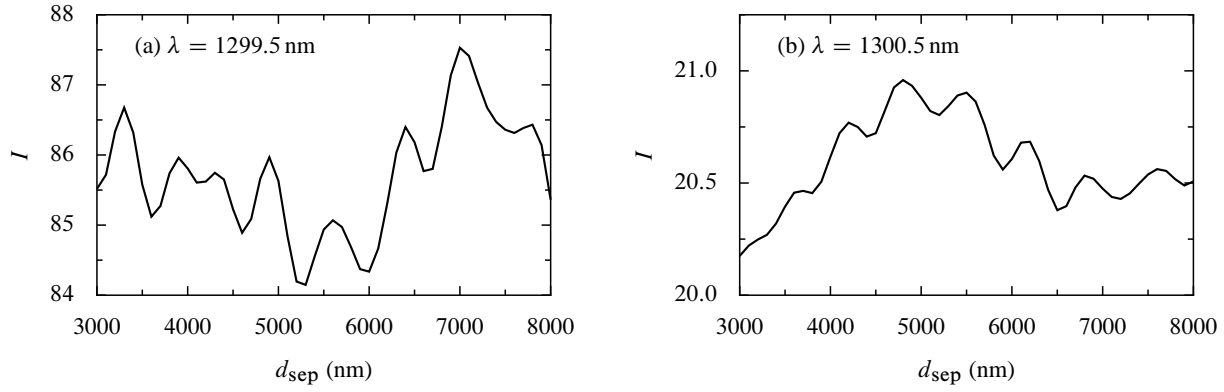


Figure 4.19 Dependence of the isolation I of circulator C1 on the value of d_{sep} for two different wavelengths λ located in the neighbourhood of a maximum of $I(\lambda)$. The other parameters are fixed as $h_{\text{max}} = 500$ nm, $p = 5$, $d_{\text{PML}} = 600$ nm, $s_{\text{PML}} = \lambda$ and $d_{\text{port}} = 2250$ nm.

sarily lead to a drastic increase of the time of calculations. Therefore, we decide to leave unchanged the value $d_{\text{sep}} = 5000$ nm taken previously.

The choice of d_{port} is definitely the most difficult. In principle, the value of $d_{\text{port}}/2$ should correspond to the distance from the waveguide axis at which the magnitude of the field of the guided mode becomes comparable to that of the radiative modes excited by the cavity. Unfortunately, it is not easy to determine this distance *a priori*. The value $d_{\text{port}} = 2250$ nm taken so far corresponds to the width of a port at whose ends the magnetic field of the waveguide mode with $\lambda = 1300$ nm decays to $\sim 1\%$ of its maximum value.

Figure 4.20 shows the dependence of I on d_{port} at four different wavelengths. For ease of comparison, the plots have been normalised to the values of I obtained for $d_{\text{port}} = 3000$ nm. The curves have several interesting features. First, the isolation factor varies very rapidly for small values of d_{port} . This is not surprising: for such small port lengths, the incident field is not represented accurately, since the profile of the waveguide mode is severely truncated in the direction perpendicular to the waveguide axis. Second, for large port lengths we observe a steady, seemingly linear decay of I . In fact, a look on the plots of the field excited on these long ports reveals that in the port regions lying far from the waveguide axis the field shape does not resemble that of the guided mode any more; this effect is especially pronounced in the isolated waveguide W_3 . This indicates that the optimum port length might be close to the value of d_{port} at which the linear decay emerges; however, this value varies with the wavelength. Third, the dependence of I on d_{port} is visibly strongest at $\lambda = 1300.0$ nm, which is the wavelength closest to the peak of $I(\lambda)$. This indicates that the maximum value of $I(\lambda)$ observed for a given circulator might be strongly influenced by the choice of d_{port} . Unfortunately, this proves to be the case: the maximum isolation factors of circulator C1 obtained for $d_{\text{port}} = 1700$, 2000 and 2250 nm are 2130 , 3560 and 6140 , respectively. The extreme values differ, then, by nearly a factor of three. On a more positive note, the bandwidth $B(I_{\text{min}})$, a quantity much more important from the experimental point of view, turns out to be significantly less sensitive to the choice of port length, as long as I_{min} is not too large. For instance, the range of wavelengths in which C1 provides an isolation factor better than 100 has width 0.610 , 0.615 and 0.618 nm according to simulations performed with the three values of d_{port} quoted previously. We conclude that while the maximum isolation factors calculated with the present technique do not have absolute significance, and can at most be used for the purposes of comparison between different structures, the bandwidths are robust against changes of the domain truncation parameters. Lacking reliable guidelines on the selection of the optimum port length, we stick to the value chosen previously, i.e., $d_{\text{port}} = 2250$ nm.

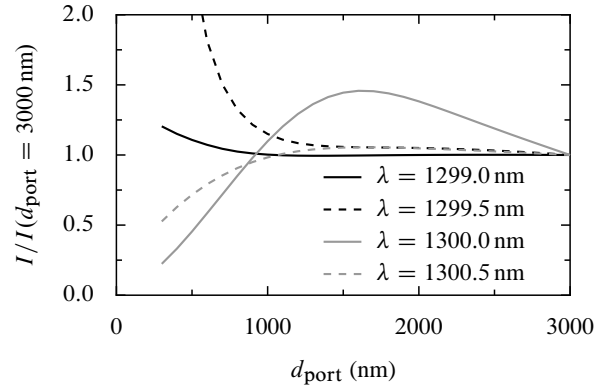


Figure 4.20 Dependence of the isolation I of circulator C1 on the value of d_{port} for four different wavelengths λ located in the neighbourhood of a maximum of $I(\lambda)$. The other parameters are fixed as $h_{\text{max}} = 500$ nm, $p = 5$, $d_{\text{PML}} = 600$ nm, $s_{\text{PML}} = \lambda$ and $d_{\text{sep}} = 5000$ nm.

It is worth noting that some authors [137, 162] have proposed a different method of handling infinite waveguides in FEM calculations. In their approach, PMLs surround the whole computational domain, including the waveguide outlets, and the incident waveguide mode is introduced into the system by imposing special boundary conditions on a cross-section of the input waveguide lying *inside* the domain. As an alternative, one could also divide the system under study in two parts: one comprising the input waveguide, and the other, the cavity with the output waveguides. In the latter, the finite-element expansion would continue to stand for the total electromagnetic field. In the former, however, the expansion would represent only the *scattered* field, i.e., the total field minus the incident waveguide mode. The latter could be introduced into the system by means of appropriate boundary conditions imposed on the junction of the two subdomains. The combined structure could then be completely surrounded in PMLs, as shown in fig. 4.21.

We have not tested any of these solutions, mostly owing to time constraints. However, they could be implemented in future if the accuracy limits of the approach followed so far become a serious issue.

4.5.3 Geometry optimisation

Having fixed most of the geometrical parameters of the circulator in the way described at the end of subsection 4.5.1, we were essentially left with the problem of optimising the values of $d_{\phi n}$ and ρ_{wg} . For the sake of simplicity, we initially focused on structures with $d_{\phi n}$ independent from n , i.e., with waveguides enclosed in rectangular “slits” of width d_{ϕ} . The bandwidth proved a rather cumbersome objective function, since it is nonzero only for structures already rather close to optimum. Therefore, the reservations from subsection 4.5.2 notwithstanding, we chose the maximum isolation factor as the objective function, hoping that circulators with large values of this parameter would also be characterised by a large bandwidth.

Figure 4.22(a) shows the geometry of the best structure that we have found, called C2 in the following. It has 3 full and 4 split rings. The slit width $d_{\phi} = 1770$ nm and the waveguide ends are located at $\rho_{\text{wg}} = 1240$ nm from the cavity centre, so that the waveguides cross the outermost full ring. For ease of reference, the values of all the geometrical parameters of C2 are listed in table 4.5. This circulator offers maximum isolation of 3590, and the wavelength dependences of T_2 , T_3 and I are shown in fig. 4.22(b). Clearly, the curves are fairly symmetric with respect to the central wavelength $\lambda = 1300.0$ nm, which indicates that the direct coupling between waveguides is insignificant. Figure 4.22(c) shows the map of the magnetic field at $\lambda = 1300.0$ nm. At this wavelength, 88% of the input power is transmitted

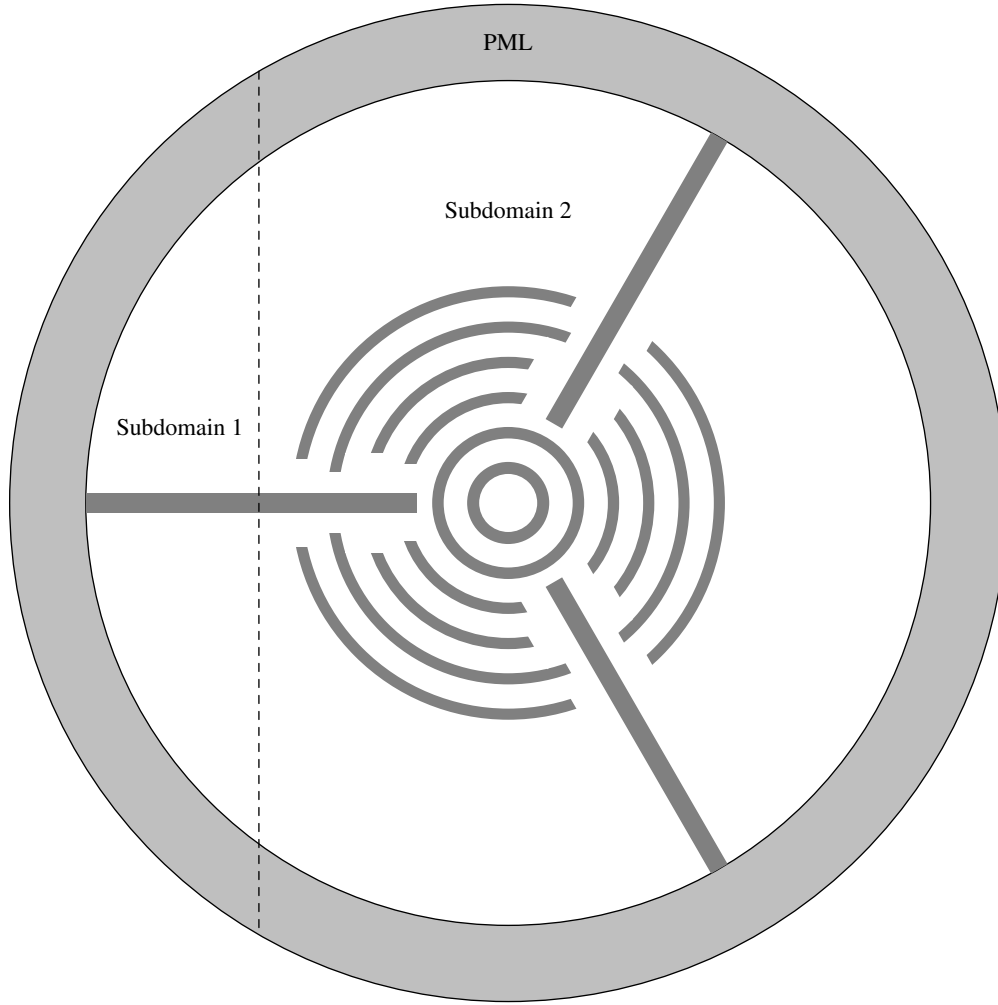


Figure 4.21 Alternative technique of domain truncation. In subdomain 1, the electromagnetic field is represented by the sum of the field of the incident waveguide mode (assumed known) and the scattered field expanded on a finite-element basis. In subdomain 2, the finite-element basis is used to expand the total field. Electromagnetic continuity conditions are imposed on the interface separating the two subdomains (dashed line).

to waveguide 2; the rest is not reflected, but mainly lost to the surrounding free space. Far from the peak, the amount of these losses can exceed 50%. This behaviour contrasts with that of the PC circulator, where almost 100% of the input power remains in the waveguide system due to the quasi-perfect isolation provided by the surrounding periodic lattice. The 20-dB bandwidth $B(100)$ of circulator C2 is 0.729 nm.

The grey curves in fig. 4.22(b) show the transmittance curves of circulator C2 as predicted by the coupled-wave model with radiation losses taken into account, presented in subsection 4.2.2. The values of the parameters ω_0 , $\Delta\omega$, γ and γ_1 were found by fitting the expressions for T_2 and T_3 obtained from eqs. (4.26) to the values calculated numerically. The Levenberg-Marquardt algorithm was used as the fitting procedure. The best fit was obtained for parameters corresponding to $\lambda_0 \equiv 2\pi c/\omega_0 = 1299.9$ nm, $\Delta\lambda \equiv 2\pi c\Delta\omega/\omega_0^2 = 2.3$ nm, $Q \equiv \omega_0/(2\gamma) = 370$ and $Q_1 \equiv \omega_0/(2\gamma_1) = 5730$. Clearly, there is a good match between the theoretical and numerical curves; its quality would probably be further improved by taking into account the direct coupling between waveguides, which causes the slight asymmetry of the numerical plots. The quality factor related to losses, Q_1 , is significantly lower than that of an isolated cavity with 7 full rings, which is as large as 107,000. This is obviously due to the presence of slits. On

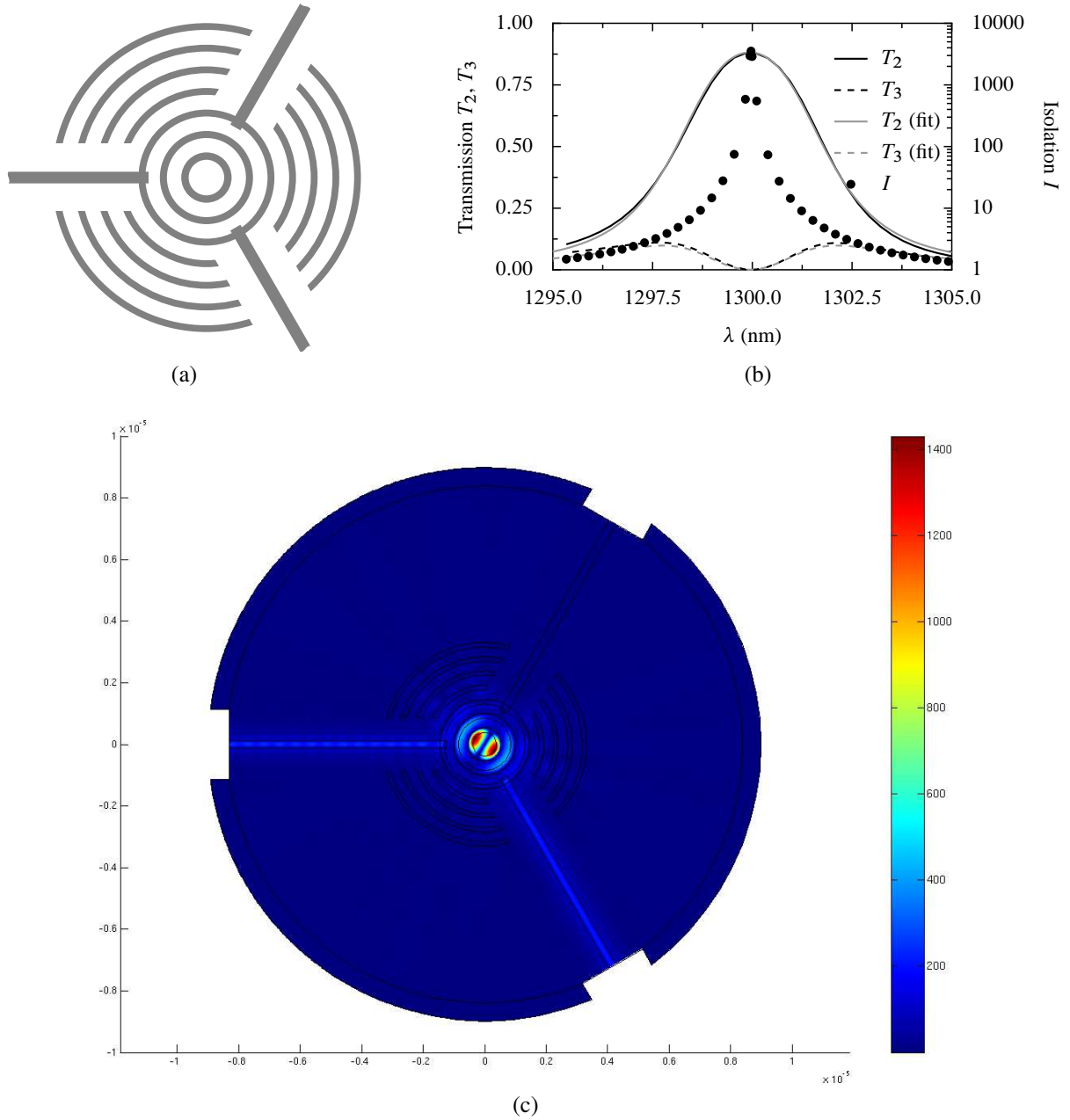


Figure 4.22 (a) Geometry of circulator C2. (b) Wavelength dependence of the transmission (left axis) and isolation (right axis) of this circulator. (c) Magnitude of the magnetic field in the circulator at the wavelength $\lambda = 1300.0$ nm, corresponding to the maximum isolation. The waveguide mode is incident from the left.

the other hand, the position of the ends of the waveguides (just inside the third innermost ring) is in good accord with the predictions made at the end of subsection 4.5.1.

We have found this device fairly tolerant to variations of the slit width d_ϕ ; figs. 4.23(a)–(b) show the plot of the maximum isolation and bandwidth of C2 when this parameter is varied. It can be seen that the bandwidth stays above 0.5 nm in a 300-nm-wide range of d_ϕ . The constraints on ρ_{wg} are more stringent: as shown in fig. 4.23(c), the corresponding range of ρ_{wg} is only about 40 nm wide.

The performance of this structure changes rather abruptly when the number of rings is modified. For instance, if the seventh ring is removed, the maximum isolation decreases to only 140 and the bandwidth to 0.386 nm. However, it is possible to improve these figures by readjusting the slit widths and the

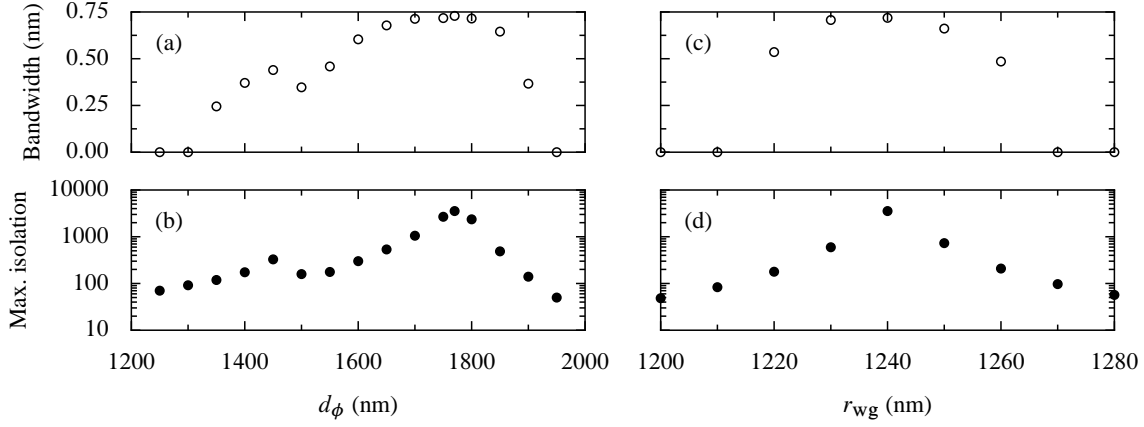


Figure 4.23 Tolerance of the maximum isolation I_{\max} and the bandwidth $B(100)$ of circulator C2 to perturbations of the parameters (a)–(b) d_ϕ and (c)–(d) ρ_{wg} .

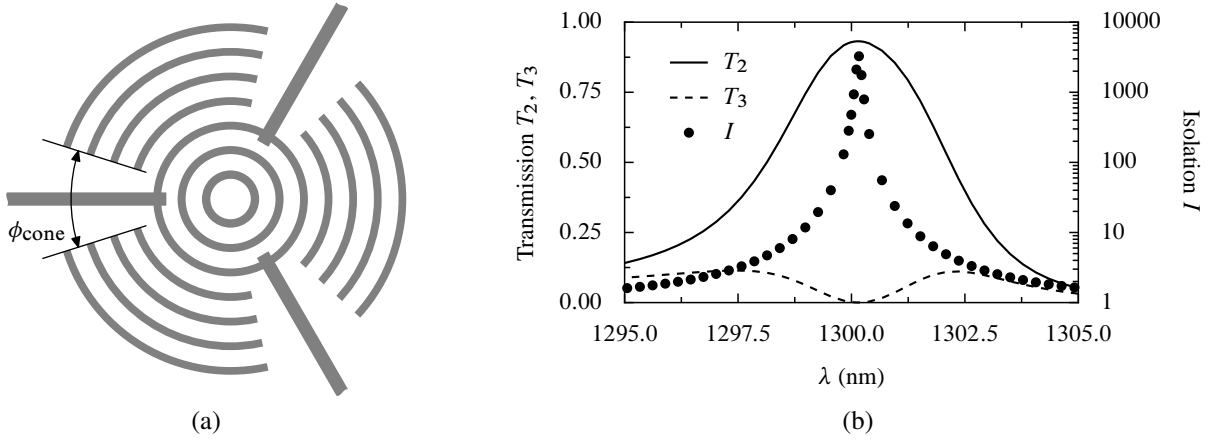


Figure 4.24 (a) Geometry of a circulator with conical slits surrounding the waveguides. The values of the various parameters have been chosen to match those of circulator C3. (b) Wavelength dependence of the transmission (left axis) and isolation (right axis) of this circulator.

position of the waveguide ends: for $\rho_{wg} = 1250$ nm and $d_\phi = 1570$ nm (10% less than in the 7-ring case) I_{\max} reaches 2140 and the bandwidth 0.603 nm.

It is interesting to note that both for 6 and 7 rings the optimum angular length of the removed sectors of the outermost ring is almost the same: $\sim 34^\circ$. This led us to test the performance of a second class of structures, in which the outer rings are truncated along radial lines instead of ones parallel to the waveguides, so that the latter are enclosed by conical rather than rectangular air slits, as illustrated in fig. 4.24(a). We found the optimum cone aperture ϕ_{cone} to be 35.1° , which is close to the value obtained in the simulations of the first class of structures (with $d_{\phi n}$ independent from n). The optimum position of the waveguide end, $\rho_{wg} = 1210$ nm, is also only slightly different from the original one. More importantly, the maximum isolation and bandwidth decrease much less (from 3300 to 700 and from 0.770 to 0.708 nm, respectively) when the seventh ring is removed. This relative insensitivity to the details of the geometrical structure of the exterior region of the device is the behaviour that one would intuitively expect from a well-designed circulator; therefore, structures with conical slits seem closer to the ideal than those with rectangular ones. Figure 4.24(b) shows the wavelength dependence of T_2 , T_3 and I of the optimum 7-ring circulator with conical slits, referred to as C3. Its parameters are listed in table 4.5.

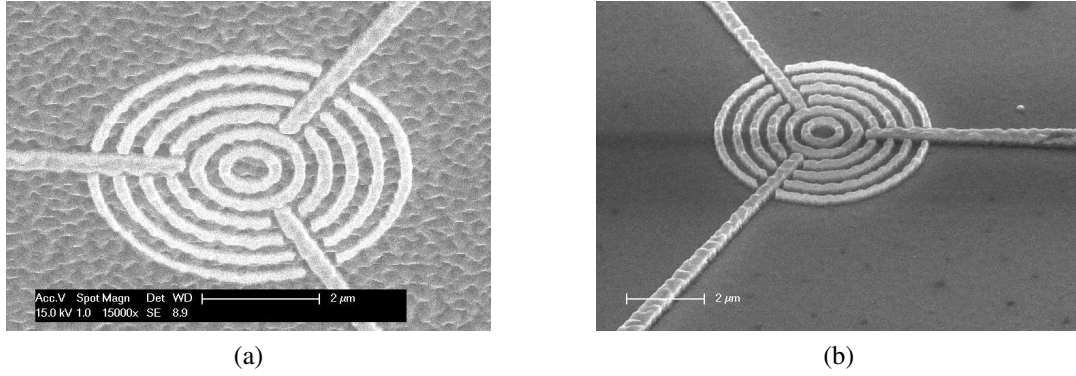


Figure 4.25 Microphotographs of a rib-waveguide-based circulator etched in a BIG layer grown on a GGG substrate (courtesy of L. Magdenko and B. Dagens, Institut d'Électronique Fondamentale, Orsay, France). **(a)** Tungsten mask before etching. **(b)** Complete circulator after etching.

4.5.4 Fabrication

Our collaborators from Institut d'Électronique Fondamentale (Orsay, France) have developed a technique of fabricating magnetophotonic structures in BIG thin films [163]. The films used in experiments, supplied by the GEMAC team from Versailles, France, were grown on GGG substrates by pulse layer deposition. The circulators were fabricated by inductively coupled plasma ion etching the BIG layer in a mixture of boron trichloride and argon, with a nanostructured tungsten layer used as a mask. An example circulator fabricated in this way is shown in fig. 4.25.

To evaluate the optical properties of the manufactured structures, a series of measurements of the power transmitted to the two output waveguides was made. The transmittances to the two output branches were found not to be completely equal. However, reversal of the polarisation of the applied SEMF brought no discernible change of the transmission levels. Apparently, then, the observed difference between T_2 and T_3 was due to fabrication imperfections rather than to nonreciprocal effects.

4.6 Simulations of three-dimensional axisymmetric cavities

4.6.1 Evaluation of possible three-dimensional geometries

Motivation We strongly suspected that the incorrect operation of the fabricated circulators was due to the fact that their design had been based solely on two-dimensional simulations. While we had attempted to take the three-dimensional (3D) nature of the true physical system into account by using the effective-index model to find the material properties of the high- and low-index regions of the simulated structures, this was evidently not enough. Indeed, the effective-index description is known to give erroneous results for high-contrast systems, such as those considered in this chapter [164]. In any case, its accuracy can only be evaluated by comparing its predictions with results of rigorous 3D calculations.

Owing to the time requirements of full-blown 3D simulations, which would be necessary to analyse complete circulators consisting of a cavity coupled to waveguides, we decided to implement first a method allowing to calculate the eigenmodes of axisymmetric 3D cavities. In this case it is possible to profit from the knowledge of the azimuthal dependence of the eigenmodes to restrict the computational mesh to a single meridional (ρz) plane of the cavity. Our calculations were made with the finite-element method, described in detail in section 5.3.

High-contrast cavities We began by considering the simplest type of structures, in which the rings are etched in a layer of BIG with thickness d_{BIG} , sandwiched between a GGG substrate and air, as shown

in fig. 4.26(a). We set $d_{\text{BIG}} = 340 \text{ nm}$ and took the refractive indices of BIG and GGG to be $n_{\text{BIG}} = 2.51$ and $n_{\text{GGG}} = 1.97$. The effective index of the unetched areas was calculated to be 2.25, while that of the etched rings was set to the index of air, $n_{\text{air}} = 1$. The radii of the rings were determined with the procedure described in section 4.3, with the target wavelength $\lambda = 1300 \text{ nm}$. For future reference, we shall denote this just described geometry with the symbol G1.

Very soon it became apparent that cavities of type G1 behaved very badly in 3D. In fact, they do not seem to support any well-localised modes near the design wavelength $\lambda = 1300 \text{ nm}$. This turns out to be easily explicable: sufficiently far from the cavity centre, a circular Bragg grating can be well approximated by a linear grating with period $d = \frac{1}{4}\lambda(n_0^{-1} + n_1^{-1})$, where n_0 and n_1 denote the refractive indices of etched and unetched areas. If d is larger than $\lambda/(2n_{\text{GGG}})$, all Bloch eigenmodes of the grating will leak into the GGG substrate [165, p. 203]. Unfortunately, this is the case with G1-type structures: $d = 469 \text{ nm} > \lambda/(2n_{\text{GGG}}) = 330 \text{ nm}$.

Low-contrast cavities In view of the failure of the effective-index description of structures of type G1, we have studied a handful of geometries liable to be approximated better by the effective-index model. They were proposed by L. Magdenko and B. Dagens (Institut d'Electronique Fondamentale, Orsay, France).

The first structure that was considered is shown in fig. 4.26(b). In this case, the BIG layer is left unetched, and the necessary effective-index contrast between successive rings is introduced by etching an additional high-index layer deposited on top of BIG. This geometry has distinct theoretical and experimental advantages. First, owing to the continuity of the BIG layer, it supports everywhere a locally guided mode. This lets us avoid the problem that the effective index, defined with the help of the propagation constant of the fundamental guided mode of a given region, is in fact undetermined for regions where *no guided modes exist*. Conventionally, these areas are attributed the index of the sub- or superstrate but, as noted by Hammer and Ivanova [164], this choice is not based on any rigorous arguments. In the case of the geometry from fig. 4.26(b), the effective index is well-defined everywhere and one can hope that this will improve the accuracy of the effective-index description.

From the experimental point of view, the structure in question has the advantage that it does away with the necessity of etching the BIG layer. This process, while already successfully demonstrated [163], remains less well developed than the nanostructuring of materials such as silicon or indium phosphide. On the other hand, the presence of a MO material both in the high- and low-index rings will necessarily diminish the SEMF-induced mode coupling strength, owing to the cancellation effect described in ref. 148. A possible solution consists in depriving the uncovered areas of BIG of their MO properties, which can be experimentally achieved by ion implantation.

The structure shown in fig. 4.26(b) is characterised by the refractive index n_{spl} of the supplementary layer, its thickness d_{spl} , and the thickness of the BIG layer, d_{BIG} . We have taken $n_{\text{spl}} = 3.50$, corresponding to the index of amorphous silicon around the wavelength $\lambda = 1300 \text{ nm}$. The choice of d_{spl} and d_{BIG} was motivated by two competing goals. On one hand, the supplementary layer had to be sufficiently thick to provide an appreciable contrast of the effective index of the etched and unetched areas. On the other hand, d_{spl} could not be chosen too large for fear of generating a second *s*-polarised guided mode in the unetched region and of displacing too large a fraction of the guided mode's energy away from the BIG layer, which would diminish the MO properties of the system. As a compromise, the two thicknesses were taken as $d_{\text{spl}} = 80 \text{ nm}$ and $d_{\text{BIG}} = 280 \text{ nm}$. The effective indices of the etched and unetched regions were then calculated as 2.19 and 2.50, and the fraction of energy of the guided mode of the unetched region contained in BIG was found to be 0.48. For convenience, the just described geometry will henceforth be referred to as G2.

In another type of structures, shown in fig. 4.26(c), the etched BIG layer of thickness d_{BIG} is covered

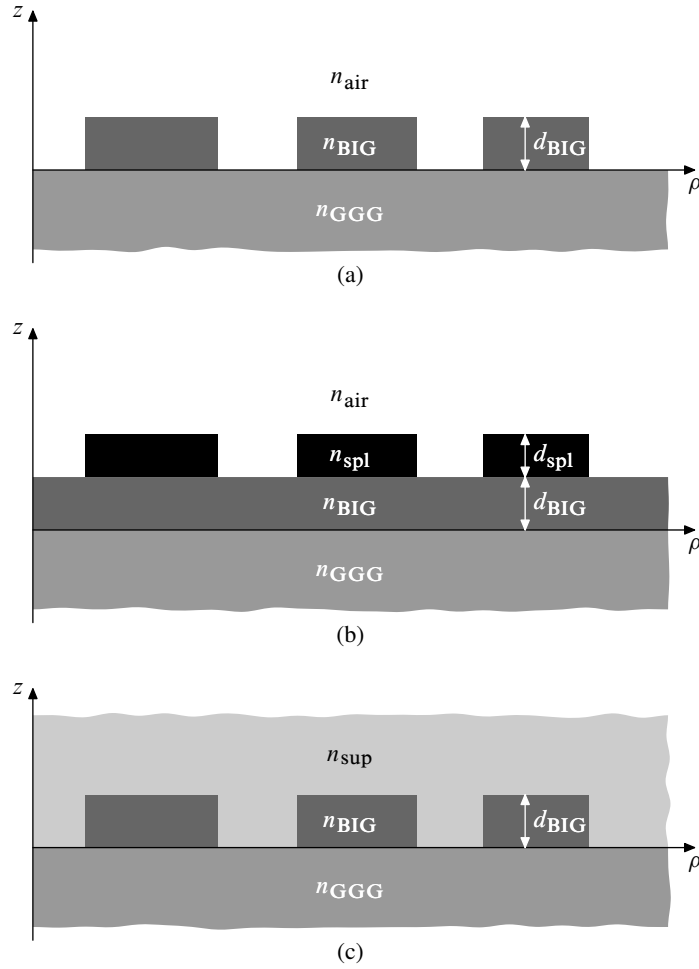


Figure 4.26 Schematics of 3D structures of types **(a)** G1, **(b)** G2, and **(c)** G3 and G4 (which differ only with the value of n_{sup}).

with a solid superstrate with refractive index n_{sup} close to that of GGG. In this way, the index contrast between the etched and unetched areas is lessened and one can expect the effective-index approximation to be more accurate. We considered mainly systems with $n_{\text{sup}} = 1.97$ (exactly equal to the refractive index of GGG) or $n_{\text{sup}} = 1.90$ (refractive index of silicon nitride) and chose d_{BIG} to be 330 nm. Structures with these parameters will be called G3 and G4 in the following. The effective indices of their unetched regions were calculated to be 2.275 and 2.282, respectively, whereas those of the etched areas were set to $\min(n_{\text{GGG}}, n_{\text{sup}})$, i.e., 1.97 and 1.90.

Table 4.6 summarises the results obtained for a handful of structures. Three cavities, designed for azimuthal orders $l = 1, 4$ and 10, were tested for each of the geometry types G2, G3 and G4. In addition, for cavities of type G2 two distributions of the MO coefficient g were investigated. In one series of simulations, the whole BIG layer was assumed to be uniformly magnetised, so that g was taken to be 0.1 throughout that layer. In the other, the areas of BIG not covered with silicon were assumed to be deprived of their MO properties and, consequently, attributed $g = 0$. For ease of reference, these two variants of geometry G2 will be called G2(a) and G2(b).

The magnitude the relative frequency splitting $\Delta\omega/\omega_0$ obtained in 3D simulations does not differ drastically from that predicted by 2D ones. The observed deviation is easily explicable by the fact that not the whole vertical profile of the unetched areas has MO properties. Anyway, the coupling strength of the eigenmodes of most of the cavities listed in table 4.6 exceeds that of the 2D high-contrast cavity

Type	l	λ_+	λ_-	$\Delta\omega/\omega_0$ (3D)	$\Delta\omega/\omega_0$ (2D)	Q_+	Q_-	Q_{avg}
G2(a)	1	$1.27779 + 0.00618i$	$1.27833 + 0.00617i$	-0.00042	—	103	104	103
	4	$1.27546 + 0.00607i$	$1.27633 + 0.00611i$	-0.00068	—	105	104	105
	10	$1.27564 + 0.00582i$	$1.27666 + 0.00588i$	-0.00080	—	110	109	109
G2(b)	1	$1.27892 + 0.00616i$	$1.27727 + 0.00618i$	0.00129	0.00166	104	103	104
	4	$1.27722 + 0.00603i$	$1.27466 + 0.00615i$	0.00200	0.00286	106	104	105
	10	$1.27764 + 0.00570i$	$1.27475 + 0.00600i$	0.00227	0.00342	112	106	109
G3	1	$1.28103 + 0.00461i$	$1.27926 + 0.00498i$	0.00138	0.00224	139	128	134
	4	$1.28102 + 0.00355i$	$1.27829 + 0.00391i$	0.00213	0.00356	180	164	172
	10	$1.28032 + 0.00179i$	$1.27724 + 0.00206i$	0.00241	0.00408	357	310	334
G4	1	$1.28550 + 0.00722i$	$1.28366 + 0.00773i$	0.00143	0.00207	89	83	86
	4	$1.28675 + 0.00606i$	$1.28403 + 0.00662i$	0.00212	0.00348	106	97	102
	10	$1.28710 + 0.00401i$	$1.28415 + 0.00454i$	0.00229	0.00411	160	141	151

Table 4.6 Results of 3D calculations of the eigenmodes of cavities with geometries G2(a), G2(b), G3 and G4. The symbols λ_- and λ_+ denote the wavelengths of the modes with azimuthal order l and $-l$. In addition to the relative frequency splitting $\Delta\omega/\omega_0$ of the modes of the 3D cavities, calculated as $(\text{Re } \lambda_+ - \text{Re } \lambda_-)/[(\text{Re } \lambda_+ + \text{Re } \lambda_-)/2]$, the values obtained for the corresponding infinite 2D cavities are also given; they are calculated as in section 4.3. The symbols $Q_{\pm} = (\text{Re } \lambda_{\pm})/(2 \text{Im } \lambda_{\pm})$ stand for the quality factors of the modes with order l and $-l$. Finally, Q_{avg} is defined as $(Q_+ + Q_-)/2$.

presented at the end of section 4.3. This can be attributed to the decrease of the effective-index contrast between etched and unetched areas, and is in accord with the observation from ref. 148 that the reduced coupling strength of a 2D high-contrast cavity can be augmented three times by making its core of demagnetised BIG instead of air.

As opposed to the values of $\Delta\omega/\omega_0$, well preserved in the 2D-to-3D transition, the quality factors of the 3D cavities are on average ten times smaller than the quality factors obtained with 2D calculations (related only to the in-plane confinement). The geometry that fares best, G3, provides barely $Q = 334$. In addition, even the small deviation from symmetry induced by changing the superstrate's refractive index from 1.97 to 1.90 decreases the quality factor by about 50%.

Figures 4.27, 4.28 and 4.29 show the maps of the z components of the magnetic field and the cross product $\vec{E}_e^* \times \vec{E}_o$ of the electric fields of the even and odd eigenmodes of the G2-, G3- and G4-type cavities designed for the azimuthal order $l = 10$, in the absence of SEMF. Comparison of figs. 4.28(a) and 4.29(a) gives testimony to the substantial increase of out-of-plane radiation losses in the cavity of type G4 with respect to that of type G3: the field in the asymmetric cavity features a prominent beam directed into the substrate, which is absent from that of the symmetric cavity's eigenmode. The field in the G2-type cavity from fig. 4.27 is well localised in the vertical direction, and the low quality factor of this mode seems to stem from the excitation of the fundamental p -polarised mode of the highly asymmetric GGG-BIG-air multilayer, as evidenced by the relatively large amplitude of the E_z field component on the plot from fig. 4.27(b).

Both $\Delta\omega/\omega_0$ and Q typically increase with l (the exception is the geometry G2, for which little change of Q is observed). This effect is further illustrated in fig. 4.30(a), which shows the l -dependence of $\Delta\omega/\omega_0$ and Q of circulators of type G3. Figure 4.30(b), in turn, presents the dependence of these parameters on the number of high-index rings, N , with l fixed to 10. It can be seen that $\Delta\omega/\omega_0$ and Q reach their asymptotic values around $N = 25$.

To sum up, the results listed in table 4.6 attest that the SEMF-induced coupling strength of the eigenmodes of structures G2, G3 and G4 is sufficient to cause a substantial frequency splitting; even in

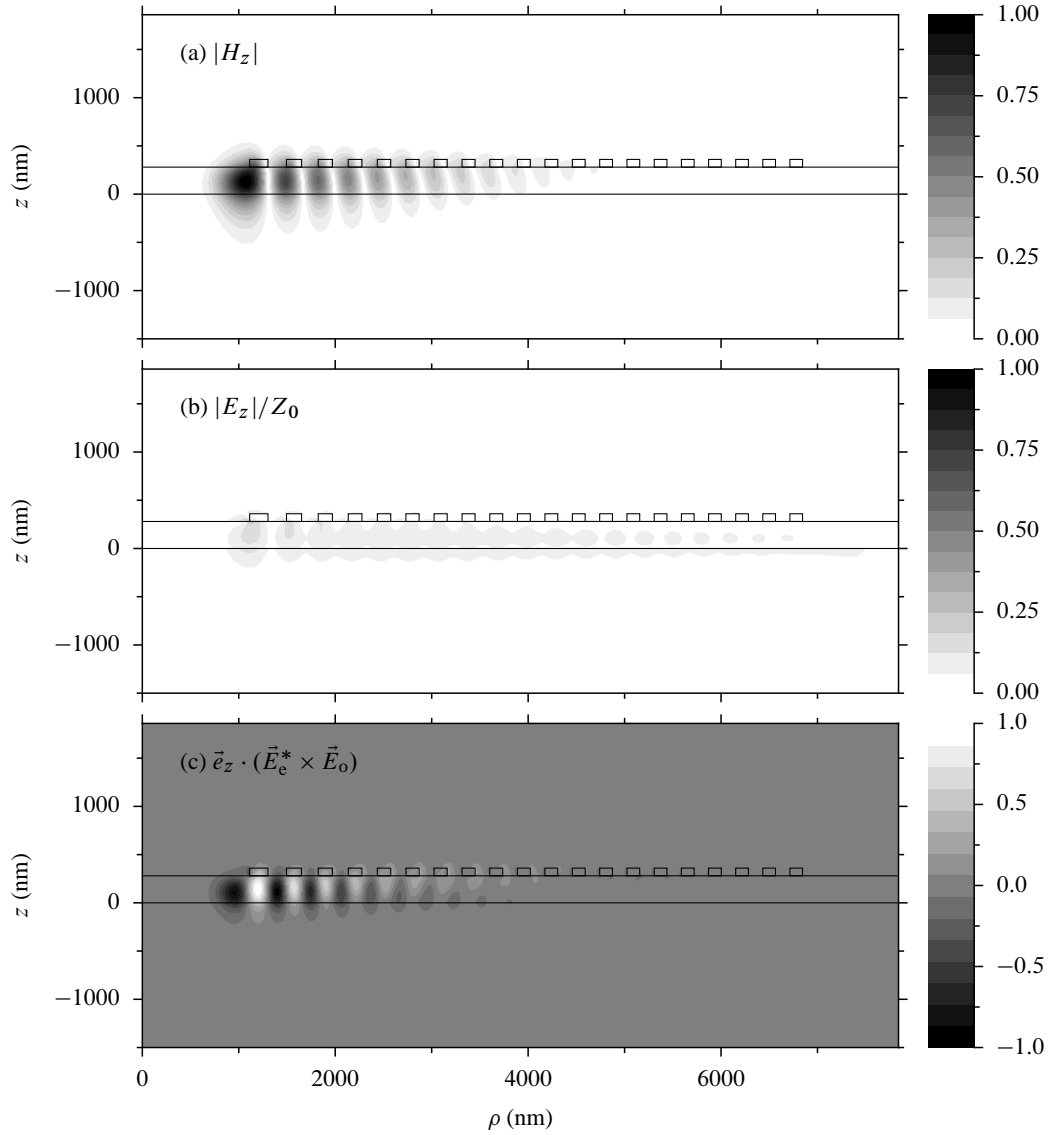


Figure 4.27 **(a)** Magnitude of the z component of the magnetic field of the eigenmodes of the G2-type cavity designed for $l = 10$, in the absence of SEMF. **(b)** Magnitude of the z component of the electric field divided by Z_0 . The colour scale is the same for parts (a) and (b). **(c)** The z component of the cross product $\vec{E}_e^* \times \vec{E}_o$ of the electric fields of the even and odd modes of the same cavity, which occurs as the integrand in the expression for the SEMF-induced mode coupling strength [34].

the unfavourable case of geometry G2 with uniformly MO BIG the frequency splitting of high- l modes is fairly large. However, the quality factor of these cavities is unsatisfactory. The cavity design must clearly be further improved to make the resulting devices usable in practice.

4.6.2 Towards cavities with higher quality factor

There are several routes that might potentially lead to an increase of Q . First, one could augment further the azimuthal order of the cavity mode; fig. 4.30(b) lets us expect that this will lead to a rise of Q . Indeed, we have verified that the G3-type cavity designed for $l = 40$ has $Q = 1760$. This growth of Q is achieved, however, at the expense of a significant enlargement of the cavity volume, which may not always be desirable.

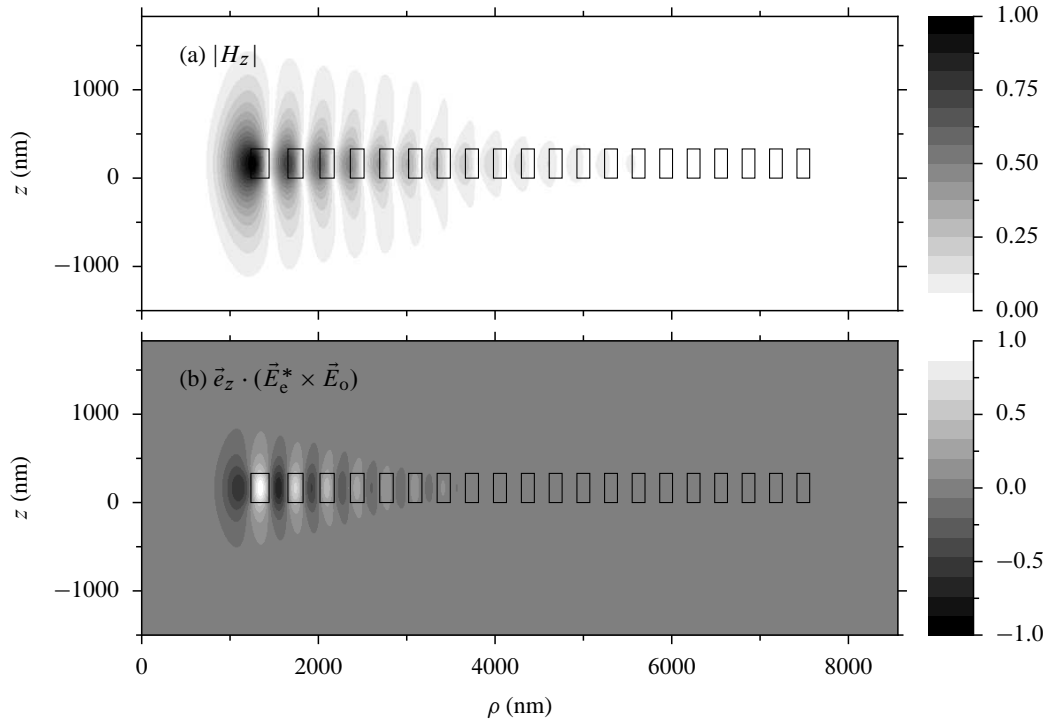


Figure 4.28 (a) Magnitude of the z component of the magnetic field of the eigenmodes of the G3-type cavity designed for $l = 10$, in the absence of SEMF. (b) The z component of the cross product $\vec{E}_e^* \times \vec{E}_o$ of the electric fields of the even and odd modes of the same cavity. The plot of $|E_z|/Z_0$ has been omitted because this field component is very small.

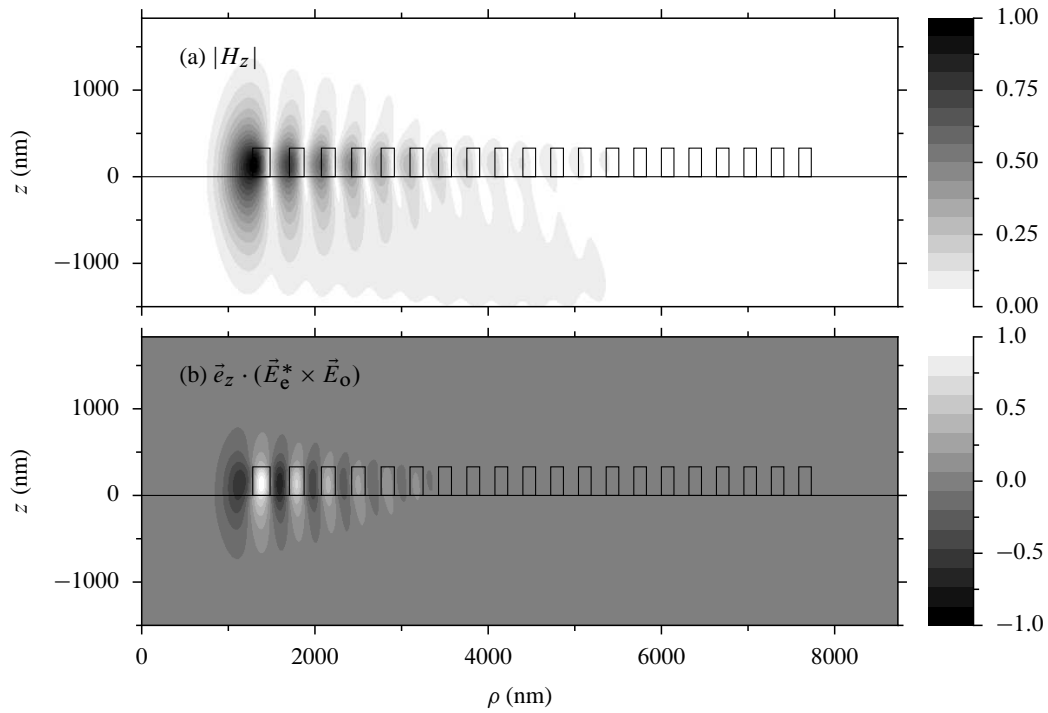


Figure 4.29 Same as fig. 4.28, but for the G4-type cavity.

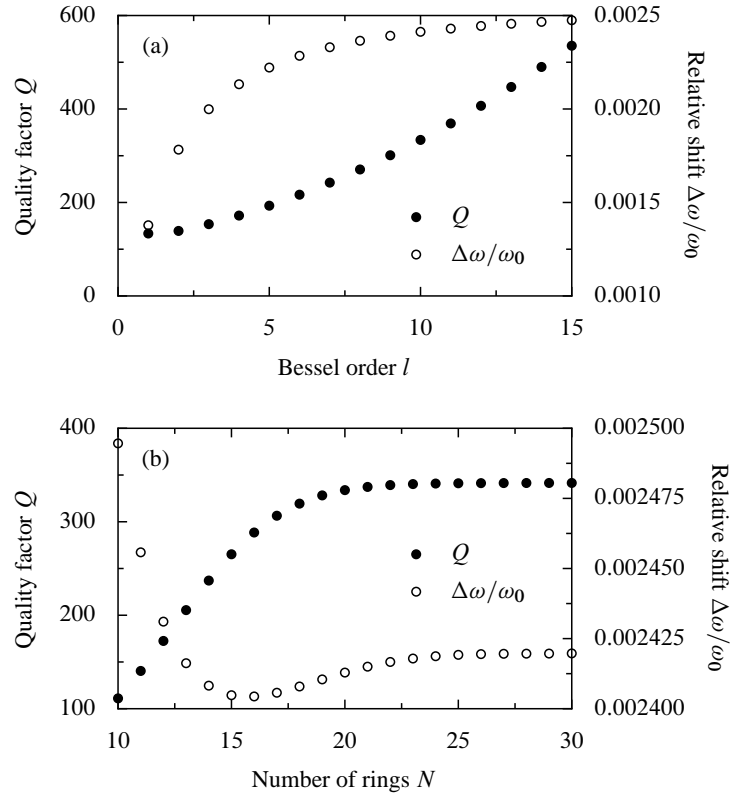


Figure 4.30 Dependence of the relative frequency splitting $\Delta\omega/\omega_0$ and quality factor Q of G3-type cavities **(a)** on the azimuthal order l with fixed number of high-index rings $N = 20$ and **(b)** on the number of rings N with fixed $l = 10$.

Second, one might look for ways of improving the accuracy of the effective-index approximation. As we have mentioned before, the effective index of regions supporting no guided modes is not rigorously defined. We have tested the influence of changing the value taken for the effective index of the etched areas of G4-type cavities from 1.90 to 1.97 and found that it brought about a 20-percent growth of Q . However, the wavelength of the cavity modes shifted by 2.5 nm further away from the design value of 1300 nm, which indicates that the increase of Q was not due to an improvement in the accuracy of the effective-index description. We have also tried the variational effective-index method proposed by Hammer and Ivanova [164], but found it to degrade both the quality factor and the match between the predicted and true value of the frequency of cavity modes.

Third, one should certainly profit from the extensive research on the optimisation of PC cavities done in the course of the last decade. As discussed in the review by Lalanne et al. [166], the approaches to this subject proposed so far can be divided into two large classes.

Some authors [167, 168] treat a PC cavity as a system consisting of many “elementary” cells of size comparable to the lattice constant of the surrounding PC. In each such cell, they expand the field in the basis of the cell’s Bloch eigenstates. Often, each cell supports only one guided mode (one that does not radiate energy in the vertical direction). The radiation loss from the cavity is then regarded as resulting from the scattering of the guided modes into radiative ones at the intercell boundaries. To reduce this loss, the geometry of each cell must then be adjusted so as to improve the match between the profiles of the guided modes of successive cells.

Unfortunately, this approach cannot be directly applied to axisymmetric structures, since it relies on the idea of expanding the field in each cell in its Bloch basis. Maxwell’s equations in cylindrical

coordinates are not invariant with respect to translations in the radial direction, however, even if the permittivity and permeability are; therefore the Bloch's theorem does not carry over to systems periodic in the radial direction. On the other hand, sufficiently far from the z axis, an *approximate* version of the Bloch's theorem can certainly be formulated. The results from a recent paper [169] indicate that this approximate formalism is fairly accurate even in small distances from the axis. Thus, it might be possible to apply the ideas from refs. 167 and 168 to axisymmetric systems. This will be the subject of future work.

Other researchers [170–173] base their cavity optimisation procedures on the link between the cavity's radiation pattern and the Fourier transform of its electromagnetic field. The quality factor Q of a cavity mode can be written as $Q = (\text{Re } \omega)U/P$, where ω is the mode's frequency, U stands for the time-averaged energy stored in its electromagnetic fields, and P is the rate of energy loss [166, 172]. Treating the cavity as an aperture antenna, one can relate the out-of-plane energy loss rate P_\perp to the 2D Fourier transforms of the ρ and ϕ field components on two planes, one lying in the substrate and the other in the superstrate of the cavity [174, 175]. Englund et al. [172] have gone one step further, rewriting P_\perp in terms of the z components of \vec{E} and \vec{H} :

$$P_\perp = \sum_{\sigma=\text{sub},\text{sup}} \frac{Z_\sigma k_\sigma}{8\pi^2} \int_{k_x^2 + k_y^2 \leq k_\sigma^2} dk_x dk_y \frac{\sqrt{k_\sigma^2 - k_x^2 - k_y^2}}{k_x^2 + k_y^2} \left[\frac{1}{Z_\sigma^2} |\tilde{E}_{z\sigma}(k_x, k_y)|^2 + |\tilde{H}_{z\sigma}(k_x, k_y)|^2 \right], \quad (4.48)$$

where $Z_\sigma \equiv \sqrt{(\mu_0 \mu_\sigma)/(\epsilon_0 \epsilon_\sigma)}$ is the (absolute) impedance of medium σ (substrate or superstrate), $k_\sigma \equiv k_0 \sqrt{\epsilon_\sigma \mu_\sigma}$ and

$$\tilde{F}_{z\sigma}(k_x, k_y) \equiv \frac{1}{2\pi} \int_{-\infty}^{\infty} dx \int_{-\infty}^{\infty} dy F_z(x, y, z_\sigma) e^{-i(k_x x + k_y y)} \quad (4.49)$$

denotes the 2D Fourier transform of the field F_z on the plane $z = z_\sigma$. The plane $z = z_{\text{sub}}$ can be taken to lie just below the interface of the substrate and the guiding layer, and the plane $z = z_{\text{sup}}$, just above the boundary between the guiding layer and the superstrate. It is important to note that the integrals in eq. (4.48) run only over the light cones. One concludes that to obtain a high- Q cavity it is necessary to sweep all the peaks of the Fourier transforms $\tilde{E}_{z\sigma}$ and $\tilde{H}_{z\sigma}$ away from the circle $k_x^2 + k_y^2 \leq k_\sigma^2$ [171].

In the axisymmetric case it is possible to simplify eq. (4.48). It can be shown [176, section 9.3] that the 2D Fourier transform of a function $f(\rho, \phi) \equiv f_l(\rho) e^{il\phi}$ is

$$\tilde{f}(k_\rho, \theta) \equiv \tilde{f}_l(k_\rho) e^{il\theta}, \quad (4.50a)$$

where

$$\tilde{f}_l(k_\rho) \equiv \int_0^\infty d\rho \rho f_l(\rho) J_l(k_\rho \rho) \quad (4.50b)$$

is the l th-order Hankel transform of $f(\rho)$. The symbols (ρ, ϕ) and (k_ρ, θ) denote the polar coordinates in the direct and reciprocal space. Using eqs. (4.50) one can bring eq. (4.48) into the form

$$P_\perp = \sum_{\sigma=\text{sub},\text{sup}} \frac{Z_\sigma k_\sigma}{4\pi} \int_0^{k_\sigma} dk_\rho \frac{\sqrt{k_\sigma^2 - k_\rho^2}}{k_\rho} \left[\frac{1}{Z_\sigma^2} |\tilde{E}_{z\sigma}(k_\rho)|^2 + |\tilde{H}_{z\sigma}(k_\rho)|^2 \right]. \quad (4.51)$$

Figure 4.31(a) shows the squared norms of the Hankel transforms $Z_{\text{sub}}^{-1} \tilde{E}_{z,\text{sub}}(k_\rho)$ and $\tilde{H}_{z,\text{sub}}(k_\rho)$ of the clockwise-rotating eigenmode of a G2-type cavity designed for $l = 10$ and comprising as much as 40 high-index rings (to eliminate border effects related to insufficient lateral size). The plane z_{sub} is

taken to lie 1 nm below the top boundary of the substrate. The curves obtained with 3D FEM simulations are juxtaposed with that stemming from Hankel-transforming the H_z field of the eigenmode of the corresponding 2D cavity (this mode is purely p -polarised, so the E_z component vanishes). Clearly, the peaks of all the curves are fairly well localised outside the light cone, whose boundary, $k_\rho = 1.97k_0$, is marked with a vertical line. Remarkably, the areas under the curves $Z_{\text{sub}}^{-2}|\tilde{E}_{z,\text{sub}}(k_\rho)|^2$ and $|\tilde{H}_{z,\text{sub}}(k_\rho)|^2$ obtained with 3D calculations are roughly equal, while the E_z component should vanish according to 2D simulations. This confirms our earlier conclusions that the low quality factor of the eigenmodes of G2-type cavities stems from the excitation of a p -polarised guided mode of the multilayer rather than from radiation losses.

The corresponding plots obtained for G3- and G4-type cavities are shown in figs. 4.31(b) and (c). While the transforms calculated in the 2D case are virtually indistinguishable, there is a marked difference in the 3D case: the transform of H_z of the mode of the G4-type cavity extends considerably further into the light cone than that corresponding to the G3-type structure. This is reflected in the lower quality factor of the mode of the former cavity, as evidenced in table 4.6. In contrast to what we saw in the previous paragraph, for G3- and G4-type cavities the part played by the E_z component is completely negligible.

In all the three systems considered here, the refractive index of the substrate is at least equal to that of the superstrate. Hence, radiation loss into the substrate dominates over that into the superstrate and, for brevity, we omit the discussion of the Hankel transforms of the fields on $z = z_{\text{sup}}$.

Advocates of the Fourier-transform-based optimisation of PC cavities have demonstrated that the quality factor–mode volume ratio of an eigenmode of a given structure can be increased by adjusting its geometry so as to lessen the decay rate of the mode field near the centre of the cavity. This narrows the peak of the Fourier transform, so that, provided that the centre of the peak lies outside the light cone, the integral of the squared norm of the Fourier transform over the light cone diminishes. This design rule has been summarised as “light should be confined gently in order to be confined strongly” [173].

Unfortunately, it is not easy to establish a link between the geometry of the cavity and the shape of its eigenmode field. Englund et al. [172] have derived an approximate formula for the permittivity profile of a cavity supporting a mode with a prescribed spatial dependence. However, they assumed that the field near the centre of the cavity could be approximated by that of a PC waveguide mode close to cut-off, i.e., with a very flat dispersion curve. For axisymmetric structures, this assumption is not met: near the z axis, the cavity mode could possibly be approximated with a guided mode of the multilayer, whose dispersion relation is in general not flat. Moreover, the formula derived by Englund et al. is based on the application of the perturbation theory rather far from its domain of validity—to describe discontinuous high-amplitude perturbations of permittivity. Therefore, its predictions might conceivably be not always accurate.

The last method that can be tried is the adjustment of ring dimensions based on a purely numerical optimisation algorithm. We have made some limited attempts at this sort of optimisation, parametrising the cavity geometry by the seven variables r_c , a_h , b_h , c_h , a_1 , b_1 and c_1 , defined as follows. The symbol r_c denotes the radius of the central low-index hole. The widths of the high-index rings are taken to be

$$w_{h,n} = a_h + \frac{b_h}{n} + \frac{c_h}{n^2} \quad \text{with} \quad n = 1, 2, \dots, \quad (4.52a)$$

whereas these of the low-index rings are set to

$$w_{l,n} = a_1 + \frac{b_1}{n+1} + \frac{c_1}{(n+1)^2} \quad \text{with} \quad n = 1, 2, \dots \quad (4.52b)$$

These particular functional forms were chosen because of their ability of approximating well the ring width distributions generated by the procedure from section 4.3. As the optimisation routine, we used

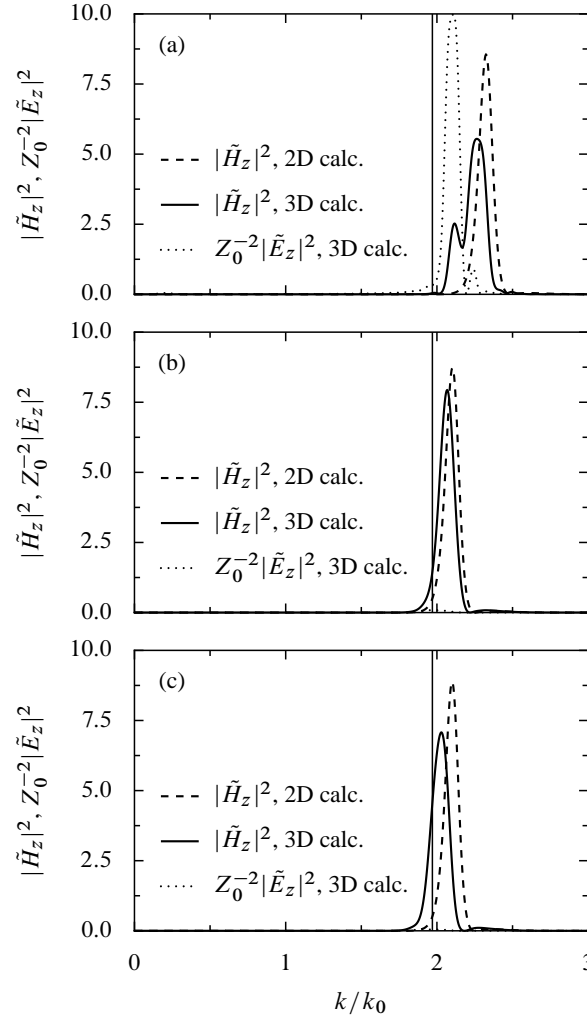


Figure 4.31 Squared norms of the Hankel transforms of the eigenmode fields of the cavities of types **(a)** G2, **(b)** G3 and **(c)** G4 designed to support modes with $l = 10$ at wavelength $\lambda = 1300$ nm. In each plot, the Hankel transforms of H_z and E_z of the eigenmodes of the respective 3D cavities, calculated at the plane lying 1 nm below the substrate-BIG interface, are juxtaposed with the Hankel transform of the H_z field of the eigenmode of the corresponding 2D cavity. The vertical line at $k = 1.97k_0$ marks the boundary of the light cone of the substrate.

the trust-region-based gradient-free NEWUOA algorithm by Powell [177]. The objective function was initially taken as

$$\tau \equiv \left(\frac{\Delta\omega}{\omega_0} \right)^\alpha Q_{\text{avg}}^\beta \quad (4.53)$$

with the exponents α and β chosen heuristically as $\alpha = 2$ and $\beta = 1$ to favour cavities with a large frequency splitting. Later it was found necessary to prevent a drift of the wavelength of the cavity eigenmodes far away from the design value of $\lambda = 1300$ nm; this was done by multiplying τ by an additional penalty factor

$$\tau_p \equiv \frac{1}{1 + e^{-\gamma(\lambda - \lambda_{\min})}} \frac{1}{1 + e^{-\gamma(\lambda_{\max} - \lambda)}} \quad (4.54)$$

with $\gamma = 0.2 \text{ nm}^{-1}$, $\lambda_{\min} = 1250$ nm and $\lambda_{\max} = 1350$ nm. At the start of the optimisation algorithm, the seven parameters were set so as to mimic the ring width distribution obtained with the procedure described in section 4.3.

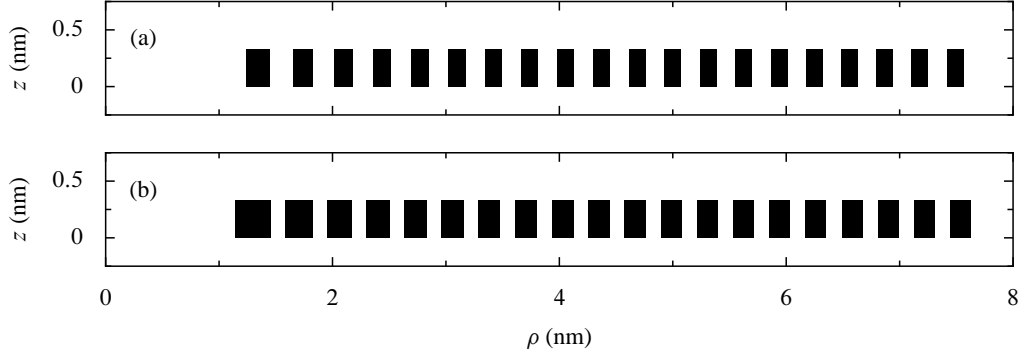


Figure 4.32 Geometry of **(a)** the original and **(b)** the numerically optimised cavity G3-type cavity designed for the azimuthal order $l = 10$. The shaded areas are the cross-sections of BIG rings, which are immersed in a material with refractive index 1.97.

We have not yet tested extensively the above optimisation algorithm, applying it so far only to a few special cases. One of them was the 20-ring G3-type cavity designed to support a mode with $l = 10$ at the wavelength $\lambda = 1300$ nm, whose geometry is shown in fig. 4.33(a). According to table 4.6 the average quality factor of the counter-propagating modes of this cavity is 334 and the relative frequency splitting, 0.00241. Using the just described procedure to optimise the radii of the rings, we arrived at the geometry shown in fig. 4.32(b). The average Q factor of the resonant mode of this structure is as large as 2630. One can suspect this Q factor to be limited by in-plane rather than out-of-plane losses, since it is already higher than the Q factor of the corresponding 20-ring 2D cavity, 2156. Remarkably, the observed improvement of the mode confinement does not occur at a cost of deterioration of the MO properties of the cavity, whose relative frequency splitting, 0.00260, is even slightly larger than that of the original structure. Figure 4.33 shows the map of the z components of the magnetic field and of the cross product $\vec{E}_e^* \times \vec{E}_o$ of the eigenmodes of this cavity, as well as the squared norms of the Hankel transforms $Z_{\text{sub}}^{-1} \tilde{E}_{z,\text{sub}}(k_\rho)$ and $\tilde{H}_{z,\text{sub}}(k_\rho)$. Comparing these curves with those from fig. 4.31(b), it can be seen that the peak of $|\tilde{H}_{z,\text{sub}}(k_\rho)|^2$ of the optimised structure is indeed more tightly localised outside the light cone of GGG.

4.7 Conclusions and perspectives

The research presented in this chapter was founded on the algorithm for the design of z -invariant axisymmetric MO cavities that in the presence of a uniform SEMF exhibit maximum frequency splitting (section 4.3). In sections 4.4 and 4.5 we put forth a number of designs of three-port circulators incorporating such cavities and operating according to the model presented in section 4.2. Lastly, in section 4.6, we studied the properties of the proposed cavities in a 3D setting, using full 3D simulations.

In the course of this work, we increasingly tried to take into account the 3D nature of real integrated systems, in which the components are etched in BIG thin layers grown on GGG substrates. Initially, we performed purely 2D calculations, using bulk indices of the constituent materials. To some extent, this approach was justified: the algorithm from section 4.3 was based on 2D considerations, and it was necessary to compare the performance of the cavities designed by its help against those proposed before [34, 37, 150], which were also evaluated in a purely 2D setting.

At the next stage, we attempted to take into account the multilayer structure of the experimental system with the effective-index approximation, which is fairly widely used to bring the results of 2D simulations of, in particular, PC-slab-based devices closer to reality. The design of the rib-waveguide-based circulators, reported on in section 4.5, was done in this way. However, measurements of the transmittance

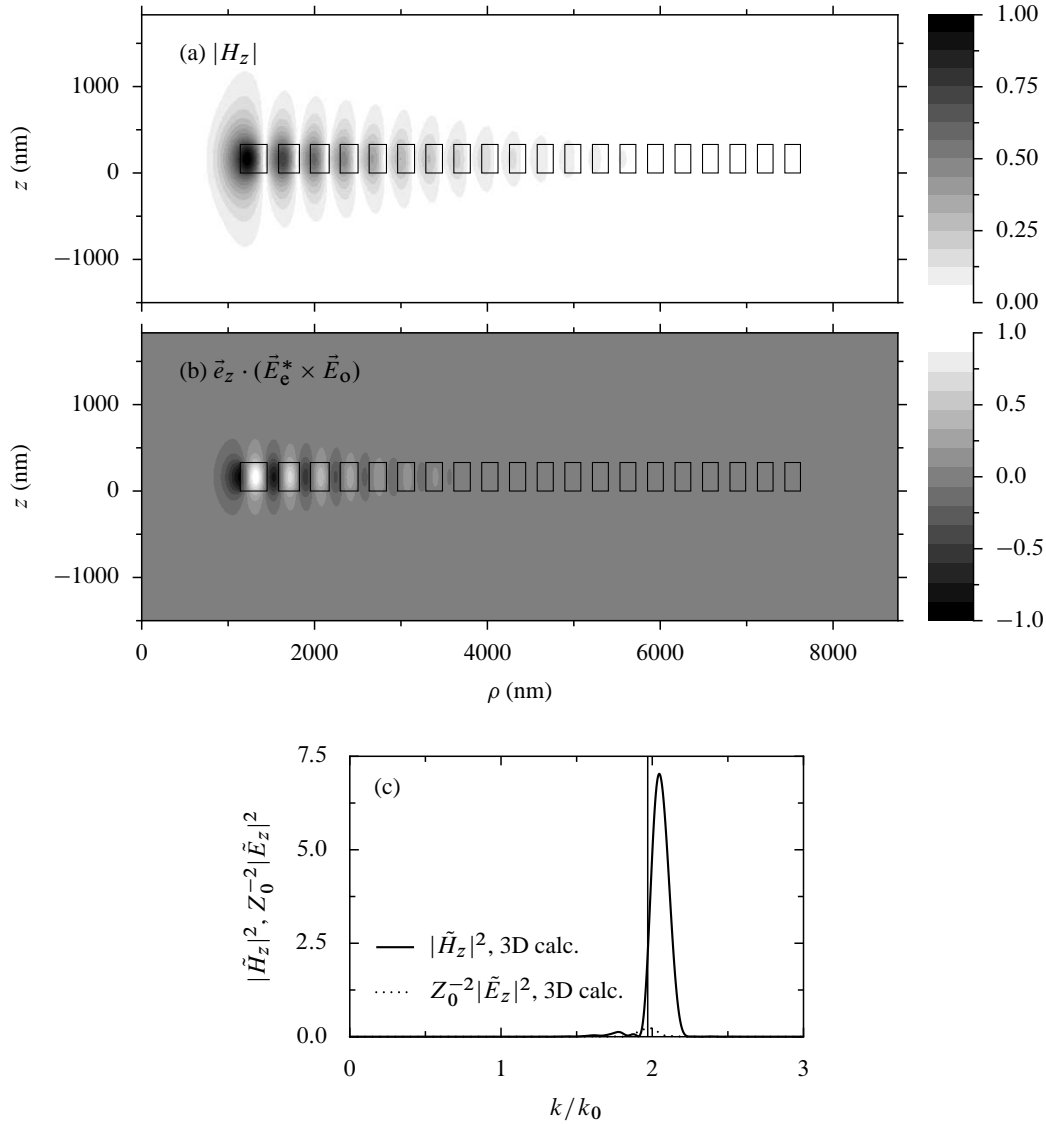


Figure 4.33 (a) Magnitude of the z component of the magnetic field of the eigenmodes of the optimised G3-type cavity designed for $l = 10$, in the absence of SEMF. (b) The z component of the cross product $\vec{E}_e^* \times \vec{E}_o$ of the electric fields of the even and odd modes of the same cavity. (c) Squared norms of the Hankel transforms of the eigenmode fields H_z and E_z at the plane located 1 nm below the surface of the substrate.

through fabricated components of this type revealed that the behaviour of the 3D cavity differed strongly from the predictions of the 2D model. It became apparent that full 3D simulations were inevitable.

The results of these calculations, summarised in section 4.6, proved that resonant cavities designed by help of the effective-index approximation do have good MO properties: the SEMF-induced splitting of the frequencies of their eigenmodes is indeed spectacular. However, the cavities suffer from substantial radiation losses in the vertical direction. The outcome of the various attempts at increasing the quality factor of these cavities, presented in subsection 4.6.2, points to the conclusion that 3D simulations are, unfortunately, all but unavoidable. They are required not only in the somewhat “brute-force” numerical optimisation of ring widths described at the end of subsection 4.6.2, but also in the approach based on Bloch’s theorem, which we have not tested, but which definitely looks promising.

Regardless of the way in which a cavity is designed, it must still be integrated with waveguides. The results from section 4.5, while based on the effective-index approximation and therefore inaccurate, do

provide some insight into the problem of cavity–rib–waveguide coupling. In particular, they confirm that the optimum location of the waveguide ends can be approximately determined by analysing the quality factors of cavities with a varying number of rings. Therefore, if the distance from the cavity centre to the ends of 3D waveguides is figured out with this method, some nonreciprocal isolation should be observable in experiment. Clearly, though, some numerical fine-tuning of this distance will be necessary to optimise the maximum isolation and the operation bandwidth of the device. Three-dimensional simulations of a complete circulator would be prohibitively slow. However, as a workaround one might try the method of Andreani and Gerace [178], who successfully calculated the diffraction losses of eigenmodes of PC slabs by expanding the fields in terms of a few lowest guided modes of a specific multilayer (dependent on the structure of the slab) and including the radiation losses in a perturbative way.

Chapter 5

Numerical methods

5.1 Multiple-scattering method for systems containing gyrotropic media

In section 4.4 we presented results of numerical simulations of the scattering of electromagnetic waves by 2D PCs composed of circular cylinders etched in a MO, and thus anisotropic, matrix. The multiple-scattering method used to make these calculations was originally derived for isotropic materials [38]. Here we show that it can be extended with very little effort to the case of gyrotropic media.

The most important assumption of the method, which is described in detail in refs. 38, 39 and 40, is that the field F_z (standing for E_z for s -polarised waves and H_z for p -polarised ones) in the medium surrounding the scatterers is governed by the Helmholtz equation

$$\nabla^2 F_z + k_0^2 n^2 F_z = 0, \quad (5.1)$$

where $k_0 \equiv \omega/c$, ω denotes the frequency, and n is the refractive index of the medium in question. It can be shown that in each circular annulus surrounding a particular scatterer S_i and intersecting no other scatterers the field F_z can be decomposed into three parts: F_{zi}^{src} , the incident field coming directly from the source, F_{zi}^{inc} , the field scattered towards S_i by other scatterers, and F_{zi}^{scatt} , the field scattered by S_i itself. Each of these fields can be written in the form of a Fourier-Bessel series:

$$F_{zi}^{\text{src}}(\rho_i, \phi_i) = \sum_{m \in \mathbb{Z}} a_{im}^{\text{src}} J_m(k_0 n \rho_i) e^{im\phi_i}, \quad (5.2a)$$

$$F_{zi}^{\text{inc}}(\rho_i, \phi_i) = \sum_{m \in \mathbb{Z}} a_{im}^{\text{inc}} J_m(k_0 n \rho_i) e^{im\phi_i}, \quad (5.2b)$$

$$F_{zi}^{\text{scatt}}(\rho_i, \phi_i) = \sum_{m \in \mathbb{Z}} b_{im} H_m^{(1)}(k_0 n \rho_i) e^{im\phi_i}, \quad (5.2c)$$

where a_{im}^{src} , a_{im}^{inc} and b_{im} are constant coefficients, $J_m(x)$ and $H_m^{(1)}(x)$ denote the Bessel and Hankel functions of the first kind, and (ρ_i, ϕ_i) are polar coordinates defined with respect to the centre of the annulus. With the so-called Graf's theorem, a link can be established between the series (5.2) expressed in coordinate systems associated with different scatterers. This makes it possible to write F_{zi}^{inc} in terms of F_{zj}^{scatt} for all $j \neq i$. Moreover, a linear relation exists between the Fourier-Bessel coefficients of the sum $F_{zi}^{\text{src}} + F_{zi}^{\text{inc}}$ and those of F_{zi}^{scatt} . With \vec{a}_i and \vec{b}_i denoting the column vectors of the coefficients $(a_{im}^{\text{src}} + a_{im}^{\text{inc}})$ and b_{im} , respectively, this relation can be expressed as

$$\vec{b}_i = \hat{S}_i \vec{a}_i, \quad (5.3)$$

where \hat{S}_i is conventionally called the *scattering matrix* of S_i . Its entries can be obtained by imposing the electromagnetic boundary conditions on the inner surface of the annulus mentioned above. Their

derivation is particularly simple for a homogeneous isotropic circular scatterer with refractive index n_i ; in this case, the total field F_z inside S_i can also be written as a Fourier-Bessel series,

$$F_{zi}^{\text{int}}(\rho_i, \phi_i) = \sum_{m \in \mathbb{Z}} c_{im} J_m(k_0 n_i \rho_i) e^{im\phi_i}, \quad (5.4)$$

and since the surface of S_i coincides with a constant coordinate line of the polar coordinate system anchored at the centre of S_i , field matching can be done analytically and in fact the matrix \hat{S}_i becomes diagonal.

We shall now show that Maxwell's equations describing wave propagation in a homogeneous medium can also be reduced to a Helmholtz equation if the medium has gyrotropic permittivity and permeability of the form

$$\hat{\epsilon} \equiv \begin{bmatrix} \epsilon_t & i\epsilon_g & 0 \\ -i\epsilon_g & \epsilon_t & 0 \\ 0 & 0 & \epsilon_z \end{bmatrix} \quad \text{and} \quad \hat{\mu} \equiv \begin{bmatrix} \mu_t & i\mu_g & 0 \\ -i\mu_g & \mu_t & 0 \\ 0 & 0 & \mu_z \end{bmatrix}. \quad (5.5)$$

We shall focus on p polarisation; the results for s polarisation can be obtained from the duality principle [65, p. 72–73]. Substituting eqs. (5.5) into Maxwell's equations for p polarisation, eqs. (1.7), and writing the differential operators explicitly in Cartesian coordinates, we get

$$\frac{\partial E_y}{\partial x} - \frac{\partial E_x}{\partial y} = i\omega\mu_0\mu_z H_z, \quad (5.6a)$$

$$\frac{\partial H_z}{\partial y} = -i\omega\epsilon_0(\epsilon_t E_x + i\epsilon_g E_y), \quad (5.6b)$$

$$-\frac{\partial H_z}{\partial x} = -i\omega\epsilon_0(-i\epsilon_g E_x + \epsilon_t E_y). \quad (5.6c)$$

Solving the two last equations for the components of \vec{E} , we obtain

$$E_x = \frac{1}{i\omega\epsilon_0(\epsilon_g^2 - \epsilon_t^2)} \left(i\epsilon_g \frac{\partial H_z}{\partial x} + \epsilon_t \frac{\partial H_z}{\partial y} \right), \quad (5.7a)$$

$$E_y = \frac{1}{i\omega\epsilon_0(\epsilon_g^2 - \epsilon_t^2)} \left(-\epsilon_t \frac{\partial H_z}{\partial x} + i\epsilon_g \frac{\partial H_z}{\partial y} \right). \quad (5.7b)$$

Substitution of these expressions into eq. (5.6a) yields

$$\frac{\partial^2 H_z}{\partial x^2} + \frac{\partial^2 H_z}{\partial y^2} + k_0^2 \left(\epsilon_t - \frac{\epsilon_g^2}{\epsilon_t} \right) \mu_z H_z = 0. \quad (5.8)$$

Thus, the field H_z fulfils a Helmholtz equation with an “effective refractive index”

$$n' \equiv [(\epsilon_t - \epsilon_g^2/\epsilon_t)\mu_z]^{1/2}. \quad (5.9)$$

It is also possible to derive analytically the expression for the entries of the scattering matrix \hat{S} of a homogeneous gyrotropic cylinder S of radius R embedded in a gyrotropic matrix. We need to impose the conditions of continuity of the components of the electric and magnetic fields tangential to the surface of S , i.e., H_z and E_ϕ . The field H_z on the exterior side of the surface of S is given by

$$H_z^{\text{ext}}(R, \phi) = \sum_{m \in \mathbb{Z}} [a_m J_m(k_0 n'_{\text{ext}} R) + b_m H_m^{(1)}(k_0 n'_{\text{ext}} R)] e^{im\phi}, \quad (5.10a)$$

and on the interior side,

$$H_z^{\text{int}}(R, \phi) = \sum_{m \in \mathbb{Z}} c_m J_m(k_0 n'_{\text{int}} R) e^{im\phi}; \quad (5.10b)$$

in these formulas, the subscripts “int” and “ext” label quantities measured on the interior and exterior side of the surface of S . Equations (5.7) imply that

$$E_\phi = \frac{1}{i\omega\epsilon_0(\epsilon_g^2 - \epsilon_t^2)} \left(-\epsilon_t \frac{\partial H_z}{\partial r} + \frac{ig}{r} \frac{\partial H_z}{\partial \phi} \right), \quad (5.11)$$

hence

$$E_\phi^{\text{ext}}(R, \phi) = -\frac{1}{i\omega\epsilon_0} \sum_{m \in \mathbb{Z}} \left[a_m \frac{(m\epsilon_{g,\text{ext}}/R) J_m(k_0 n'_{\text{ext}} R) + \epsilon_{t,\text{ext}} k_0 n'_{\text{ext}} J'_m(k_0 n'_{\text{ext}} R)}{\epsilon_{g,\text{ext}}^2 - \epsilon_{t,\text{ext}}^2} + b_m \frac{(m\epsilon_{g,\text{ext}}/R) H_m^{(1)}(k_0 n'_{\text{ext}} R) + \epsilon_{t,\text{ext}} k_0 n'_{\text{ext}} H_m^{(1)'}(k_0 n'_{\text{ext}} R)}{\epsilon_{g,\text{ext}}^2 - \epsilon_{t,\text{ext}}^2} \right] e^{im\phi}, \quad (5.12a)$$

$$E_\phi^{\text{int}}(R, \phi) = -\frac{1}{i\omega\epsilon_0} \sum_{m \in \mathbb{Z}} c_m \frac{(m\epsilon_{g,\text{int}}/R) J_m(k_0 n'_{\text{int}} R) + \epsilon_{t,\text{int}} k_0 n'_{\text{int}} J'_m(k_0 n'_{\text{int}} R)}{\epsilon_{g,\text{int}}^2 - \epsilon_{t,\text{int}}^2} e^{im\phi}, \quad (5.12b)$$

where the symbols $J'_m(x)$ and $H_m^{(1)'}(x)$ denote the derivatives of the Bessel and Hankel functions at x . To condense the notation, we can rewrite eqs. (5.10) and (5.12) in the form

$$H_z^{\text{ext}}(R, \phi) = \sum_{m \in \mathbb{Z}} (A_m^H a_m + B_m^H b_m) e^{im\phi}, \quad H_z^{\text{int}}(R, \phi) = \sum_{m \in \mathbb{Z}} C_m^H c_m e^{im\phi}, \quad (5.13a)$$

$$E_\phi^{\text{ext}}(R, \phi) = \sum_{m \in \mathbb{Z}} (A_m^E a_m + B_m^E b_m) e^{im\phi}, \quad E_\phi^{\text{int}}(R, \phi) = \sum_{m \in \mathbb{Z}} C_m^E c_m e^{im\phi}, \quad (5.13b)$$

where the definitions of the constant coefficients A_m^H etc. can be obtained straightforwardly by comparing the above expressions with eqs. (5.10) and (5.12). Imposing now the conditions $H_z^{\text{ext}}(R, \phi) = H_z^{\text{int}}(R, \phi)$ and $E_\phi^{\text{ext}}(R, \phi) = E_\phi^{\text{int}}(R, \phi)$ for all $\phi \in [0, 2\pi)$ and noting that, owing to the orthogonality of the functions $e^{im\phi}$ ($m \in \mathbb{Z}$) on this interval, the sums over m can be dropped, we arrive finally at the formulas

$$b_m = -\frac{A_m^H C_m^E - A_m^E C_m^H}{B_m^H C_m^E - B_m^E C_m^H} a_m, \quad (5.14a)$$

$$c_m = -\frac{A_m^H B_m^E - A_m^E B_m^H}{B_m^H C_m^E - B_m^E C_m^H} a_m. \quad (5.14b)$$

Thus, by virtue of eq. (5.14a), we conclude that the scattering matrix \hat{S} of a gyrotropic cylinder embedded in a gyrotropic matrix is diagonal and its elements are given by

$$S_{mn} = -\frac{A_m^H C_m^E - A_m^E C_m^H}{B_m^H C_m^E - B_m^E C_m^H} \delta_{mn}. \quad (5.15)$$

We have thus demonstrated that only minor modifications of the multiple-scattering method are necessary to make it able to tackle gyrotropic materials. First, the refractive index n supplied to the argument of Bessel functions must be replaced by the “effective refractive index” n' defined in eq. (5.9). Second,

the formulas for the entries of the scattering matrix of a cylinder acquire additional terms proportional to the off-diagonal elements of the material property tensors.

It is natural to ask whether these steps suffice for different classes of anisotropic materials. The answer is, unfortunately, negative. For instance, consider the case of a medium with permittivity $\hat{\epsilon} \equiv \text{diag}(\epsilon_x, \epsilon_y, \epsilon_z)$ with $\epsilon_x \neq \epsilon_y$. The transformation of Maxwell's equations into the Helmholtz equation comes now at the price of the change of coordinates

$$(x, y) \mapsto (s_x x, s_y y) \quad \text{with} \quad \frac{s_x}{s_y} = \sqrt{\frac{\epsilon_y}{\epsilon_x}} \neq 1. \quad (5.16)$$

An unwelcome side-effect of this change of coordinates is the mapping of circles into ellipses. This has two consequences. First, the elements of the scattering matrix of a circular cylinder cease to be diagonal and have to be determined in a more complicated way than that presented above, since after the mapping the cylinder's surface does not coincide any more with a line of constant polar coordinates. Second, if it is the matrix (rather than the scatterer) that is anisotropic, the mapping (5.16) may cause the circles circumscribing the scatterers to overlap. It is well known that if this overlap is sufficiently large, the Fourier-Bessel expansion (5.6c) of the scattered field becomes invalid and the multiple-scattering theory in its classical form cannot be applied [179, 180].

5.2 Calculation of photonic-crystal band structures with Fourier-Bessel expansions

5.2.1 Introduction

The multiple-scattering method, whose extension to MO materials we have presented in the previous section, has long been recognised as one of the most efficient techniques of modelling finite PCs composed of circular cylinders. The reason for this is twofold: first, the basis functions used to expand the fields are exact solutions of Maxwell's equations, and hence they are well-adapted for the representation of these fields; second, since the basis functions are separable in polar coordinates, it is easy to apply the electromagnetic boundary conditions at the surfaces of the cylinders.

In view of these advantages of the multiple-scattering method, it is tempting to extend its domain of application to the calculation of band structures of *infinite* PCs. Such an extension has indeed been made both for PCs composed of cylinders and spheres [41–47]. In this approach it is necessary to calculate explicitly the field produced by an infinite number of scatterers arranged on a periodic lattice, which can be expressed by a series termed a *lattice sum*. Unfortunately, lattice sums are slowly convergent, and special techniques needed for acceleration of their computation complicate significantly the implementation of the method with respect to the finite-system case.

Here we propose a much simpler technique of calculating band structures of PCs composed of circular cylinders. Like the multiple-scattering method, it relies on Fourier-Bessel field expansions, but it dispenses with the calculation of lattice sums. The underlying idea is very simple: the field in a unit cell of a PC is expanded in terms of particular solutions of the Helmholtz equation, and the Bloch conditions on the boundaries of the cell are imposed by collocation (point matching). This approach is actually similar to the technique used in the fictitious-sources method to avoid the calculation of periodic Green's functions in simulations of gratings [48]. The method is easy in implementation and it leads to exponential convergence of the band structure, potentially yielding very high relative accuracy, as will be demonstrated in the following.

The proposed method shares many features with the technique of Dirichlet-to-Neumann mappings developed in the group of Lu [49, 50]. In their approach, a field expansion in particular solutions of the

Helmholtz equation is used to calculate a finite-dimensional approximation of the Dirichlet-to-Neumann operator that maps the distribution of the field on the unit cell's boundary to that of the normal derivative of this field. The resulting operator can then be used to calculate the band structure of the PC. Our method is more direct and more efficient, since it does not require the construction of the Dirichlet-to-Neumann matrix, and hence dispenses with the need of performing a matrix inversion. On the other hand, it is also less powerful, since a Dirichlet-to-Neumann operator can be used for the sake of computing not only a band structure, but also, for instance, the transmission and reflection coefficients of a finite or semi-infinite PC [50]. One could say that while the method of Lu et al. is more general, ours has been specifically tailored to band-structure calculations.

In the next subsection we shall present the formulation of the proposed technique. Some concrete numerical examples of its application will be given in subsection 5.2.3, and the obtained results will be briefly discussed in subsection 5.2.4.

5.2.2 Formulation

Let us consider a 2D PC whose unit cell, shown in fig. 5.1(a), is composed of M nonoverlapping circular inclusions of radius r_m , permittivity $\hat{\epsilon}_m$ and permeability $\hat{\mu}_m$ ($m = 1, 2, \dots, M$), embedded in a matrix with permittivity $\hat{\epsilon}_0$ and permeability $\hat{\mu}_0$. The tensors $\hat{\epsilon}_m$ and $\hat{\mu}_m$ ($m = 0, 1, \dots, M$) are assumed to have the (gyrotropic) form

$$\hat{\epsilon}_m \equiv \begin{bmatrix} \epsilon_{tm} & i\epsilon_{gm} & 0 \\ -i\epsilon_{gm} & \epsilon_{tm} & 0 \\ 0 & 0 & \epsilon_{zm} \end{bmatrix} \quad \text{and} \quad \hat{\mu}_m \equiv \begin{bmatrix} \mu_{tm} & i\mu_{gm} & 0 \\ -i\mu_{gm} & \mu_{tm} & 0 \\ 0 & 0 & \mu_{zm} \end{bmatrix}. \quad (5.17)$$

As we have shown in section 5.1, for p polarisation, the Maxwell's equations in a homogeneous region with permittivity $\hat{\epsilon}_m$ and permeability $\hat{\mu}_m$ reduce to the Helmholtz equation for the z component of the magnetic field, H_z :

$$\nabla^2 H_z + k_m^2 H_z = 0, \quad (5.18)$$

where

$$k_m \equiv \frac{\omega}{c} \left(\epsilon_{tm} - \frac{\epsilon_{gm}^2}{\epsilon_{tm}} \right)^{1/2}. \quad (5.19)$$

The corresponding equation for s polarisation can be obtained simply from the duality principle [65, p. 72–73]. Vekua [181, section 22] showed that every regular solution of the Helmholtz equation (5.18) in a multi-connected domain $D \equiv D_0 \setminus (C_1 \cup C_2 \cup \dots \cup C_M)$, where D_0 , C_1 , C_2 , \dots , C_M are simply-connected domains and $C_1, C_2, \dots, C_M \subset D_0$, can be approximated uniformly by a linear combination of the functions

$$J_l(k_m \rho) e^{il\phi} \quad \text{and} \quad Y_l(k_m \rho_m) e^{il\phi_m} \quad \text{for} \quad l \in \mathbb{Z} \quad \text{and} \quad m = 1, 2, \dots, M, \quad (5.20)$$

where (ρ, ϕ) are standard polar coordinates and (ρ_m, ϕ_m) are the polar coordinates defined with respect to the point $O_m \in C_m$ [see fig. 5.1(b)].

We shall use Vekua's theorem to determine the representation of the field in the PC unit cell shown in fig. 5.1(a). We divide it into $M' \geq M$ polygonal subcells, each containing exactly one circular inclusion. (For numerical purposes it can be advantageous to introduce subcells containing no “physical” inclusions; these can be treated as if they contained an inclusion with permittivity $\hat{\epsilon}_0$, permeability $\hat{\mu}_0$ and a sufficiently small radius.) Inside the inclusion of the m th subcell, the solution of the Helmholtz equation can be approximated by the series

$$H_{z,\text{in}}^{(L)}(\rho_m, \phi_m) \equiv \sum_{l=-L}^L c_{ml}^{(L)} J_l(k_m \rho_m) e^{il\phi_m}, \quad (5.21)$$

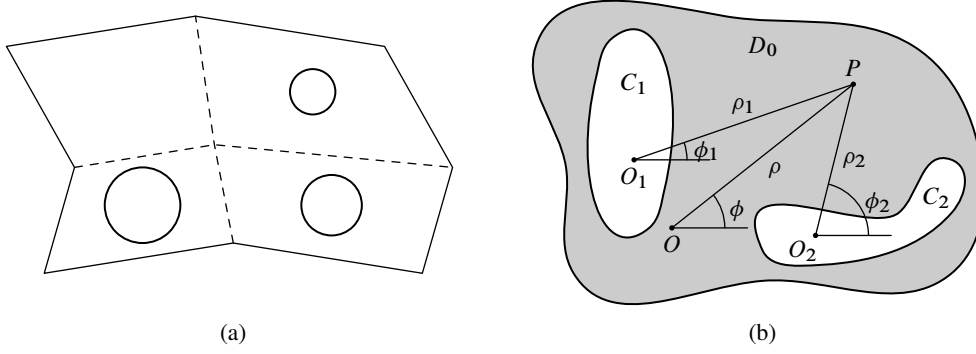


Figure 5.1 (a) Geometry of a PC's unit cell that contains $M = 3$ circular inclusions embedded in a homogeneous matrix. It is subsequently divided into $M' = 4$ quadrilateral subcells. (b) Schema of the domain D referred to in Vekua's theorem. Note that the symbol D_0 denotes the whole interior of the large contour, whereas D stands for the shaded region.

with the polar coordinates (ρ_m, ϕ_m) defined with respect to the origin O_m lying in the centre of the inclusion. In turn, the field outside the inclusion can be approximated by

$$H_{z,\text{out}}^{(L)}(\rho_m, \phi_m) \equiv \sum_{l=-L}^L [a_{ml}^{(L)} J_l(k_0 \rho_m) + b_{ml}^{(L)} Y_l(k_0 \rho_m)] e^{il\phi_m}. \quad (5.22)$$

The superscripts (L) in the above formulas stress that, according to Vekua's theorem, the system (5.20) is *complete*, but need not be a *basis*. In other words, it is not guaranteed, for instance, that there exist coefficients a_{ml} and b_{ml} ($l \in \mathbb{Z}$) such that the series

$$\sum_{l \in \mathbb{Z}} [a_{ml} J_l(k_0 \rho_m) + b_{ml} Y_l(k_0 \rho_m)] e^{il\phi_m} \quad (5.23)$$

converges to the true solution $H_{z,\text{out}}(\rho_m, \phi_m)$. What is guaranteed is that a finite superposition of the functions (5.20) can be found that approximates $H_{z,\text{out}}(\rho_m, \phi_m)$ to any desired accuracy $\epsilon > 0$. This is quite sufficient for practical purposes. An example illustrating clearly the difference between a basis and a complete set is given by Christensen [182, pp. 98–99]. For compactness of notation, the superscripts (L) will be dropped from now on.

At the present stage, to each subcell correspond three families of unknown coefficients: a_{ml} , b_{ml} and c_{ml} . The former two can be easily expressed in terms of the latter one by imposing analytically the electromagnetic boundary conditions at the surfaces of the circular inclusions. This is done exactly in the same way as in the multiple-scattering method, and has been detailed in ref. 40 for the isotropic case and in section 5.1 of this thesis for the gyrotropic case. Therefore, we do not describe it again here. In any case, this procedure leads to expressions of the form

$$a_{ml} = A_{ml} c_{ml} \quad \text{and} \quad b_{ml} = B_{ml} c_{ml}, \quad (5.24)$$

where A_{ml} and B_{ml} are known. Substituting them to eq. (5.22), we get

$$H_{z,\text{out}}(\rho_m, \phi_m) \equiv \sum_{l=-L}^L c_{ml} [A_{ml} J_l(k_0 \rho_m) + B_{ml} Y_l(k_0 \rho_m)] e^{il\phi_m}. \quad (5.25)$$

To determine the values of c_{ml} , we impose appropriate boundary conditions at discrete collocation points distributed on the inter-subcell boundaries, which can be divided into two classes. On an interface of two

subcells belonging to the same unit cell, we impose the continuity of H_z and its derivative normal to that interface. (The continuity of the tangential derivative should follow, in the limit of infinitely many collocation points, from the continuity of H_z itself.) On an external boundary of a unit cell, in turn, we impose Bloch conditions on H_z and its normal derivative. Assuming that the number of collocation points is equal to half the number of unknowns c_{ml} , the above procedure leads to a homogeneous system of linear equations, whose matrix is square and depends on the Bloch vector \vec{k} . This system is subsequently transformed into a generalised eigenvalue problem for one of the components of \vec{k} , as will be demonstrated on an example later in this section.

In the meantime, there is a technical difficulty to be resolved. As we have seen, we have always an even number of boundary conditions. However, the expansion (5.25) contains an odd number $(2L + 1)$ of coefficients c_{ml} . In order to match the number of equations and that of unknowns, it is necessary to dispense with one coefficient. To this end, we follow a procedure used in spectral Fourier-expansion techniques [183, subsection 2.2.1]. We rewrite the exponential functions $e^{il\phi_m}$ in eq. (5.25) in terms of the trigonometric functions $\cos(l\phi_m)$ and $\sin(l\phi_m)$, and use the relations $J_{-l}(x) = (-1)^l J_l(x)$, $Y_{-l}(x) = (-1)^l Y_l(x)$, $A_{m,-l} = A_{ml}$ and $B_{m,-l} = B_{ml}$ to convert the series from eq. (5.25) to the form

$$H_{z,\text{out}}(\rho_m, \phi_m) \equiv \sum_{l=0}^L [A_{ml} J_l(k_0 \rho_m) + B_{ml} Y_l(k_0 \rho_m)] [d_{ml}^c \cos(l\phi_m) + d_{ml}^s \sin(l\phi_m)], \quad (5.26)$$

where

$$d_{ml}^c \equiv c_{ml} + (-1)^l c_{m,-l} \quad \text{and} \quad d_{ml}^s \equiv i[c_{ml} - (-1)^l c_{m,-l}]. \quad (5.27)$$

We set now $d_{mL}^s = 0$, obtaining

$$\begin{aligned} H_{z,\text{out}}(\rho_m, \phi_m) \equiv & \sum_{l=0}^L d_{ml}^c [A_{ml} J_l(k_0 \rho_m) + B_{ml} Y_l(k_0 \rho_m)] \cos(l\phi_m) \\ & + \sum_{l=1}^{L-1} d_{ml}^s [A_{ml} J_l(k_0 \rho_m) + B_{ml} Y_l(k_0 \rho_m)] \sin(l\phi_m) \end{aligned} \quad (5.28)$$

and reducing the total number of unknowns to $2L$.

We shall now present in detail the conversion of the square system of linear equations resulting from the collocation procedure to an eigenvalue problem, considering the example case of a PC composed of a hexagonal lattice of cylinders, shown in fig. 5.2(a). Its unit cell can be chosen as the Wigner-Seitz cell delimited by the segments Σ_i ($i = 1, 2, \dots, 6$). Since it contains only a single inclusion, it is not necessary to divide it into subcells. Let us assume that on each segment Σ_i $L/3$ collocation points with polar coordinates $(\rho_{1,ij}, \phi_{1,ij})$ ($j = 1, 2, \dots, L/3$) are distributed so that the positions of the points lying on opposite sides of the cell differ by a lattice vector. Let us denote by \hat{H}_i the matrix of size $(L/3, 2L)$ that, right-multiplied by the vector of unknowns $\vec{d} \equiv [d_{1,0}^c, d_{1,1}^c, \dots, d_{1,L}^c, d_{1,1}^s, d_{1,2}^s, \dots, d_{1,L-1}^s]^T$, will produce the vector of values of the field H_z at the collocation points lying on the segment Σ_i . From eq. (5.28), the elements of \hat{H}_i are given by

$$(\hat{H}_i)_{jl} = [A_{1l} J_l(k_0 \rho_{1,ij}) + B_{1l} Y_l(k_0 \rho_{1,ij})] \times \begin{cases} \cos(l\phi_{1,ij}) & \text{for } l = 0, 1, \dots, L, \\ \sin(l\phi_{1,ij}) & \text{for } l = L + 1, L + 2, \dots, 2L. \end{cases} \quad (5.29)$$

The analogous matrix that, right-multiplied by \vec{d} , will produce the vector of derivatives of H_z taken in the direction normal to Σ_i will be denoted by \hat{H}'_i .

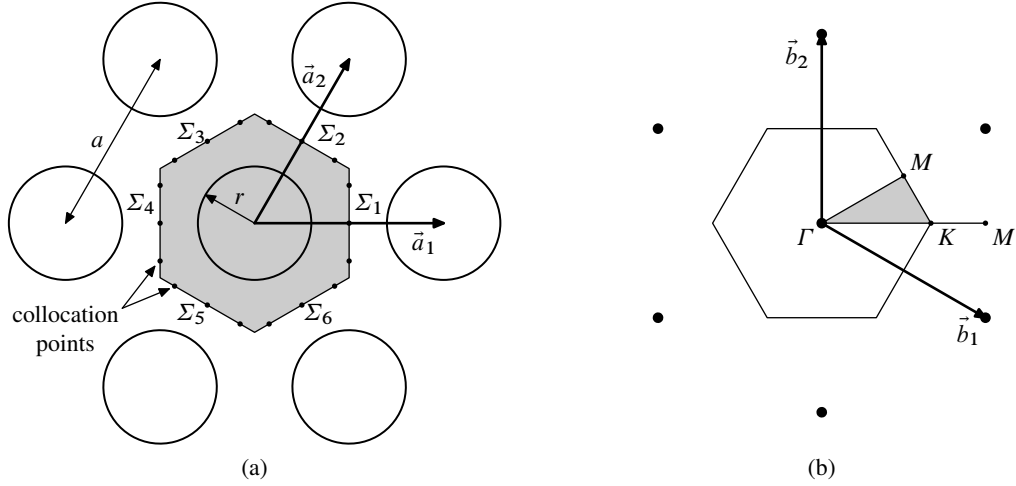


Figure 5.2 (a) Geometry of a hexagonal-lattice PC composed of circular air holes etched in a dielectric matrix. A Wigner-Seitz unit cell is marked by shading. (b) Reciprocal space of this PC. Large dots mark the positions of reciprocal lattice points. The hexagonal first Brillouin zone is also shown; its irreducible part ΓMK has been shaded.

In this matrix notation, the equations resulting from imposition of the Bloch boundary conditions at all the collocation points take then the form

$$\begin{aligned}
 \hat{H}_1 \vec{d} &= e^{i\vec{k} \cdot \vec{a}_1} \hat{H}_4 \vec{d}, & \hat{H}'_1 \vec{d} &= -e^{i\vec{k} \cdot \vec{a}_1} \hat{H}'_4 \vec{d}, \\
 \hat{H}_2 \vec{d} &= e^{i\vec{k} \cdot \vec{a}_2} \hat{H}_5 \vec{d}, & \hat{H}'_2 \vec{d} &= -e^{i\vec{k} \cdot \vec{a}_2} \hat{H}'_5 \vec{d}, \\
 \hat{H}_3 \vec{d} &= e^{i\vec{k} \cdot (\vec{a}_2 - \vec{a}_1)} \hat{H}_6 \vec{d}, & \hat{H}'_3 \vec{d} &= -e^{i\vec{k} \cdot (\vec{a}_2 - \vec{a}_1)} \hat{H}'_6 \vec{d},
 \end{aligned} \tag{5.30}$$

where $\vec{a}_1 \equiv (a, 0)$ and $\vec{a}_2 \equiv (\frac{1}{2}a, \frac{\sqrt{3}}{2}a)$ denote the basis vectors of the hexagonal lattice shown in fig. 5.2(a). The Bloch vector \vec{k} can be expressed as $\vec{k} = k_1 \vec{b}_1 + k_2 \vec{b}_2$, where $\vec{b}_1 \equiv \frac{2\pi}{a}(1, -1/\sqrt{3})$ and $\vec{b}_2 \equiv \frac{2\pi}{a}(0, 2/\sqrt{3})$ are the basis vectors of the reciprocal lattice of the PC in question, shown in fig. 5.2(b), and have the property $\vec{a}_i \cdot \vec{b}_j = 2\pi\delta_{ij}$. Consequently, eqs. (5.30) can be rewritten as

$$\begin{aligned}
 (\hat{H}_1 - e^{2\pi i k_1} \hat{H}_4) \vec{d} &= 0, & (\hat{H}'_1 + e^{2\pi i k_1} \hat{H}'_4) \vec{d} &= 0, \\
 (\hat{H}_2 - e^{2\pi i k_2} \hat{H}_5) \vec{d} &= 0, & (\hat{H}'_2 + e^{2\pi i k_2} \hat{H}'_5) \vec{d} &= 0, \\
 (e^{2\pi i k_1} \hat{H}_3 - e^{2\pi i k_2} \hat{H}_6) \vec{d} &= 0, & (e^{2\pi i k_1} \hat{H}'_3 + e^{2\pi i k_2} \hat{H}'_6) \vec{d} &= 0.
 \end{aligned} \tag{5.31}$$

To bring this system into the form of an eigenvalue problem, we can fix the value of some linear combination of k_1 and k_2 . For instance, calculations of the band structure of the hexagonal-lattice PC from fig. 5.2(a) are most often done along the boundaries of the irreducible fragment of its first Brillouin zone, the triangle ΓMK , shown in fig. 5.2(b). On the segment ΓM , the Bloch vector \vec{k} has the form $\vec{k} = \kappa \vec{b}_1 + \kappa \vec{b}_2$ with $0 \leq \kappa \leq \frac{1}{2}$. Thus, setting $k_1 = k_2 \equiv \kappa$ in eq. (5.31) and reordering terms, we obtain the linear eigenvalue problem

$$\begin{bmatrix} \hat{H}_1 \\ \hat{H}'_1 \\ \hat{H}_2 \\ \hat{H}'_2 \\ \hat{H}_3 - \hat{H}_6 \\ \hat{H}'_3 + \hat{H}'_6 \end{bmatrix} \vec{d} = e^{2\pi i \kappa} \begin{bmatrix} \hat{H}_4 \\ -\hat{H}'_4 \\ \hat{H}_5 \\ -\hat{H}'_5 \\ \hat{0} \\ \hat{0} \end{bmatrix} \vec{d}. \tag{5.32}$$

Since the matrices \hat{H}_i and \hat{H}'_i have dimensions $(L/3, 2L)$, it can be easily verified that the matrices in the above equation are square.

Things are slightly more complex for the segment ΓK . There, the Bloch vector $\vec{k} = 2\kappa\vec{b}_1 + \kappa\vec{b}_2$ with $0 \leq \kappa \leq \frac{1}{3}$, and eqs. (5.31) reduce to the *quadratic* eigenvalue problem

$$\begin{bmatrix} \hat{H}_1 \\ \hat{H}'_1 \\ \hat{H}_2 \\ \hat{H}'_2 \\ \hat{H}_6 \\ \hat{H}'_6 \end{bmatrix} \vec{d} + e^{2\pi i \kappa} \begin{bmatrix} \hat{0} \\ \hat{0} \\ -\hat{H}_5 \\ \hat{H}'_5 \\ -\hat{H}_3 \\ \hat{H}'_3 \end{bmatrix} \vec{d} + e^{4\pi i \kappa} \begin{bmatrix} -\hat{H}_4 \\ \hat{H}'_4 \\ \hat{0} \\ \hat{0} \\ \hat{0} \\ \hat{0} \end{bmatrix} \vec{d} = 0. \quad (5.33)$$

This problem can be solved in a number of ways [184]. The most popular of them, which we employ here, is *linearisation*: given an equation of the form $(\hat{A} + \lambda\hat{B} + \lambda^2\hat{C})\vec{x} = 0$, one defines $\vec{y} \equiv \lambda\vec{x}$ and solves a linear eigenvalue problem of double size, e.g.,

$$\begin{bmatrix} \hat{A} & \hat{B} \\ \hat{0} & \hat{I} \end{bmatrix} \begin{bmatrix} \vec{x} \\ \vec{y} \end{bmatrix} = \begin{bmatrix} \hat{0} & -\hat{C} \\ \hat{I} & \hat{0} \end{bmatrix} \begin{bmatrix} \vec{x} \\ \vec{y} \end{bmatrix}, \quad (5.34)$$

where \hat{I} denotes the identity matrix. Alternative linearisations are also possible, but they are advantageous primarily if the original quadratic eigenvalue problem has a particular structure—for instance, is symmetric—which is not the case here.

The band structure on the KM segment could be calculated by solving a third eigenvalue problem obtained from eq. (5.31) by imposing the constraint $k_1 + k_2 = 1$. However, owing to the six-fold rotational symmetry of the PC from fig. 5.2(a), its dispersion diagram on KM is identical with that on the segment KM' , shown in fig. 5.2(b), which is collinear with ΓK . Thus, the band structure on ΓK and KM' can be obtained simultaneously by solving the eigenvalue problem (5.33); values of κ belonging to the intervals $[0, \frac{1}{3}]$ and $[\frac{1}{3}, \frac{1}{2}]$ will then correspond to Bloch vectors lying on the segments ΓK and KM' , respectively.

5.2.3 Numerical examples

We shall now apply the method introduced in the previous subsections to the determination of the band structure of several example PCs. The results obtained with this technique will be compared to those produced by another, well-tested code. We shall also examine the convergence rate of Fourier-Bessel expansions and discuss some technical details of the implementation of the proposed method.

We begin with the simple case of a PC composed of a hexagonal lattice of air holes of radius $r = 0.3a$, where a is the lattice constant, etched in a dielectric matrix with refractive index 2.5, as shown schematically in fig. 5.2(a); this is in fact the PC introduced in section 4.4. First, it is necessary to check whether the proposed method yields results convergent with increasing truncation order L . We shall therefore study how the changes in L influence the magnitude of the Bloch vector \vec{k} of the state located on the ΓM segment and having frequency $\omega = 0.40 \times 2\pi c/a$ (chosen arbitrarily). In practice, the determination of the error of a calculated value of k is complicated by the fact that the exact magnitude of \vec{k} is not known. As a workaround, given a series of values k_i ($i = 1, 2, \dots, N_L$) obtained at several monotonically increasing truncation orders L_i , we shall take as a reference the value k_i for which the expression $(|k_i - k_{i-1}| + |k_i - k_{i+1}|)/|k_i|$ is smallest.

The collocation points on all boundaries Σ_i ($i = 1, 2, \dots, 6$) of the unit cell will be initially placed at the Gauss-Legendre quadrature points, i.e., at the roots of the Legendre polynomial of order $L/3 + 1$ [183, p. 252]. This choice will be later demonstrated to be near-optimal.

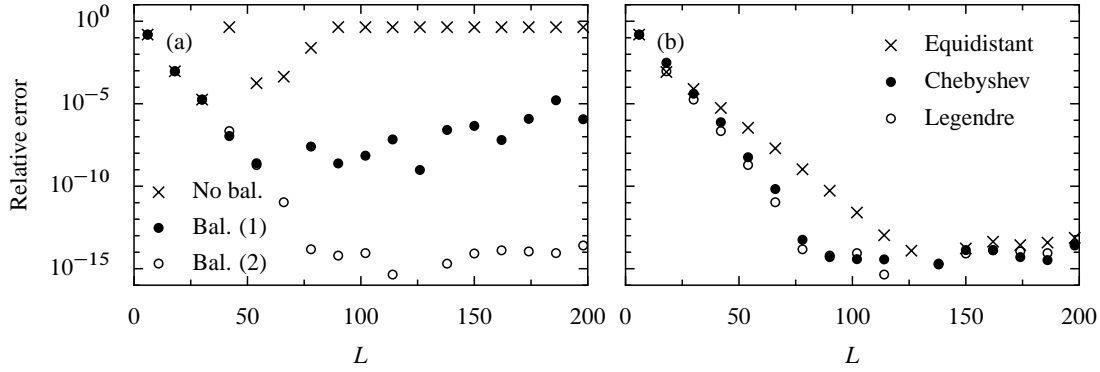


Figure 5.3 (a) Convergence of the magnitude of the Bloch vector \vec{k} of the state located on the ΓM segment in the first Brillouin zone of the hexagonal-lattice PC shown in fig. 5.2(a). The frequency was fixed to $\omega = 0.40 \times 2\pi c/a$. The different data series refer to results obtained with different levels of eigenvalue-problem balancing. Crosses: no balancing. Black circles: out-of-the-box balancing as provided by LAPACK. White circles: balancing preceded by elimination of nonzero matrix entries due to round-off error, as described in the text. (b) Convergence of k with three different distributions of collocation points: equidistant points (crosses), Gauss-Chebyshev quadrature points (black circles), Gauss-Legendre quadrature points (white circles).

Since Bessel functions of different orders vary greatly in magnitude for a fixed argument, the eigenvalue problems (5.32) and (5.33) very quickly become numerically close to singular if no rescaling of the basis functions is done. This leads to erroneous results. As a remedy, it is possible to scale the basis functions manually, e.g., by normalising them to the value they attain at a typical (in some sense) distance from the collocation points to the origin of the coordinate system. However, we found it more convenient to rely on the matrix-pair balancing algorithm due to Ward [185], which can be invoked automatically by the generalised non-symmetric eigensolver routine *ggev* from the LAPACK library [186]. In fig. 5.3 the points marked with black circles show the convergence of k calculated in this way with the truncation order L . Clearly, relative accuracy of $\sim 10^{-7}$ is achieved in a fairly wide range of truncation orders. However, there is still room for improvement, since the machine precision is much higher ($\sim 10^{-16}$).

The performance of the balancing algorithm of Ward [185] is degraded by the presence of small matrix elements due to round-off error [187, *balance* function]. Such entries do occur in our case; they correspond to collocation points located on nodal lines of trigonometric functions $\cos(l\phi_m)$ and $\sin(l\phi_m)$ of various orders l [cf. eq. (5.29)]. It is impractical to locate such points by hand. Therefore we have used instead a heuristic procedure that looks for matrix entries smaller than a given fraction γ of the average magnitude of the elements of the column they lie in. These entries are subsequently replaced with zeros. The value $\gamma = 10^{-10}$ seems to work well. As demonstrated by the series marked with white circles in fig. 5.3(a), introduction of this procedure leads to a significant increase of the attainable relative accuracy, which reaches 10^{-14} .

We have also studied the dependence of the convergence rate on the placement of collocation points. Three distributions were considered: Gauss-Legendre, Gauss-Chebyshev and equispaced. As shown in fig. 5.3(b), the former two yield approximately the same convergence rate of k (the Gauss-Legendre distribution performing marginally better), while the equispaced points fare distinctly worse. These tendencies have also been observed for other frequencies and PC geometries. Thus, in the remaining examples we use the Gauss-Legendre distribution.

In figs. 5.4(a) and (b) the band structures of the crystal from fig. 5.2 computed for p and s polarisations with the method under study are compared with the data obtained using the MPB library [188]. For both polarisations, a perfect visual agreement can be seen.

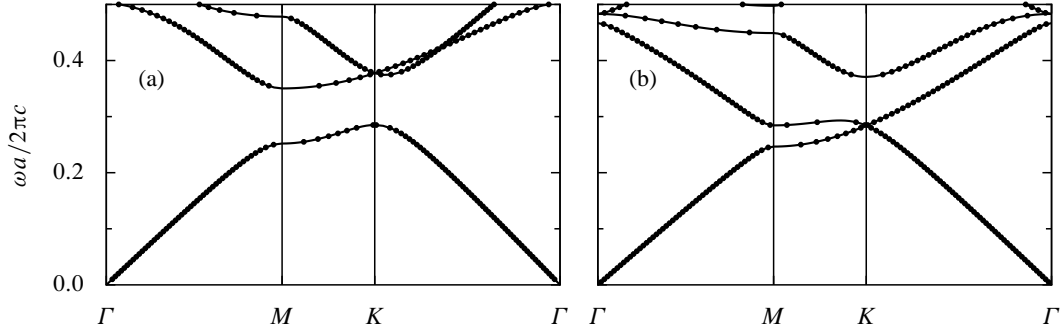


Figure 5.4 Comparison of the (a) p -polarisation and (b) s -polarisation band structure of the hexagonal-lattice crystal from fig. 5.2, calculated with the method described here (points) and with the MPB library (lines).

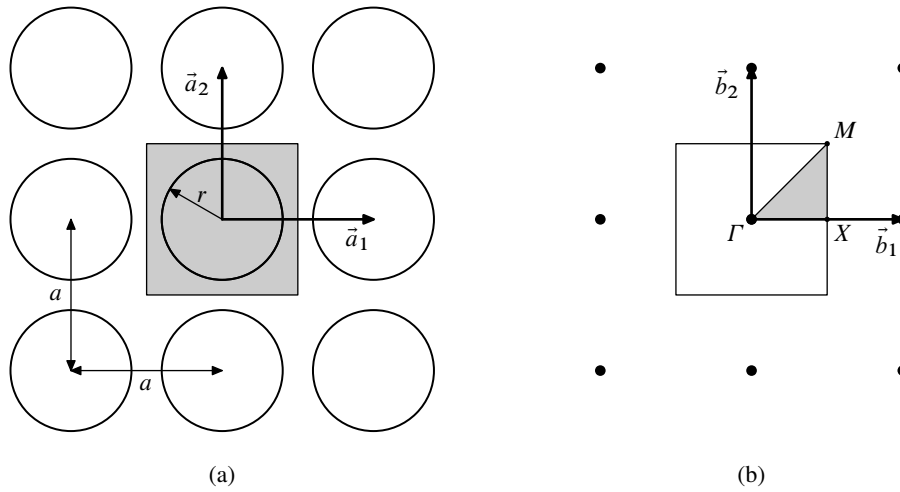


Figure 5.5 (a) Geometry of a square-lattice PC composed of circular air holes etched in a dielectric matrix. A Wigner-Seitz unit cell is marked by shading. (b) Reciprocal space of this PC. Large dots mark the positions of reciprocal lattice points. The square first Brillouin zone is also shown; its irreducible part ΓMX has been shaded.

We shall now move on to the analysis of the square-lattice PC shown in fig. 5.5(a), composed of air holes of radius r etched in a dielectric matrix with refractive index 3.4. We shall focus on the case of large r (close to $\frac{1}{2}a$). Without Vekua's theory, one could have doubts about the validity of the method for $r > a(1 - \sqrt{2})/2 \approx 0.29a$, since in this case the circumscribed circle of a unit cell crosses the inclusions from the neighbouring cells, and hence it is not clear whether a Fourier-Bessel representation of the field near the cell corners is valid. We shall show that even for $r \approx \frac{1}{2}a$ the method still produces correct results, in accordance with Vekua's assertion.

Figure 5.6 shows the juxtaposition of the band structures of the PC from fig. 5.5(a) with $r = 0.49a$ obtained with the present technique and with MPB. As before, a perfect visual agreement is apparent. In turn, in fig. 5.7 we compare the convergence of the magnitude of the vector \vec{k} of a Bloch state lying on the ΓM segment for the two polarisations and three values of r : $0.45a$, $0.49a$ and $0.50a$. In each case, the frequency is fixed so as to correspond to k roughly equal to $0.25a$. It can be seen that in the p polarisation case the convergence slows down distinctly as r approaches $0.50a$; this is probably related to the occurrence of field singularities at the points of contact of neighbouring holes. Such singular fields cannot be represented efficiently with a regular function basis. Even so, a relative accuracy of $\sim 10^{-4}$ is attainable with a reasonable number of basis functions.

Comparison of figs. 5.3(a) and 5.7 shows that the ultimate relative error of the calculations done for

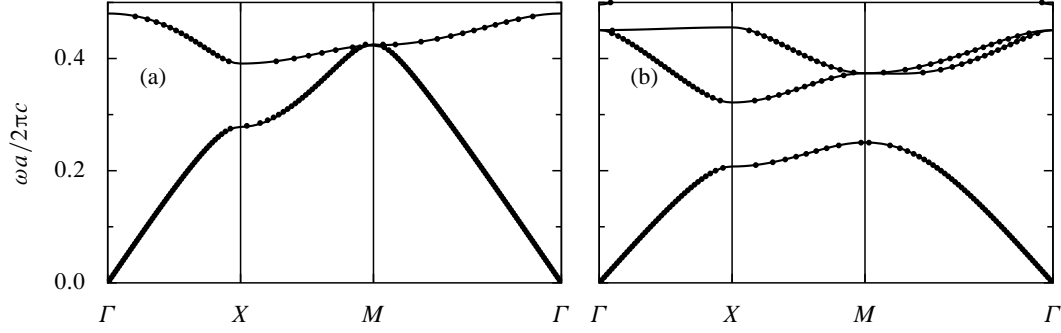


Figure 5.6 Comparison of the (a) p -polarisation and (b) s -polarisation band structure of the square-lattice crystal from fig. 5.5, calculated with the method described here (points) and with the MPB library (lines).

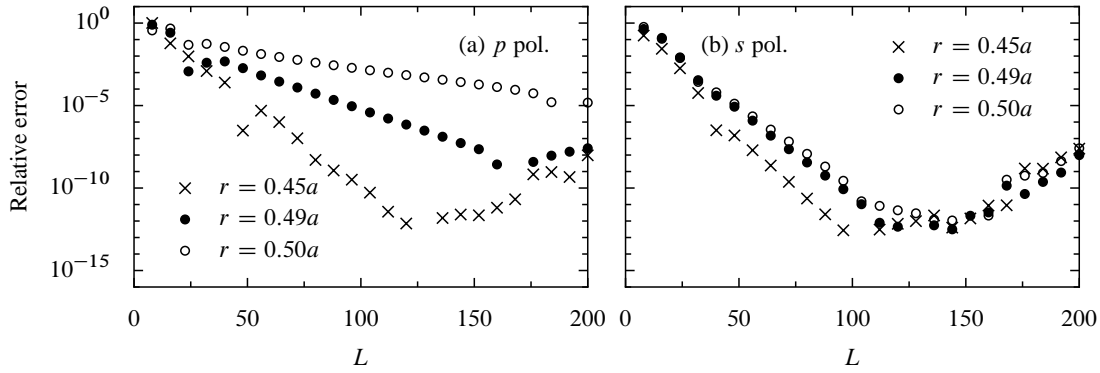


Figure 5.7 Convergence of the magnitude of the Bloch vector \vec{k} of the state located on the ΓM segment in the first Brillouin zone of the square-lattice PC shown in fig. 5.5(a) for (a) p polarisation and (b) s polarisation. The frequency was fixed to: (a) $\omega = 0.38 \times 2\pi c/a$ for $r = 0.45a$; $\omega = 0.40 \times 2\pi c/a$ for $r = 0.49a$; and $\omega = 0.47 \times 2\pi c/a$ for $r = 0.50a$; (b) $\omega = 0.35 \times 2\pi c/a$ for $r = 0.45a$; $\omega = 0.40 \times 2\pi c/a$ for $r = 0.49a$; and $\omega = 0.40 \times 2\pi c/a$ for $r = 0.50a$. In all these cases, $k \approx 0.25 \times 2\pi/a$.

the square-lattice PC is slightly larger than in the hexagonal-lattice case. This is probably caused by the fact that the spread of the radial coordinates of the collocation points placed on a square is greater than on a hexagon. Therefore the range of values taken by any given basis function at different collocation points is larger in the former case, and this reduces the efficiency of the balancing algorithm.

The third example to be studied is the PC composed of a hexagonal lattice of “shamrocks”, i.e., patterns of three adjacent circular air holes of radius $0.2a$, shown in fig. 5.8(a). The PC matrix is assumed to be magneto-optical, with a tensorial permittivity of the form (4.31) with $\epsilon = (2.5)^2$ and $g = 0.1$; these parameters correspond roughly to those of BIG in the infrared range (see section 4.4). In this structure, which has already been discussed briefly in section 3.4.3, both the spatial inversion symmetry and the time-reversal symmetry of Maxwell’s equation are broken; therefore, it is nonreciprocal and its band structure has no centre of symmetry. A particularly striking consequence of this fact is the existence of unidirectional band gaps. Such a band gap appears, for instance, in the neighbourhood of frequency $\omega = 0.3915 \times 2\pi c/a$. Figure 5.8(b) shows the equifrequency curve at this value of ω . Clearly, there exist propagative bands at $k_x = \pi/(3a)$ (close to the K points), whereas there are none at $k_x = -\pi/(3a)$ (close to the K' points). As noted in ref. 115, a slab of such a PC can be used as an isolator.*

* As a historical note, we mention that the unidirectional-mirror effect caused by the lifting of the spatial inversion symmetry, described in ref. 115, had originally been discovered in the PC shown in fig. 5.8(a). However, it was subsequently found that a PC composed of triples of slightly overlapping holes provides a larger unidirectional gap and would be easier to manufacture. Such a system cannot be directly handled by the method presented here; therefore, calculations of its band

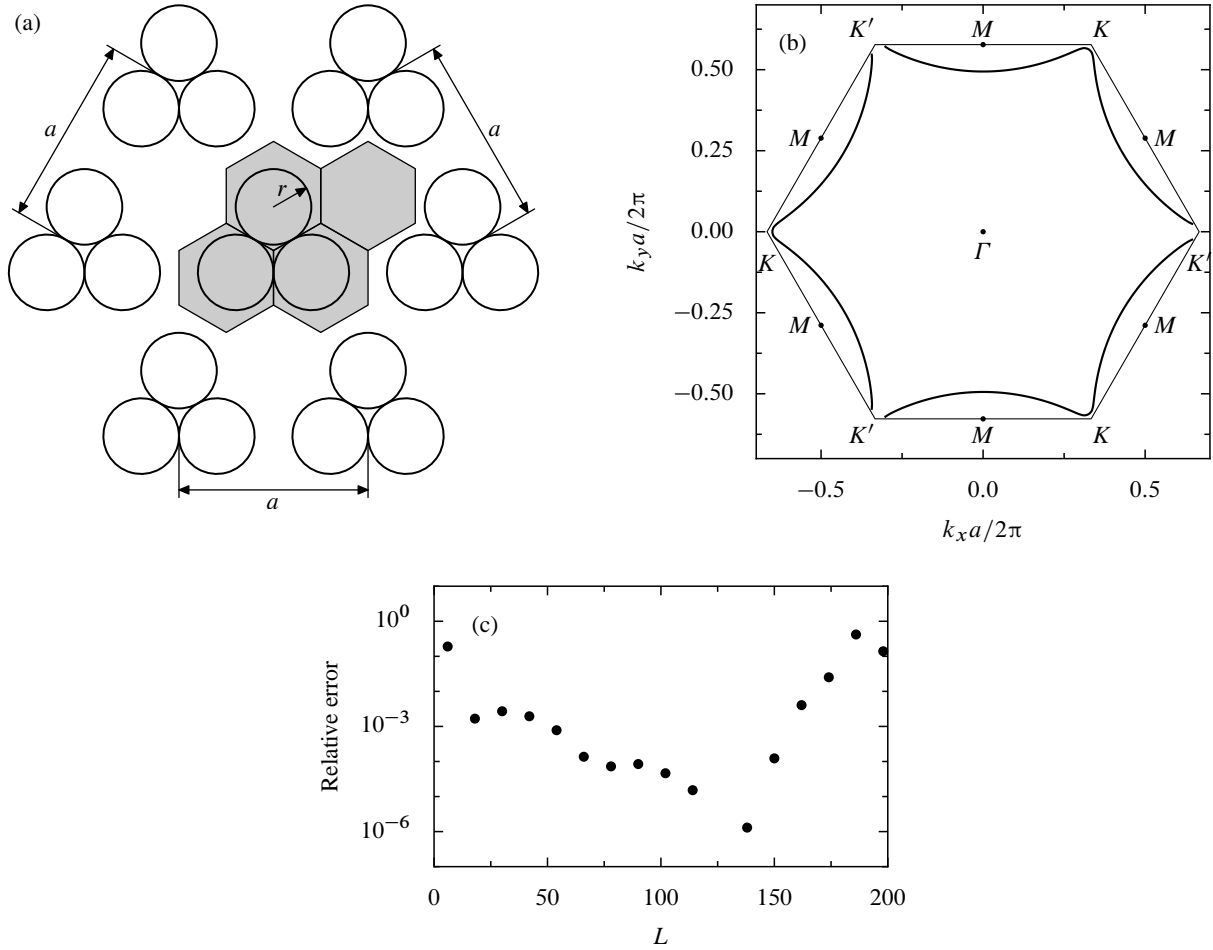


Figure 5.8 (a) Geometry of the PC composed of a hexagonal lattice of groups of three adjacent circular holes etched in a magneto-optical matrix. The shaded region is the unit cell composed of four hexagonal subcells that was used in calculations. (b) p -polarisation equifrequency curve of this crystal at $\omega = 0.3915 \times 2\pi c/a$. (c) Convergence of the magnitude of the Bloch vector \vec{k} of the state located on the ΓM segment in the first Brillouin zone of this crystal at the same frequency.

The calculations of the equifrequency curve shown in fig. 5.8(b) were made by dividing the PC's unit cell into four hexagonal subcells outlined in fig. 5.8(a), one of them empty. Owing to the presence of field singularities at the cylinder junction points and the offset of the inclusion centres with respect to the hexagon centres, which causes a wider spread of the radial coordinates of different collocation points, only a moderate relative accuracy of $\sim 10^{-5}$ was attained in simulations, as evidenced by the convergence plot from fig. 5.8(c). For very large truncation orders ($L \geq 150$) round-off error increasingly corrupts the results.

In section 4.4 another class of PC systems was studied with the method proposed here: waveguides embedded in the hexagonal-lattice crystal from fig. 5.2. The band structures of two such waveguides are plotted in fig. 4.9. These calculation were done using the supercell technique, with artificial quasi-periodic boundary conditions imposed on the segments $\Sigma_1 - \Sigma_4$ of the supercell shown schematically in fig. 5.9.

structure reported in ref. 115 were performed with the MPB library [188].

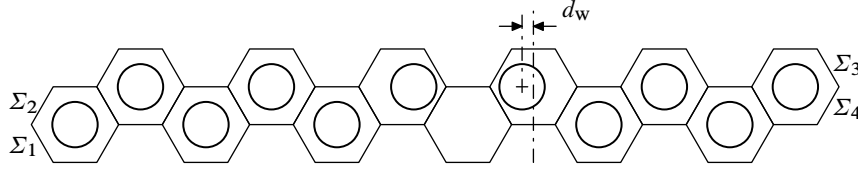


Figure 5.9 Geometry of the supercell used for the calculation of the waveguide dispersion relations shown in fig. 4.9.

5.2.4 Conclusions

In this section we have presented a method of calculating band structures of 2D PCs composed of circular cylinders by help of Fourier-Bessel expansions. Its cardinal virtue is its high efficiency: owing to the exponential convergence of the method, it is possible to achieve a relative accuracy better than 10^{-10} at a modest computational cost. Therefore the proposed technique can provide extremely accurate reference values for the purposes of testing other numerical methods. High accuracy is also invaluable in studies of tiny effects, such as the nonreciprocity induced by a static magnetic field at optical frequencies.

For PCs whose unit cell need not be divided into subcells, the method has an extremely simple implementation. On the other hand, if multiple subcells are present, the necessary bookkeeping can be tricky; however, it should be possible to automatise the imposition of the appropriate boundary conditions to a certain degree. Disadvantages of the technique in question lie primarily in its restriction to systems containing *circular* inclusions and in the degradation of its accuracy for subcells whose shape deviates markedly from that of a circle concentric with the embedded inclusion. This latter problem might possibly be alleviated with more advanced matrix-pair balancing algorithms, such as those presented in ref. 189.

5.3 Finite-element simulations of three-dimensional axisymmetric cavities

5.3.1 Introduction

In this section we shall describe the finite-element (FE) method used to calculate the eigenmodes of open 3D axisymmetric cavities containing gyrotropic materials. This technique was used to obtain the results presented in section 4.6.

There are two major approaches to FE simulations of axisymmetric systems [60, p. 912–913]. Early researchers [190, 191] made use of the possibility of expressing all the components of the electromagnetic fields \vec{E} and \vec{H} in such systems in terms of the so-called coupled azimuthal potentials ρE_ϕ and ρH_ϕ , which were subsequently discretised with standard nodal FEs. However, Maxwell's equations written in terms of these potentials have nonphysical singularities at certain radii, whose presence affects adversely the accuracy of calculations.

In 1993, Lee et al. [192] proposed an alternative approach to the problem of finding the eigenmodes of a closed axisymmetric cavity. He formulated the equations in terms of the two meridional (ρ and z) components of the electric fields, expanded into curl-conforming vector elements, and the electric azimuthal potential ρE_ϕ , expanded into nodal elements. The boundary conditions on the z axis were not yet treated in a sophisticated way. Therefore, the expressions for the elements of the matrices representing the discretised equations contained singular integrals, whose computation can be numerically demanding. Later, Chinellato [193] established a solid mathematical foundation for this approach, introducing also a set of carefully crafted techniques for the calculation of the singular integrals. Combined with a PML-based truncation of the computational domains, this method was used for the determination of the eigenmodes of open dielectric axisymmetric resonators [194]. Hiptmair and Ledger [195]

extended it to FEs of arbitrary order, so-called *hp* FEs, which allow to obtain exponential convergence, even if field singularities are present, by combining mesh refinement with an increase of the element order.

In the meantime, however, it had been shown that the enforcement of the boundary conditions on the z axis is facilitated if a particular change of variables is made so that the vector FEs are used to expand a specific combination of the azimuthal and meridional components of \vec{E} rather than the “pure” meridional part [196, 197]. This change of variables removes also all singular integrals. Greenwood and Jin applied this idea to simulations of wave scattering [51] and radiation [198] by axisymmetric bodies, using PMLs to truncate the computational domain. Finally, Venkatarayalu [52] proposed an algorithm of elimination of unwanted static (zero-frequency) cavity eigenmodes from the FE approximation space, which is reputed to accelerate the convergence of iterative eigenvalue solvers.

The particular variant of the axisymmetric FE method implemented during this thesis combines elements of several works cited above. It is probably closest to that of Greenwood and Jin [51]: vector FEs are used to expand a superposition of the azimuthal and meridional components of \vec{E} ; exponential Fourier expansions in the azimuthal direction are used rather than trigonometric ones; and the computational domain is truncated with PMLs. On the other hand, unlike Greenwood and Jin, we look for the eigenmodes of the modelled system rather than its response to an incident field; thus, in a manner similar to that of Venkatarayalu [52], we derive an eigenvalue problem rather than an inhomogeneous system of equations. Finally, like Hiptmair and Ledger [195], we use relatively high-order FE expansions in order to improve the efficiency of calculations. The original contribution of our work is the extension of the method to the case of media with gyrotropic material properties. Before, it had been formulated only for diagonal permittivity and permeability tensors, which are used to represent PMLs adapted to cylindrical coordinates [51, 53, 54].

In the next subsection we present the derivation of our algorithm. Some issues, in particular the manner of boundary condition enforcement on the z axis, are discussed in rather more detail than it has been done in literature [51, 52, 196].* We hope that their pedagogical derivation here will be useful for future researchers intending to use or program the FE method for axisymmetric structures. Subsection 5.3.3 is devoted to the numerical implementation of the proposed technique. Finally, in subsection 5.3.4 we evaluate its accuracy.

Several examples of the application of the method to the calculation of the eigenmodes of specific cavities can be found in section 4.6.

5.3.2 Formulation

Axisymmetric systems We begin by defining precisely what we mean by an axisymmetric structure. A system characterised by position-dependent permittivity and permeability tensors is said to be *axisymmetric* if the representations of these tensors in *cylindrical coordinates* (ρ, ϕ, z) are independent from the azimuthal coordinate ϕ . It is instructive to check in what circumstances a tensor field whose Cartesian components are constant in some area of space stays independent from ϕ when it is transformed to cylindrical coordinates. Consider, for instance, the permittivity tensor $\hat{\epsilon}$. Its Cartesian components are defined by the relation

$$\begin{bmatrix} D_x \\ D_y \\ D_z \end{bmatrix} = \begin{bmatrix} \epsilon_{xx} & \epsilon_{xy} & \epsilon_{xz} \\ \epsilon_{yx} & \epsilon_{yy} & \epsilon_{yz} \\ \epsilon_{zx} & \epsilon_{zy} & \epsilon_{zz} \end{bmatrix} \begin{bmatrix} E_x \\ E_y \\ E_z \end{bmatrix}, \quad (5.35)$$

* We have not had access to ref. 197, in which this topic is probably also considered.

where $\vec{E} \equiv (E_x, E_y, E_z)^T$ is the electric field and $\vec{D} \equiv (D_x, D_y, D_z)^T$ the electric displacement. Since the Cartesian components of a vector \vec{F} are related to the cylindrical ones by

$$\begin{bmatrix} F_x \\ F_y \\ F_z \end{bmatrix} = \begin{bmatrix} \cos \phi & -\sin \phi & 0 \\ \sin \phi & \cos \phi & 0 \\ 0 & 0 & 1 \end{bmatrix} \begin{bmatrix} F_\rho \\ F_\phi \\ F_z \end{bmatrix}, \quad (5.36)$$

the tensor $\hat{\epsilon}$ in cylindrical coordinates will take the form

$$\begin{aligned} \hat{\epsilon}^{(\text{cyl})} &= \begin{bmatrix} \cos \phi & -\sin \phi & 0 \\ \sin \phi & \cos \phi & 0 \\ 0 & 0 & 1 \end{bmatrix}^{-1} \begin{bmatrix} \epsilon_{xx} & \epsilon_{xy} & \epsilon_{xz} \\ \epsilon_{yx} & \epsilon_{yy} & \epsilon_{yz} \\ \epsilon_{zx} & \epsilon_{zy} & \epsilon_{zz} \end{bmatrix} \begin{bmatrix} \cos \phi & -\sin \phi & 0 \\ \sin \phi & \cos \phi & 0 \\ 0 & 0 & 1 \end{bmatrix} \\ &= \frac{1}{2} \begin{bmatrix} \epsilon_{xx} + \epsilon_{yy} & \epsilon_{xy} - \epsilon_{yx} & 0 \\ -(\epsilon_{xy} - \epsilon_{yx}) & \epsilon_{xx} + \epsilon_{yy} & 0 \\ 0 & 0 & 2\epsilon_{zz} \end{bmatrix} + \begin{bmatrix} 0 & 0 & \epsilon_{xz} \\ 0 & 0 & \epsilon_{yz} \\ \epsilon_{zx} & \epsilon_{zy} & 0 \end{bmatrix} \cos \phi \\ &\quad + \begin{bmatrix} 0 & 0 & \epsilon_{yz} \\ 0 & 0 & -\epsilon_{xz} \\ \epsilon_{zy} & -\epsilon_{zx} & 0 \end{bmatrix} \sin \phi + \frac{1}{2} \begin{bmatrix} \epsilon_{xx} - \epsilon_{yy} & \epsilon_{xy} + \epsilon_{yx} & 0 \\ \epsilon_{xy} + \epsilon_{yx} & -(\epsilon_{xx} - \epsilon_{yy}) & 0 \\ 0 & 0 & 0 \end{bmatrix} \cos 2\phi \\ &\quad + \frac{1}{2} \begin{bmatrix} \epsilon_{xy} + \epsilon_{yx} & -(\epsilon_{xx} - \epsilon_{yy}) & 0 \\ -(\epsilon_{xx} - \epsilon_{yy}) & -(\epsilon_{xy} + \epsilon_{yx}) & 0 \\ 0 & 0 & 0 \end{bmatrix} \sin 2\phi. \end{aligned} \quad (5.37)$$

Obviously, in order that $\epsilon^{(\text{cyl})}$ be independent of ϕ , all the terms proportional to trigonometric functions of ϕ in the above expression must vanish. This is the case if and only if $\epsilon_{xx} = \epsilon_{yy}$, $\epsilon_{xy} = -\epsilon_{yx}$ and $\epsilon_{xz} = \epsilon_{yz} = \epsilon_{zx} = \epsilon_{zy} = 0$. Thus, a permittivity tensor field having a locally constant Cartesian representation will be independent from ϕ after transformation to cylindrical coordinates if and only if it has the form

$$\hat{\epsilon}^{(\text{Cart})} = \begin{bmatrix} \epsilon_t & i\epsilon_g & 0 \\ -i\epsilon_g & \epsilon_t & 0 \\ 0 & 0 & \epsilon_z \end{bmatrix} \quad (5.38)$$

(the imaginary unit has been introduced into the off-diagonal components purely for future convenience and for consistency with other parts of this manuscript). It is worth noting that from eq. (5.37) it follows that in this case $\hat{\epsilon}^{(\text{cyl})} = \hat{\epsilon}^{(\text{Cart})}$. Obviously, the above reasoning can be repeated for the permeability tensor $\hat{\mu}$.

In this way we have shown that axisymmetric systems may not contain physical* materials whose permittivity or permeability tensors have a form other than (5.38).

Statement of the problem We seek the (leaky) eigenmodes of an open axisymmetric cavity with the given permittivity $\hat{\epsilon}(\rho, z)$ and permeability $\hat{\mu}(\rho, z)$ (in the rest of this section, components of material property tensors will be assumed to be given in cylindrical coordinates unless mentioned otherwise), fulfilling the Sommerfeld's boundary conditions [60, p. 294] at infinity. Since it is not possible to discretise the whole space \mathbb{R}^3 with FEs, simulations will be done on the finite cylindrical domain

$$\Omega_0 \equiv \{(\rho, \phi, z) | 0 \leq \rho \leq R \text{ and } 0 \leq \phi < 2\pi \text{ and } Z_- \leq z \leq Z_+\}. \quad (5.39)$$

* This conclusion does not apply to "numerical" media such as PMLs, which need not have piecewise-constant Cartesian representations of the permittivity and permeability tensors.

In order to suppress spurious reflections on the boundaries of Ω_0 , its surface will be coated with PMLs, treated numerically as special anisotropic media, whose nature will be specified later in this section. On the whole surface of Ω_0 perfect-electric-conductor boundary conditions will be imposed.

Wave equation We shall now demonstrate that the independence of $\hat{\epsilon}$ and $\hat{\mu}$ from ϕ allows to convert the vector wave equation for the electric field \vec{E} in Ω_0 into an infinite set of decoupled equations for the restriction of \vec{E} to a single meridional plane of Ω_0 .

Eliminating the magnetic field \vec{H} from the time-harmonic source-free Maxwell's equations (1.4a)–(1.4b), we get

$$\vec{\nabla} \times [\hat{\mu}^{-1} \cdot (\vec{\nabla} \times \vec{E})] = k_0^2 \hat{\epsilon} \cdot \vec{E}, \quad (5.40)$$

where $k_0 \equiv \omega/c$ is the free-space wave number. The electric field \vec{E} can be expanded in a Fourier series with respect to ϕ :

$$\vec{E}(\rho, \phi, z) = \sum_{l \in \mathbb{Z}} \vec{E}_l(\rho, z) e^{il\phi}, \quad (5.41)$$

so that eq. (5.40) becomes

$$\sum_l \vec{\nabla} \times \{[\hat{\mu}(\rho, z)]^{-1} \cdot [\vec{\nabla} \times \vec{E}_l(\rho, z) e^{il\phi}]\} = k_0^2 \sum_l \hat{\epsilon}(\rho, z) \cdot \vec{E}_l(\rho, z) e^{il\phi}. \quad (5.42)$$

In cylindrical coordinates,

$$\vec{\nabla} = \vec{\nabla}_t + \vec{e}_\phi \rho^{-1} \partial_\phi, \quad \text{where} \quad \vec{\nabla}_t \equiv \vec{e}_\rho \partial_\rho + \vec{e}_z \partial_z. \quad (5.43)$$

Since all functions in eq. (5.42) depend on ϕ only through factors $e^{il\phi}$, differentiation over ϕ reduces to multiplication by il . As a result, eq. (5.42) can be rewritten as

$$\sum_l \vec{\nabla}_l \times \{[\hat{\mu}(\rho, z)]^{-1} \cdot [\vec{\nabla}_l \times \vec{E}_l(\rho, z)]\} e^{il\phi} = k_0^2 \sum_l \hat{\epsilon}(\rho, z) \cdot \vec{E}_l(\rho, z) e^{il\phi}, \quad (5.44)$$

where

$$\vec{\nabla}_l \equiv \vec{\nabla}_t + \vec{e}_\phi il \rho^{-1}. \quad (5.45)$$

From the linear independence of the functions $e^{il\phi}$ ($l \in \mathbb{Z}$) on the interval $[0, 2\pi]$ it follows that eq. (5.44) is equivalent to a system of decoupled equations on individual Fourier coefficients $\vec{E}_l(\rho, z)$:

$$\vec{\nabla}_l \times \{[\hat{\mu}(\rho, z)]^{-1} \cdot [\vec{\nabla}_l \times \vec{E}_l(\rho, z)]\} = k_0^2 \hat{\epsilon}(\rho, z) \cdot \vec{E}_l(\rho, z) \quad \text{for each } l \in \mathbb{Z}. \quad (5.46)$$

Thus, the eigenmodes of an axisymmetric system can be classified according to their azimuthal order l and found by solving separately each of the equations (5.46) for the field $\vec{E}_l(\rho, z)$ defined on the 2D domain

$$\Omega \equiv \{(\rho, z) | 0 \leq \rho \leq R \text{ and } Z_- \leq z \leq Z_+\}. \quad (5.47)$$

Needless to say, this brings substantial savings in computational time in comparison to the solution of the original equation (5.40) defined on the 3D domain Ω_0 . The geometry of the domain Ω is shown schematically in fig. 5.10.

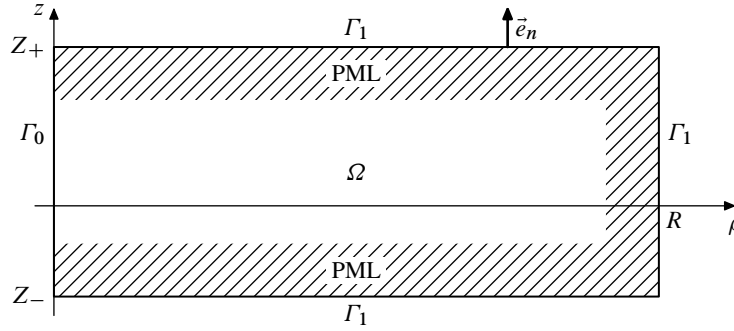


Figure 5.10 Geometry of the domain Ω . Regions filled with PMLs are hatched.

Weak form The FE method is based on the Galerkin's technique, itself a representative of the class of weighted-residual methods for solving differential equations. In these methods, a generalised differential eigenvalue problem [like the one from eq. (5.46)] of the general form $\mathcal{A}u = \lambda \mathcal{B}u$, where \mathcal{A} and \mathcal{B} are differential operators, u is the unknown function, and λ is the eigenvalue, is converted into a system of algebraic linear equations by (i) expanding u in a series of known *basis functions* u_n and (ii) requiring that an appropriately defined inner product $(v_n, \mathcal{R}u)$ of a number of *test functions* v_n with the *residual* $\mathcal{R}u \equiv \mathcal{A}u - \lambda \mathcal{B}u$ vanish. In the Galerkin's method the set of test functions is chosen to be identical with that of basis functions [199, section 3.1].

Boundary conditions can be incorporated into the equation $(v_n, \mathcal{R}u) = 0$ using integration by parts. This leads to the *weak form* of a differential equation, in which the original equation and its associated boundary conditions are merged in a single formula.

We shall now derive the weak form of eq. (5.46). We define the inner product in the usual way,

$$(\vec{v}, \vec{u}) \equiv \iint_{\Omega} \vec{v}^*(\rho, z) \cdot \vec{u}(\rho, z) d\Omega. \quad (5.48)$$

The condition that the inner product of an arbitrary test function \vec{v} with the residual of eq. (5.46) vanish takes then the form (henceforth we omit the superscript l in \vec{E}_l)

$$\iint_{\Omega} \vec{v}^* \cdot \{ \vec{\nabla}_l \times [\hat{\mu}^{-1} \cdot (\vec{\nabla}_l \times \vec{E})] \} d\Omega = k_0^2 \iint_{\Omega} \vec{v}^* \cdot \hat{\epsilon} \cdot \vec{E} d\Omega \quad (5.49)$$

It can be shown that the following integration-by-parts formula is valid:

$$\iint_{\Omega} \vec{v}^* \cdot (\vec{\nabla}_l \times \vec{u}) d\Omega = \iint_{\Omega} (\vec{\nabla}_l \times \vec{v})^* \cdot \vec{u} d\Omega - \oint_{\partial\Omega} (\vec{v}^* \times \vec{u}) \cdot \vec{e}_n dl; \quad (5.50)$$

here, \vec{v} and \vec{u} are arbitrary sufficiently regular functions, $\partial\Omega$ is the boundary of Ω , and \vec{e}_n denotes the unit vector normal to $\partial\Omega$ and directed outwards. Applying this formula to eq. (5.49), we get

$$\iint_{\Omega} (\vec{\nabla}_l \times \vec{v})^* \cdot \hat{\mu}^{-1} \cdot (\vec{\nabla}_l \times \vec{E}) d\Omega - \oint_{\partial\Omega} \{ \vec{v}^* \times [\hat{\mu}^{-1} \cdot (\vec{\nabla}_l \times \vec{E})] \} \cdot \vec{e}_n dl = k_0^2 \iint_{\Omega} \vec{v}^* \cdot \hat{\epsilon} \cdot \vec{E} d\Omega. \quad (5.51)$$

Later in this subsection we shall use the boundary conditions to dispense with the contour integral in the above equation.

Boundary conditions The contour $\partial\Omega$ can be divided into two parts: that lying on the z axis, denoted henceforth Γ_0 , and the rest, denoted Γ_1 (see fig. 5.10). The segment Γ_1 is a subset of the surface of the original 3D domain Ω_0 . Therefore the boundary condition imposed on it has already been specified to be of the perfect-electric-conductor type. In contrast, the segment Γ_0 does not belong to the surface of Ω_0 , and the boundary conditions on it have still to be determined. They will follow from the physical requirement that the limits $\lim_{\rho \rightarrow 0} \vec{E}(\rho, \phi, z)$ and $\lim_{\rho \rightarrow 0} \vec{H}(\rho, \phi, z)$ exist and be independent from ϕ for all $z \in [Z_-, Z_+]$.

For an eigenmode of a given order l , $\vec{E}(\rho, \phi, z) = \vec{E}(\rho, z) e^{il\phi}$. Using eq. (5.36) and rewriting $\cos \phi$ and $\sin \phi$ in terms of the exponential functions $e^{\pm i\phi}$, we obtain that

$$E_x(\rho, \phi, z) = \frac{1}{2} \{ [E_\rho(\rho, z) + iE_\phi(\rho, z)] e^{i(l+1)\phi} + [E_\rho(\rho, z) - iE_\phi(\rho, z)] e^{i(l-1)\phi} \}, \quad (5.52a)$$

$$E_y(\rho, \phi, z) = \frac{1}{2i} \{ [E_\rho(\rho, z) + iE_\phi(\rho, z)] e^{i(l+1)\phi} - [E_\rho(\rho, z) - iE_\phi(\rho, z)] e^{i(l-1)\phi} \}, \quad (5.52b)$$

$$E_z(\rho, \phi, z) = E_z(\rho, z) e^{il\phi}. \quad (5.52c)$$

Thus the limits of these expressions with $\rho \rightarrow 0$ exist and are independent from ϕ only if

$$\left\{ \begin{array}{ll} \text{for } l = 0, & \text{(a) } E_\rho(0, z) = 0 \quad \text{and} \quad \text{(b) } E_\phi(0, z) = 0, \end{array} \right. \quad (5.53)$$

$$\left\{ \begin{array}{ll} \text{for } |l| = 1, & \text{(a) } E_\rho(0, z) + ilE_\phi(0, z) = 0 \quad \text{and} \quad \text{(b) } E_z(0, z) = 0, \end{array} \right. \quad (5.54)$$

$$\left\{ \begin{array}{ll} \text{for } |l| > 1, & \text{(a) } E_\rho(0, z) = 0, \quad \text{(b) } E_\phi(0, z) = 0 \quad \text{and} \quad \text{(c) } E_z(0, z) = 0. \end{array} \right. \quad (5.55)$$

Turning now to the magnetic field, from eq. (1.4a) we get

$$\begin{aligned} \vec{H}(\rho, \phi, z) &= [i\omega\mu_0\hat{\mu}(\rho, z)]^{-1} \cdot [\vec{\nabla} \times \vec{E}(\rho, \phi, z)] \\ &= [i\omega\mu_0\hat{\mu}(\rho, z)]^{-1} \cdot [\vec{\nabla}_l \times \vec{E}(\rho, z)] e^{il\phi}. \end{aligned} \quad (5.56)$$

Reasoning analogously as in the case of the electric field, we obtain the conditions

$$\left\{ \begin{array}{ll} \text{for } l = 0, & \text{(a) } [\hat{\mu}^{-1} \cdot (\vec{\nabla}_l \times \vec{E})]_\rho(0, z) = 0 \quad \text{and} \quad \text{(b) } [\hat{\mu}^{-1} \cdot (\vec{\nabla}_l \times \vec{E})]_\phi(0, z) = 0, \end{array} \right. \quad (5.57)$$

$$\left\{ \begin{array}{ll} \text{for } |l| = 1, & \text{(a) } [\hat{\mu}^{-1} \cdot (\vec{\nabla}_l \times \vec{E})]_\rho(0, z) + il[\hat{\mu}^{-1} \cdot (\vec{\nabla}_l \times \vec{E})]_\phi(0, z) = 0 \quad \text{and} \\ & \text{(b) } [\hat{\mu}^{-1} \cdot (\vec{\nabla}_l \times \vec{E})]_z(0, z) = 0, \end{array} \right. \quad (5.58)$$

$$\left\{ \begin{array}{ll} \text{for } |l| > 1, & \text{(a) } [\hat{\mu}^{-1} \cdot (\vec{\nabla}_l \times \vec{E})]_\rho(0, z) = 0, \quad \text{(b) } [\hat{\mu}^{-1} \cdot (\vec{\nabla}_l \times \vec{E})]_\phi(0, z) = 0 \quad \text{and} \\ & \text{(c) } [\hat{\mu}^{-1} \cdot (\vec{\nabla}_l \times \vec{E})]_z(0, z) = 0. \end{array} \right. \quad (5.59)$$

Finite-element expansions From now on we restrict our attention to the case $|l| \geq 1$. The derivations go slightly differently for modes with order $l = 0$, and such modes are less interesting for us, since they do not exhibit the twofold degeneracy required in a cavity forming part of a circulator. Following refs. 51, 196, 197 and 52, we introduce the following change of variables:

$$\vec{E}_t \equiv \vec{e}_\rho E_\rho + \vec{e}_z E_z = (il)^{-1} (\vec{e}_\rho E_\phi - \rho \vec{E}'_t). \quad (5.60)$$

We expand the azimuthal component of \vec{E} into nodal FE basis functions $u_{\phi n}^0(\rho, z)$ ($n = 1, 2, \dots, N_\phi$):

$$E_\phi = \sum_{n=1}^{N_\phi} E_{\phi n} u_{\phi n}^0, \quad (5.61)$$

and the new field \vec{E}'_t , tangential to the meridional plane ρz , into curl-conforming vector FE basis functions $\vec{u}_{tn}^0(\rho, z)$ ($n = 1, 2, \dots, N_t$):

$$\vec{E}'_t = \sum_{n=1}^{N_t} E'_{tn} \vec{u}_{tn}^0. \quad (5.62)$$

The coefficients $E_{\phi n}$ and E'_{tn} are the unknowns to be determined. The restrictions of the functions $u_{\phi n}^0$ and of both components of \vec{u}_{tn}^0 to any element are polynomials in ρ and z . The functions $u_{\phi n}^0$ are continuous on Ω , whereas \vec{u}_{tn}^0 have the property that their tangential components are continuous across element borders; as a result, $\nabla_t \times \vec{u}_{tn}^0$ is finite everywhere.

Gathering together eqs. (5.60)–(5.62), we obtain thus the following FE expansion of the electric field \vec{E} ,

$$\vec{E} = [\vec{e}_\phi + (il)^{-1}\vec{e}_\rho]E_\phi - (il)^{-1}\rho\vec{E}'_t = \sum_{n=1}^{N_\phi} E_{\phi n}\vec{u}_{\phi n} + \sum_{n=1}^{N_t} E'_{tn}\vec{u}_{tn}, \quad (5.63)$$

in terms of the *azimuthal basis functions*

$$\vec{u}_{\phi n} \equiv [\vec{e}_\phi + (il)^{-1}\vec{e}_\rho]u_{\phi n}^0 \quad (n = 1, 2, \dots, N_\phi) \quad (5.64)$$

and the *meridional basis functions*

$$\vec{u}_{tn} \equiv -(il)^{-1}\rho\vec{u}_{tn}^0 \quad (n = 1, 2, \dots, N_t). \quad (5.65)$$

Imposition of boundary conditions We shall now demonstrate that the chosen form of FE expansions allows to impose conditions (5.53) and (5.57) in a simple way, as well as to remove from the integrals in eq. (5.51) all singular weights, stemming from the presence of the term $\vec{e}_\phi il\rho^{-1}$ in definition (5.45) of $\vec{\nabla}_l$. We shall assume that *close to the z axis* the tensor $\hat{\mu}$ has the gyrotropic form

$$\hat{\mu} = \begin{bmatrix} \mu_t & i\mu_g & 0 \\ -i\mu_g & \mu_t & 0 \\ 0 & 0 & \mu_z \end{bmatrix} \quad (5.66)$$

As will be shown in section 5.3.3, this is the case even if PMLs are present.

We begin by expressing E_ρ , E_z and all the components of $\vec{\nabla}_l \times \vec{E}$ in terms of E_ϕ and \vec{E}'_t . Using eq. (5.60), after some straightforward algebra we obtain

$$E_\rho = (il)^{-1}(E_\phi - \rho E'_\rho), \quad (5.67a)$$

$$E_z = (il)^{-1}\rho E'_z, \quad (5.67b)$$

$$(\vec{\nabla}_l \times \vec{E})_\rho = -\partial_z E_\phi - E'_z, \quad (5.67c)$$

$$(\vec{\nabla}_l \times \vec{E})_\phi = (il)^{-1}[\partial_z E_\phi + E'_z - \rho(\partial_z E'_\rho - \partial_\rho E'_z)], \quad (5.67d)$$

$$(\vec{\nabla}_l \times \vec{E})_z = \partial_\rho E_\phi + E'_\rho. \quad (5.67e)$$

Owing to the regularity properties of the basis functions used to expand the fields E_ϕ and \vec{E}'_t , discussed above, the limits of expressions (5.67) with $\rho \rightarrow 0$ exist and are equal to

$$E_\rho(0, z) = (il)^{-1}E_\phi(0, z), \quad (5.68a)$$

$$E_z(0, z) = 0, \quad (5.68b)$$

$$(\vec{\nabla}_l \times \vec{E})_\rho(0, z) = -(\partial_z E_\phi)(0, z) - E'_z(0, z), \quad (5.68c)$$

$$(\vec{\nabla}_l \times \vec{E})_\phi(0, z) = (il)^{-1}[(\partial_z E_\phi)(0, z) + E'_z(0, z)], \quad (5.68d)$$

$$(\vec{\nabla}_l \times \vec{E})_z(0, z) = (\partial_\rho E_\phi)(0, z) + E'_\rho(0, z). \quad (5.68e)$$

Let us now study the cases $|l| = 1$ and $|l| > 1$ in turn.

For $|l| = 1$, conditions (5.54) on the electric field on the z axis are satisfied automatically: the fulfilment of condition (5.54b) follows directly from eq. (5.68b), while that of condition (5.54a) is the

consequence of eq. (5.68a) and the observation that $l = l^{-1}$ if $|l| = 1$. The satisfaction of condition (5.58a) also follows from eqs. (5.68c) and (5.68d), as can be verified by hand (the assumption that $\hat{\mu}$ is gyrotropic on the z axis is crucial here). In contrast, condition (5.58b) is not met automatically, and it will need to be imposed weakly by help of the contour-integral term in eq. (5.51), as will be demonstrated below.

For $|l| > 1$, only condition (5.55c) is automatically fulfilled, by virtue of eq. (5.68b). To satisfy conditions (5.55a), (5.55b), (5.59a) and (5.55b), homogeneous Dirichlet boundary conditions on E_ϕ and E'_z on Γ_0 must explicitly be imposed by removing from the series (5.63) the functions $\vec{u}_{\phi n}$ and \vec{u}_{tn} whose ϕ or z components are nonzero on Γ_0 . As in the case $|l| = 1$, the remaining condition (5.59c) will be imposed weakly.

For all values of l , of course, the perfect-electric-conductor boundary conditions $\vec{e}_n \times \vec{E} = 0$ on Γ_1 must also be imposed; this can be done in the manner described in the previous paragraph, by removing appropriate terms from expansion (5.63).

We are now ready to tackle the contour integral from eq. (5.51). The integration path $\partial\Omega$ is the sum of Γ_0 and Γ_1 ; let us consider first the latter part of this contour. From the identity $(\vec{a} \times \vec{b}) \cdot \vec{c} = (\vec{c} \times \vec{a}) \cdot \vec{b}$, where \vec{a} , \vec{b} and \vec{c} are arbitrary vectors, we get

$$\int_{\Gamma_1} \{\vec{v}^* \times [\hat{\mu}^{-1} \cdot (\vec{\nabla}_l \times \vec{E})]\} \cdot \vec{e}_n \, dl = \int_{\Gamma_1} (\vec{v} \times \vec{e}_n)^* \cdot \hat{\mu}^{-1} \cdot (\vec{\nabla}_l \times \vec{E}) \, dl. \quad (5.69)$$

But since in the Galerkin's method the set of test functions is identical with that of basis functions and, as we have said above, the latter will be chosen so as to fulfil the perfect-electric-conductor boundary conditions on Γ_1 , the cross product $\vec{v} \times \vec{e}_n$ will vanish on Γ_1 and this part of the integration path will bring no contribution to the integral. Integration over Γ_0 is more interesting. Using the aforementioned identity one more time, we convert the integral to the form

$$\int_{\Gamma_0} \{\vec{v}^* \times [\hat{\mu}^{-1} \cdot (\vec{\nabla}_l \times \vec{E})]\} \cdot \vec{e}_n \, dl = \int_{\Gamma_0} \vec{v}^* \cdot \{[\hat{\mu}^{-1} \cdot (\vec{\nabla}_l \times \vec{E})] \times \vec{e}_n\} \, dl. \quad (5.70)$$

Since on Γ_0 the unit vector $\vec{e}_n = -\vec{e}_\rho$,

$$\int_{\Gamma_0} \{\vec{v}^* \times [\hat{\mu}^{-1} \cdot (\vec{\nabla}_l \times \vec{E})]\} \cdot \vec{e}_n \, dl = - \int_{\Gamma_0} [\hat{\mu}^{-1} \cdot (\vec{\nabla}_l \times \vec{E})]_z v_\phi^* \, dl + \int_{\Gamma_0} [\hat{\mu}^{-1} \cdot (\vec{\nabla}_l \times \vec{E})]_\phi v_z^* \, dl. \quad (5.71)$$

By conditions (5.58b) and (5.59c), for all $l \geq 1$ the z component of $\hat{\mu}^{-1} \cdot (\vec{\nabla}_l \times \vec{E})$ should vanish on Γ_0 ; hence, the first term on the right-hand side of eq. (5.71) will approach zero as the FE approximation of a given cavity eigenmode tends to the true solution. Therefore, we shall omit this term from the discretised equation (5.51). On the other hand, the second term will vanish because, as we have said above, the chosen FE expansions satisfy automatically the condition that $E_z = 0$ on Γ_0 [conditions (5.54b) and (5.55c)]; hence, v_z will disappear on this part of the integration contour.

In this way we have shown that the contour integral can be dropped from the weak form (5.51) of the vector wave equation of an axisymmetric system. We arrive thus at the final form of this equation:

$$\iint_{\Omega} (\vec{\nabla}_l \times \vec{v})^* \cdot \hat{\mu}^{-1} \cdot (\vec{\nabla}_l \times \vec{E}) \, d\Omega = k_0^2 \iint_{\Omega} \vec{v}^* \cdot \hat{\epsilon} \cdot \vec{E} \, d\Omega. \quad (5.72)$$

Conversion into algebraic eigenvalue problem In order to convert eq. (5.72) into a system of algebraic equations, we write it separately for each test function $\vec{v} = \vec{u}_{\phi n}$ ($n = 1, 2, \dots, N_\phi$) and $\vec{v} = \vec{u}_{tn}$

($n = 1, 2, \dots, N_t$), substituting for \vec{E} expansion (5.63). We assume the cylindrical representation of the permittivity tensor to have the form

$$\hat{\epsilon} = \begin{bmatrix} \epsilon_\rho & i\epsilon_g & 0 \\ -i\epsilon_g & \epsilon_\phi & 0 \\ 0 & 0 & \epsilon_z \end{bmatrix}, \quad (5.73)$$

and the permeability tensor to be diagonal,

$$\hat{\mu} = \begin{bmatrix} \mu_\rho & 0 & 0 \\ 0 & \mu_\phi & 0 \\ 0 & 0 & \mu_z \end{bmatrix}, \quad (5.74)$$

with the additional constraint that $\mu_\rho = \mu_\phi$ close to the z axis, which is necessary for the boundary conditions on that axis to be met.* The reader will certainly have noted that we have let the tensors $\hat{\epsilon}$ and $\hat{\mu}$ take a more general form than the gyrotropic one from eq. (5.38). This is because we allow for the presence of PMLs, whose material properties need not have a piecewise-constant Cartesian representation. After some algebra, we obtain the following generalised eigenvalue problem:

$$\begin{bmatrix} \hat{A}_{\phi\phi} & \hat{A}_{\phi t} \\ \hat{A}_{t\phi} & \hat{A}_{tt} \end{bmatrix} \begin{bmatrix} \vec{E}_\phi \\ \vec{E}'_t \end{bmatrix} = k_0^2 \begin{bmatrix} \hat{B}_{\phi\phi} & \hat{B}_{\phi t} \\ \hat{B}_{t\phi} & \hat{B}_{tt} \end{bmatrix} \begin{bmatrix} \vec{E}_\phi \\ \vec{E}'_t \end{bmatrix}, \quad (5.75)$$

where \vec{E}_ϕ and \vec{E}'_t denote the column vectors of coefficients $E_{\phi n}$ and E'_{tn} , respectively (the underbars have been added to distinguish these symbols from those denoting components of \vec{E}), whereas the entries of matrices $\hat{A}_{\alpha\beta}$ and $\hat{B}_{\alpha\beta}$ ($\alpha, \beta = \phi, t$) are given by

$$(\hat{A}_{\phi\phi})_{mn} = \iint_{\Omega} (\mu_z^{-1} \partial_\rho u_{\phi m}^0 \partial_\rho u_{\phi n}^0 + \mu_\rho^{-1} \partial_z u_{\phi m}^0 \partial_z u_{\phi n}^0 + l^{-2} \mu_\phi^{-1} \partial_z u_{\phi m}^0 \partial_z u_{\phi n}^0) \rho \, d\rho \, dz, \quad (5.76a)$$

$$\begin{aligned} (\hat{A}_{\phi t})_{mn} = & \iint_{\Omega} \{ \mu_z^{-1} \partial_\rho u_{\phi m}^0 u_{\rho n}^0 + \mu_\rho^{-1} \partial_z u_{\phi m}^0 u_{zn}^0 \\ & + l^{-2} \mu_\phi^{-1} \partial_z u_{\phi m}^0 [u_{zn}^0 - \rho(\vec{\nabla}_t \times \vec{u}_{tn}^0)_z] \} \rho \, d\rho \, dz, \end{aligned} \quad (5.76b)$$

$$(\hat{A}_{t\phi})_{mn} = (\hat{A}_{\phi t})_{nm}, \quad (5.76c)$$

$$\begin{aligned} (\hat{A}_{tt})_{mn} = & \iint_{\Omega} \{ \mu_z^{-1} u_{\rho m}^0 u_{\rho n}^0 + \mu_\rho^{-1} u_{zm}^0 u_{zn}^0 \\ & + l^{-2} \mu_\phi^{-1} [u_{zm}^0 - \rho(\vec{\nabla}_t \times \vec{u}_{tm}^0)_z][u_{zn}^0 - \rho(\vec{\nabla}_t \times \vec{u}_{tn}^0)_z] \} \rho \, d\rho \, dz, \end{aligned} \quad (5.76d)$$

$$(\hat{B}_{\phi\phi})_{mn} = \iint_{\Omega} [(l^{-2} \epsilon_\rho - 2l^{-1} \epsilon_g + \epsilon_\phi) u_{\phi m}^0 u_{\phi n}^0] \rho \, d\rho \, dz, \quad (5.76e)$$

$$(\hat{B}_{\phi t})_{mn} = \iint_{\Omega} [(-l^{-2} \epsilon_\rho + l^{-1} \epsilon_g) u_{\phi m}^0 u_{\rho n}^0] \rho^2 \, d\rho \, dz, \quad (5.76f)$$

$$(\hat{B}_{t\phi})_{mn} = (\hat{B}_{\phi t})_{nm}, \quad (5.76g)$$

$$(\hat{B}_{tt})_{mn} = \iint_{\Omega} l^{-2} (\epsilon_\rho u_{\rho m}^0 u_{\rho n}^0 + \epsilon_z u_{zm}^0 u_{zn}^0) \rho^3 \, d\rho \, dz. \quad (5.76h)$$

In these formulas $u_{\rho n}^0$ and u_{zn}^0 denote the ρ and z components of the basis function \vec{u}_{tn}^0 . It has been assumed that all the functions $u_{\phi n}^0$ and \vec{u}_{tn}^0 are real-valued.

* It is equally possible to handle the slightly more general case with $\mu_{\rho\phi} = -\mu_{\phi\rho} \neq 0$, at the cost of more complicated formulas.

5.3.3 Numerical implementation

Software We have implemented the method presented in the previous subsection using the Hermes C++ library [55, 56], which significantly facilitates the development of FE-method-based codes. First, it provides ready-made implementations of commonly used classes of FEs, including standard nodal FEs and vector curl-conforming FEs, up to the polynomial order 10. Both triangular and quadrilateral, recti- and curvilinear elements are available. Second, the library completely automatises the matrix assembly, allowing also to impose Dirichlet and Neumann boundary conditions on selected portions of the computational domain's boundary. In principle, a user of Hermes needs only to write functions calculating the integrals occurring in the weak form of the differential equation at hand and to specify the geometry of the computational domain along with the boundary conditions.

Meshing A characteristic feature of axisymmetric cavities produced by etching multilayer structures is that the material interfaces in any meridional plane are almost always parallel to the ρ or z axis. This is the case with all the structures studied in section 4.6. Therefore we have meshed the domain Ω with rectangular FEs with sides parallel to \vec{e}_ρ and \vec{e}_z . The process of mesh generation for a typical cavity goes as follows. In the first step, Ω is divided into as many conforming elements as are necessary to ensure that each interface between two different materials coincides with an interelemental boundary. The elements created in this way are subsequently subdivided into smaller ones with side lengths approximately equal to a predefined constant h_{ideal} . If desired, the resulting mesh is further uniformly refined by splitting each element into quarters. This step can be repeated as many times as necessary.

FE expansions The unknown fields E_ϕ and \vec{E}'_t are expanded into hierarchical polynomial bases provided by Hermes. The expansion order p , defined as the maximum degree of the polynomials included in these expansions, is taken to be the same in all elements.

Quadratures All the matrix entries (5.76) are calculated with Gauss-Legendre quadratures. In elements containing materials with constant $\hat{\epsilon}$ and $\hat{\mu}$, we employ quadratures of the minimum order necessary to ensure their exactness (for the given expansion order p). In elements containing PMLs, whose material properties depend on the position in a non-polynomial way (see below), the quadrature order is chosen as greater by ten than that which would ensure exact integration for constant $\hat{\epsilon}$ and $\hat{\mu}$.

Eigenvalue problem solving To solve the complex sparse non-symmetric generalised eigenvalue problem (5.75), we have used the Krylov-Schur iterative sparse eigenvalue solver implemented in the SLEPc library [57–59]. Hermes provides interfaces to several popular sparse linear equation solvers; unfortunately, at present it does not offer integration with any eigenvalue solvers. Therefore we have written a custom interface between Hermes and SLEPc.

The vector wave equation (5.40) incorporates Gauss's law $\vec{\nabla} \cdot (\hat{\epsilon} \cdot \vec{E}) = 0$, but only if $k_0 \neq 0$ [200]. As a result, eq. (5.75), derived from (5.40), possesses a large cluster of spurious static solutions that do not obey Gauss's law. Therefore even if the lowest-frequency eigenmodes of a given cavity are desired, they cannot be found by using an iterative eigenvalue solver to find a few lowest-magnitude eigenvalues of (5.75). Rather, a shift-and-invert transformation of (5.75) must be used to bring the part of its spectrum closest to a prescribed *shift* σ into the neighbourhood of zero, so that the eigenmodes belonging to this part of the spectrum may be found by the iterative algorithm [59]. Such spectral transformations are handled transparently by SLEPc.

It is possible to modify the bases used for field expansions so as to eliminate altogether the spurious static solutions [201]. Another possibility consists in modifying an iterative eigenvalue solver so as to prevent it from converging to a solution violating Gauss's law. This technique has recently been demonstrated by Venkatarayalu [52]. Although these approaches probably improve the efficiency of

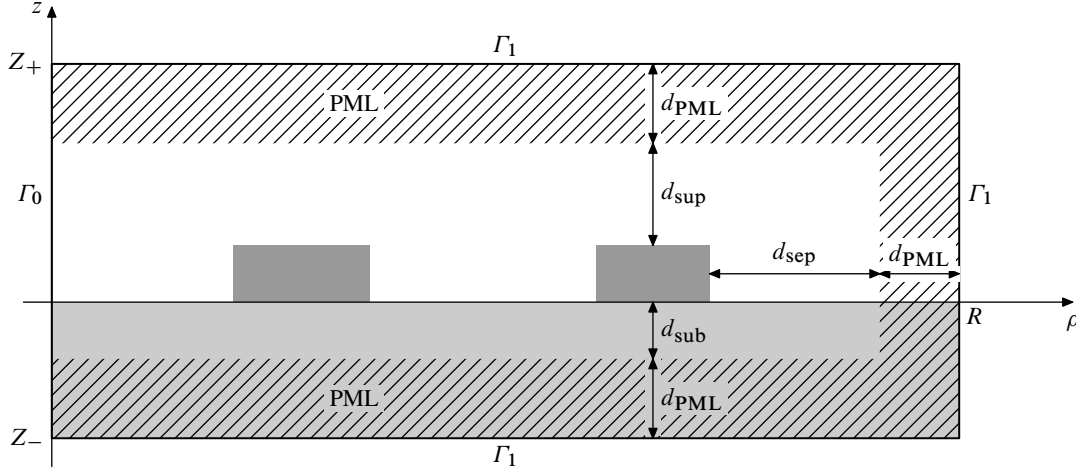


Figure 5.11 Geometry of an example domain Ω . Darker regions have larger permittivity. PMLs are hatched.

calculations—in particular, a sparse matrix inversion required by a shift-and-invert transformation is avoided—their implementation is quite non-trivial. We have therefore stuck to shift-and-invert transformations, which we found to work very reliably.

Perfectly matched layers As mentioned in the previous subsection, to suppress spurious reflections due to the finite size of the computational domain, the boundary Γ_1 is coated from inside by PMLs of thickness d_{PML} , as shown in fig. 5.11. We use standard PMLs adapted for cylindrical coordinates, which can be interpreted as anisotropic materials with diagonal permittivity tensors $\hat{\epsilon} = \epsilon \hat{\Lambda}$ and $\hat{\mu} = \mu \hat{\Lambda}$, where ϵ and μ are the material parameters of the “real” media adjacent to PMLs and the diagonal tensor $\hat{\Lambda} \equiv \text{diag}(\Lambda_\rho, \Lambda_\phi, \Lambda_z)$ is responsible for the absorbing properties of the PML. Its elements are given by [51, 54]

$$\Lambda_\rho \equiv \frac{S_z \tilde{\rho}}{S_\rho \rho}, \quad \Lambda_\phi \equiv \frac{S_z S_\rho \rho}{\tilde{\rho}} \quad \text{and} \quad \Lambda_z \equiv \frac{S_\rho \tilde{\rho}}{S_z \rho}, \quad (5.77)$$

where

$$S_\rho(\rho) \equiv 1 + i s_{\text{PML}} \left[U \left(\frac{\rho - (R - d_{\text{PML}})}{d_{\text{PML}}} \right) \right]^2, \quad (5.78a)$$

$$S_z(z) \equiv 1 + i s_{\text{PML}} \left[U \left(\frac{(Z_- + d_{\text{PML}}) - z}{d_{\text{PML}}} \right) \right]^2 + i s_{\text{PML}} \left[U \left(\frac{z - (Z_+ - d_{\text{PML}})}{d_{\text{PML}}} \right) \right]^2, \quad (5.78b)$$

$$\tilde{\rho}(\rho) \equiv \rho + i s_{\text{PML}} \frac{[U(\rho - (R - d_{\text{PML}}))]^3}{3 d_{\text{PML}}^2} \quad (5.78c)$$

and $U(x)$ is x if $x > 0$ and zero otherwise. The real parameter s_{PML} is called the *PML strength*. It is worth noting that for $\rho \leq R - d_{\text{PML}}$ we have $S_\rho(\rho) = \tilde{\rho}(\rho) = 1$; hence, $\Lambda_\rho = \Lambda_\phi = S_z$, in accord with our earlier assumption that the tensor $\hat{\mu}$ should be gyrotropic close to the z axis.

5.3.4 Evaluation of accuracy

The accuracy of calculations made with the proposed technique is affected by a number of factors, which can be divided into two groups. The first of them includes the parameters of the FE expansion itself:

- typical element size h ,
- expansion order p .

#	r_{in} (nm)	r_{out} (nm)	#	r_{in} (nm)	r_{out} (nm)
1	1236	1443	11	4618	4765
2	1656	1828	12	4933	5079
3	2019	2181	13	5246	5392
4	2363	2519	14	5559	5705
5	2696	2849	15	5872	6017
6	3023	3174	16	6184	6329
7	3346	3496	17	6495	6640
8	3667	3816	18	6806	6951
9	3986	4134	19	7117	7262
10	4303	4450	20	7428	7572

Table 5.1 Radii of the high-index rings of the G4-type cavity used to test the accuracy of calculations. The symbols r_{in} and r_{out} denote the inner and outer radius of a ring, respectively.

n_{ref}	p	λ_+	λ_-
0	1	$1.25199 + 0.00612i$	$1.25194 + 0.00610i$
0	2	$1.24329 + 0.00367i$	$1.24022 + 0.00419i$
0	3	$1.25691 + 0.00340i$	$1.25384 + 0.00387i$
0	4	$1.26034 + 0.00333i$	$1.25728 + 0.00379i$
1	1	$1.25900 + 0.00362i$	$1.25597 + 0.00411i$
1	2	$1.26133 + 0.00333i$	$1.25827 + 0.00378i$
1	3	$1.26148 + 0.00331i$	$1.25842 + 0.00376i$
2	1	$1.26145 + 0.00331i$	$1.25839 + 0.00376i$
2	2	$1.26149 + 0.00331i$	$1.25843 + 0.00376i$

Table 5.2 Influence of the number of mesh refinements, n_{ref} , and the expansion order p on the calculated values of the wavelengths λ_{\pm} of the counter-rotating modes of the cavity described in the text. The remaining parameters were chosen as $d_{\text{sub}} = d_{\text{sup}} = 600$ nm, $d_{\text{sep}} = d_{\text{PML}} = 500$ nm and $s_{\text{PML}} = 6$.

The second is formed by the domain truncation parameters:

- substrate thickness d_{sub} ,
- superstrate thickness d_{sup} ,
- distance from the outermost inhomogeneity in the multilayer to the inner boundary of the radial PML, d_{sep} ,
- PML thickness, d_{PML} ,
- PML strength, s_{PML} .

In fig. 5.11 graphical definitions of the first four items from the above list are shown.

To determine the values of the above parameters required to get a reasonable accuracy, we have studied the influence of their variation of the calculated values of the wavelengths λ_+ and λ_- of the modes with azimuthal order $l = 10$ and -10 of a particular G4-type cavity (see section 4.6) containing 20 high-index rings, whose radii are listed in table 5.1.

We began by testing the dependence of λ_{\pm} on h and p . The former was varied as follows: first, in the way described in subsection 5.3.3, we generated an initial mesh composed of rectangular elements with side lengths roughly equal to $h_{\text{ideal}} = 150$ nm, and subsequently we refined it uniformly n_{ref} times. Table 5.2 lists the values of λ_{\pm} obtained for a number of combinations (n_{ref} , p); the values of the remaining parameters are specified in the caption of that table. Clearly, at least one level of refinement is necessary to get accurate results. This is probably related to the occurrence of field singularities at the edges of

$n_{\text{sub}} = n_{\text{sup}}$	λ_+	λ_-
0.1	$1.26135 + 0.00311i$	$1.25831 + 0.00354i$
0.2	$1.26146 + 0.00319i$	$1.25842 + 0.00364i$
0.3	$1.26150 + 0.00325i$	$1.25845 + 0.00370i$
0.4	$1.26150 + 0.00329i$	$1.25845 + 0.00374i$
0.5	$1.26150 + 0.00330i$	$1.25844 + 0.00376i$
0.6	$1.26149 + 0.00331i$	$1.25843 + 0.00376i$
0.7	$1.26148 + 0.00331i$	$1.25843 + 0.00376i$
0.8	$1.26148 + 0.00331i$	$1.25843 + 0.00376i$
0.9	$1.26148 + 0.00331i$	$1.25842 + 0.00376i$
1.0	$1.26148 + 0.00331i$	$1.25842 + 0.00376i$

Table 5.3 Influence of the substrate and superstrate thicknesses, d_{sub} and d_{sup} (taken equal to each other) on the calculated values of the wavelengths λ_{\pm} of the counter-rotating modes of the cavity described in the text. The remaining parameters were chosen as $n_{\text{ref}} = 1$, $p = 3$, $d_{\text{sep}} = d_{\text{PML}} = 500$ nm and $s_{\text{PML}} = 6$.

rings; these singularities can be clearly seen on plots of the meridional components of \vec{E} . It is well known [202, section 3.3] that the convergence of a FE expansion can be accelerated by an additional refinement of the elements at whose corners singularities occur.

In any case, the data in table 5.2 show that the wavelengths obtained for $(n_{\text{ref}}, p) = (1, 3)$, $(2, 1)$ and $(2, 2)$ differ only with the sixth significant digit. Therefore, one can expect them to have absolute accuracy of at least 0.1 nm. This is enough for the purposes of the evaluation of the wavelength splitting $\Delta\lambda \equiv \lambda_+ - \lambda_-$ between the counter-rotating modes, which is typically on the level on 2–3 nm. For the remaining calculations we fixed $n_{\text{ref}} = 1$ and $p = 3$.

We studied next the sensitivity of λ_{\pm} to the changes of d_{sub} and d_{sup} , for simplicity taking them to be equal. The results, listed in table 5.3, indicate that the influence of these parameters is negligible (λ_{\pm} does not change by more than 0.03 nm) as soon as they are chosen larger than 100 nm. We decided therefore to stay with the originally assigned values, $d_{\text{sub}} = d_{\text{sup}} = 600$ nm. We have also calculated λ_{\pm} as a function of d_{sep} ranging from 100 nm to 800 nm, and found all the obtained values to be identical to six significant digits. In future calculations we continue to take $d_{\text{sep}} = 500$ nm.

Lastly, we evaluated the dependence of λ_{\pm} on the PML parameters, d_{PML} and s_{PML} . We made two series of calculations, in which the PML strength was fixed to 6 and 12, respectively, while its thickness was varied from 100 to 800 nm. The results are given in table 5.4. Clearly, for both PML strengths the wavelengths λ_{\pm} converge quickly to practically the same values (± 0.01 nm).

To sum up, the parameters related to the truncation of Ω have been found to affect little the results of calculations. Thus, one can be reasonably confident that the data presented in section 4.6, which were obtained with $n_{\text{ref}} = 1$, $p = 3$, $d_{\text{sub}} = d_{\text{sup}} = 600$ nm, $d_{\text{sep}} = d_{\text{PML}} = 500$ nm and $s_{\text{PML}} = 6$, are accurate to about ± 0.05 nm, which corresponds to a relative error of 4×10^{-5} .

d_{PML}	$s_{\text{PML}} = 6$		$s_{\text{PML}} = 12$	
	λ_+	λ_-	λ_+	λ_-
0.1	$1.25945 + 0.00388i$	$1.25617 + 0.00423i$	$1.26114 + 0.00439i$	$1.25796 + 0.00488i$
0.2	$1.26107 + 0.00385i$	$1.25793 + 0.00430i$	$1.26163 + 0.00331i$	$1.25858 + 0.00378i$
0.3	$1.26148 + 0.00350i$	$1.25841 + 0.00396i$	$1.26147 + 0.00330i$	$1.25842 + 0.00375i$
0.4	$1.26151 + 0.00334i$	$1.25845 + 0.00380i$	$1.26148 + 0.00330i$	$1.25842 + 0.00376i$
0.5	$1.26149 + 0.00331i$	$1.25843 + 0.00376i$	$1.26148 + 0.00331i$	$1.25842 + 0.00376i$
0.6	$1.26148 + 0.00331i$	$1.25843 + 0.00376i$	$1.26148 + 0.00331i$	$1.25842 + 0.00376i$
0.7	$1.26148 + 0.00331i$	$1.25843 + 0.00376i$	$1.26148 + 0.00331i$	$1.25843 + 0.00376i$
0.8	$1.26148 + 0.00331i$	$1.25842 + 0.00376i$	$1.26148 + 0.00331i$	$1.25843 + 0.00376i$

Table 5.4 Influence of the PML thickness d_{PML} and PML strength s_{PML} on the calculated values of the wavelengths λ_{\pm} of the counter-rotating modes of the cavity described in the text. The remaining parameters were chosen as $n_{\text{ref}} = 1$, $p = 3$, $d_{\text{sub}} = d_{\text{sup}} = 600$ nm and $d_{\text{sep}} = 500$ nm.

Chapter 6

Conclusions and perspectives

The work whose results have been presented in this thesis encompasses a fairly wide range of topics, concerning mostly, but not exclusively, those related to PCs. Here we attempt to summarise these results, putting them in perspective, highlighting those we find the most important, and offering some ideas on future work.

In chapter 2, the most theoretical one in this thesis, we formulated an effective-medium model of 2D PCs. Using this model, we conducted an in-depth study of the validity of the effective-medium description of PCs exhibiting the negative-refraction effect. We believe this to have been the first analysis encompassing both the propagative and the evanescent region and not limited to at most a few discrete incidence angles. We think we provided convincing arguments that the effective-medium approximation of PCs with negative refraction is too simplistic and, therefore, such PCs cannot be used as a drop-in replacement of homogeneous negative-index media.

The rest of the manuscript was more device-oriented. In chapter 3 we presented an algorithm for the design of AR gratings for PCs and showed its applicability to certain specific PC components. At the same time, we strived to be explicit about its limitations, which stem from its reliance on a number of approximations.

It needs to be stressed that the possibilities offered by the numerical shape optimisation procedure, which is the last step of the proposed algorithm, have not been exploited in full in the examples presented in section 3.4. For instance, in the case of a flat lens, it is not sufficient that the device pass (almost) all the incident energy; creation of a high-quality image requires also that the waves incident at different angles arrive on the image plane with appropriate phases. Thus, it might be more judicious to formulate the objective function (to be minimised) in terms of the amplitudes and phases of the *transmitted* waves rather than the reflected ones. This would also allow to optimise the transmission of the evanescent waves, and hence, possibly, to overcome the diffraction limit.

In chapter 4 we reported on our work on magneto-optical circulators. The crucial step was the idea of studying closely the class of resonant cavities having the rotational symmetry. It led to the formulation of a novel design principle for uniformly magnetised, and therefore manufacturable, cavities that nonetheless exhibit a substantial mode frequency splitting. We then initially pursued the beaten path of PC-based circulator designs. It was M. Vanwolleghem (Institut d'Electronique Fondamentale, Orsay, France) who first suggested testing simpler systems based on uniform waveguides. Despite initial problems with securing a sufficient degree of coupling between such waveguides and the central cavity (it was not possible to use side-coupling owing to an extreme phase mismatch between the waveguide and cavity modes), we finally succeeded by employing butt-coupling instead of side-coupling and optimising the shape of the waveguide slot.

As we have remarked in section 4.5.4, the circulator designed on the basis of 2D calculations did not fare well in experiment owing to excessive out-of-plane losses. In March 2010 it was therefore deemed necessary to turn to 3D simulations. Good progress has already been made; in particular, at

the end of section 4.6.2 we presented a 3D cavity with markedly reduced radiation losses. To arrive at an experimental demonstration of a working circulator, however, further work is still necessary. The optimisation should be repeated using the exact value of the refractive index of the potential coating material, silicon nitride. More importantly, we do not understand yet the mechanism for the improvement of the mode confinement provided by the optimised cavity. A Bloch-mode-based theory might be able to explain this effect. We also hope that it will lead to successful designs—no longer based on the effective-index approximation—of *uncoated* cavities, which should have smaller footprint than coated ones, thanks to stronger in-plane mode localisation.

Even if a satisfactory 3D model of axisymmetric cavities is established in future, some numerical optimisation of their geometry may still be necessary, or at least desirable. It is well known that gradient-based optimisation techniques are in general more efficient than derivative-free methods, such as the NEWUOA algorithm used thus far. It should be quite possible to calculate the derivative of the frequency splitting $\Delta\omega$ of a given cavity over the radius of any particular ring, symbolically denoted r here. The derivative of the eigenvalue k_0^2 of the problem eq. (5.75) over r is simple to calculate, at least assuming that there are no repeated eigenvalues:

$$\frac{\partial k_0^2}{\partial r} = \vec{y}^\dagger \cdot \left(\frac{\partial \hat{A}}{\partial r} - k_0^2 \frac{\partial \hat{B}}{\partial r} \right) \cdot \vec{x}, \quad (6.1)$$

where \vec{x} and \vec{y} are the right and left eigenvectors corresponding to k_0^2 and normalised so that $\vec{y}^\dagger \cdot \hat{B} \cdot \vec{x} = 1$. (See refs. 203 and 204 for a review on the computation of eigenvalue derivatives.) The derivatives of \hat{A} and \hat{B} over r can be evaluated from the explicit formulas (5.76) for their entries.

An optimised cavity will eventually need to be integrated with the input and output waveguides. Which numerical method will be most suitable for the simulation of the complete 3D system is not clear yet; some views on this matter have been offered in the conclusions to chapter 4.

Finally, as noted in section 4.1.3, Yu et al. [155] have recently proposed theoretically an isolator based on time-dependent refractive-index modulation. In the structure presented in their article, introduction of a boundary separating the modulated and unmodulated parts of the waveguides is needed; this requires a precise alignment of the electric field enforcing the modification of the refractive index. It might be possible to employ the ideas developed in chapter 4, and in particular the design rule from section 4.3, to dispense with the necessity of introducing domains free from the modulating field.

Bibliography

- [1] R. Nagarajan, C. Joyner, J. Schneider, R.P., J. Bostak, T. Butrie, A. Dentai, V. Dominic, P. Evans, M. Kato, M. Kauffman, et al., *J. Sel. Top. Quant. Electron.* **11**, 50 (2005).
- [2] R. Nagarajan, M. Kato, J. Pleumeekers, P. Evans, D. Lambert, A. Chen, V. Dominic, A. Mathur, P. Chavarkar, M. Missey, et al., *J. Opt. Netw.* **6**, 102 (2007).
- [3] S. C. Nicholes, M. L. Mašanović, B. Jevremović, E. Lively, L. A. Coldren, and D. J. Blumenthal, *J. Lightwave Technol.* **28**, 641 (2010).
- [4] *Infinera's 400 Gb/s PIC sets new record for integration*, <http://www.infinera.com/j7/servlet/NewsItem?newsItemID=150>.
- [5] W. A. Harrison, *Solid state theory* (Dover, New York, 1980).
- [6] E. Ozbay, *Science* **311**, 189 (2006).
- [7] R. G. Hunsperger, *Integrated optics: theory and technology* (Springer, New York, 2009).
- [8] E. Yablonovitch, *Phys. Rev. Lett.* **58**, 2059 (1987).
- [9] S. John, *Phys. Rev. Lett.* **58**, 2486 (1987).
- [10] R. D. Meade, A. Devenyi, J. D. Joannopoulos, O. L. Alerhand, D. A. Smith, and K. Kash, *J. Appl. Phys.* **75**, 4753 (1994).
- [11] A. Mekis, J. C. Chen, I. Kurland, S. Fan, P. R. Villeneuve, and J. D. Joannopoulos, *Phys. Rev. Lett.* **77**, 3787 (1996).
- [12] K. Busch, G. von Freymann, S. Linden, S. Mingaleev, L. Tkeshelashvili, and M. Wegener, *Phys. Rep.* **444**, 101 (2007).
- [13] B. Gralak, S. Enoch, and G. Tayeb, in *Metamaterials: physics and engineering explorations*, edited by N. Engheta and R. W. Ziolkowski (Wiley, New York, 2006), chap. 10, pp. 261–283.
- [14] B. Gralak, S. Enoch, and G. Tayeb, *J. Opt. Soc. Am. A* **17**, 1012 (2000).
- [15] H. Kosaka, T. Kawashima, A. Tomita, M. Notomi, T. Tamamura, T. Sato, and S. Kawakami, *Appl. Phys. Lett.* **74**, 1212 (1999).
- [16] H. Kosaka, T. Kawashima, A. Tomita, M. Notomi, T. Tamamura, T. Sato, and S. Kawakami, *Phys. Rev. B* **58**, R10096 (1998).
- [17] J. B. Pendry, *Phys. Rev. Lett.* **85**, 3966 (2000).

- [18] N. Fabre, L. Lalouat, B. Cluzel, X. Mélique, D. Lippens, F. de Fornel, and O. Vanbésien, *Phys. Rev. Lett.* **101**, 073901 (2008).
- [19] J. Amet, F. I. Baida, G. W. Burr, and M. Bernal, *Photonics Nanostruct. Fundam. Appl.* **6**, 47 (2008).
- [20] V. G. Veselago, *Sov. Phys. Usp.* **10**, 509 (1968).
- [21] T. Decoopman, G. Tayeb, S. Enoch, D. Maystre, and B. Gralak, *Phys. Rev. Lett.* **97**, 073905 (2006).
- [22] J. Ushida, M. Tokushima, M. Shirane, A. Gomyo, and H. Yamada, *Phys. Rev. B* **68**, 155115 (2003).
- [23] A. Efros and A. Pokrovsky, *Solid State Commun.* **129**, 643 (2004).
- [24] R. Biswas, Z. Y. Li, and K. M. Ho, *Appl. Phys. Lett.* **84**, 1254 (2004).
- [25] B. Momeni, A. Asghar Eftekhari, and A. Adibi, *Opt. Lett.* **32**, 778 (2007).
- [26] Z. Lu and D. W. Prather, *Opt. Express* **15**, 8340 (2007).
- [27] R. Pierre and B. Gralak, *J. Mod. Opt.* **55**, 1759 (2008).
- [28] B. Momeni, M. Badieirostami, and A. Adibi, *J. Opt. Soc. Am. B* **24**, 2957 (2007).
- [29] Y. Wu, J. Li, Z.-Q. Zhang, and C. T. Chan, *Phys. Rev. B* **74**, 085111 (2006).
- [30] V. Yannopapas and A. Moroz, *J. Phys. Cond. Mat.* **17**, 3717 (2005).
- [31] V. Yannopapas and N. V. Vitanov, *Phys. Rev. B* **74**, 193304 (2006).
- [32] V. Yannopapas, *Phys. Rev. B* **75**, 035112 (2007).
- [33] G. Scherrer, M. Hofman, W. Śmigaj, B. Gralak, X. Melique, O. Vanbésien, D. Lippens, C. Dumas, B. Cluzel, and F. de Fornel, *Appl. Phys. Lett.* **97**, 071119 (2010).
- [34] Z. Wang and S. Fan, *Appl. Phys. B* **81**, 369 (2005).
- [35] H. Dötsch, N. Bahlmann, O. Zhuromskyy, M. Hammer, L. Wilkens, R. Gerhardt, P. Hertel, and A. F. Popkov, *J. Opt. Soc. Am. B* **22**, 240 (2005).
- [36] D. R. Goff, *Fiber optic reference guide* (Focal Press, Amsterdam, 2002).
- [37] Z. Wang and S. Fan, *Opt. Lett.* **30**, 1989 (2005).
- [38] D. Felbacq, G. Tayeb, and D. Maystre, *J. Opt. Soc. Am. A* **11**, 2526 (1994).
- [39] G. Tayeb and D. Maystre, *J. Opt. Soc. Am. A* **14**, 3323 (1997).
- [40] D. Maystre, S. Enoch, and G. Tayeb, in *Electromagnetic theory and applications for photonic crystals*, edited by K. Yasumoto (CRC Press, Boca Raton, 2005), chap. 1.
- [41] N. Stefanou, V. Karathanos, and A. Modinos, *J. Phys. Cond. Mat.* **4**, 7389 (1992).
- [42] N. Stefanou, V. Yannopapas, and A. Modinos, *Comp. Phys. Commun.* **113**, 49 (1998).

- [43] N. Stefanou, V. Yannopapas, and A. Modinos, *Comp. Phys. Commun.* **132**, 189 (2000).
- [44] N. A. Nicorovici, R. C. McPhedran, and L. C. Botten, *Phys. Rev. E* **52**, 1135 (1995).
- [45] S. K. Chin, N. A. Nicorovici, and R. C. McPhedran, *Phys. Rev. E* **49**, 4590 (1994).
- [46] K. Ohtaka and Y. Tanabe, *J. Phys. Soc. Jpn.* **65**, 2265 (1996).
- [47] A. Moroz, *Phys. Rev. B* **51**, 2068 (1995).
- [48] R. Pierre, Ph.D. thesis, Institut Fresnel, Marseille (2008).
- [49] J. Yuan and Y. Y. Lu, *J. Opt. Soc. Am. A* **23**, 3217 (2006).
- [50] Y. Huang and Y. Y. Lu, *J. Lightwave Technol.* **24**, 3448 (2006).
- [51] A. D. Greenwood and J. Jin, *IEEE Trans. Antennas Propag.* **47**, 620 (1999).
- [52] N. V. Venkatarayalu, *Int. J. Numer. Model.* **23**, 231 (2010), ISSN 0894-3370.
- [53] J. Jin, *The finite element method in electromagnetics* (Wiley, New York, 2002).
- [54] F. Teixeira and W. Chew, *IEEE Microw. Guided Wave Lett.* **7**, 371 (1997), ISSN 1051-8207.
- [55] *Hermes – higher-order modular finite element system (user’s guide)*, <http://hpfem.org> (2010).
- [56] P. Solin, *Partial differential equations and the finite element method* (Wiley, 2005).
- [57] V. Hernandez, J. E. Roman, and V. Vidal, *ACM Trans. Math. Software* **31**, 351 (2005).
- [58] V. Hernandez, J. E. Roman, E. Romero, A. Tomas, and V. Vidal, <http://www.grycap.upv.es/slepc> (2009).
- [59] V. Hernandez, J. E. Roman, E. Romero, A. Tomas, and V. Vidal, *SLEPc Users Manual* (2009).
- [60] J. G. Van Bladel, *Electromagnetic fields* (Wiley, 2007).
- [61] J. D. Jackson, *Classical electrodynamics* (Wiley, New York, 1998).
- [62] W. Śmigaj and B. Gralak, *Phys. Rev. B* **77**, 235445 (2008).
- [63] W. Śmigaj and B. Gralak, *Proc. SPIE* **6987**, 698726 (2008).
- [64] C. Giacovazzo, ed., *Fundamentals of crystallography* (Oxford University Press, Oxford, 1992).
- [65] C. G. Someda, *Electromagnetic waves* (Chapman & Hall, London, 1998).
- [66] S. Boscolo, C. Conti, M. Midrio, and C. G. Someda, *J. Lightwave Technol.* **20**, 304 (2002).
- [67] P. Kuchment, *Floquet theory for partial differential equations* (Birkhäuser Verlag, Basel, 1993).
- [68] R. Petit, in *Electromagnetic theory of gratings*, edited by R. Petit (Springer, Berlin, 1980), chap. 1, pp. 1–52.
- [69] M. Nevière and E. Popov, *Light propagation in periodic media. Differential theory and design* (Marcel Dekker, New York, 2002).
- [70] Z.-Y. Li and K.-M. Ho, *Phys. Rev. B* **68**, 155101 (2003).

- [71] L. C. Botten, T. P. White, A. A. Asatryan, T. N. Langtry, C. M. de Sterke, and R. C. McPhedran, *Phys. Rev. E* **70**, 056606 (2004).
- [72] E. Istrate, A. A. Green, and E. H. Sargent, *Phys. Rev. B* **71**, 195122 (2005).
- [73] L. Li, *J. Opt. Soc. Am. A* **13**, 1024 (1996).
- [74] P. Vincent, in *Electromagnetic theory of gratings*, edited by R. Petit (Springer, Berlin, 1980), chap. 4, pp. 101–122.
- [75] E. Popov and B. Bozhkov, *Appl. Opt.* **39**, 4926 (2000).
- [76] W. Śmigaj, Master's thesis, Faculty of Physics, Adam Mickiewicz University in Poznań (2007).
- [77] M. Plihal and A. A. Maradudin, *Phys. Rev. B* **44**, 8565 (1991).
- [78] J. F. Cornwell, *Group theory and electronic energy bands in solids* (North-Holland, Amsterdam, 1969).
- [79] K. Sakoda, *Optical properties of photonic crystals* (Springer, Berlin, 2001).
- [80] M. Tinkham, *Group theory and quantum mechanics* (McGraw-Hill, New York, 1964).
- [81] Y.-C. Chang, *Phys. Rev. B* **25**, 605 (1982).
- [82] T. Koschny, P. Markoš, D. R. Smith, and C. M. Soukoulis, *Phys. Rev. E* **68**, 065602(R) (2003).
- [83] D. Seetharamdoo, R. Sauleau, K. Mahdjoubi, and A.-C. Tarot, *J. Appl. Phys.* **98**, 3505 (2005).
- [84] T. Koschny, P. Markoš, E. N. Economou, D. R. Smith, D. C. Vier, and C. M. Soukoulis, *Phys. Rev. B* **71**, 245105 (2005).
- [85] R. Liu, T. J. Cui, D. Huang, B. Zhao, and D. R. Smith, *Phys. Rev. E* **76**, 026606 (2007).
- [86] K. F. Riley, M. P. Hobson, and S. J. Bence, *Mathematical Methods for Physics and Engineering* (Cambridge University Press, Cambridge, 2006).
- [87] J. A. Dobrowolski, D. Poitras, P. Ma, H. Vakil, and M. Acree, *Appl. Opt.* **41**, 3075 (2002).
- [88] E. B. Grann and M. G. Moharam, *J. Opt. Soc. Am. A* **13**, 988 (1996).
- [89] H. A. Macleod, *Thin-film optical filters* (Institute of Physics, Bristol, 2001).
- [90] S. J. Orfanidis, *Electromagnetic waves and antennas*, <http://www.ece.rutgers.edu/~orfanidi/ewa> (2008).
- [91] D. H. Raguin and G. M. Morris, *Appl. Opt.* **32**, 1154 (1993).
- [92] D. H. Raguin and G. M. Morris, *Appl. Opt.* **32**, 2582 (1993).
- [93] R. Bräuer and O. Bryngdahl, *Appl. Opt.* **33**, 7875 (1994).
- [94] H. Kikuta, H. Toyota, and W. Yu, *Opt. Rev.* **10**, 63 (2003).
- [95] S. Xiao, M. Qiu, Z. Ruan, and S. He, *Appl. Phys. Lett.* **85**, 4269 (2004).
- [96] L. C. Botten, T. P. White, C. M. de Sterke, and R. C. McPhedran, *Phys. Rev. E* **74**, 026603 (2006).

- [97] Z. Li, E. Ozbay, H. Chen, J. Chen, F. Yang, and H. Zheng, *J. Phys. D* **40**, 5873 (2007).
- [98] S.-G. Lee, J.-S. Choi, J.-E. Kim, H.-Y. Park, and C.-S. Kee, *Opt. Express* **16**, 4270 (2008).
- [99] J.-M. Park, S.-G. Lee, H. Y. Park, J.-E. Kim, and M.-H. Lee, *J. Opt. Soc. Am. B* **26**, 1967 (2009).
- [100] Y. Jin and S. He, *Phys. Lett. A* **360**, 461 (2007).
- [101] B. Zhang and M. Y. Li, *Eur. Phys. J. D* **45**, 321 (2007).
- [102] T. Baba and D. Ohsaki, *Jpn. J. Appl. Phys.* **40**, 5920 (2001).
- [103] T. Baba, T. Matsumoto, and M. Echizen, *Opt. Express* **12**, 4608 (2004).
- [104] T. Matsumoto, S. Fujita, and T. Baba, *Opt. Express* **13**, 10768 (2005).
- [105] T. Matsumoto, K. Eom, and T. Baba, *Opt. Lett.* **31**, 2786 (2006).
- [106] F. J. Lawrence, L. C. Botten, K. B. Dossou, and C. M. de Sterke, *Appl. Phys. Lett.* **93**, 121114 (2008).
- [107] F. J. Lawrence, L. C. Botten, K. B. Dossou, C. M. de Sterke, and R. C. McPhedran, *Phys. Rev. A* **80**, 023826 (2009).
- [108] J. Witzens, M. Hochberg, T. Baehr-Jones, and A. Scherer, *Phys. Rev. E* **69**, 046609 (2004).
- [109] B. Momeni and A. Adibi, *Appl. Phys. Lett.* **87**, 171104 (2005).
- [110] W. H. Press, B. P. Flannery, S. A. Teukolsky, and W. T. Vetterling, *Numerical recipes in C* (Cambridge University Press, 1992).
- [111] W. Śmigaj, B. Gralak, R. Pierre, and G. Tayeb, in *SPP4 Surface Plasmon Photonics Conference* (2009).
- [112] W. Śmigaj, B. Gralak, R. Pierre, and G. Tayeb, *Opt. Lett.* **34**, 3532 (2009).
- [113] D. W. Prather, S. Shi, J. Murakowski, G. J. Schneider, A. Sharkawy, C. Chen, B. L. Miao, and R. Martin, *J. Phys. D* **40**, 2635 (2007).
- [114] S. G. Johnson, M. Ibanescu, M. A. Skorobogatiy, O. Weisberg, J. D. Joannopoulos, and Y. Fink, *Phys. Rev. E* **65**, 066611 (2002).
- [115] M. Vanwolleghem, X. Checoury, W. Śmigaj, B. Gralak, L. Magdenko, K. Postava, B. Dagens, P. Beauvillain, and J.-M. Lourtioz, *Phys. Rev. B* **80**, 121102(R) (2009).
- [116] R. E. Collin, *Foundations for microwave engineering* (Wiley-IEEE, New York, 2001).
- [117] D. M. Pozar, *Microwave engineering* (Wiley, New York, 1998).
- [118] F. Olislager, *Electromagnetic waveguides and transmission lines* (Oxford University Press, Oxford, 1999).
- [119] D. D. Stancil and A. Prabhakar, *Spin waves. Theory and applications* (Springer, New York, 2009).
- [120] Y. Shoji and T. Mizumoto, *Opt. Express* **15**, 13446 (2007).

- [121] M. Vanwolleghem, private communication (2009).
- [122] B. Vertruyen, R. Cloots, J. S. Abell, T. J. Jackson, R. C. da Silva, E. Popova, and N. Keller, *Phys. Rev. B* **78**, 094429 (2008).
- [123] H. Takeda and S. John, *Phys. Rev. A* **78**, 023804 (pages 15) (2008).
- [124] J. Lettieri, V. Vaithyanathan, S. K. Eah, J. Stephens, V. Sih, D. D. Awschalom, J. Levy, and D. G. Schlom, *Appl. Phys. Lett.* **83**, 975 (2003).
- [125] M. J. Steel, M. Levy, and R. M. Osgood, *J. Lightwave Technol.* **18**, 1297 (2000).
- [126] A. Figotin and I. Vitebsky, *Phys. Rev. E* **63**, 066609 (2001).
- [127] Z. Yu, Z. Wang, and S. Fan, *Appl. Phys. Lett.* **90**, 121133 (2007).
- [128] A. B. Khanikaev and M. J. Steel, *Opt. Express* **17**, 5265 (2009).
- [129] R. Wolfe, V. J. Fratello, and M. M. Powell, *J. Appl. Phys.* **63**, 3099 (1988).
- [130] R. Wolfe, R. A. Lieberman, V. J. Fratello, R. E. Scotti, and N. Kopylov, *Appl. Phys. Lett.* **56**, 426 (1990).
- [131] H. Dammann, E. Pross, G. Rabe, and W. Tolksdorf, *Appl. Phys. Lett.* **56**, 1302 (1990).
- [132] F. Auracher and H. H. Witte, *Opt. Commun.* **13**, 435 (1975).
- [133] J. Fujita, M. Levy, R. M. Osgood, L. Wilkens, and H. Dötsch, *Appl. Phys. Lett.* **76**, 2158 (2000).
- [134] N. Kono and M. Koshiha, *Opt. Express* **13**, 9155 (2005).
- [135] O. Zhuromskyy, M. Lohmeyer, N. Bahlmann, P. Hertel, H. Dötsch, and A. F. Popkov, *Opt. Quantum Electron.* **32**, 885 (2000).
- [136] N. Bahlmann, M. Lohmeyer, O. Zhuromskyy, H. Dötsch, and P. Hertel, *Opt. Commun.* **161**, 330 (1999).
- [137] N. Kono and Y. Tsuji, *J. Lightwave Technol.* **22**, 1741 (2004).
- [138] W. Zaets and K. Ando, *IEEE Photon. Technol. Lett.* **11** (1999).
- [139] M. Takenaka and Y. Nakano, in *Proceedings of the 11th International Conference on Indium Phosphide and Related Materials* (1999), pp. 289–292.
- [140] M. Vanwolleghem, W. Van Parys, D. Van Thourhout, R. Baets, F. Lelarge, O. Gauthier-Lafaye, B. Thedrez, R. Wirix-Speetjens, and L. Lagae, *Appl. Phys. Lett.* **85**, 3980 (2004).
- [141] W. Van Parys, B. Moeyersoon, D. Van Thourhout, R. Baets, M. Vanwolleghem, B. Dagens, J. Decobert, O. Le Gouezigou, D. Make, R. Vanheertum, et al., *Appl. Phys. Lett.* **88** (2006).
- [142] T. Amemiya, H. Shimizu, M. Yokoyama, P. N. Hai, M. Tanaka, and Y. Nakano, *Appl. Opt.* **46**, 5784 (2007).
- [143] H. Hemme, H. Dötsch, and P. Hertel, *Appl. Opt.* **29**, 2741 (1990).
- [144] L. Tang, S. M. Drezdson, and T. Yoshie, *Opt. Express* **16**, 16202 (2008).

- [145] S. M. Drezdzon and T. Yoshie, *Opt. Express* **17**, 9276 (2009).
- [146] Z. Wang, Y. D. Chong, J. D. Joannopoulos, and M. Soljačić, *Phys. Rev. Lett.* **100**, 013905 (2008).
- [147] Z. Wang, Y. Chong, J. D. Joannopoulos, and M. Soljačić, *Nature* **461**, 772 (2009).
- [148] W. Śmigaj, J. Romero-Vivas, B. Gralak, L. Magdenko, B. Dagens, and M. Vanwolleghem, *Opt. Lett.* **35**, 568 (2010).
- [149] W. Suh, Z. Wang, and S. Fan, *IEEE J. Quantum Electron.* **40**, 1511 (2004).
- [150] Z. Wang and S. Fan, *Photonics Nanostruct. Fundam. Appl.* **4**, 132 (2006).
- [151] N. Kono and M. Koshiba, in *Integrated Photonics Research and Applications/Nanophotonics* (OSA, 2006), p. IMD3.
- [152] N. Kono, K. Kakihara, K. Saitoh, and M. Koshiba, *Opt. Express* **15**, 7737 (2007).
- [153] K. Gallo, G. Assanto, K. R. Parameswaran, and M. M. Fejer, *Applied Physics Letters* **79**, 314 (2001).
- [154] Z. Yu and S. Fan, *Nat. Photonics* **3**, 91 (2009).
- [155] Z. Yu, G. Veronis, Z. Wang, and S. Fan, *Phys. Rev. Lett.* **100**, 023902 (2008).
- [156] J. D. Joannopoulos, S. G. Johnson, J. N. Winn, and R. D. Meade, *Photonic crystals* (Princeton University Press, Princeton, 2008).
- [157] J. Scheuer, *J. Opt. Soc. Am. B* **24**, 2178 (2007).
- [158] Abramowitz, M. and Stegun, I. A., ed., *Handbook of mathematical functions* (Dover, New York, 1970).
- [159] S. Mazoyer, J. P. Hugonin, and P. Lalanne, *Phys. Rev. Lett.* **103**, 063903 (2009).
- [160] W. Śmigaj, *J. Opt. Soc. Am. A* **24**, 3309 (2007).
- [161] *Comsol Multiphysics, version 3.5a, RF module user's guide* (2008).
- [162] Y. Tsuji and M. Koshiba, *J. Lightwave Technol.* **20**, 463 (2002).
- [163] L. Magdenko, E. Popova, M. Vanwolleghem, C. Pang, F. Fortuna, T. Maroutian, P. Beauvillain, N. Keller, and B. Dagens, *Wafer-scale fabrication of magneto-phonic structures in Bismuth Iron Garnet thin film*, to appear in *Microelectron. Eng.* (2010).
- [164] M. Hammer and O. V. Ivanova, *Opt. Quantum Electron.* **41**, 267 (2009).
- [165] A. Hessel, in *Antenna theory*, edited by R. E. Collin and F. J. Zucker (McGraw-Hill, New York, 1969), vol. 2, chap. 19.
- [166] P. Lalanne, C. Sauvan, and J. P. Hugonin, *Laser Photonics Rev.* **2**, 514 (2008).
- [167] P. Lalanne and J. P. Hugonin, *IEEE J. Quantum Electron.* **39**, 1430 (2003).
- [168] C. Sauvan, G. Lecamp, P. Lalanne, and J. P. Hugonin, *Opt. Express* **13**, 245 (2005).

- [169] A. Kitagawa and J. Sakai, *Phys. Rev. A* **80**, 033802 (2009).
- [170] K. Srinivasan and O. Painter, *Opt. Express* **11**, 579 (2003).
- [171] K. Srinivasan and O. Painter, *Opt. Express* **10**, 670 (2002).
- [172] D. Englund, I. Fushman, and J. Vučković, *Opt. Express* **13**, 5961 (2005).
- [173] Y. Akahane, T. Asano, B. Song, and S. Noda, *Nature* **425**, 944 (2003).
- [174] E. V. Jull, *Aperture antennas and diffraction theory* (Peter Peregrinus Ltd., New York, 1981).
- [175] C. Balanis, *Antenna theory, analysis and design* (Wiley, New York, 1997).
- [176] R. Piessens, in *Transforms and applications handbook*, edited by A. D. Poularikas (CRC, Boca Raton, 2000), chap. 9.
- [177] M. Powell, in *Large-scale nonlinear optimization*, edited by G. Di Pillo and M. Roma (Springer, 2006), pp. 255–297.
- [178] L. C. Andreani and D. Gerace, *Phys. Rev. B* **73**, 235114 (2006).
- [179] D. Maystre and M. Cadilhac, *Journal of Mathematical Physics* **26**, 2201 (1985).
- [180] D. Maystre, *P. Electromagn. Res.* **57**, 55 (2006).
- [181] I. N. Vekua, *New methods for solving elliptic equations* (North-Holland, Amsterdam, 1967).
- [182] O. Christensen, *An introduction to frames and Riesz bases* (Birkhäuser, Boston, 2003).
- [183] J. S. Hesthaven, S. Gottlieb, and D. Gottlieb, *Spectral methods for time-dependent problems* (Cambridge University Press, Cambridge, 2007).
- [184] F. Tisseur and K. Meerbergen, *SIAM Rev.* **43**, 235 (2001), ISSN 0036-1445.
- [185] R. C. Ward, *SIAM J. Sci. Stat. Comput.* **2**, 141 (1981).
- [186] E. Anderson, Z. Bai, C. Bischof, S. Blackford, J. Demmel, J. Dongarra, J. Du Croz, A. Greenbaum, S. Hammarling, A. McKenney, et al., *LAPACK users' guide* (SIAM, Philadelphia, 1999).
- [187] *MATLAB 7 function reference, release 2010a*, <http://www.mathworks.com> (2010).
- [188] *MIT Photonic Bands (MPB)*, <http://ab-initio.mit.edu/mpb> (2003).
- [189] T. Betcke, *SIAM J. Matrix Anal. Appl.* **30**, 1320 (2008).
- [190] M. A. Morgan, S. Chang, and K. K. Mei, *IEEE Trans. Antennas Propag.* **25**, 413 (1977).
- [191] M. A. Morgan and K. K. Mei, *IEEE Trans. Antennas Propag.* **27**, 202 (1979).
- [192] J. Lee, G. M. Wilkins, and R. Mitra, *IEEE Transactions on Microwave Theory Techniques* **41**, 1981 (1993).
- [193] O. Chinellato, Ph.D. thesis, Swiss Federal Institute of Technology, Zürich (2005).
- [194] O. Chinellato, P. Arbenz, M. Streiff, and A. Witzig, *Future Gener. Comput. Syst.* **21**, 1263 (2005).

- [195] R. Hiptmair and P. D. Ledger, *Int. J. Numer. Meth. Engng* **62**, 1652 (2005).
- [196] M. Wong, M. Prak, and V. Hanna, in *IEEE MTT-S Dig.* (1995), pp. 285–288.
- [197] P. Lacoste and Y. Gay, in *Mathematical and numerical aspects of wave propagation phenomena* (SIAM, 1991), pp. 746–749, cited after ref. 196.
- [198] A. D. Greenwood and J. Jin, *IEEE Trans. Antennas Propag.* **47**, 1260 (1999).
- [199] J. P. Boyd, *Chebyshev and Fourier spectral methods* (Dover, New York, 2000).
- [200] D. Sun, J. Manges, X. Yuan, and Z. Cendes, *IEEE Antennas Propag. Mag.* **37**, 12 (1995).
- [201] I. Munteanu, *ICS Newslett.* **9**, 10 (2002).
- [202] C. Schwab, *p- and hp- finite element methods: theory and applications in solid and fluid mechanics* (Oxford University Press, Oxford, 1998).
- [203] Z. Xu and B. Wu, *Int. J. Numer. Meth. Engng* **75**, 945 (2008).
- [204] N. P. van der Aa, H. G. Ter Morsche, and R. R. M. Mattheij, *Electron. J. Lin. Algebra* **16**, 300 (2007).

Conception et modélisation numérique de composants optiques en nanophotonique intégrée

Résumé Cette thèse est consacrée à la conception et l'analyse théorique de différents composants en optique intégrée.

Nous présentons un modèle de milieu effectif pour les cristaux photoniques (CPs) 2D qui rend compte des effets de surface, puis un algorithme pour la conception de réseaux antiréfléchissants grand-angle pour ces CPs. Ces réseaux permettent d'améliorer significativement la transmission à travers une lentille plate d'indice négatif.

Nous proposons une nouvelle génération de circulateurs magnétooptiques compacts, fonctionnant dans un champ magnétique extérieur uniforme et constitués d'une cavité résonnante en anneaux circulaires couplée directement à des guides d'ondes standards.

Nous généralisons la méthode multipolaire 2D aux matériaux gyrotropiques et la formulons sans « lattice sums » pour les structures périodiques. Enfin, nous décrivons en détail la méthode des éléments finis pour le calcul des modes propres des cavités 3D en anneaux circulaires et matériaux gyrotropiques.

Mots clés cristaux photoniques, composants magnétooptiques, théories du milieu effectif, réseaux antiréfléchissants, méthodes numériques, optique intégrée.

Design and numerical modelling of integrated optical components

Abstract This thesis is devoted to the design and theoretical and numerical analysis of a number of photonic crystal (PC) components. In its first part we study the influence of the surface structure of two-dimensional (2D) PCs on their optical properties. We formulate an effective-medium model of such PCs, able to reproduce the commonly observed strong dependence of their effective parameters on the position of their truncation plane. We then develop an algorithm for the design of compact wide-angle antireflection gratings for 2D PCs and show them to improve significantly the transmission through a PC flat lens.

In the second part of the manuscript we introduce a new approach to the design of resonant cavities to be used in compact magneto-optical circulators. In contrast to structures proposed previously, they are devoid of oppositely-polarised magnetic domains, which significantly facilitates their fabrication. We show that these cavities need not be embedded in PCs, but can be coupled directly with standard rib waveguides.

Some numerical techniques developed in the course of this thesis are presented in the last part of the manuscript. We extend the multiple-scattering method to the case of gyrotropic materials and introduce a straightforward and extremely accurate method for the calculation of band structures of 2D PCs composed of circular cylinders, based on Fourier-Bessel expansions. Finally, we describe the implementation of the finite-element method for the calculation of eigenmodes of open, axisymmetric, three-dimensional cavities containing gyrotropic materials.

Keywords photonic crystals, magneto-optical devices, effective-medium theory, antireflection gratings, numerical methods, integrated optics.

Laboratoire d'accueil Équipe CLARTE, Institut Fresnel, Campus de Saint Jérôme,
avenue Escadrille Normandie-Niemen, 13397 Marseille Cedex 20
Formation doctorale physique théorique et mathématique